First Principles Study of the Electronic and Magnetic Properties of Defective Carbon Nanostructures

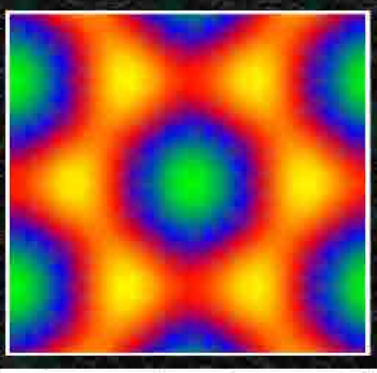

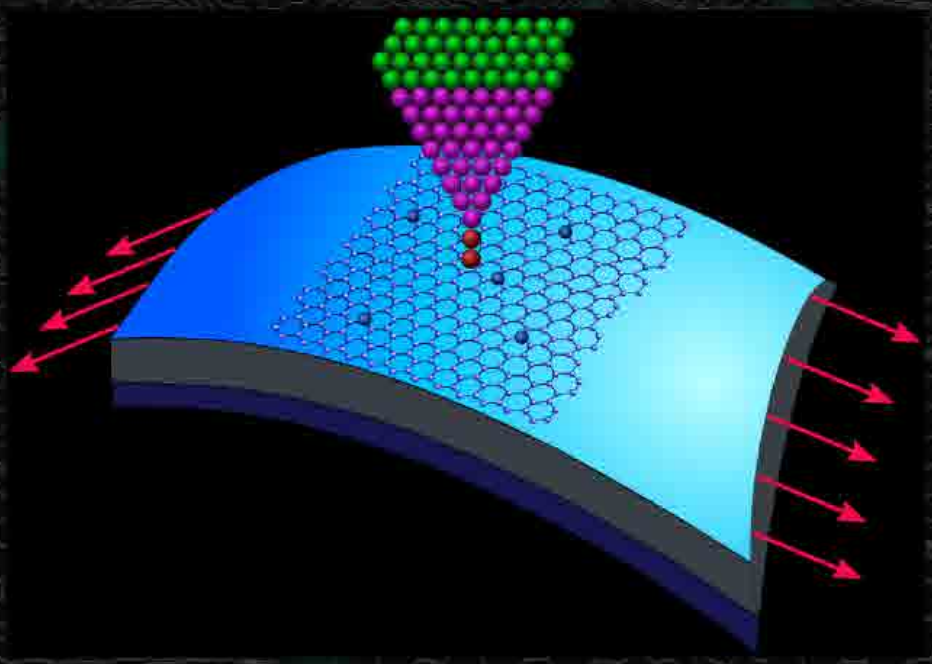

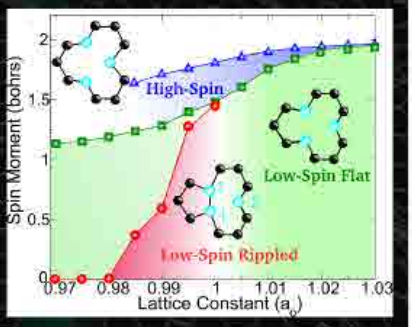

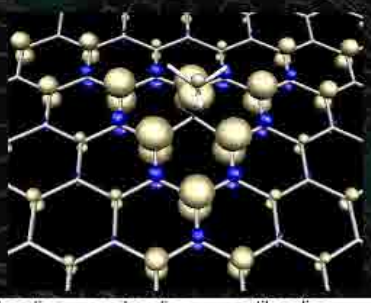

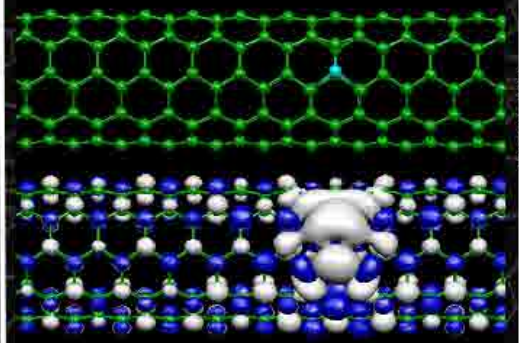

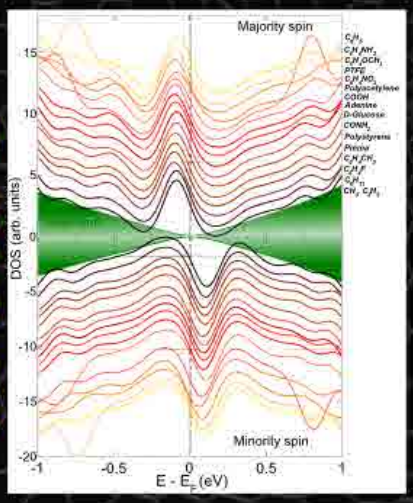

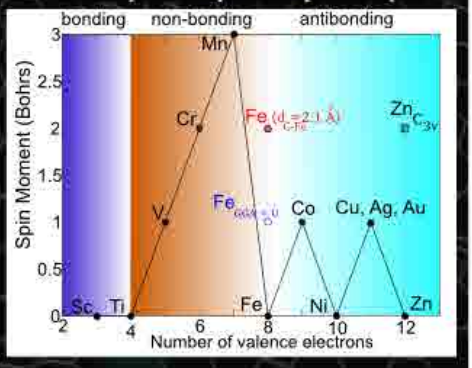

Doctoral Thesis submitted by
Elton Jose Gomes Santos
for the degree of Doctor in Physics

Universidad del País Vasco
Euskal Herriko Unibertsitatea

Ph.D Thesis

First-Principles Study of the Electronic and Magnetic Properties of Defective Carbon Nanostructures

Elton Jose Gomes Santos

Thesis supervisors: Daniel Sánchez Portal and Andrés Ayuela Fernández

Physics of Nanostructures and Advanced Materials, Department of Materials Science, University of Basque Country

July 2011

author's e-mail: elton.jose@gmail.com

ISBN: 978-84-695-1245-6

To Gurea and our extended family

Perhaps I can best describe my experience of doing mathematics in terms of a journey through a dark unexplored mansion. You enter the first room of the mansion and it's completely dark. You stumble around bumping into the furniture, but gradually you learn where each piece of furniture is. Finally, after six months or so, you find the light switch, you turn it on, and suddenly it's all illuminated. You can see exactly where you were. Then you move into the next room and spend another six months in the dark. So each of these breakthroughs, while sometimes they're momentary, sometimes over a period of a day or two, they are the culmination of - and couldn't exist without - the many months of stumbling around in the dark that precede them.

- Sir Andrew John Wiles

Faster, stronger, higher. You need to improve always.

- An olympic games proverb

Acknowledgements

The work presented in this Ph.D thesis was made possible by support of the Physics of Nanostructures and Advanced Materials Group at the Donostia International Physics Center (DIPC) and Centro Mixto CSIC-UPV/EHU (CFM), under the supervision of Prof. Pedro Miguel Echenique Landiribar. Many other colleagues in the group have greatly contributed to my work and enriched my life. Words are not enough to express my gratitude of all the memorable moments of my stay in DIPC and CFM. I would like to extend my sincere gratitude to all those that had given me a helpful hand in the past 4,5 years. Among them, I am especially grateful to:

My supervisors Daniel Sánchez Portal and Andrés Ayuela Fernández for their supervisions and scientific guidance. I would like to thank them for their support, encouragement, insight, hand-to-hand education and advices, as well as for their extensive feedback on my manuscripts and presentations. They always allowed me to pursue my own ideas and treated me, since the very first day on the same footing as a collaborator, listening to my suggestions and ideas, and having confidence in my potential. It has been a great pleasure and inspiration to work with you!

Pedro Miguel Echenique Landiribar, for his support and always present scientific view of the life. I am very grateful to him for sharing his wide physics wisdom with me during my first years in the Ph.D study as well as his good advices. I truly admire his optimism and permanent positive attitude which represented to me a vast source of motivation and energy to keep on track.

Mads Brandbyge, for his hospitality at my stays at Technical University of Denmark (DTU), fall 2009 and spring 2010, and for his endless energy for doing fruitful and inspiring comments. I very much enjoyed the pleasant working environment at DTU and the many hours expend in the "theory room 022" in weekends, holidays, etc, either alone or in the nice company of Mads Engelund, Jing Tao Lu, Joachim Alexander Fürst, Tue Gunst. I thank Mads Brandbyge not only for the privileged opportunity to work in his group but also for discovering such a kind and friendly person. I would like also to thank Prof. Antti-Pekka Jauho at DTU for the introduction about transport methods and Green's function formalism. His valuable course has given me the right tools to treat many problems in theoretical electronics as well as in scattering process.

The DIPC and CFM staff, Ana López de Goicoechea, Marimar Alvarez, Amaia Etxaburu, Txomin Romero Asturiano, Belen Isla, Carmen Martin, Luz Fernandez, Elixabete Mendizabal Ituarte, Maria Formoso Ferreiro, Karmela Alonso Arreche, Iñigo Aldazabal Mensa and Timoteo Horcajo (*In memoriam*), for making everything to work so fluently.

Sampsa Juhana Riikonen who helped me a lot in my first years with the SIESTA method and to understand the real life of a PhD student. Thank you for the many excursions that we

did together and for the friendship that remains so far.

Some people in the Physics of Nanostructures and Advanced Materials Group for sharing with me their time, experiences and for offering a pleasant working environment. They are Ricardo Díez Muiño, Andrés Arnau Pino, Javier Aizpurua, Iñaki Juaristi, Maite Alducin, Sebastian Bergeret, Eugene Chulkov, Ivo souza, Enrique Ortega, Vyacheslav Silkin, Angel Alegria, Lucia Vitali and Thomas Frederiksen. A special thank you goes to Thomas Frederiksen with whom I have had a lot of fun times and discussions about the TranSiesta code.

My beloved parents, Gomes and Letice, in the far away Brazil. For the constant support, to believe in my dreams all the time and to teach me how to think like a winner. I love you!

A person that for many days, nights, weekends and holidays of calculations, literature research, writing and rewriting articles, preparation of talks or meetings, etc, always has been with me. My sincerely thank you to my lovely wife Gurea. Definitely, without her encouragement, motivation, support, huge patience and trust this work would not have been possible. She has been my muse and a never ending source of inspiration, whom that has given me the strength and confidence to go forward and win the day-to-day battles. Life would not be the same as meaningful with her out!

Our extended family, Malkoa Zarandona Porras, Zuriñe Zarandona Porras, Felipe Otaño, Eliazar Porras, Kelyane Gomes, Marcos Gerser, Keyla Gomes, Alysson Correia, Ana Leticie, Matheus Gomes, Bat and Waity. For many moments together and for your love.

Finally, but not least, our friends, Txeffo, Lus, Angeloso, Carlos, Igor, Sergio, Patri, Maria, Leire, Yaiza, for enjoyable fun moments, Caminos de Santiago, excursions, dinners, lunchs, parties, bike trips, etc, or for just being there when you need.

Elton J. G. Santos,
Donostia-San Sebastián, August 16th 2011

Contents

Chapter 1

Introduction

This chapter serves to put into context the results presented in this thesis. We point out the importance of carbon nanostructures on today's science and technology. We give a brief overview on their structural and electronic properties. We start by presenting the graphene layer in 2D and it is followed by carbon nanotubes where the layer is rolled up into a quasi-1D structure. The electronic and scattering properties are affected by defects such as impurities and adsorbates, which can also generate magnetism. Finally the outline of the remaining part of the thesis is given.

1.1 Carbon

"Life exists in the universe only because the carbon atom possesses certain exceptional properties". Even said long time ago by Sir James Jeans, this sentence still contains an enormous amount of information about carbon if just some imagination and thinking are applied. During the industrial revolution in 19th century, carbon became one of the key elements for the development of new technologies in the modern world (railway, steel, chemical industries, etc). Nowadays, carbon is expected to be determinant for the next technological revolution coming soon. Like Silicon in the 20th century, which allowed the semiconductor industry to develop the current high performance electronics in less than eighty years, the hopes are that carbon and its new allotropes will allow for a similar development in a much shorter period of time. The reasons to look for alternatives to Silicon are that its physical characteristics that are useful for electronics will reach their limits in the nearly future [1]. For instance, the Complementary Metal-Oxide Semiconductor (CMOS) transistor would be close to its fundamental limits of a charge-based switch around 2024. In the meantime, it has become custom to change our notebook, digital camera, mobile phone, etc for a faster and better updated version at a timescale ranging from months to a few years. Therefore, other alternatives should be considered to process the ever increasing amount of data and information that nowadays life requires. The alternative in this context is to go to a *nanometer* scale or to a *nanotechnology* approach which has the carbon nanostructures as a model for new advances [2].

In his famous speech *"There is plenty of room at the bottom"* [3], Feynmann predicted the direct manipulation on the atomic scale as the novel challenge to be faced by the scientific community. In particular, he thought about the possibility of making electronic components on this lenght scale. The realization hereof can be boiled down to Moore's law which states

that the transistor density on integrated circuits (IC) doubles every two years [4]. As pointed out in the *Los Angeles Times*, if the same rate of performance improvement versus cost held for airlines, a flight from New York to Paris would cost one cent and will take less than a second. This has been made possible by the great advances in lithography which allowed ever denser and more complex IC. In agreement with Moore, IC and scaling are *"the cheap way to do electronics"* [5]. Even with large increases in lithography tool cost to fabricate microscale silicon-based transistors, the cost per transistor has decreased by many orders of magnitude during the last forty years. Conversely, at the same period of time, the cost of lithography equipment increased from \$10,000 to \$35 millions as shown in Figure 1.1 and is likely to remain increasing in the next near future. Nevertheless, this device scaling and performance enhancement can not continue forever. A number of limitations of fundamental scientific as well as technological nature place limits on the ultimate size and performance of silicon devices. This calls for new approaches such as the use of carbon nanomaterials as the key components of the device (e.g. conducting channel), for which the term carbon electronics has been coined. There are many reasons that highlight the role of carbon nanomaterials as the next paradigm for Moore's law. To cite some of them: **Temperature tolerance and stability**, carbon has higher thermal conductivity than conventional CMOS structures which could improve the operation temperature reducing it considerably; **Speed**, in the recently discovered graphene, electrons and holes can move through its structure ballistically, travelling for micrometers up to 2000 times faster than in silicon; **Size** , carbon nanostructures have the potential to dramatically extend the miniaturisation that has driven the density and speed advantages of the IC phase of Moore's law; **Power**, at the very small size scales needed to create ever denser device arrays, silicon generates too much resistance to electron flow, creating more heat than can be dissipated and consuming too much power. On the other hand, graphene, for instance, has no such restrictions [6]. Thus, these emerging carbon-based materials seem to offer new possibilities for future technologies that go beyond those of the CMOS applications. In the following sections we study some of the carbon nanostructures giving more details on their electronic and structural properties.

1.2 Carbon and its allotropes

Carbon exists in many allotropic forms. This is a signature of the very rich chemistry of carbon, the central materials for life on earth. Recently, some of the carbon allotropes have attracted a large amount of research and interest. This is partly driven by the promise of new technological applications, some of which have been already demonstrated in the laboratories. To cite some carbon allotropes, the sp^2 (graphene, nanotubes, fullerenes) and sp^3 (diamond) hybridised carbon networks are of particular interest because they have remarkable properties compared to other materials. Some of these properties include high hardness, mechanical resistance, resistance to radiation damage, anomalous quantum Hall effect, excellent thermal conductivity, biocompatibility and superconductivity. The recent discovered graphene, for example, has uncommon electronic and transport properties such as a high carrier mobility. The electrons in graphene can move without collisions over great distances, even at room temperature. Consequently, graphene has the ability to conduct electrical currents 10 to 100 times greater than conventional silicon-based semiconductors with very small head dissipation. In particular, this is one of the many features that makes graphene a promising candidate for

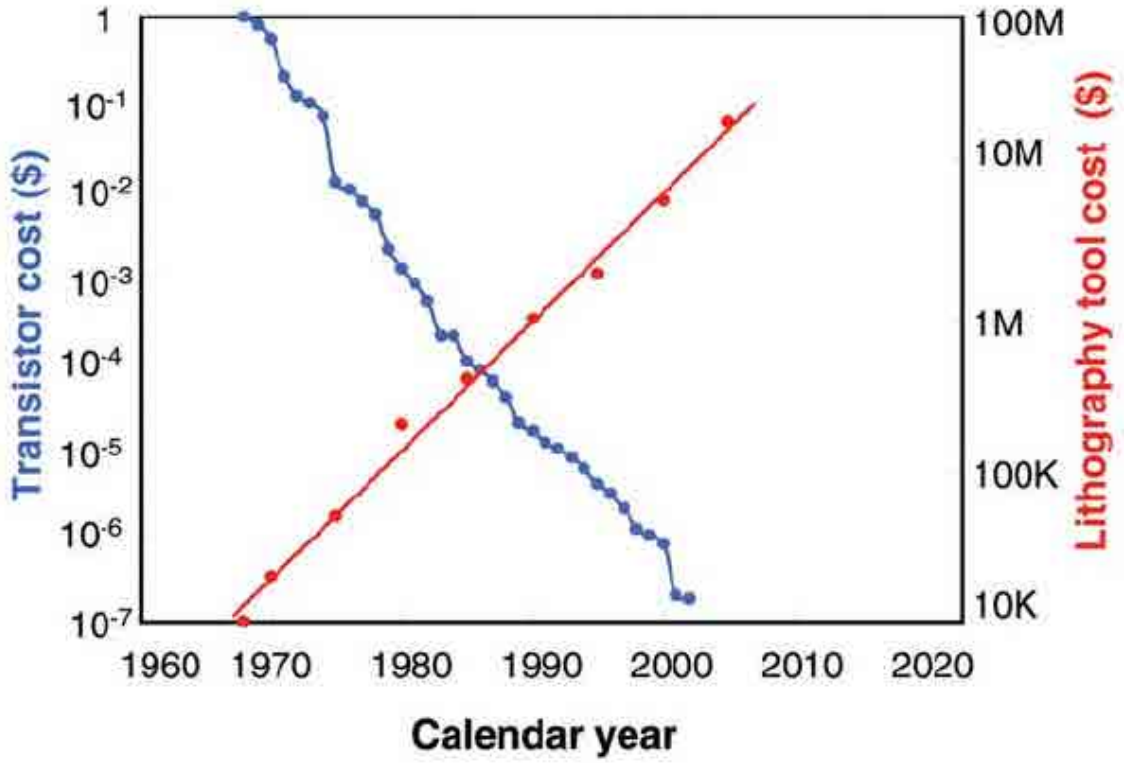

Figure 1.1: Lithography tool cost and transistor cost versus years. Reproduced from Ref. [5].

future electronic applications and has attracted a great interest in science and technology research. The number of papers in this field is growing exponentially as shown in Figure 1.2. The field has already two Nobel prizes: one in chemistry given to Curl, Kroto and Smalley in 1996 *"for the discovery of fullerenes"*; and another in physics, to Geim and Novoselov in 2010 *"for groundbreaking experiments regarding the two-dimensional material graphene"*; and still waiting for the third one in nanotubes (Iijima and Bethune?); this research community does not seem to stop growing up for the next few years and beyond. Furthermore, part of this growth is reflected by an acceleration of the increase in the upward slope of the number of publication of the graphene curve as shown in Figure 1.2 and in the number of researchers that are entering the field. It is also noteworthy that although the nanocarbon community had grown rapidly from the discovery of fullerenes in 1985, and later by nanotube-based research in 1991, graphene itself did not attract much attention until the 2004 publications of Geim and Novoselov [7].

The concept of graphene has been around for a long time since 1947 when P. R. Wallace published the first tight-binding model for a single graphite sheet [9]. He showed the unusual semimetallic behavior in this material and obtained the linear $E(k)$ dispersion around the K point of the Brillouin zone. However, at that time the interest in carbon nanostructures was minuscule and the only carbon material that had some relevance was graphite. In the years following Wallace's paper, graphene played an important role since it made the theoretical framework for understanding the electronic structure of other carbon allotropes that were progressively discovered (see Figure 1.3). For instance, fullerenes can be generated from graphene by introducting pentagons that create positive curvature defects, and hence,

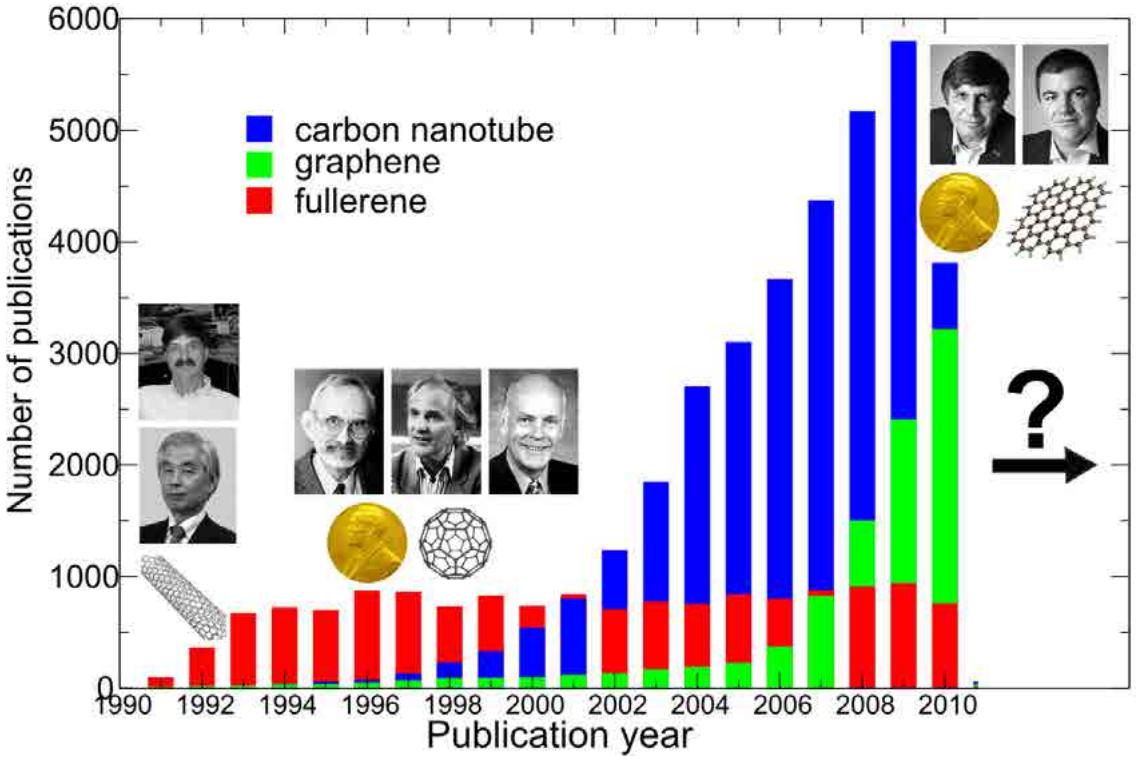

Figure 1.2: Record of publications from *ISI Web of Knowledge* with "carbon nanotube(s)" or "graphene(s)" or "fullerene(s)" in the topic. Insets from: The Nobel Foundation (nobelprize.org), Microscopy Society of America (www.microscopy.org), Metrolic (www.metrolic.com), NANOid (www.nanoid.co.uk), and IBM (domino.research.ibm.com).

fullerenes can be thought as a 0D nanocarbon. Although this idea seems to be simple, the experimental route to form these carbon cages from a flat graphene sheet is still a topic of research [10, 11]. Fullerene formation is based on four critical steps in a top-down mechanism starting from graphene flakes as is seen in Figure 1.4. Carbon nanotubes, in its turn, are obtained by rolling graphene along certain directions and connecting the carbon bonds as shown in Figure 1.5. Thus carbon nanotubes have only hexagons and can be thought as a 1D.

In the following, we shall describe the main properties of graphene and carbon nanotubes (CNT) with the focus on the electronic and structural features that will be important for this thesis.

1.3 Electronic Structure

1.3.1 Graphene

The peculiar electronic structure of graphene allows us to understand the quantum properties of other carbon nanostructures. The band structure of graphene at low energies, was first deduced by Wallace in 1947 [9] and can analytically be obtained within the π-orbital tight-binding approximation. This approximation treats just the p_z electron in each C atom as the main state relevant for describing the full electronic structure. C possesses four valence electrons, three of them form covalent σ bonds with the neighbours in the plane, and the fourth

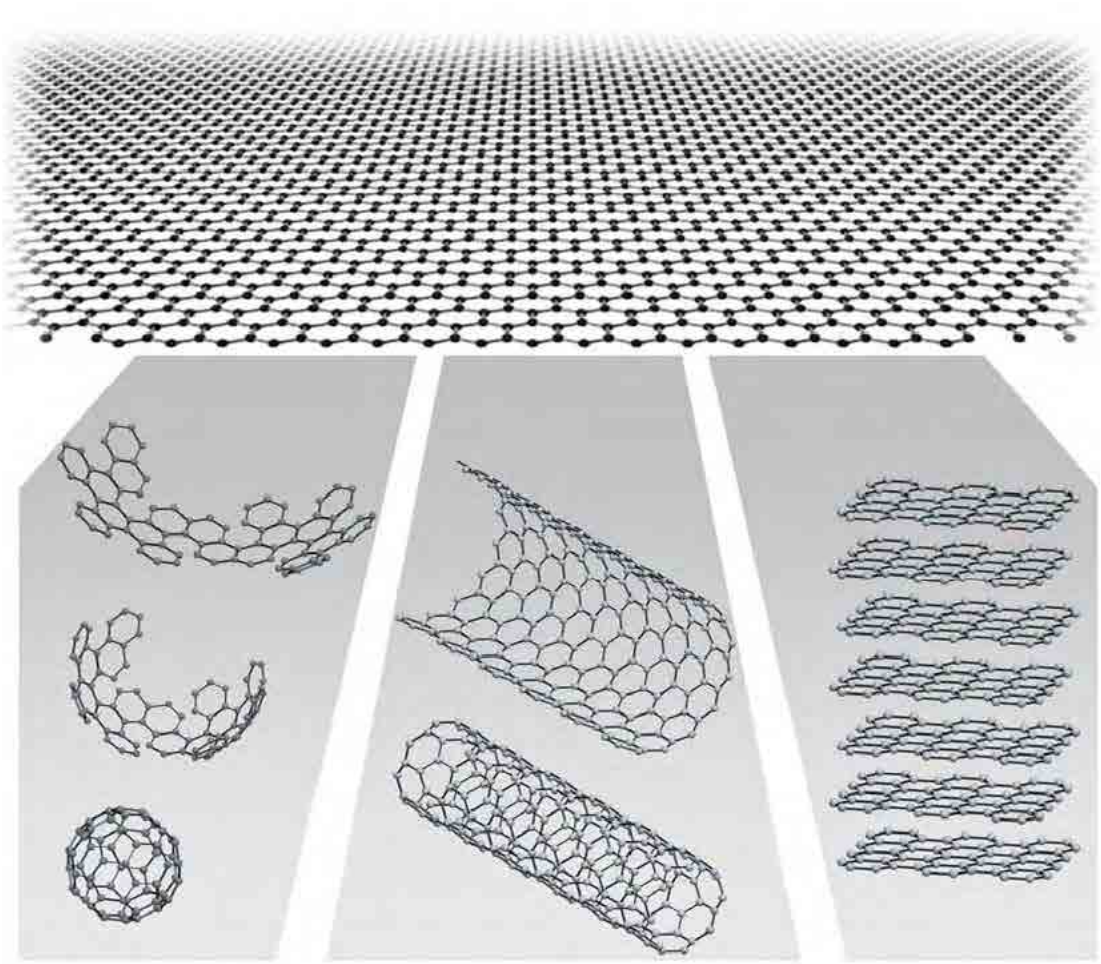

Figure 1.3: Graphene is the building block of all graphitic materials. It is considered as the basis for graphite, carbon nanotube and fullerenes (buckyballs). Reproduced from Ref. [8].

electron (π) is assumed to be located at the orbital perpendicular to the surface. Thus, for the flat layer the π-state is decoupled from the other C σ-states by symmetry (odd under inversion in the plane) and it can be calculated separately. With the help of Bloch theorem applied to the two-dimensional periodic lattice shown in Figure 1.6, the Hamiltonian in reciprocal space is a 2×2 matrix dependent on the **k**-vector:

$$\mathrm{H}(\boldsymbol{k}) = \varepsilon_o \boldsymbol{I} - \gamma_o \begin{pmatrix} 0 & 1 + e^{-i\boldsymbol{k}\cdot\boldsymbol{a_1}} + e^{-i\boldsymbol{k}\cdot\boldsymbol{a_2}} \\ 1 + e^{i\boldsymbol{k}\cdot\boldsymbol{a_1}} + e^{i\boldsymbol{k}\cdot\boldsymbol{a_2}} & 0 \end{pmatrix} \tag{1.1}$$

where the hopping energy for nearest neighbors is $\gamma_o = 2.7$ eV. This equation has two eigenvalues symmetric around ε_o:

$$E(\boldsymbol{k}) = \varepsilon_o \pm \gamma_o |1 + e^{i\boldsymbol{k}\cdot\boldsymbol{a_1}} + e^{i\boldsymbol{k}\cdot\boldsymbol{a_2}}| \tag{1.2}$$

In cartesian coordinates the lattice vectors can be written as $a_{1,2} = a(\sqrt{3}e_x \pm e_y)/2$ with $a = \sqrt{3}d_{C-C}$ (see Figure 1.6), where d_{C-C} is the distance C-C, and the energies can be expressed as:

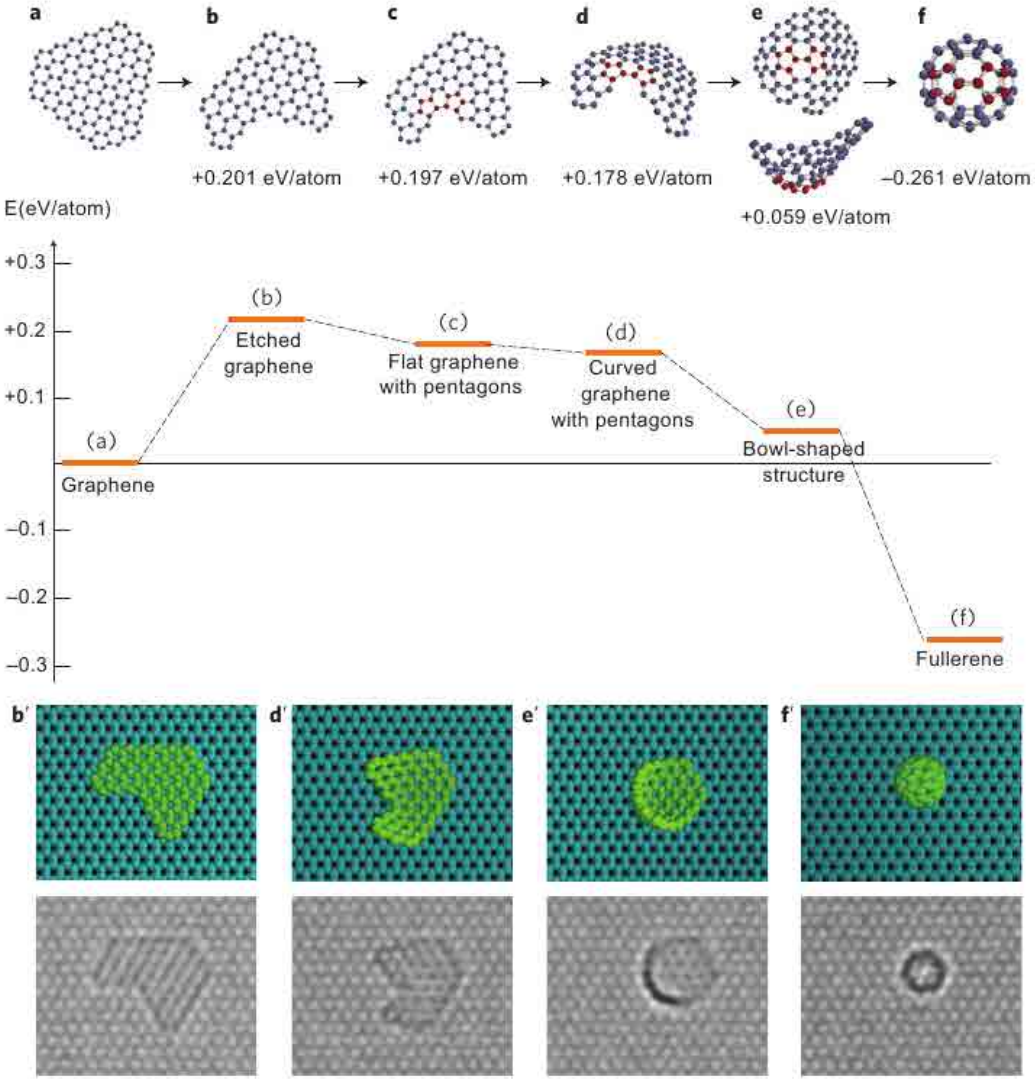

Figure 1.4: Quantum simulations and Transmission Electron Microscopy (TEM) experiments shed light on critical stages of fullerene formation from a graphene flake. The process begins with the loss of C atoms at the edge (a, b-insets), followed by the formation of pentagons (b, c) that curve the flake (c, d) and leading to zipping the flake edges (d, e) which results in the fullerene C_{60}. The reader can look at [10] for more details. Reproduced from Ref. [10].

$$\begin{aligned} E(\boldsymbol{k}) = & \quad \varepsilon_o \pm \gamma_o |1 + e^{i(a/2)(\sqrt{3}k_x + k_y)} + e^{i(a/2)(\sqrt{3}k_x - k_y)}| \\ = & \quad \varepsilon_o \pm \gamma_o \sqrt{1 + 4\cos(\sqrt{3}k_x a/2)\cos(\sqrt{k}_y a/2) + 4\cos^2(\sqrt{k}_y a/2)} \end{aligned} \tag{1.3}$$

The characteristic shape of the resulting band structure $E(\boldsymbol{k})$ is displayed in Figure 1.7. There are two symmetric bands coming from the eigenvalues $E(\boldsymbol{k})$. They touch at six points, where $E(\boldsymbol{k}) = 0$, but only two of them are inequivalent. Henceforth they will be called Dirac points with momenta $\boldsymbol{K}$ and $\boldsymbol{K}^{'}$, respectively. This band structure is symmetrical with respect to the Dirac points, and since there is one electron per atom, a neutral graphene sample will

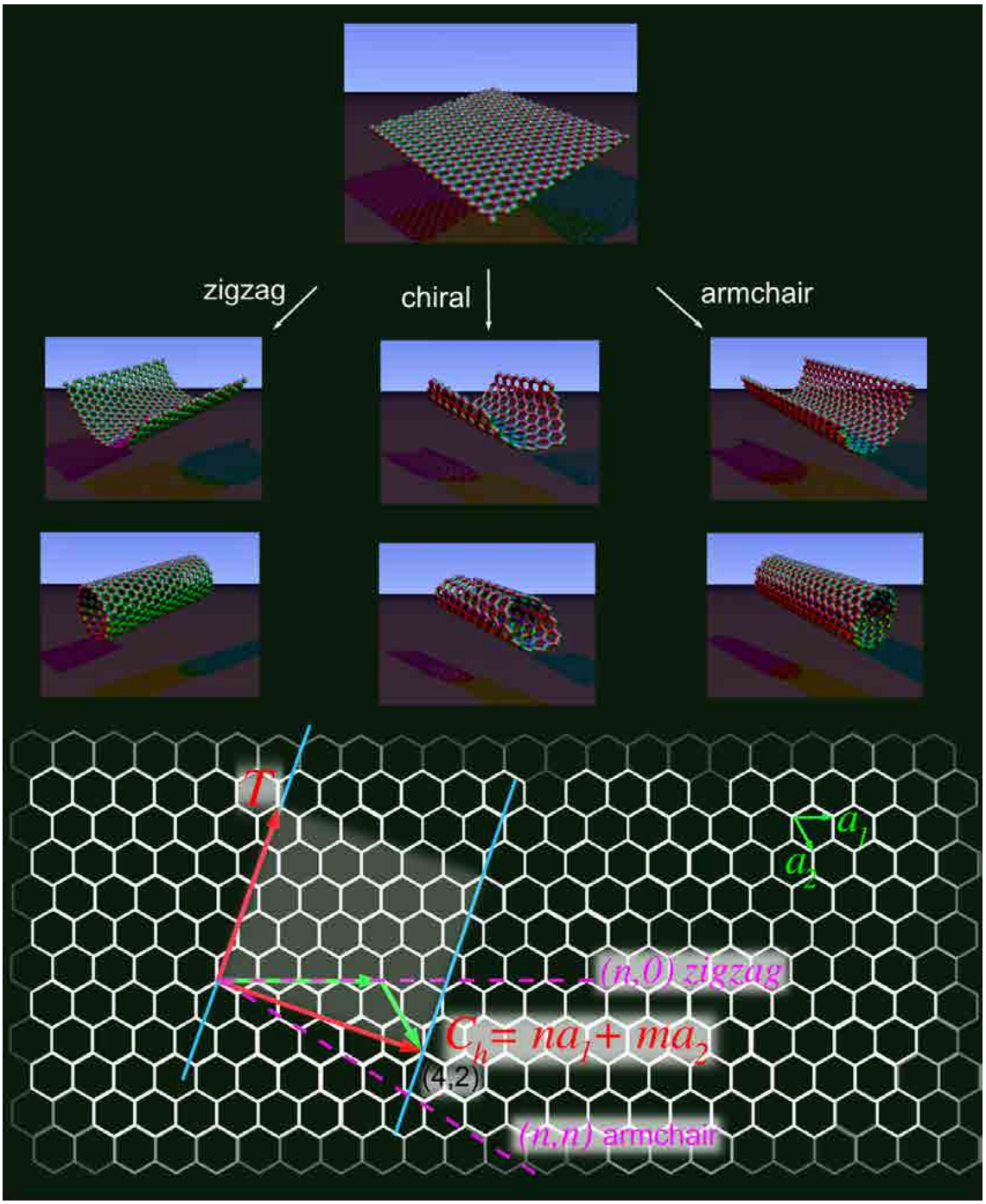

Figure 1.5: The structure of graphene and carbon nanotubes. A nanotube can be formed by rolling a ribbon of graphene along a lattice vector, C_h, defined by two integers, (n, m), such as the (4,2) lattice vector show here. Specifically, (n, n) nanotubes (armchair) are always metallic, and (n, m) nanotubes with $n - m = 3j$, where $j = 1, 2, 3, ...$, are nearly metallic. Tubes with $n - m \neq 3j$ are semiconductors. Insets for nanotubes are reproduced from WikiCommons.

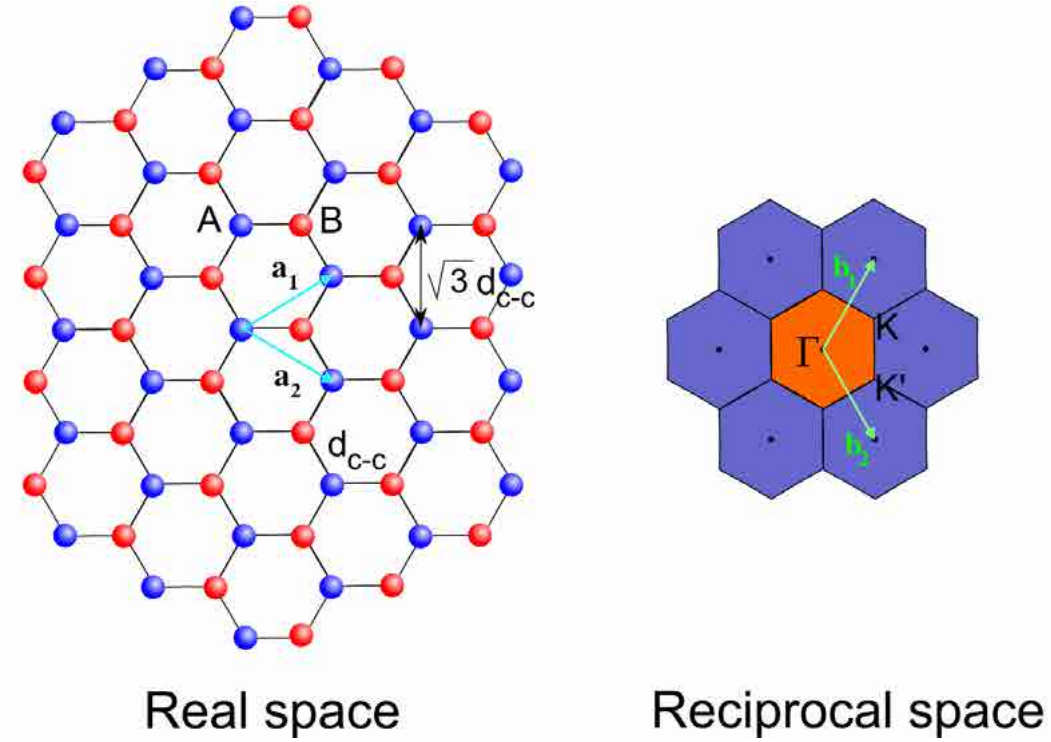

Figure 1.6: The honeycomb structure of graphene along with its first Brillouin zone in reciprocal space. The lattice vectors $\mathbf{a}_1$ and $\mathbf{a}_2$ have an angle of 60^o and a length $a = \sqrt{3}d_{C-C} \sim 2.46$ Å. The reciprocal lattice vectors $\mathbf{b}_i$ $(i = 1, 2)$, defined by $b_i \cdot b_j = 2\pi\delta_{ij}$ form an angle of 120^o and have a length of $a_i = 4\pi/\sqrt{3}d_{C-C} \sim 5.11$ Å^{-1}.

be at half-filling (π bands), i.e. Dirac points also form the Fermi surface of neutral graphene. Corrections by considering next nearest neighbors and orbital overlaps can break this electron-hole symmetry [12]. As shown in Figure 1.7, the dispersion relation close to the Dirac points can be linearised. Let us take one of the Dirac points, say $\boldsymbol{K}$, and make an expansion around it, $\boldsymbol{k} = \boldsymbol{K} + \boldsymbol{q}$, for small $\boldsymbol{q}$ compared to $\boldsymbol{K}$ we find:

$$E(\boldsymbol{K} + \boldsymbol{q}) = E(\boldsymbol{q}) \approx \pm v_F \hbar |\boldsymbol{q}| \tag{1.4}$$

where $v_F = \sqrt{3}a\gamma_o/2\hbar$ is called the Fermi velocity. By replacing numerical values, we find $v_F \approx 10^6$ m/s. A similar result can be obtained for $\boldsymbol{K}'$, where another valley exists. This result implies that the speed of electrons in graphene is constant, despite of any $k-$ or energy$-$dependence. This behaviour is similar to that of photons. Notice that a plot of the dispersion relation, as shown in Figure 1.7, has a peculiar shape of two opposed cones whose tips touch at the Dirac point. This is the reason why the upper band and the lower band are commonly called Dirac cones. Thus, for graphene samples whose chemical potential is placed near the *neutrality point*, that corresponds to the upper cone empty and the lower cone full, then its low-energy excitations have a linear dispersion relation. Moreover, this conical form mimicks the dispersion of a relativistic, massless, Dirac particles. This is by far one of the most striking property of graphene.

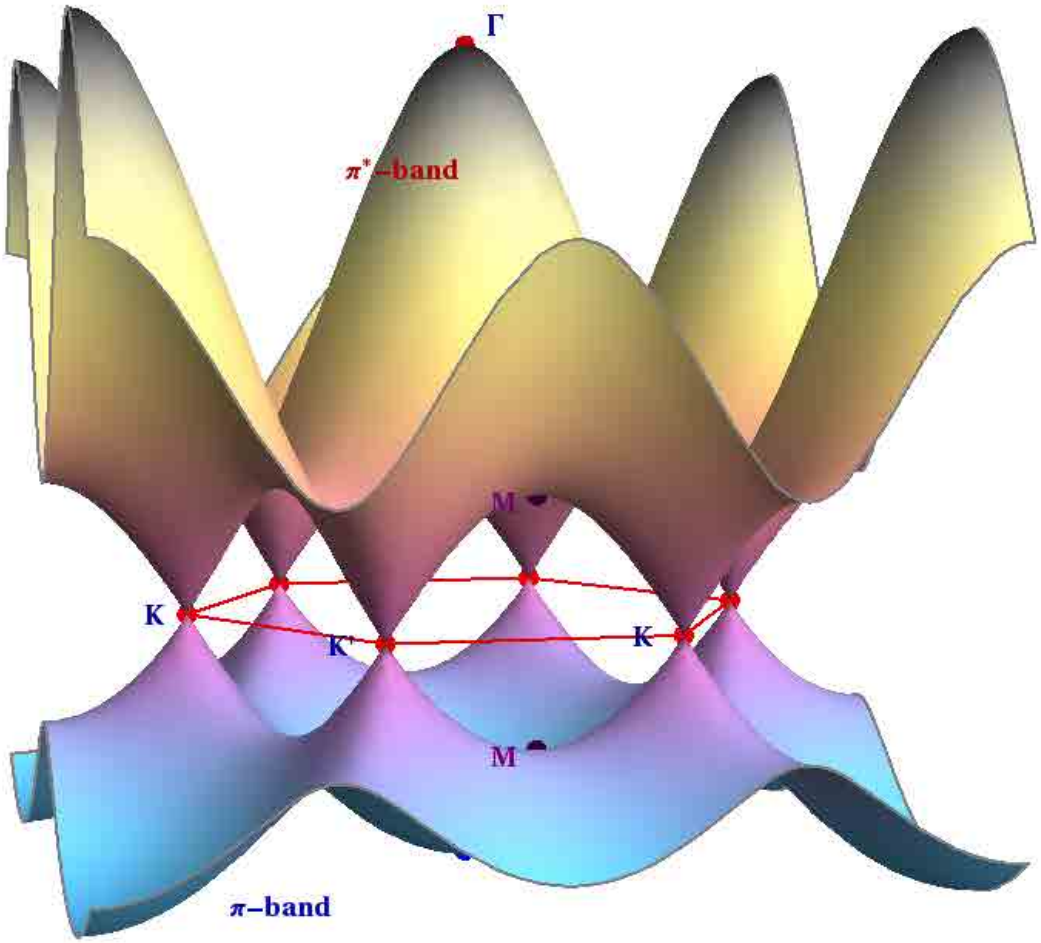

Figure 1.7: Band structure of graphene monolayer obtained by a π-orbital tight-binding approximation (Eq.1.3). The Fermi surface is reduced to Fermi points at the corners of the hexagonal Brillouin zone ($\boldsymbol{K}$ and $\boldsymbol{K'}$). Figure done with the MATHEMATICA program.

1.3.2 Carbon Nanotubes

The electronic structure of CNT's is usually discussed starting from the band structure of graphene and using the *zone folding approximation*. As already commented, the CNT can be formed by rolling a strip of graphene in a cylinder as seen in Figure 1.5. Thus, the electrical properties of carbon nanotubes have their origins in the electronic structure of graphene. Depending on the way that the graphene sheet is rolled up, carbon nanotubes can display a different set of electronic properties. Figure 1.5 also illustrates the common types of carbon nanotubes that can be formed in this process: zigzag, chiral and armchair. Their structures are specified by a pair of integers (n, m) that defines the lattice vector $\boldsymbol{C}_h = n\boldsymbol{a_1} + m\boldsymbol{a_2}$, that describes the nanotube circumference ($C_h = \pi d_{CNT}$, where d_{CNT} is the tube diameter), and the translational periodicity along the axis is given by the vector $\boldsymbol{T} = \frac{2m+n}{gcd(2n+m,2m+n)}\boldsymbol{a_1} - \frac{2n+m}{gcd(2n+m,2m+n)}\boldsymbol{a_2}$, which is perpendicular to $\boldsymbol{C}_h$. The factor $gcd(a, b)$ determines the greatest common divisor of the two integers a and b (see Ref. [13] for more details). For a given (n, m) nanotube index the graphene electronic band structure is then sectioned along the directions given by the nanotube Brillouin zone, whose spacing and lenght are related to (n, m). The

general form of the energy dispersion for any CNT is given by:

$$E(\mu, k_z) = E^g(\mu \boldsymbol{K_1} + k_z \frac{\boldsymbol{K_2}}{|\boldsymbol{K_2}|}) \text{ with } \mu = 0, \cdots, N-1 \text{ and } -\frac{\pi}{T} \leq k_z < \frac{\pi}{T} \tag{1.5}$$

where E^g is the graphene dispersion relation, N is the number of graphene unit cells inside the CNT unit cell, and $\boldsymbol{K_1}$ and $\boldsymbol{K_2}$ are the basis wavevectors in CNT Brillouin zone and are defined as follows: $\boldsymbol{K_1} \cdot \boldsymbol{T} = 0$, $\boldsymbol{K_1} \cdot \boldsymbol{C}_h = 2\pi$; and $\boldsymbol{K_2} \cdot \boldsymbol{T} = 2\pi$, $\boldsymbol{K_2} \cdot \boldsymbol{C}_h = 0$.

The zone folding approximation is based on the constraint that any electronic wave function of graphene must obey the condition $\psi(\boldsymbol{r} + \boldsymbol{C}_h) = \psi(\boldsymbol{r})$. In reciprocal space, this leads to a selection criterion for allowed **k** vectors based on the relation $\boldsymbol{C_h} \cdot \boldsymbol{k} = 2\pi\mu$, where μ is an integer. This shows the periodic boundary condition of quantum confinement around the nanotube circumference, which means that only stationary states having an integer number μ of wavelengths with period $k = 2\pi/|\boldsymbol{C}_h|$ are allowed around the circumferential perimeter. On the other hand, the linear momentum k_z changes continuously along the tubes axis as a result of the translational periodic boundary condition.

The **K** point at the corner of the Brillouin zone can be expressed as $\boldsymbol{K} = (2\boldsymbol{b_1} + \boldsymbol{b_2})/3$ leading to a simple rule that determines whether this point belongs to the set of allowed **k** vectors in the rolled up system:

$$\frac{\boldsymbol{C}_h \cdot \boldsymbol{K}}{2\pi} = \frac{(n\boldsymbol{a_1} + m\boldsymbol{a_2}) \cdot (2\boldsymbol{b}_1 + \boldsymbol{b}_2)/3}{2\pi} = \frac{2n+m}{3} \tag{1.6}$$

what can also be expressed as

$$\begin{aligned} 2n + m &= 3\mu \\ n - m + n + 2m &= 3\mu \\ (2n + m) - (2m + n) &= n - m \end{aligned} \tag{1.7}$$

which is equivalent to the condition for $n - m$ to be an integer multiple of 3. Whenever this condition holds, the **K** point fulfills the periodic boundary conditions, so that the Fermi energy (E_F) of graphene is in the spectrum of the CNT, i.e. the CNT is metallic[1]. In other cases, the closest lines of allowed **k** vectors miss the Fermi point by $\delta k = 2/3d_{CNT}$. Within the linear approximation at the **K** points, this results in a gap of $\Delta E_{gap} = 2v_F\hbar\delta k = \frac{4v_F\hbar}{3d_{CNT}}$. These concepts can be seen straightforwardly in Figure 1.8 that shows the two-dimensional Brillouin zone of graphene but with the cutting lines superposed.

Generally, the zone-folding approximation works reasonably well for large diameter CNTs but breaks down in thin CNTs due to curvature effects. In armchair CNTs this does not have much qualitative effects, because the bands crossing at the charge neutrality point are strictly protected by the intrinsic supersymmetry of the system [14]. In thin "metallic" zigzag and chiral CNTs, however, the calculation with more refined tight-binding parametrisation reveals a tiny gap opening at the Fermi energy [15, 16], which has also been confirmed experimentally [17].

[1] In other words, a CNT is metallic if a cutting line passes through a Dirac point $\boldsymbol{K}$ or $\boldsymbol{K}'$, otherwise is semiconductor.

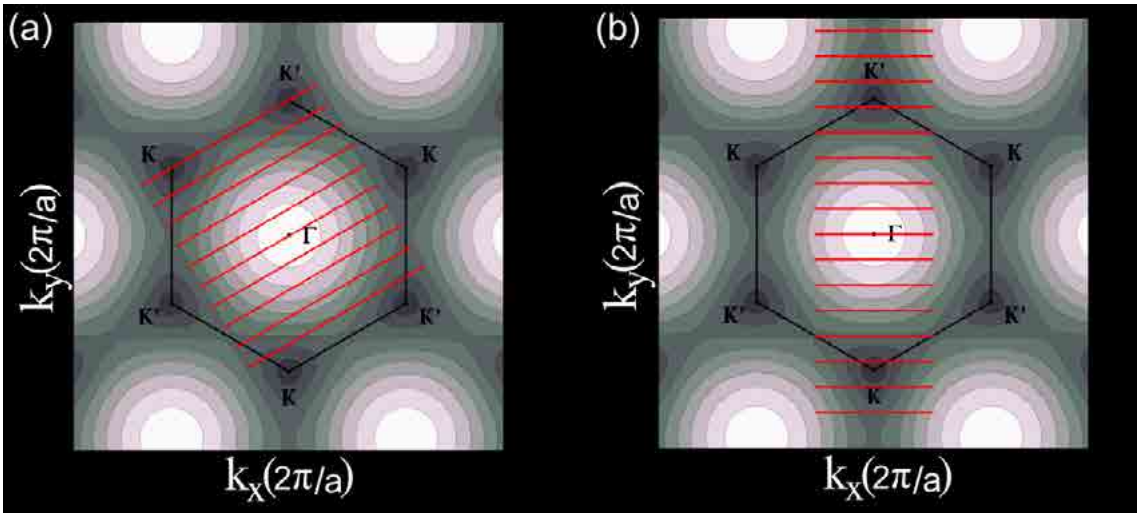

Figure 1.8: Two-dimensional Brillouin zone of graphene (k_x, k_y) displayed in terms of equi-energy lines with the Dirac points $\boldsymbol{K}$ or $\boldsymbol{K}^{'}$ at the vertices of the hexagon and with the Γ point at the center. Red lines denote allowed wavevectors when graphene is folded to form (a) a (5,5) and (b) a (8,0) single-wall carbon nanotube. Figure done with the MATHEMATICA program.

This quantisation rule leads to the formation of metallic or semiconducting nanotubes depending on the structural details of the tubes. These two properties are by far the most important reasons for carbon nanotubes to be explored in the context of an alternative to Si-technology for electronics. However, the controllable synthesis of carbon nanotubes delays progress. Until now, the microscopic growth process of carbon nanotubes remains unclear. Some models take into account the kinetics of carbon atoms on the surface of metallic nanoparticle (e.g. Fe) and look for migration barriers and the dependence on the different paths for diffusion. Although the results point that the shape or facet of the nanoparticle surface play an important role on the active sites for the diffusion of carbon during the growing nanotube, open questions still remain [18]. The growth of defect-free nanotubes continuously up to macroscopic lenghts and the extreme sensitivity of nanotube electronic features on the structural parameters are significant challenges for the future of this field [19].

1.4 Structural properties

1.4.1 Graphene as a two-dimensional crystal

Another striking property of graphene is its two dimensional character with a thickness of one-atom. Purely two-dimensional systems with long-range order, like a two-dimensional crystal, were supposed not to exist either because they had never been found in nature, and because there were reasonable theoretical arguments supporting this absence. The explanation was given by Landau and Peierls [21, 22] and later Mermin [23]. It is fundamentally based on the Mermin-Wagner theorem, that states that in dimensions $d \leq 2$, continuous symmetries cannot be spontaneously broken at finite temperature in systems with sufficiently short-range interactions. This means that no matter how low the temperature is, the energy cost associated with the creation of long-range fluctuations is small and outweighed by the entropy gain.

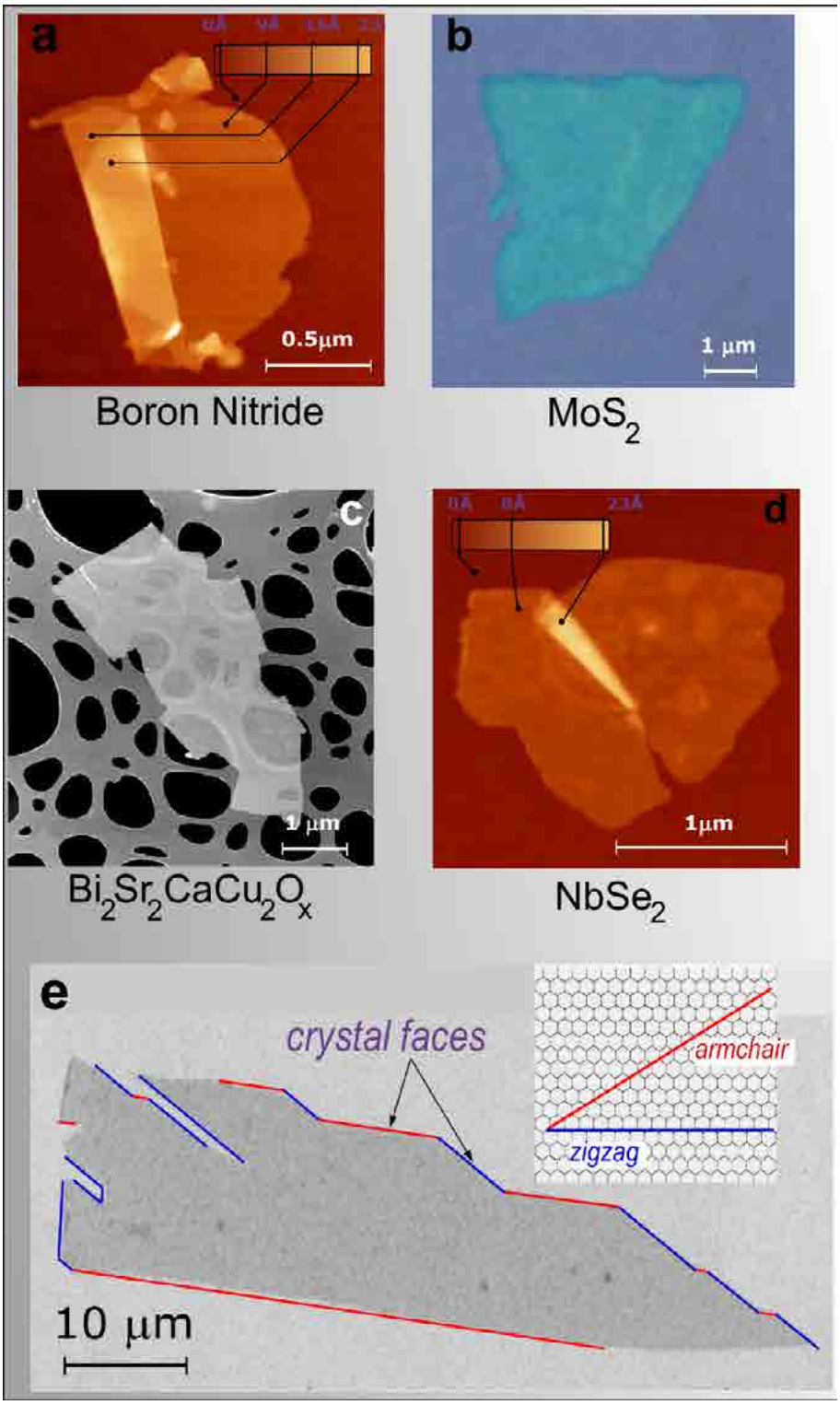

Figure 1.9: Two dimensional crystals that are one-atom to few-atoms thick. Single-layer of: **a** Boron Nitrite seen by atomic force microscopy (AFM); **b** MoS_2, by optical microscope; **c** $Bi_2Sr_2CaCu_2O_x$, by scanning electron microscopy (SEM); **d** $NbSe_2$, by AFM; and finally **e** graphene, by scanning-electron micrograph which shows the zigzag and armchair edges, which are indicated by blue and red lines and also displayed in the inset. Adapted from Refs. [7, 8, 20].

There are some examples that could be used to show this feature, for instance, in the two-dimensional Ising model [24]. With a Hamiltonian given by:

$$H = -J \sum_{<i,j>} \boldsymbol{S_i} \cdot \boldsymbol{S_j} \tag{1.8}$$

with nearest neighbour coupling J and spins $\boldsymbol{S_i}$, the average magnetization can be calculated as $< S^{1st} >= 1 - (1/2) \sum_{\alpha} < \sigma\alpha^2 >$, where

$$\sum_{\alpha} < \sigma\alpha^2(0) >= \frac{1}{\beta J} \int^{1/a} \frac{d^2k}{(2\pi)^2} \frac{1}{k^2} \tag{1.9}$$

where a is the lattice spacing, σ and α the field fluctuations, or low energy excitations. The integral above has a term proportional to

$$\int^{1/a} k^{-1}\, dk \tag{1.10}$$

which is logarithmically divergent. This means that low energy excitations at low temperatures lead already to deviations from the ground state. This argument explains why no thermally stable magnetic order occurs in two dimension (and even on one).

We now translate these concepts to graphene theory and formulate the problem in terms of vibrations or phonons: The thermal fluctuations of phonon modes lead to displacements of atoms that become comparable to interatomic distances at any finite temperature. In fact, the melting temperature of thin films rapidly decreases with decreasing thickness, and they become unstable (separate into islands or decompose) at a thickness of, typically, dozens of atomic layers [25]. For this reason, atomic monolayers have so far been known only as an integral part of larger three-dimensional structures, usually grown epitaxially on top of monocrystals with matching crystal lattices.

Two dimensional materials were assumed not to exist until 2004. However, new experiments were able to isolate graphene [7] and other free-standing two-dimensional crystals [20], for example, single-layer boron nitride, $NbSe_2$ and MoS_2, as seen in Figure 1.9. Graphene is a two-dimensional crystal living in a three-dimensional world, and the latter can provide a mechanism to stabilize the in-plane stretching fluctuations by coupling them to out-of-plane bending modes. Real samples would be crumpled, something that was experimentally confirmed [26]. In those experiments, graphene on a scaffold geometry developes some "ripples" which have static undulations of typical sizes $\sim 5 - 10\ nm$ and height variation $\sim 0.5\ nm$.

1.4.2 Ripples at free-standing graphene

However, the origin of the observed corrugation in graphene is still controversial, since depending on the particular experiment is not clear whether ripples are formed spontaneously or induced by corrugations from the substrate, or by some chemical agent present in the environment. In the case of graphene on top of SiO_2, there are experimental evidences indicating that the corrugations come from the substrate, because a clear correlation between both of them was observed [27, 28]. However, in the case of suspended graphene spontaneous formation of ripples after heating and cooling the samples has also recently been reported [29].

First attempts to answer why graphene crumples are given by soft-condensed matter theory. A continuous model of the membranes embedded in three dimensions [30] showed that although mostly flat membranes exist, they are not perfectly flat, but they have intrinsic ripples. In fact, corrugations of graphene flakes have been observed [26, 31] recently by Transmission Electron Microscopy (TEM) and diffraction techniques which somehow agree with this theory [30]. Those experiments are summarised in Figure 1.10. The flat graphene sheet in real space (Fig.1.10(a)) and its 3D Fourier transform (Fig.1.10(c)) consist of a set of rods perpendicular to the reciprocal hexagonal lattice. For that graphene, the intensity of diffraction peaks could vary with the tilt angle, but without broadening. If the peaks become wider with increasing tilt angle it indicates that the rods move around their average direction (Fig. 1.10(d)-(i)) and form cones indicating that the sheet is slightly corrugated (Fig. 1.10(b)). Such roughness results in a diffraction pattern formed for an ensemble of two-dimensional crystallites with different orientations in relation to the average plane. Figure 1.10(e)-(f) show the diffraction patterns for 0^o and 14^o tilt angles, respectively. The broadening of the diffraction peaks is large for the latter pattern and it is marked by the arrows. This behaviour vanishes for an increasing number of layers as we can see in Figure 1.10(g). The peak broadening can also be seen in Figure 1.10(h) which illustrates the evolution of the peak width for different tilt angles. The peaks are sharp at normal incidence and their width increases almost linearly with tilt angle.

1.5 Magnetism in Carbon-Based Materials

The observation of magnetism in, until a few years ago, so considered non-magnetic materials is receiving much attention, both experimental and theoretically [32]. Materials that already possess attractive properties, such as low density, biocompatibility, plasticity, capacity to form diverse structures, and that, in principle, could develop magnetic features have stimulated the field of magnetism based in light-elements. Among all candidates, carbon-based systems are currently gaining special importance [33]. Carbon-based magnetic materials would greatly extend the limits of technologies relying on the magnetism of d and f elements or diluted magnetic semiconductors. Room temperature metal-free magnets could find applications in medicine, nanotechnology and telecommunications, and give the prospect for carbon-based electronics as already described in the previous sections. Additionally, carbon-based materials are quite promising for spintronics and related applications due to their long spin relaxation and decoherence times owing to the low intrinsic spin-orbit interaction and the low hyperfine interaction of the electron spins with the carbon nuclei [34–37]. Therefore, to find alternative routes to create pristine magnetic carbon is an important research topic and it will be the subject of the next section.

1.5.1 Radiation-induced defect formation and ferromagnetism

Graphite in its ideal pristine form is diamagnetic. Nevertheless, several experimental groups recently reported the occurrence of ferromagnetic signals of different strengths in graphite samples after proton irradiation [38, 39], chemical modification, electron bombardment, or hydrogen plasma treatment [33], even at room temperatures. The presence of magnetic metals as dopants was experimentally excluded (or it was present only at negligible level), indicating

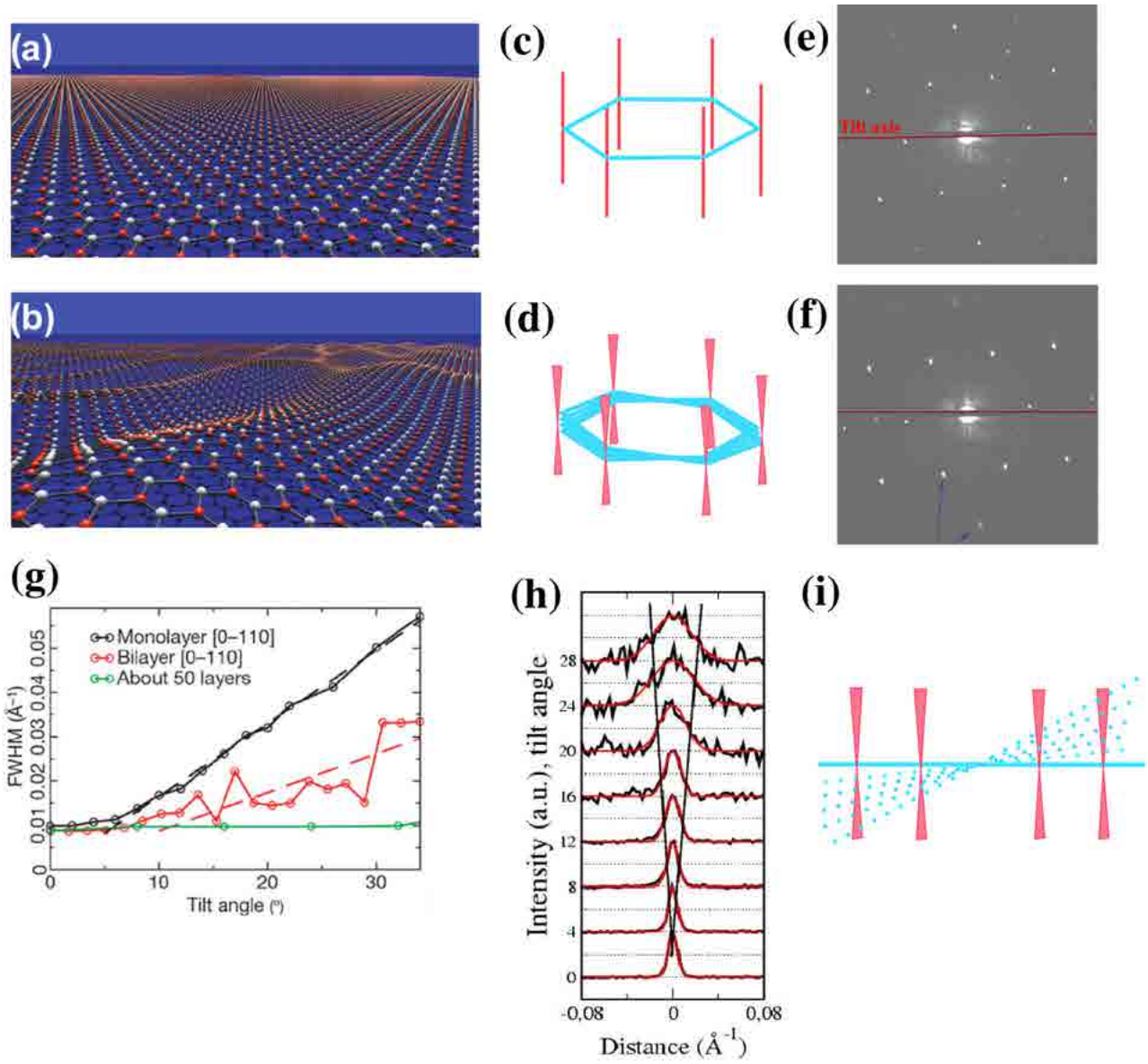

Figure 1.10: Graphene monolayer at a (a) flat and (b) rippled geometry. (c) The reciprocal space for a flat graphene sheet, in which the diffraction intensities form a sharp set of rods (red). (d) Similar to panel (c) but for the corrugated graphene where the diffracted intensities are obtained by a superposition of many rods with slightly different orientation. (e),(f) Electron diffraction patterns from a graphene monolayer under incidence angles of 0^o and 14^o, respectively. The tilt axis is horizontal. (g) Full widths at half maxima (FWHM) for some diffraction peak in monolayer, bilayer and graphite as a function of the tilt angle. The dashed lines are the linear fits yielding the average roughness. (h) Peak profiles reflection for different incidence angles (black line) and Gaussian fits (red curve), with an offset that corresponds to the tilt angle in degrees. A cone that connects the curves at approximately their FWHM is drawn as guide to the eye. (i) Side view of the peak broadening for different diffraction beams which turns the rods into cone-shaped volume. Thus, the the diffraction spots become blurred at large angles what is indicated by the dotted lines. Adapted from Ref. [26, 31].

that magnetism should come from the graphite itself. Although the origin of magnetic order in pure carbon is only poorly understood, some guesses have been considered.

Radiation damage of matter is governed by the displacement of atoms from their equilibrium positions due to electronic excitations and direct collisions of high-energy particles with the nuclei. In metals and narrow band gap semiconductors electronic excitations quench instantaneously, leaving collisions with nuclei as the main mechanism responsible for the creation of defects in graphite and related carbon materials [40]. If the kinetic energy transferred from a high-energy electron or ion to the nucleus is higher than the displacement threshold T_d, a carbon atom can leave its initial position to form a metastable defect structure on a subpicosecond time scale. Such events are called knock-on displacements. For highly anisotropic layered carbon materials the threshold of the off-plane displacement is $T_d^{\perp} \sim 15 - 20eV$ [41], while the creation of a defect due to the in-plane knock-on collision requires higher transferred energies $T_d^{\parallel} \geq 30eV$. Possible defects produced by radiation damage include separated and intimate pairs (Frenkel-pairs) [42, 43] of interstitial atoms and vacancies, and in-plane topological defects involving non six-membered rings, e.g. Stone-Wales defect [44]. Thus, it is believed that the appearance of bound states due to lattice disorder is one of the main driving forces for a decrease in the diamagnetism and an increase in the spin density in graphite [33].

Several theoretical studies have also suggested that the intrinsic magnetism is due to the presence of undercoordinated carbon orbitals originated by impurities, boundaries or defects [45,46]. All these defects produce also quasilocalized states close to the E_F and can give rise to a net magnetic moment. It is worth noting that these states extend over several nanometers around the defects and, in the case of vacancies, can form a characteristic superstructure recognised as $(\sqrt{3} \times \sqrt{3})R30^o$ in STM images. By analysing the position and the orientation of the superstructures, one can locate the defect and determine the sublattice to which the vacancy belongs [47]. The fact that quasilocalized states lie at E_F suggests that magnetism can be induced by electronic exchange. It has been argued recently, that Stoner ferromagnetism with high Curie temperatures T_c can be expected for sp electron systems [48]. Furthermore, the narrow impurity band is an essential ingredient for the ferromagnetism observed in those systems. However, one should take care of the inhomogeneous spatial distribution of defects in the system in order to obtain good estimates of T_c [48].

1.6 Vacancy-induced magnetism

1.6.1 $\pi-$Vacancy

As we mentioned in the previous section, several experiments have reported the observation of magnetism in carbon materials. The main explanation is due to the presence of defects, such as vacancies, cracks, or edges, that change the coordination of the carbon atoms and generate spin polarized states in the defective region, with energies close to the E_F. Defects and edges are therefore crucial to explain the magnetic properties. Based on that, the mechanism leading to ferromagnetism in carbon structures can be understood intuitively by means of the Hubbard model for the honeycomb lattice which we now introduce.

Magnetism is a physical property that is directly related to electron-electron interactions. The Hubbard model [49] helps to add the effects of electron-electron interactions to systems whose bare band structure is well described by a tight-binding model. The model assumes

that the Coulomb interaction is screened, so that it can be represented by an on-site repulsion term of strength U. The Hamiltonian for the model reads:

$$H = -t \sum_{<i,j>,\sigma} c^{\dagger}_{i\sigma} c_{j\sigma} + U \sum_{i,\sigma} n_{i\uparrow} n_{i\downarrow} \tag{1.11}$$

where $< i, j >$ stands for nearest neighbors of the honeycomb lattice and σ for the spin degree of freedom ($\uparrow$, $\downarrow$). The first term in Eq. (1.11) corresponds to the one-orbital per site p_z tight-binding model that is obtained as the interactions are switched off. An approximate value of the Hubbard coupling U in graphene can be estimated in several ways from first principles calculations. The values obtained usually lie in the range $U/t \approx 1 - 2$ [50], but higher values have also been quoted [12]. Due the exponential growth of the Hilbert space dimension with the number of sites N a standard way to solve the Hubbard model is by means of a mean-field theory. A direct exact diagonalization of the Hubbard model (1.11) at half-filling is only possible for systems until about 20 sites [51]. Thus, in order to treat problem with more than just few atoms Eq.1.11 is approximated by:

$$H^{MF} = -t \sum_{<i,j>,\sigma} c^{\dagger}_{i\sigma} c_{j\sigma} + U \sum_{i,\sigma} (\langle n_{i\uparrow} \rangle n_{i\downarrow} + n_{i\uparrow} \langle n_{i\downarrow} \rangle - \langle n_{i\uparrow} \rangle \langle n_{i\downarrow} \rangle) \tag{1.12}$$

where i and j runs over all lattice sites and $t \sim 2.5$ eV.

Graphene is an example of a bipartite lattice, i.e. a lattice consisting on two different sublattices A and B where atoms A are only linked to atoms B and vice-versa. Concerning the ground state of a Hubbard model in such a lattice, Elliott Lieb [52] proved a useful theorem for a repulsive value of the Hubbard interaction U, the ground state of the half-filled lattice is non-degenerate and has a total spin equal to half the number of unbalanced atoms $2S = N_A - N_B$. This rule has been confirmed recently in a number of studies of graphene with vacancies, edges or larger defects [53–55], and in the graphene bilayer [56]. As a result, Lieb's theorem has become a paradigm for magnetic studies in graphene clusters and nanographite [50]. The major part of these works have an imbalance between the two sublattices, $N_A \neq N_B$. For instance, a vacancy removes an atom of a given site. An additional complication beyond the scope of Lieb's theorem has to be taken into account. When an atom is removed, two scenarios are possible. Either the disrupted bonds remain as dangling bonds or the structure undergoes a bond reconstruction with several possible outcomes (we will come to this point in the next sections). In both cases, a local distortion of the lattice is expected.

In the following discussion, however, it is assumed that, as first approximation, the creation of a vacancy has the effect of removing a p_z orbital at a lattice point, together with its conduction band electron. This is the so-called a π-vacancy[2]. In this sense, the physics of the conduction band electrons is still described by Eq. 1.12, where now the hopping to the vacancy sites is forbidden. If the distribution of vacancies is uneven between the two sublattices, zero energy levels or quasilocalized states will necessarily appear at E_F. In other words, whenever the two sublattices are not balanced with respect to their number of atoms, there will appear $N_A - N_B$ states with energy $E = E_F$ and localized at the majority sublattice [12, 52]. The ground state at half-filling has either a spin up or spin down occupying the localized state at

[2]We have used vacancies to exemplify this rule, but it holds as well as for a hydrogen atom on top of a graphene atom as we will see in the next section.

$E = E_F$, so a net magnetic moment localizes around the vacancy for an arbitrarily small value of the Coulomb interaction U [57]. In Figure 1.11(a) we show a typical spin density around a vacancy in a π-tight binding model. It can be seen that short-range ferrimagnetic order is induced around the vacancy site. The spin density on the opposite sublattice to the vacancy is larger than that on the same sublattice.

We now consider two vacancies at the same sublattice (e.g. (A,A)). In this situation, the ground state is degenerate at $U = 0$ with four degenerate states appearing at E_F as seen in Figure 1.11(b). Without the Coulomb interaction, singlet and triplet states are degenerate and Lieb's theorem guarantees that the triplet state becomes the ground state in the presence of a Hubbard U (> 0). At finite U a local moment is induced around both vacancies and they couple ferromagnetically. Figure 1.11(c) also shows the weak modification of the local spin moment M_t^{local} as a function of U for different distances l_{max} from the vacancy site.

When two vacancies are at different sublattices (e.g. (A,B)) the problem becomes different. Now, the eigenvalues generated by the vacancies do not vanish in general (see Figure 1.11(d)). When the distance r between them is large, the energy position of the vacancy state goes to zero [53, 55, 57]. This means that vacancies interact: a vacancy at sublattice A creates a state with a wavefunction which is only finite on sublattice B, and vice-versa, and sites of type A and B are connected by the electronic Hamiltonian. This results in a splitting between the two quasilocalized states associated with the vacancies on different sublattices and they move from $E = E_F$ (see inset (II) in Figure 1.11(b)). At any value of U, two of the quasilocalized states are now occupied and the total moment vanishes. This still agrees with the Lieb's theorem [52], but it is possible to have a non-zero local magnetic moment at each vacancy site. Figure 1.11(e) shows the behaviour of the total sublattice magnetization M_{tot}^s as a function of the distance r between two vacancies located at different sublattices. When the distance is small between them, $r/a \leq 6$, no local magnetic moment appears. However, when they are far away from each other, a local moment is induced around each vacancy. In this case, the induced net moments at the defect sites are antiparallel. This can be understood as a consequence of the antiferromagnetic tendency of the half-filled honeycomb lattice. In fact, the net moments induced around defects are also equal in magnitude. In Figure 1.11(c) we see that a critical value of U_{cr} is needed to create a finite moment in the system. Although we have only focus on vacancies in an infinite graphene layer, the results discussed here also hold for ribbons [54] and other carbon geometries [50]. It is noteworthy that the quasilocalized states around E_F have a strong directional character, as we can see in Figure 1.11(f) for two monovacancies in an armchair graphene nanoribbon. Depending on the alignment between the two vacancies, their magnetic coupling is not invariant against the exchange of positions because the quasilocalized states could hybridise differently [54]. In the inset of Figure 1.11(f) the splitting energy differs when both vacancies are positioned in a *tail-tail* ($B + A$) or *head-head* ($A + B$) configuration. The physics of a π-vacancy in graphenic nanostructures is thus a rich topic which will have an important place in the next parts of the present thesis. Therefore, the interpretations and arguments exposed in this section will be used below.

1.6.2 Real carbon vacancy

So far, we have focused on the electronic properties of a π-vacancy in graphenic nanostructures. However, the vacancy in the real word reconstructs due to the other sp electrons that are not considered explicitly in the Hubbard Hamiltonian Eq.(1.12). The vacancy can thus display

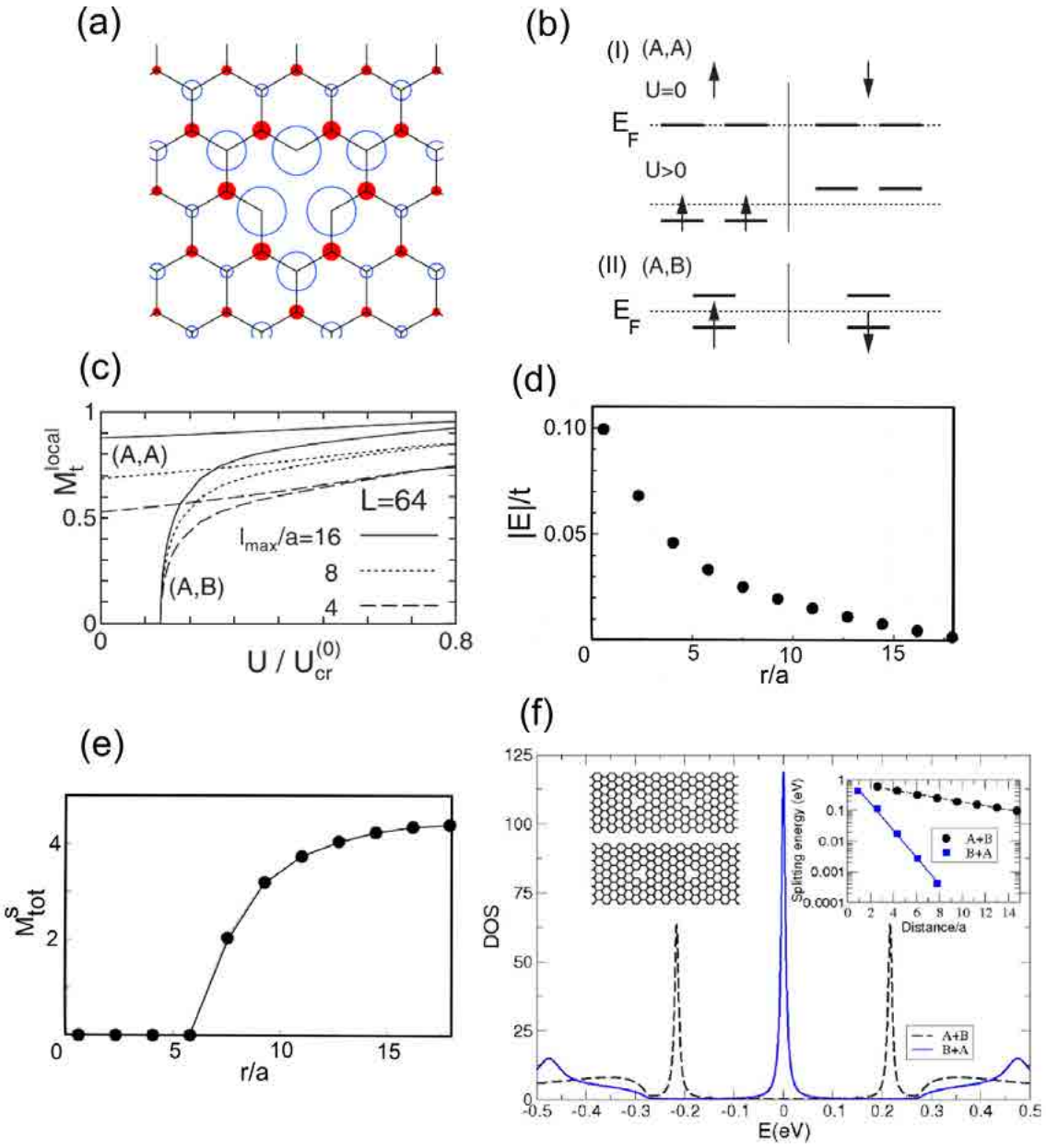

Figure 1.11: (a) Spin density around a vacancy in graphene using a p_z-tight binding model. The area of the circles is proportional to the magnitude of the spin density at each lattice point. Empty and filled circles represent positive and negative magnetic moments, respectively. (b) Spin configuration at the ground state with two vacancies (I) at the same sublattice and (II) at the opposite one. In panel (I), when $U = 0$ four levels appear at the E_F, with two levels per spin channel. At finite U (> 0), the degeneracy is split up with two states being occupied of spin up. In panel (II), despite of the value of U, two of the states are occupied and the total moment always vanishes. (c) Local spin moment M_t^{local} as a function of U for a lattice $L \times L$. The value U_{cr} denotes the critical value of U when a finite moment appears. The value l_{max} is the distance between the vacancy sites. (d) Energy E of a vacancy state created by two vacancies at different sublattices as a function of the distance r. (e) Total sublattice magnetization M_{tot}^s as a function of the distance r between two vacancies in different sublattices. The lattice constant is $a = 2.46$. (f) DOS for an armchair ribbon of $W = 7a$ with two vacancies in different orientations. The solid lines correspond to the $B + A$ case (left lower inset) and the dashed lines correspond to the $A + B$ case (left upper inset). Right inset: Bonding-antibonding energy splitting as a function of the distance between vacancies for two different alignments. Adapted from Refs. [54, 55, 57].

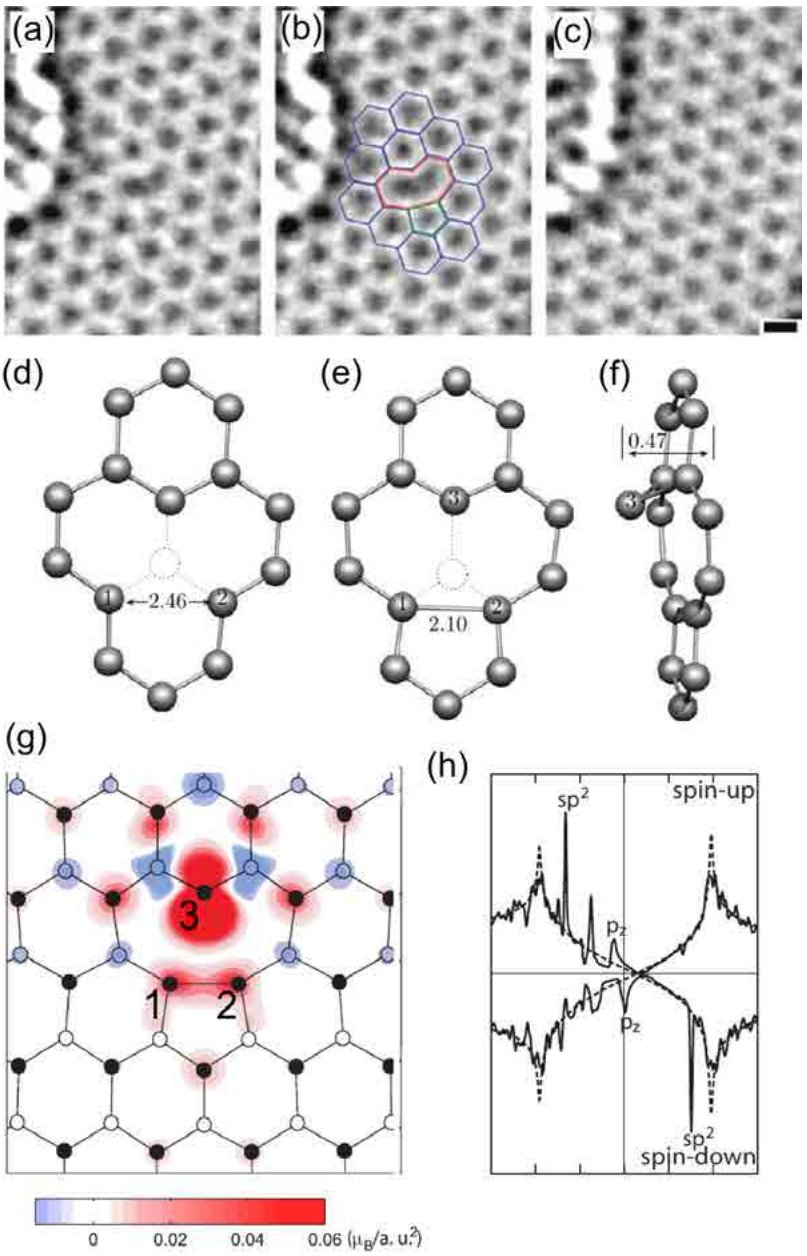

Figure 1.12: (a)-(c) High resolution-TEM (HRTEM) image sequence of a monovacancy in a graphene monolayer: (a) original image of the defect and (b) with the atomic configuration superimposed on top (a pentagon is marked in green); (c) relaxation to unperturbed lattice after 4 s. (d) Structure of a symmetric D_{3h} vacancy in graphene with the missed C atom drawn with dashed lines. (e) and (f) are the top and the side views, respectively, to the optimised structures of the distorted C_s vacancy. The distances are given in Å by the number in the figures. The atoms 1 and 2 suffered a Jahn-Teller distortion that reduce the energy of the system and formed the pentagon-like bonding structure. (g) Calculated spin density projection on the graphene plane around the vacancy defect. (h) Density of states (DOS) for spin-up and spin-down channels after the creation of the monovacancy. The dashed line shows the DOS of graphene. Labels indicate the character of the defect states. Adapted from Refs. [58–60].

new electronic and geometric features beyond those present in a p_z tight-binding model. In the following, we shall address the experimental observation of a monovacancy in graphene and also its basic electronic and magnetic properties.

For graphene, several experiments have observed vacancies and more complex defects [59, 61–63]. Those experiments irradiate the sample for some time using a focused electron beam. Similar to proton irradiation in graphite (as seen in Section 1.5.1) but now with a subnanometer spot (e.g. $\sim 1-3$ Å). Vacancies can be created with atomic precision at predefined positions. For instance, we show a sequence of HRTEM images taken at room temperature of a reconstructed monovacancy in a single-layer graphene in Figure 1.12 (a)-(c). The vacancy is observed by the formation of a pentagon-like bond (see Figure 1.12(b)). After a few seconds the missing atom is replaced by a mobile adatom on the graphene surface as is seen in Figure 1.12(c). The monovacancy reconstructs in a geometry of C_s symmetry different from the D_{3h} structure displayed in Figure 1.11(a). The D_{3h} vacancy undergoes a Jahn-Teller distortion. This effect is shown by first principles calculations [60] which predict an energy lowering of about 0.20 eV, divided into two parts: (i) the in-plane and symmetry preserving distortion with 0.09 eV, and (ii) the out-of-plane and symmetry lowering with 0.11 eV. The reconstructed geometries are plotted in Figure 1.12(e)-(f). For the symmetric D_{3h} vacancy (Figure 1.12(d)), the bond length between the first nearest neighbour atoms to the vacancy and the next-nearest neighbours is shortened to 1.37 Å while the nearest-neighbour bond length in perfect graphene is ~ 1.42 Å. This distortion preserves the symmetry and lowers the energy by $\sim$0.09 eV. Other bond lengths are only slightly changed. For the ground-state C_s, the distortion forms a pentagon-like structure with a bond length of $\sim$2.1 Å.

The bond formation that accompanies the symmetry lowering lowers the energy by $\sim$0.10 eV. Atom 3 suffers an out-of-plane displacement. This can be explained because the paired electrons in the new bond between atoms 1 and 2 in Figure 1.12(e) repel the electron on the opposite atom 3, so that the easiest direction for moving is an out-of-plane displacement of few tenths of an Angstrom [60]. We show the spin density projection on the graphene surface generated by the reconstructed monovacancy in Figure 1.12(g). Most of the spin moment of the vacancy ($\sim$1.04 μ_B) is due to atom 3, with a resulting spin pattern that only follows approximately the original bipartite character of the graphene lattice. The bipartite character is actually broken by the $1-2$ bond.

Although this description of the monovacancy seems to be detailed, substantially, as we will see in Chapter 5, this picture is still incomplete in order to fully understand the magnetism of monovacancies in graphene. There are more ingredients that determine the stability of spin solutions in a vacancy and its interplay with the global structure can create novel effects.

1.7 Impurities in graphene

To exploit the unique electronic properties of graphene requires to understand the effects of impurities in this material. Impurities are inevitable sources of electron scattering left from the production process and they may limit electron transport in graphene to a substantial extent. However, apart from being just undesirable, impurities provide a powerful tool for controlling the electronic properties of graphene. In solid state materials, a clear application of impurity states is the doping of semiconductor. In addition, impurities in graphene allow us to address fundamental questions: for instance, impurity states in this material are directly related to

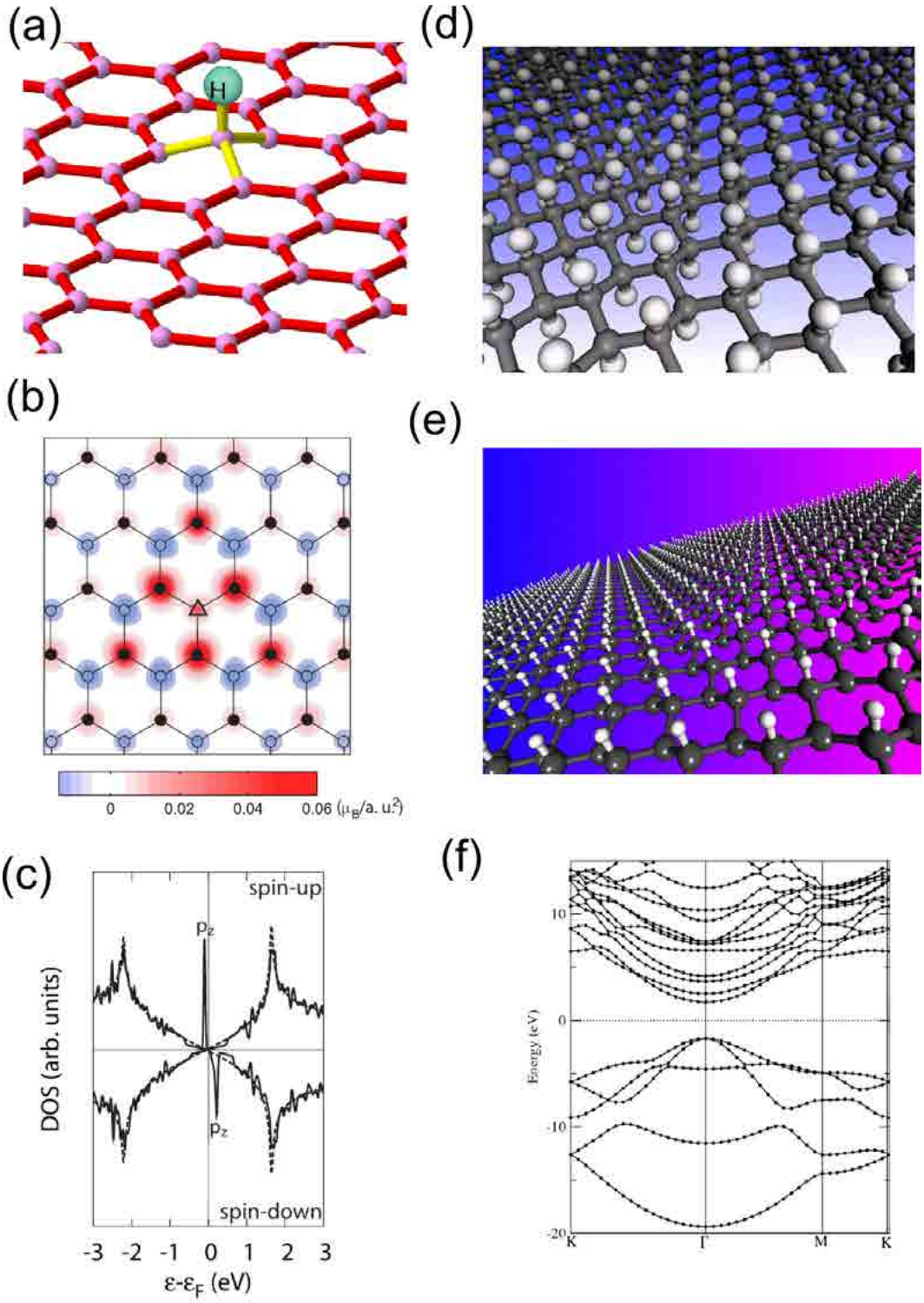

Figure 1.13: (a) Geometry of a H atom chemisorbed on top of a C atom in graphene. (b) Spin density projection around the H atom. (c) The resulting density of states (DOS) for spin-up and spin-down states after the doping. The dashed line shows the DOS of the ideal graphene. Labels indicate the character of the defect states. (d) Structure of the full hydrogenated graphene monolayer, graphane, in the chair conformation. The panel shows the hexagonal carbon network with carbon in the sp^3 hybridization. (e) Geometry of half-hydrogenated graphene monolayer (graphone) that was predicted to display magnetic behaviour. (f) Band structure of graphane with a clear band gap. Adapted from Refs. [58, 64–67].

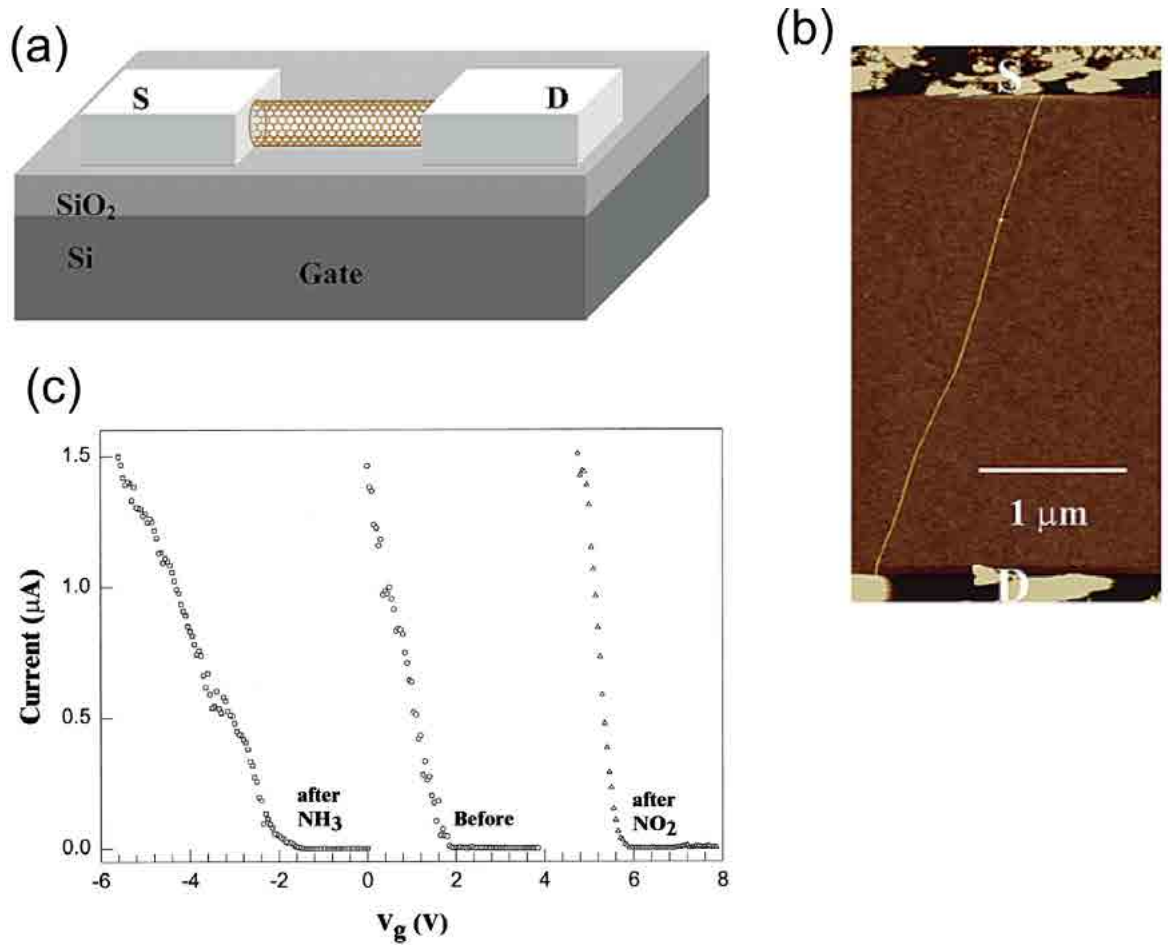

Figure 1.14: (a) Schematic structure of a back-gated CNT-FET device. (b) AFM image of the device: CNT with a backgate made by SiO_2 and source (S) and drain (D) electrodes. (c) Chemical gating effects in the semiconducting CNT. Current versus gate voltage curves before (circles) and after NO_2(triangles) or NH_3 (squares) exposures. The measurements with NH_3 and NO_2 were carried out successively after sample recovery. Adapted from Refs. [72, 73].

scattering of relativistic quasiparticles [68–71]. In this section we describe how adsorbates and impurities modify the electronic properties of graphenic nanostructures. We describe how magnetism can be generated by using H atoms chemisorbed on graphene and we give some examples of experiments where adsorbates can modify the electron transport. Later we shall describe our own investigation on the effect of substitutional metallic impurities in graphene and CNTs, taking into account recent experimental observations.

1.7.1 H atoms chemisorbed on graphene

In the previous section we have seen how missing atoms can create a magnetic order in graphene monolayers. Despite of being a quite different defect from a vacancy, chemisorbed molecules and atoms on graphene, in particular H atoms, could also generate magnetism. Here we describe the main electronic and magnetic properties caused by this kind of functionalization in order to understand the magnetism generated by more complex adsorbates in Chapter 4.

A H atom chemisorbed on top of a C forms a σ-bond and makes the sp^2 configuration to change into an approximately sp^3 configuration, as shown in Figure 1.13(a). This removes a p_z-orbitals from the $\pi - \pi^*$ band system and generates a spin density (Figure 1.13(b)), similar to that from a monovacancy in a π-tight-binding model of graphene (see Figure 1.12(g)). If more than one H is adsorbed, the graphene sublattice will play a role: for adsorption at A-sublattice, the spin-density localises at B sublattice, and vice-versa[3]. When a H atom has been adsorbed on the surface, an unpaired electron is left on the neighbouring C atoms, which due to its resonant character is shared with the nearest neighbours. In fact, the nearest C neighbours contain most of the 1.0 μ_B magnetization. It is important to remark that there is one defect state for each spin channel. The degeneracy is lifted when the exchange-correlation effects are taken into account leading to separation of the graphene bands for spin-up and spin-down states with a magnetic moment of 1.0 μ_B per defect and exchange splitting 0.23eV at 0.5% H concentration [58] (see Figure 1.13(c)).

A recently reported material that could be seen as a fully hydrogenated version of graphene is the so-called graphane [74] which is shown in Figure 1.13(d). As graphene, pure graphane consists of a hexagonal lattice of carbon atoms, however, with atoms in a sp^3 hybridization. In addition to the three neighboring carbon atoms, each carbon atom is covalently bonded to H atoms on alternate sides of the graphene surface. Graphane, as well as graphene, can be viewed as a crystal consisting of two surfaces without an interlayer. It is thus not surprising that this material is very sensitive to its environment. By attaching H atoms only to one graphene side as shown in Figure 1.13(e) one can create a new material based on graphene. Theoretically predicted to be magnetic, this half-hydrogenated graphene or graphone [65] is seen as an alternative way to create a magnetic material based completely in light atoms. On the other hand, graphane presents a non-magnetic semiconducting behaviour [75] as seen in Figure 1.13(f).

In general, by adding functional groups to graphene its properties can be significantly changed and turned to a particular application. We will have the opportunity to discuss this fascinating problem more extensively in another chapter, being one of the topics selected for this thesis.

1.7.2 Molecular adsorption on graphene and carbon nanotubes

Other important issue of the chemistry of graphene and CNT's as well is the molecular adsorption, in addition to light atoms as H, of molecules, radicals, polymers, etc, which is also called functionalization. Similar to organic chemistry in which functional groups are added to an organic molecule in order to change its properties, the same principles also hold for carbon-based materials. By attaching functional groups to the graphitic structure, both chemical and physical features can be tailored.

Experiments showed that adsorbates on graphene and related materials can strongly affect, apart from the magnetic properties, charge transport by doping and causing scattering of electrons. Since 2000, CNT based gas sensors have been reported [72, 73, 77]. They place a semiconducting CNT on a SiO_2/Si substrate and make contacts with normal metallic electrodes. By using Si as a back gate, a field effect transistor (FET) is constructed as shown in Figure 1.14(a)-(b). The gate voltage V_g between tube and Si substrate is used to charge the

[3]The Lieb's theorem also holds for this situation.

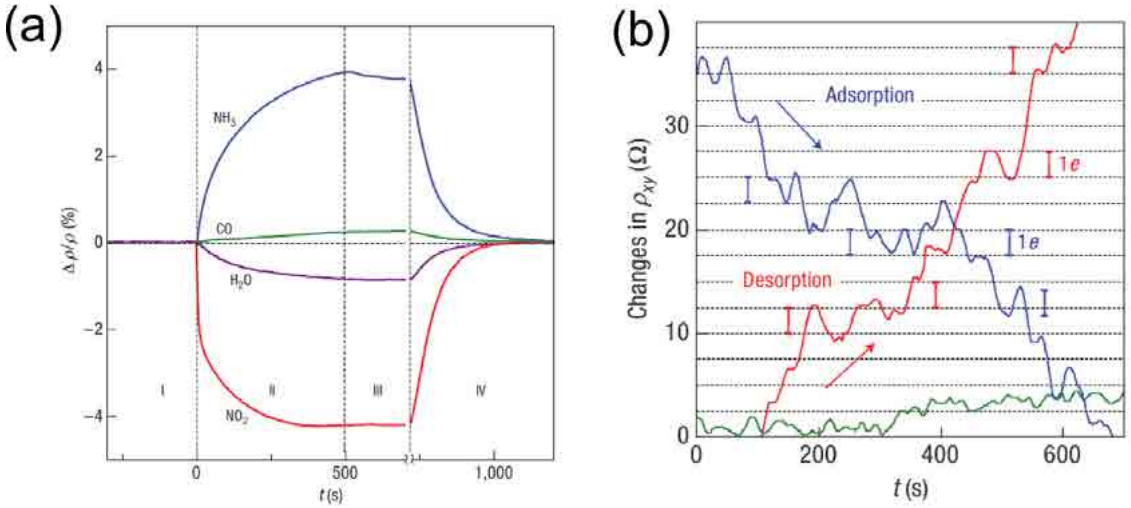

Figure 1.15: (a) Response in the resistivity ρ of single graphene layer devices to NO_2, H_2O, NH_3 and CO in concentrations of 1 ppm in He at atmospheric pressure. The positive (negative) sign of changes in ρ were added to indicate electron (hole) doping. (b) Examples of changes in Hall resistivity observed near the neutrality point during adsorption of strongly diluted NO_2 (blue curve) and its desorption in vacuum at 50 ^{o}C (red curve). The green curve is a reference of the same device thoroughly annealed and then exposed to pure He. The curves are for a three-layer device in B = 10 T. The grid lines correspond to changes in ρ_{xy} caused by adding one electron charge. Adapted from Ref. [76].

CNT and to tune the chemical potential inside it. The current through such CNT-FET turns out to be sensitive to gas exposure. Kong *et al.* [72] found a shift of the current vs. gate voltage curves in different directions upon NH_3 and NO_2 exposure (Figure 1.14(c)). Similarly, CNT-FETs are affected by other adsorbates including H_2O [73], K and O_2 .

Such setup in graphene is strongly sensitive to gas exposure [7]: the resistance R of a graphene multilayer device has been measured upon H_2O, NH_3 and C_2H_5OH adsorption. R drops down upon exposure to water, while ethanol and ammonia exposure as well as placement in vacuum increase it. Later experiments [76] studied the sensitivity of graphene based devices to active gases in more detail. Combining measurements of the longitudinal and the Hall resistivity (ρ_{xx} and ρ_{xy}, respectively) the chemically induced charge carrier concentrations Δn and their signs were determined. The measurements shown in Figure 1.15(a) demonstrate that NO_2 and H_2O act as acceptors, while NH_3 and CO are donors. For NO_2, the adsorption of single molecules seems detectable as the height of steps occurring in Hall resistance ρ_{xy} (Figure 1.15(b)). This corresponds to the removal or addition of one electron to the graphene sample [76]. Such steps occur only, when the sample is exposed to NO_2 or annealed after exposure but not, e.g., for a clean sample in He flow. Moreover, no such steps have been detected for H_2O, NH_3 or CO adsorbing on graphene. In general, the response of graphene and CNT devices to gas exposure can be different or caused by different mechanisms: for CNT devices Schottky barriers can control the response [79], whereas for graphene the Schottky effect is suppressed due to the vanishing gap.

Impurities are indeed local perturbations and to understand their effects we must investigate the induced change in the electronic properties. In the next section, we shall explore the electronic structure of graphene (and CNTs) substitutionally doped by metallic impurities. In fact, this will introduce the main subject of the thesis, which will be studied in the chapters of

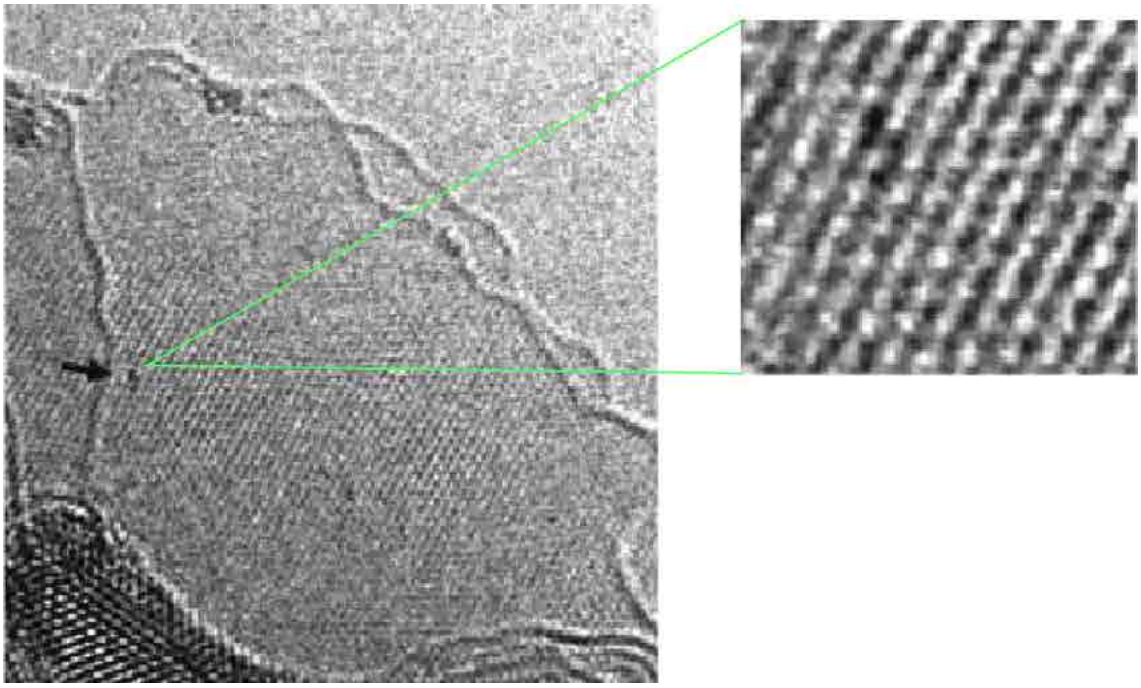

Figure 1.16: TEM image of a graphene monolayer with Pt atoms at a substitutional site. An enlarged view of the area arrowed in the left panel is seen on right inset. Adapted from Ref. [78].

results.

1.7.3 Graphene and carbon nanotubes with substitutional transition metals

We commented in the previous sections that defects and dopants severely affect some the properties of graphenic systems and can be used to tune their response. Here we focus on substitutional impurities in graphene, in which a single metal atom substitutes one or several carbon atoms in the layer. Direct experimental evidence of the existence of these kind of defects has been recently provided by Gan *et al.* [78]. Using HRTEM, these authors were able to visualise individual Au and Pt atoms incorporated into a very thin graphitic layer probably consisting of one or two graphene layers as we shown in Figure 1.16. From the real-time evolution and temperature dependence of the dynamics they obtained information about the diffusion of these atoms. Large diffusion barriers ($\sim$2.5 eV) were observed for in-plane migration, which indicates the large stability of these defects and the presence of strong carbon-metal bonds. These observations indicate that the atoms occupy substitutional positions.

In another experiment using double-wall CNT (DWCNT) [63], Fe atoms were trapped at vacancies likewise that observed in graphene layers. Figure 1.17(A)-(B) shows the STEM images before and after the electron beam was directed onto a predefined position and kept stationary for few seconds in order to create a lattice defect[4]. After irradiation, a bright spot in the dark-field image was observed. A quantitative analysis showed an increase of the scattered in-

[4]Fe atoms were previously deposited on the nanotube surface before the defect formation

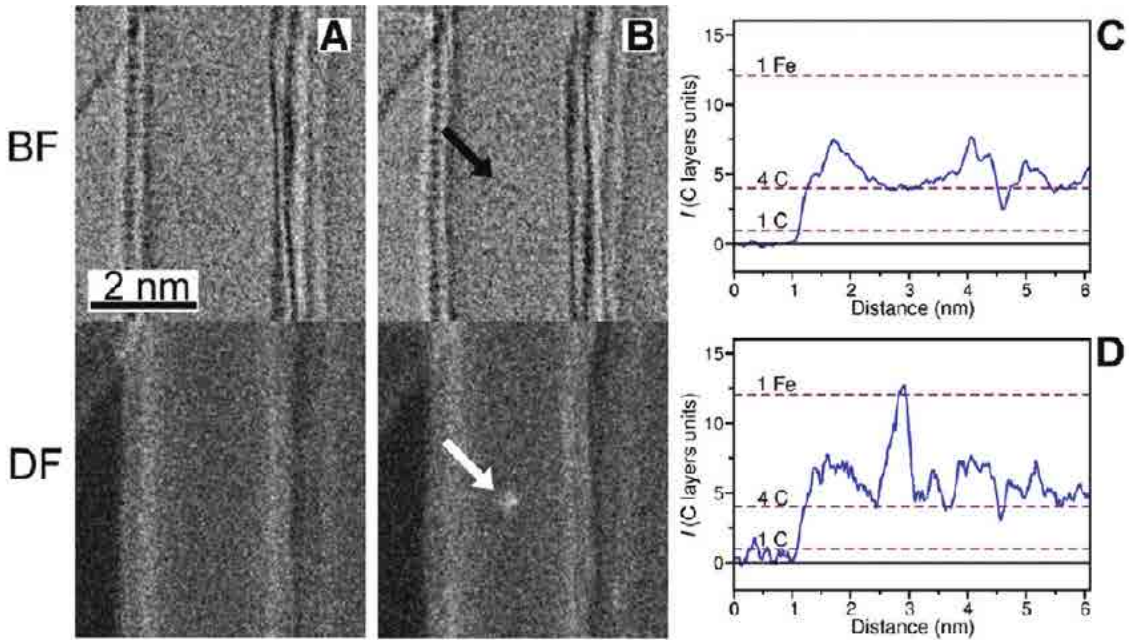

Figure 1.17: STEM images of a DWCNT at a finite temperature (475 ^{o}C) showing the trapping of Fe atoms at the irradiated area marked with an arrow. Panels (A) and (B) show the surface of the DWCNT covered with Fe nanoparticles before and after the irradiation, respectively. Panels (C) and (D) display the intensity profiles along lines perpendicular to the tube axis, respectively, from the unmodified and the irradiated DWNT areas. The dashed lines show the expected intensity levels for one and four carbon layers and for one Fe layer (just one atom). Images were obtained using dark field microscopy technique with different illuminations on the sample: Bright field (BF) and dark field (DF). Adapted from Ref. [63].

tensity at the irradiated position (Figure 1.17(D)) relative to the center of the pristine DWCNT (Figure 1.17(C)). We expect an intensity proportional to the atomic number, $I \sim Z^{1.7}$ [63]. The large peak in Figure 1.17(D) demonstrates that in the defect position, on the top or bottom side of the DWNT, a Fe atom is trapped.

Recent evidence reported substitutional Ni impurities in single-walled carbon nanotubes (SWCNT) [80] and graphitic particles (see Figure 1.18) [81]. Ushiro *et al.* [80] showed that Ni substitutional defects were present in SWCNT samples even after careful purification. According to their analysis of X-ray absorption data (XANES), the most likely configuration has a Ni atom replacing a carbon atom, as shown in Figure 1.18(b).

The presence of substitutional defects can have important implications for the interpretation of some experimental evidence. For example, substitutionals of magnetic transition metals are expected to strongly influence the magnetic properties of graphenic nanostructures. Interestingly, transition metals like Fe, Ni or Co are among the most common catalysts used for the production of SWCNT [82]. Furthermore, the experiments by Rodriguez-Manzo and Banhart [83] have demonstrated how to create individual vacancies at desired locations in carbon nanotubes using electron beams. This experiment, by combination with the observed stability of substitutional impurities, opens a route to fabricate new devices incorporating substitutional impurities in certain locations or arranged in particular ways. Such devices would allow for experimental verification of some of the unusual magnetic interactions mediated by the graphenic carbon network that have been predicted recently. [84, 85] In spite of this, the magnetic properties of substitutional transition-metal impurities in graphenic systems have not

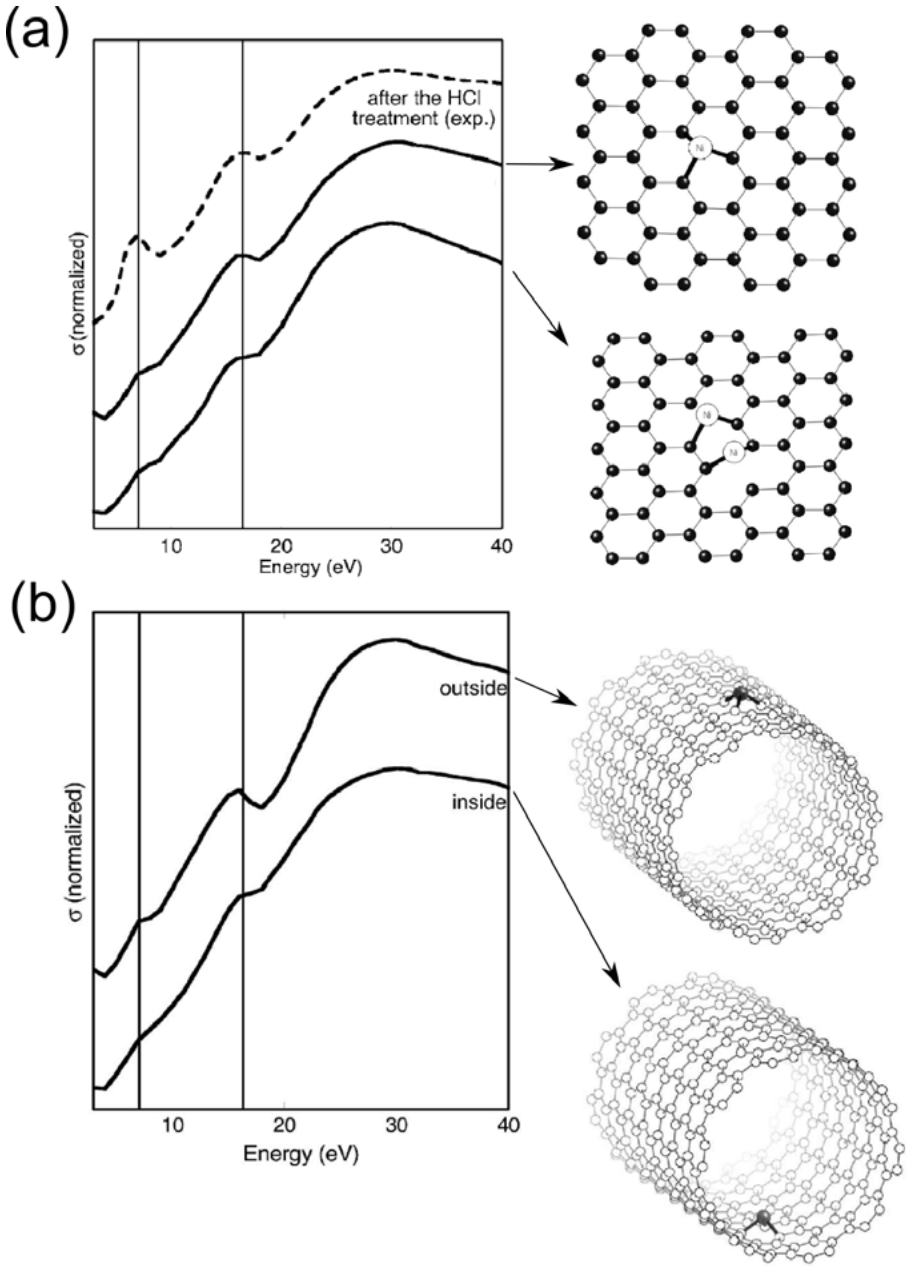

Figure 1.18: (a) Calculated Ni K-edge XANES spectra for the substitutional models taking in account a monomer and dimmer of Ni and the comparison with the observed spectrum after purification process. (b) Calculated Ni K-edge XANES spectra of a armchair CNT with Ni located outside and inside the tube wall. Adapted from Ref. [80].

been studied in detail. Few calculations have considered the effect of this kind of doping on magnetic properties of the graphenic materials and this will be one of the main goals of this thesis.

1.8 Thesis outline

Chapter 2 address a basic introduction to the treatment of the many-body problem using Density Functional Theory (DFT). Its implementation in the SIESTA code was mainly used through this thesis. Basic concepts on pseudopotentials, localized basis set, and periodic boundary conditions are briefly introduced. We show how some technical parameters used in the calculations have been optimised in order to obtain a compromise between accuracy and efficiency. In particular, the convergence tests include **k**-points sampling, electronic smearing σ, pseudopotential radius r_l and basis set. Some results for the bulk-phase of several elements and pristine graphene are presented.

Chapter 3 deals with the structural, electronic and magnetic properties of $3d$ transition metals, noble metals and Zn atoms interacting with carbon monovacancies in graphene. We propose a model based on the hybridization between the states of the metal atom, particularly the d shell, and the defect levels associated with an unreconstructed D_{3h} carbon vacancy. The predictions of this model are in good agreement with the calculated DFT band structures. With this model, we can easily understand the non-trivial behavior found for the binding energy and for the size and localization of the spin moment as we increase the number of valence electrons in the impurity.

Chapter 4 deals with the magnetism induced by metallic impurities and organic adsorbates on graphene monolayers and SWCNTs. We have found magnetism associated with substitutional Co atoms and organic adsorbates (e.g. polymers, nucleobases, diazonium salts, sugar, etc) chemisorbed on graphene through a single C-C bond. Co atoms adsorbed at carbon vacancies can be regarded as a physical realization of a simplified model of defective graphene: the π-vacancy. The analogy is even more direct between the $\pi-$vacancy and the covalent functionalization. Following this analogy, the complicated magnetic properties found in our calculations are easily understood. However, the magnetic couplings between metallic impurities as well as between organic adsorbates on graphene are complex. These exchange energies are analysed in terms of a RKKY model to extract their distance dependence.

Chapter 5 focus on the interplay between elastic and magnetic properties of defects in graphenic nanostructures. It is shown that magnetism of defects, such as in vacancies and magnetic impurities in nanotubes and graphene, can be manipulated using strain. We find that the magnetic moment of Ni-doped graphene can be controlled by applying tensile strain. The spin magnetic moments are greatly enhanced. Such deformation breaks the hexagonal symmetry of the layer as in carbon nanotubes due to curvature but in a controllable way. We also found that monovacancies in graphene can show a very rich phase diagram of spin solu-

tions and geometric configurations under a biaxial strain. The moment of the monovacancy increases with stretching while compression reduces or even kills the magnetic signal. The transition to a non-magnetic solution is linked to the rippling of graphene.

Finally, a summary and outlook are provided in **Chapter 6**.

Chapter 2

Electronic Structure Methods

A successful scheme dealing with the many-body problem is Density Functional Theory (DFT). In this Chapter, some essentials are given concerning the DFT basic theory and other technical concepts that we will used in this thesis, for instance pseudopotentials, **k**-point sampling, basis set, etc. A description of the main code that was used to perform all electronic structure calculations will be also given: SIESTA. The Chapter ends with a discussion of some tests on the convergence of the physical properties (e.g. magnetic moment, band structure, ...) studied in this thesis respect to several computational parameters.

2.1 Density Functional Theory

DFT is one of the most widely used methods for electronic structure calculations in condensed matter. Since it is an ab initio method, i.e., no fitting parameters are needed, DFT is very powerful for the research of novel materials including nano-structured systems. With today computer resources, system sizes of about a thousand atoms can be studied with many DFT methods.

2.1.1 The many-body problem

The starting point of the description of a system containing electrons and nuclei is the Hamiltonian:

$$\hat{H} = -\frac{\hbar^2}{2m_e}\sum_i \nabla_i^2 - \sum_{i,I}\frac{Z_I e^2}{|\boldsymbol{r_i} - \boldsymbol{R_I}|} + \frac{1}{2}\sum_{i\neq j}\frac{e^2}{|\boldsymbol{r_i} - \boldsymbol{r_j}|} - \sum_I \frac{\hbar^2}{2M_I}\nabla_I^2 + \frac{1}{2}\sum_{I\neq J}\frac{Z_I Z_J e^2}{|\boldsymbol{R_I} - \boldsymbol{R_J}|} \quad (2.1)$$

where lower case subscripts denote electrons, and upper case subscripts denotes nuclei. Z_I and M_I are the charge and mass of the nuclei. The inverse of the nuclear masses, $1/M_I$, can be regarded as such small quantities that the nuclear kinetic energy can be ignored. Alternatively, one can argue that the large difference in mass between the electrons and the nuclei effectively means that electrons react almost instantaneously to changes in the nuclear positions, and the nuclei can be regarded as static. This is the so-called Born-Oppenheimer approximation [86]. The relevant Hamiltonian for electronic structure calculations is thus

$$\hat{H} = \hat{T} + \hat{V}_{ext} + \hat{V}_{int} + E_{II} \tag{2.2}$$

where $\hat{T} = -\frac{1}{2}\sum_i \nabla_i^2$ describes the kinetic energy of electrons, $\hat{V}_{ext} = -\sum_{i,I} \frac{Z_I e^2}{|\boldsymbol{r_i} - \boldsymbol{R_I}|}$ is the electron-nucleus interactions, and $\hat{V}_{int} = \frac{1}{2}\sum_{i \neq j} \frac{e^2}{|\boldsymbol{r_i} - \boldsymbol{r_j}|}$ accounts for the electron-electron interactions. E_{II} is the constant energy of the nucleus-nucleus interactions. The Hamiltonian in Eq. (2.2) is essentially determined by the external potential $\hat{V}_{ext}$ (i.e., the nuclear coordinates, which also determine E_{II}) because $\hat{T}$ and $\hat{V}_{int}$ are the same for any electron problem. The properties of the interacting system with N electrons are in principle obtainable from the time-independent Schrödinger equation:

$$\hat{H}\Psi_i(\boldsymbol{r_1}, \boldsymbol{r_2}, ..., \boldsymbol{r_n}) = E_i \Psi_i(\boldsymbol{r_1}, \boldsymbol{r_2}, ..., \boldsymbol{r_n}) \tag{2.3}$$

Solving Eq. (2.3) for a realistic system containing many electrons and nuclei is difficult for more than a few atoms. The Physics Nobel Prize winner Walter Kohn had already pointed out that traditional wave-function methods are in general limited to molecules with a small total number of chemically active electrons [87]. For N particles, the full N particle wavefunction $\Psi_i(\boldsymbol{r_1}, \boldsymbol{r_2}, ..., \boldsymbol{r_N})$ has $3N$ variables and using a description with p parameters yields a space of dimension

$$M = p^{3N} \tag{2.4}$$

The total energy has to be minimised in the space of these M parameters. If we setup a maximum value of M, m, that can be calculated with our best computers we can have an estimation of our limits to calculate the electronic properties from wave-function methods. As an example, if $m = 10^9$ parameters, and $p = 3$, for example, we can see from Eq.(2.4) that

$$\begin{aligned} \ln m &= \ln(p^{3N}) \\ N &= \tfrac{1}{3}\tfrac{\ln m}{\ln p} \\ N &= \tfrac{1}{3}\tfrac{9}{0.48} = 6 \end{aligned} \tag{2.5}$$

what means that could only treat a system of 6 particles. This is what Walter Kohn has described as the exponential wall concept and essentially it reflects the interconnectedness of $\Psi_i(\boldsymbol{r_1}, \boldsymbol{r_2}, ..., \boldsymbol{r_N})$ in the $3N$-dimensional configuration space defined by all r_l being inside the 3D region containing the particles [87]. Hohenberg and Kohn's famous theorem is a (partial) solution to this problem and we will discuss in the following section.

2.1.2 Foundations of the Density Functional Theory

The theoretical foundation of DFT was made by Hohenberg and Kohn [88] who showed that there is a one-to-one correspondence between the ground state density of a system and the

external potential. In other words, two external potentials differing by more than a constant lead to two different ground state densities. Since the Hamiltonian in Eq.(2.2) is uniquely determined by the external potential, it follows that all properties, including excited states, of the system can be regarded as functionals of the ground state density. Specifically, the total energy can be considered as a functional of the density:

$$E[\rho] = T[\rho] + V_{int}[\rho] + V_{ext}[\rho] = T[\rho] + V_{int}[\rho] + \int \rho(\boldsymbol{r}) v_{ext}(\boldsymbol{r})\, d\boldsymbol{r} \tag{2.6}$$

The minimum energy is found for the ground state density ρ_o which can be obtained by using the variational principle. Considering the three-dimensional density instead of the 3N-dimensional wavevectors as the independent variable is a worth simplification, nevertheless the progress is still mostly formal. The problem is that the universal functionals $T[\rho]$ and $V_{int}[\rho]$ of the kinetic and electron-electron interaction energies are unknown [89].

2.1.3 Kohn-Sham formulation

Almost any practical use of DFT rely on the work of Kohn and Sham (KS) from the late 60's [90]. KS theory is based on a basic *ansatz*, namely that the ground state density, $\rho(r)$, of an interacting system is also the ground state density of a non-interacting system with an effective potential $v_{eff}(\boldsymbol{r})$. The electron density is determined from a single-particle Schrödinger equation:

$$\begin{aligned} \hat{h}\psi_i(\boldsymbol{r}) &= \epsilon_i \psi_i(\boldsymbol{r}) \\ (-\frac{1}{2}\nabla^2 + v_{eff}(\boldsymbol{r}))\psi_i(\boldsymbol{r}) &= \epsilon_i \psi_i(\boldsymbol{r}) \end{aligned} \tag{2.7}$$

where $\psi_i(\boldsymbol{r})$ are the single electron KS orbitals giving the density:

$$\rho(\boldsymbol{r}) = \sum_i |\psi_i(\boldsymbol{r})|^2 \tag{2.8}$$

where the sum is over the occupied states. The effective potential $v_{eff}(\boldsymbol{r})$ is given by:

$$v_{eff}(\boldsymbol{r}) = \int \frac{\rho(\boldsymbol{r}')}{|\boldsymbol{r} - \boldsymbol{r}'|}\, d\boldsymbol{r}' + V_{ext}(\boldsymbol{r}) + \frac{\delta E_{XC}[\rho(\boldsymbol{r})]}{\delta \rho(\boldsymbol{r})} \tag{2.9}$$

where the latter term is called the exchange-correlation term. The KS energy functional that needs to be calculated is:

$$E[\rho(\boldsymbol{r})] = T_s[\rho(\boldsymbol{r})] + \int V_{ext}[\rho(\boldsymbol{r})]\rho(\boldsymbol{r})\, d\boldsymbol{r} + \frac{1}{2}\int\int \frac{\rho(\boldsymbol{r})\rho(\boldsymbol{r}')}{|\boldsymbol{r} - \boldsymbol{r}'|}\, d\boldsymbol{r}\, d\boldsymbol{r}' + E_{xc}[\rho(\boldsymbol{r})] \tag{2.10}$$

The set of equations (2.7) - (2.9) is solved self-consistently in an iterative process. For instance, we start by a guess of the density $\rho(\boldsymbol{r})$, calculate $v_{eff}(\boldsymbol{r})$, solve Eq.(2.7) to obtain

$\psi_i(\boldsymbol{r})$, calculate the new density $\rho^{'}(\boldsymbol{r})$ and compare it to the initial guess. Upon convergence, the ground state energy is found from the energy functional of Eq.(2.10). The exchange and correlation term $E_{xc}[\rho(\boldsymbol{r})]$ contains all the many-body effects not included in the Hartree term $V_H[\rho] = \frac{1}{2}\int\int \frac{\rho(\boldsymbol{r})\rho(\boldsymbol{r}^{'})}{|\boldsymbol{r}-\boldsymbol{r}^{'}|}\, d\boldsymbol{r}\, d\boldsymbol{r}^{'}$. It is composed by

$$E_{xc}[\rho(\boldsymbol{r})] = T_c[\rho(\boldsymbol{r})] + V_x[\rho(\boldsymbol{r})] + V_c[\rho(\boldsymbol{r})] \tag{2.11}$$

where $T_c[\rho]$ comes from the split of the kinetic energy $T[\rho]$ (Eq. (2.6)) in two parts: $T[\rho(\boldsymbol{r})] = T_s[\rho(\boldsymbol{r})] + T_c[\rho(\boldsymbol{r})]$, where $T_s[\rho(\boldsymbol{r})] = -\frac{1}{2}\sum_i^N \int \psi_i^*(\boldsymbol{r})\nabla^2\psi_i(\boldsymbol{r})$ is the kinetic energy of non-interacting particles. The remaining of the interacting kinetic energy, $T_c[\rho(\boldsymbol{r})]$, is included by approximations. Similarly, the electron-electron interaction energy splits into a simple and complicated part: $V_{int}[\rho(\boldsymbol{r})] = V_H[\rho(\boldsymbol{r})] + V_x[\rho(\boldsymbol{r})] + V_c[\rho(\boldsymbol{r})]$, where $V_x[\rho]$ is the exchange energy, and the correlation term $V_c[\rho]$ is due to electron-electron correlations not captured in the Hartree term.

The validity of any KS-DFT calculation relies on a good approximation to E_{xc}. A widely used approximation for E_{xc} is the local density approximation (LDA) where the contribution of each volume element to the total exchange correlation energy is taken to be that of an element of a homogeneous electron gas with the density corresponding to that point:

$$E_{xc}^{LDA}[\rho(\boldsymbol{r})] = \int d\boldsymbol{r}^{'}\rho(\boldsymbol{r}^{'})\epsilon_{xc}^{homo.}[\rho(\boldsymbol{r}^{'})] \tag{2.12}$$

where $\epsilon_{xc}^{homo.}[\rho(\boldsymbol{r}^{'})]$ is the exchange-correlation energy density of a homogeneous electron gas, which is known with high accuracy [91]. The LDA has proven to give remarkably good results for many systems [89]. On the other hand, other approximations include the gradient of the density and the functional E_{xc} has the form:

$$E_{xc}^{GGA}[\rho(\boldsymbol{r})] = \int d\boldsymbol{r}^{'}\rho(\boldsymbol{r}^{'})\epsilon_{xc}[\rho(\boldsymbol{r}^{'}), |\nabla\rho(\boldsymbol{r}^{'})|] \tag{2.13}$$

Most of the calculations in this thesis were performed using the Perdew-Burke-Ernzerhof (PBE) parametrisation of GGA [92].

It is, however, important to realise that the KS eigenvalues, ϵ_i are not the true energy levels of the interacting system, Eq. (2.2). The density $\rho(\boldsymbol{r})$ is one of the few physical quantities that can be strictly obtained, at least in principle, from KS formalism. In particular, the total energy given by Eq. (2.10) is not equal to the sum of KS eigenvalues, $E_{KS}[\rho(\boldsymbol{r})] \neq \sum_i^N \epsilon_i$ [89]. $\hat{h}$, the KS Hamiltonian, is an effective one-electron Hamiltonian that introduces the effects of electron-electron interactions in a mean-field approach. In this work, we adopt a pragmatic view and, in lack of better alternatives, we take the eigenvalues of $\hat{h}$ as a starting point of our analysis, having in mind that they are only an approximate description of the one-electron excitations in the real system obtained from a mean-field approach.

Although not exact, the KS eigenvalues (ϵ_{KS}) have proven to be a reasonable starting point to understand the electronic structure of real systems. There are, however, well known (and well understood) limitations in the KS band structure. In this context, it is important to mention

that the fundamental band gap (E_g) of a semiconductor or insulator is only approximately predicted using the LDA or GGA exchange-correlation functionals. One of the reasons for that in the KS approach the gap, E_{KS}, is defined as the difference between the lowest unoccupied (ϵ_{KS}^{lumo}) and highest occupied (ϵ_{KS}^{homo}) eigenvalues which differs from the definition of the gap E_g. The latter is defined as $E_g = I - A$, where I is the ionisation potential and A the electron affinity. The relation between E_g and E_{KS} is given by $E_g = E_{KS} + \delta_{xc}$, where δ_{xc} is the derivative discontinuity, i.e., a finite kink that the exchange-correlation potential exhibits as the particle number crosses the integer number of particles N in the system [93]. In some cases δ_{xc} can be small but numerical investigations show that it is usually not negligible [94–96]. Therefore, this can limit the prediction of the fundamental gap E_g from the eigenvalues ϵ_{KS} even if the exact energy functional would be known.

2.2 The SIESTA method

Here we briefly mention some important aspects of the SIESTA method that were used in this thesis. This code was chosen due to its widespread use and efficiency. A detailed description of the SIESTA code can be found in Ref. [97]. SIESTA is an *ab initio* pseudopotential method which employs a linear combination of atomic orbitals as a basis set. Due to the use of atomic orbitals as a basis set, it seems to be similar to a tight binding technique [98] but in fact it strongly differs: the single-particle Hamiltonian is obtained by projecting the KS-DFT Hamiltonian (Eq. 2.10) onto this basis set of atomic orbitals; thus, it is not a set of fitting parameters like in empirical tight-binding methods. Many approximations necessary to solve the one-particle Hamiltonian in SIESTA as for instance the pseudopotential approach, the treatment of exchange and correlation explicitly by means of approximate functionals (e.g. LDA, GGA) and the already cited Born-Oppenheimer approximation are also commom to other ab initio methods. Apart from that, the method is also characterised by a set of parameter that controls the *accuracy* of the self-consistent KS solution. Just to cite some of them: the size (number of atomic basis orbitals) and range (radius of the basis orbitals) of the basis set, the fineness of real-space integration grid, the non-linear core correction to treat exchange-correlation interaction between core and valence states, etc.

2.2.1 Periodic boundary condition

In order to solve the KS differential equations one needs to specify the boundary conditions (BCs) for the problem. In the SIESTA method one uses periodic BCs within the supercell approach [89]. This is the natural choice for bulk crystals, which in reality are periodic. The supercell approach can also be applied to non-periodic structures if a sufficient amount of vacuum is included in the supercell, to effectively separate the objects. In this way molecules, wires, and surfaces can be studied by including vacuum in three, two, or one directions, respectively.

Since the supercell is periodic, Bloch's theorem applies and the wavefunctions can be written as

$$\psi_{n\boldsymbol{k}}(\boldsymbol{r}) = u_{n\boldsymbol{k}}(\boldsymbol{r})e^{i\boldsymbol{k}\cdot\boldsymbol{r}} \tag{2.14}$$

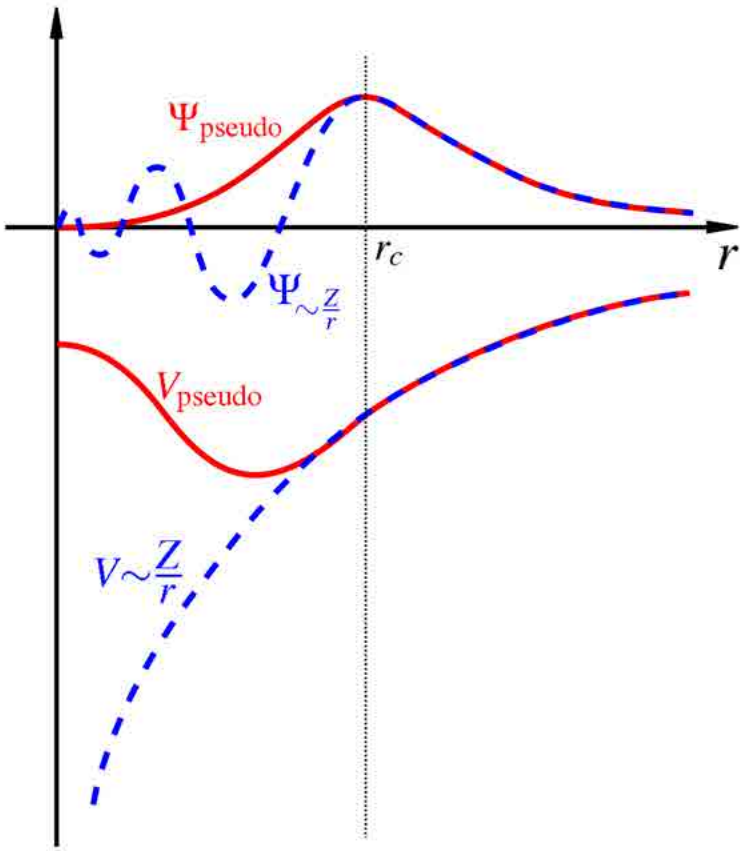

Figure 2.1: Sketch of the all-electron and pseudo potentials and their corresponding wave functions. The radius at which all-electron and pseudo potentials match is displayed as r_c. Adapted from [99].

where $u_{n\boldsymbol{k}}(\boldsymbol{r})$ has the periodicity of the supercell, $\boldsymbol{k}$ is a wave vector in the first Brillouin zone (BZ), and n is the band index. Equation (2.14) allows mapping the KS equations to the reciprocal space, where they are solved for each different $\boldsymbol{k}$ and the size of the problem is restricted to the number of orbitals in the supercell. The expectation value of some operator, $\hat{\mathrm{A}}$, is found as

$$\langle \hat{A} \rangle = \frac{1}{V_{BZ}} \int_{BZ} A(\boldsymbol{k})\, d\boldsymbol{k} \approx \sum_{\boldsymbol{k}} \omega_k A(\boldsymbol{k}) \tag{2.15}$$

where the integral is approximated by a sum over a number of k-points with weight, ω_k. If the supercell is large, the corresponding BZ is small, and few k-points are needed. In the non-periodic directions only the Γ-point ($\boldsymbol{k}_i = 0$) is usually included.

SIESTA uses fast Fourier transform (FFT) to compute the Hartree potential. The FFT algorithm computes the discrete Fourier transform and its inverse which is in principle a periodic function. This allows to solve Poisson's equation and find V_H in an easy way.

2.2.2 Pseudopotentials

In many DFT implementations, the external potential $V_{ext}(\boldsymbol{r})$ is replaced by pseudopotentials (PPs). The idea is that the core electrons which are tightly bound to the nucleus are chemically inert and can be ignored. This leaves only the valence electrons to be considered. PPs are typically generated for free atoms, but can be applied to solids and molecules since the core states almost remain the same (see Figure 2.1). In SIESTA one typically uses norm-conserving PPs of the Troullier-Martins type [100].

It is also worth noting that all the interactions between the core and valence electrons must be transferred to the pseudopotential. This separation core-valence implies a linearisation of the interaction which is an approximation for the exchange-correlation energies. Note that the exchange-correlation energies are explicitly non-linear. If the valence ρ_{val} and core $\rho^c(r)$ charge densities are well separated, as is often the case, this will introduce no serious errors. However, if there is a significant overlap between both densities, this approximation will lead to systematic errors in the total energy and reduces the transferability of the pseudopotential. In particular, this is the case for many magnetic systems, like transition metals, and they need the explicit consideration of the non-linear dependence of the energy on the core charge density. To overcome this difficulty, it was proposed that the full core charge density $\rho^c(r)$ could be replaced by a partial core charge density which is identical to the true charge density outside some radius r_c [101]. This procedure apparently simple has improved the description of materials in which the overlap between core and valence charge densities is large, e.g. many magnetic materials [89].

2.2.3 Basis set

In the numerical solution to the KS equations one expands the wave functions in terms of a basis set:

$$\psi_n(\boldsymbol{r}) = \sum_m c_{nm}\phi_m(\boldsymbol{r}) \tag{2.16}$$

This is exact, if the basis set $\{\phi_m\}$ is complete. Otherwise, the expansion is an approximation. In SIESTA the basis orbitals are localized functions centered on the atoms. At an atomic position $\boldsymbol{R}_I$, the set of orbitals are

$$\phi_{I,lmn}(\boldsymbol{r}) = \phi_{ln}(|\boldsymbol{r}_I|)Y_{lm}(\hat{\boldsymbol{r}}_I) \tag{2.17}$$

where $\boldsymbol{r}_I = (\boldsymbol{r}) - \boldsymbol{R}_I$, ϕ_{ln} is a radial function, and Y_{lm} are the real spherical harmonics with angular momentum labeled by l, m. For each value of l one can have multiple radial functions labeled by n. A single-ζ (SZ) basis set have $n = 1$, double-ζ have $n = 1, 2$, etc. In the case of carbon, the minimal basis set (SZ), consists of a single $s-$orbital ($l = 0$, $m = 0$) and three $p-$orbitals ($l = 1$, $m = 1, 0, 1$), corresponding to the four valence electrons. This basis can be expanded by five polarization $d-$orbitals ($l = 2$, $m = 2, -1, 0, +1, +2$), and is denoted single-zeta-polarized (SZP). If $n = 2$ the basis is denoted double-zeta-polarized (DZP) which is generally considered as the standard basis set in SIESTA. The radial functions have a finite

range and are strictly zero beyond a cutoff radius. The strict localization of the basis orbitals implies that the Hamiltonian matrices become very sparse.

Given the basis set, one obtains the Hamiltonian and overlap matrices:

$$\boldsymbol{H}_{\mu,\nu} = \langle \phi_\mu | \hat{H}_{KS} | \phi_\nu \rangle = \int d\boldsymbol{r} \phi^*_\mu(\boldsymbol{r}) \Big(-\frac{1}{2}\nabla^2 + v_{eff}(\boldsymbol{r}) \Big) \phi_\nu(\boldsymbol{r}) \tag{2.18}$$

$$\boldsymbol{S}_{\mu,\nu} = \langle \phi_\mu | \phi_\nu \rangle = \int d\boldsymbol{r} \phi^*_\mu(\boldsymbol{r}) \phi_\nu(\boldsymbol{r}) \tag{2.19}$$

where the index $\mu = \{I, lmn\}$ and $\nu = \{I', l'm'n'\}$ includes atom and orbital indices. The KS differential equation (2.7) now becomes a generalized eigenvalue equation

$$\boldsymbol{H}\boldsymbol{c}_i = \epsilon_i \boldsymbol{S}\boldsymbol{c}_i \tag{2.20}$$

Equation (2.20) if often used to determine the band structure of the system.

2.3 Convergence of Parameters

2.3.1 K point sampling and smearing of the electronic occupation

During this thesis some parameters used in the simulations have shown to be critical to obtain good physical and chemical properties. The convergence respect to some of these parameters (e.g. **k**-point sampling, smearing temperature, tolerance force, pseudopotentials, basis set, etc) have to be *calibrated* in due time. As a result, the influence of all relevant parameters used in this thesis was checked *prior* to performing final production calculations, what guaranteed the accuracy and transferability desired. In order to give some examples of the convergence studies performed, Figure 2.2 shows the convergence of the magnetic moment (M(μ_B)) and total energy (E_T) as a function of the **k**-sampling. The sample system utilized was a metallic $(5,5)$ SWCNT with one Ni impurity replacing a C atom in the graphenic lattice. The DZP basis set, a smearing temperature (Fermi-Dirac occupation function) of 21 meV and a mesh cutoff of 180.0 Ry was utilized[1]. It can be seen that using a low **k**-sampling there is some "noise" in both curves of M(μ_B) and E_T. This means that values lower than $\sim$12 k-points in this relative large supercell (80 atoms) do not guarantee an accurate value of the magnetic moment, even if the energy is roughly already converged. A well converged M(μ_B) is observed only from $\sim$31 k points on. This dense **k** point sampling turned to be vital to converge many of the magnetic properties of the studied defects and dopants[2].

For Ni$_{sub}$ in a $(5,5)$ SWCNT, Figure 2.3 shows the dependence of M(μ_B) and E_T as a function of the smearing temperature σ. It shows that using small values of σ, the system

[1]The smearing temperature and the mesh cutoff values were previously optimised in additional studies.

[2]In Chapter 5 we will describe the results for Ni substitutional atoms in carbon nanotubes, but in brief, the convergence is specially cumbersome because Ni $3d$ and C $2sp$, $2p_z$ defect bands exist close to the Fermi energy (E$_F$). Therefore, a large number of k-points are required to sample the band structure. Moreover, the low stability of the spin moment associated with the defects strongly depends on the tube curvature and the relative positions of the metal atoms.

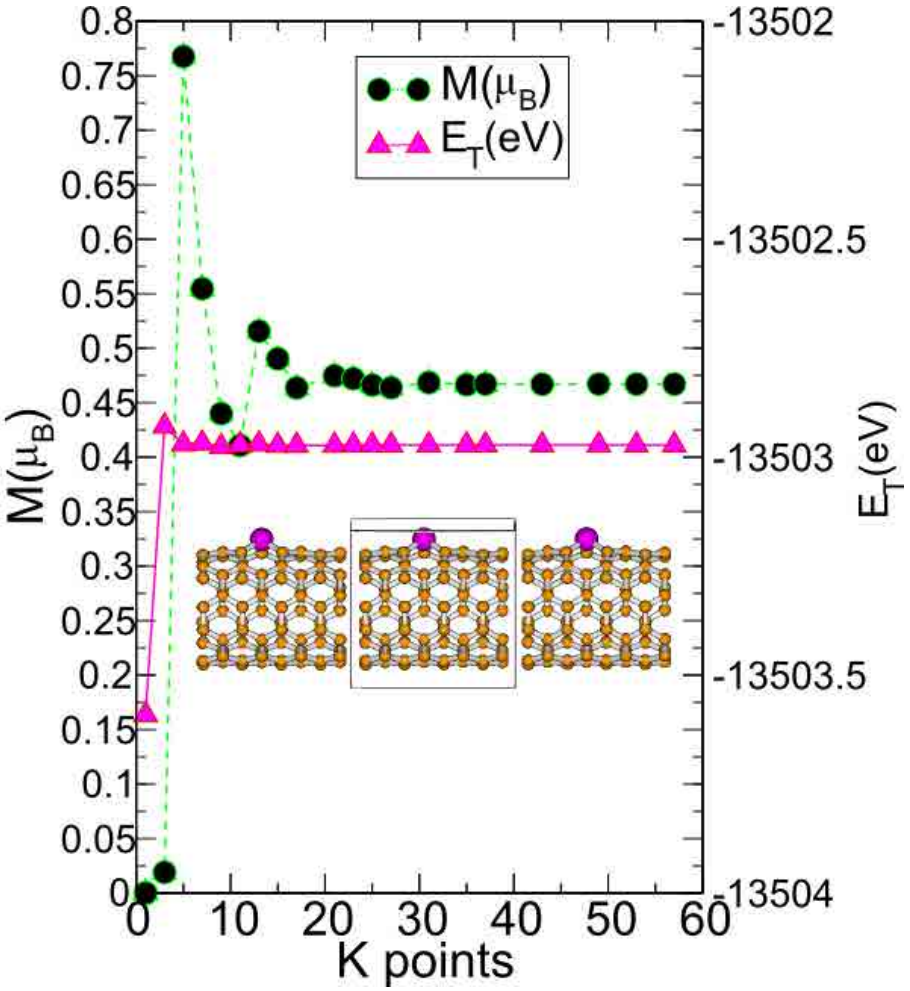

Figure 2.2: Convergence of the magnetic moment (left axis) and total energy (right axis) as a function of the k points. The system chosen for the convergence study is shown in the inset: it consists of a (5,5) single wall carbon nanotubes (SWCNT) with a lenght of 9.97 Å, 80 atoms and one Ni atom at a substitutional position in the graphenic lattice.

converges to a magnetic solution with M$\sim 0.50\mu_B$. However, with larger smearing, a non-magnetic solution is obtained even if a very fine **k**-point mesh is used. Therefore, this means that M(μ_B) is sensitive to the parameter σ chosen in the calculation. How can I find then a good criterion to pick a correct value for σ? In words of Kresse and Furthmüller [102]: *The parameter σ has to be chosen with great care*. The difficulty is easy to understand. Different magnitudes must be averaged over the Brillouin-zone. For example, the band structure energy has the expression

$$\sum_n \int_{\Omega_{BZ}} \epsilon_{nk} \Theta(\epsilon_{nk} - E_{Fnk})\, d^3k \tag{2.21}$$

where $\Theta(\epsilon_{nk} - E_{Fnk})$ is the step function, E_F the Fermi-energy and ϵ_{nk} are the energy eigenvalues. For materials with completely filled bands, for example semiconductors and insulators, no discontinuity at the occupation function exists and the integral for the band structure (Eq.(2.21)) can be calculate accurately using a relatively small set of Monkhorst-Pack

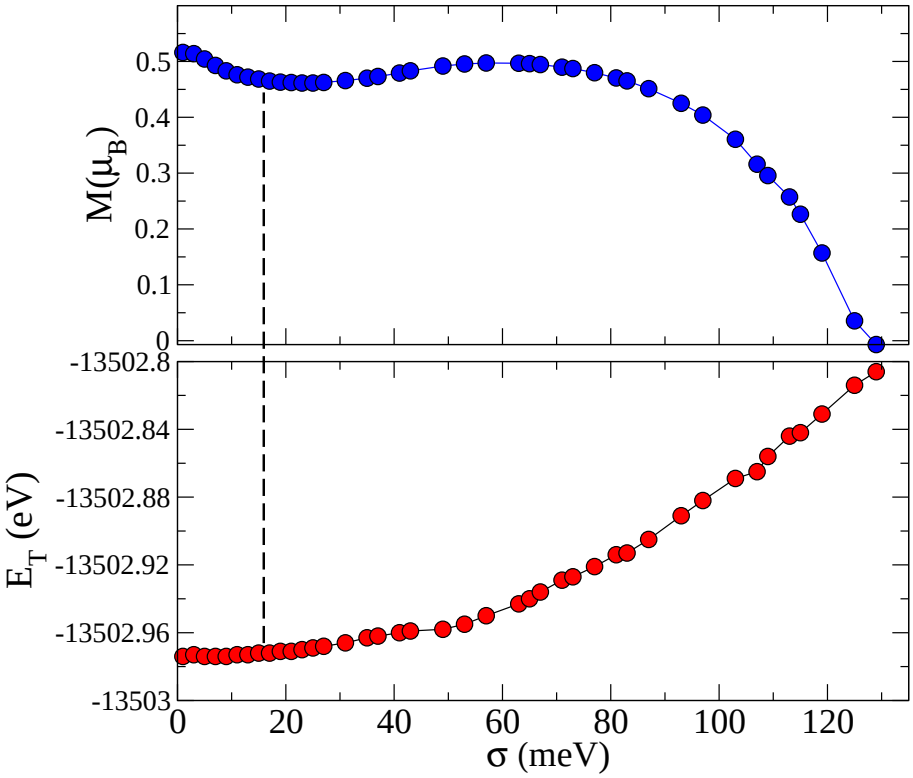

Figure 2.3: Convergence of the magnetic moment (upper panel) and total energy (bottom panel) as a function of the smearing temperature σ. The system chosen was the same as in Figure 2.2 and a **k**-point sampling consisting of $1x1x31$ k-points was utilized. Other parameters (basis set, mesh cutoff, etc) were fixed as in the previous convergence study. The dashed line markes the point in which σ was assumed to converge both magnetic moment and total energy.

k-points[3]. However, in the case of metals, this integral converges very slowly with the number of k-points because the occupancy change abruptly between 0 and 1 at the E_F. The convergence in principle can be improved by using other type of function, insteat of $\Theta(\epsilon_{nk} - E_F)$, with a smoother behaviour, for instance the Fermi-Dirac functional $f(\frac{\epsilon_{nk}-E_{Fnk}}{\sigma}) = \frac{1}{exp((\epsilon_{nk}-E_{Fnk})/\sigma)+1}$. Where $\sigma = k_BT$ and might be "interpreted" as a finite-temperature. Strictly speaking σ does not correspond to a temperature in the ab initio calculations but a finite broadening of the energy states in order to evaluate the integral in Eq.(2.21) more easily. This is a technical parameter that can play an important role in the convergence of magnetic calculations. In fact, a well chosen σ can be used as a tool to reduce the necessary **k**-sampling to calculate the electronic structure of metallic systems. In this case, an good choice of σ can be obtained only by comparing results for different k-point meshes and different values of σ which for this thesis was done.

2.3.2 Pseudopotentials and basis orbital radii

The pseudopotentials used in this thesis were constructed using the Troullier-Martins receipt [100]. For this goal a set of pseudization radii r_l for each relevant angular momentum channel

[3]The Monkhorst-Pack k-points correspond to a special set of **k** points equally spaced in the Brillouin zone [103]

Table 2.1: Cutoff radii (in Bohrs) used for the generation of the Troullier-Martins [100] norm-conserving pseudopotentials used in the SIESTA calculations. r_l stands for the cut-off radius used for the l channel, while r_{core} is the matching radius used for the construction of pseudocores in order to include non-linear core corrections for exchange and correlation [101].

	Valence	r_s (a_o)	r_p (a_o)	r_d (a_o)	r_{core}
Sc	[Ar]$4s^1 3d^2$	3.30	3.30	1.44	0.89
Ti	[Ar]$4s^1 3d^3$	2.96	2.96	1.45	0.72
V	[Ar]$4s^1 3d^4$	2.40	2.79	1.46	0.69
Cr	[Ar]$4s^1 3d^5$	2.51	2.80	1.46	0.65
Mn	[Ar]$4s^1 3d^6$	2.51	2.77	1.45	0.60
Fe	[Ar]$4s^1 3d^7$	2.10	2.10	1.68	0.67
Co	[Ar]$4s^2 3d^7$	2.37	2.48	1.68	0.67
Ni	[Ar]$4s^2 3d^8$	1.85	1.95	1.45	0.53
Cu	[Ar]$4s^1 3d^{10}$	2.33	2.30	1.79	0.53
Ag	[Kr]$5s^1 4d^{10}$	2.45	2.58	2.00	0.83
Au	[Xe,$4f^{14}$]$6s^1 5d^{10}$	2.55	2.68	2.20	0.93
Zn	[Ar]$4s^2 3d^{10}$	2.04	2.21	1.66	0.49
Li	[He]$2s^1$	2.25	2.10	2.05	–
Be	[He]$2s^2$	2.10	1.80	1.75	–
B	[He]$2s^2 2p^1$	1.40	1.40	1.75	–
C	[He]$2s^2 2p^2$	1.25	1.25	1.25	–
N	[He]$2s^2 2p^3$	1.25	1.25	1.25	–
O	[He]$2s^2 2p^4$	1.14	1.14	1.14	–
F	[He]$2s^2 2p^5$	1.19	1.19	1.19	–
Al	[Ne]$3s^2 3p^1$	1.89	1.89	1.89	–
Si	[Ne]$3s^2 3p^2$	1.89	1.89	1.89	–
P	[Ne]$3s^2 3p^3$	1.85	1.85	1.85	1.65
S	[Ne]$3s^2 3p^4$	1.60	1.85	1.75	1.45
Cl	[Ne]$3s^2 3p^5$	1.40	1.65	1.75	1.25
Ge	[Ar]$4s^2 4p^2$	1.90	2.20	3.00	1.65
Sn	[Kr]$5s^2 5p^2$	1.90	2.20	3.15	1.90
Pb	[Xe]$6s^2 6p^2$	1.98	2.80	3.51	1.50
H	$1s^1$	1.25	1.25	–	–

Table 2.2: Cutoff radii (in Bohrs) of the numerical atomic orbitals (NAOs) used in SIESTA as a basis set. The radii used for the s and polarization p shell are equal.

	r_{sp}^{NAO} (a_o)	r_d^{NAO} (a_o)
Co	8.00	4.73
Ni	10.94	6.81
Cu	8.87	5.52
Ag	10.48	6.52
Au	8.63	6.08
Zn	9.24	5.33

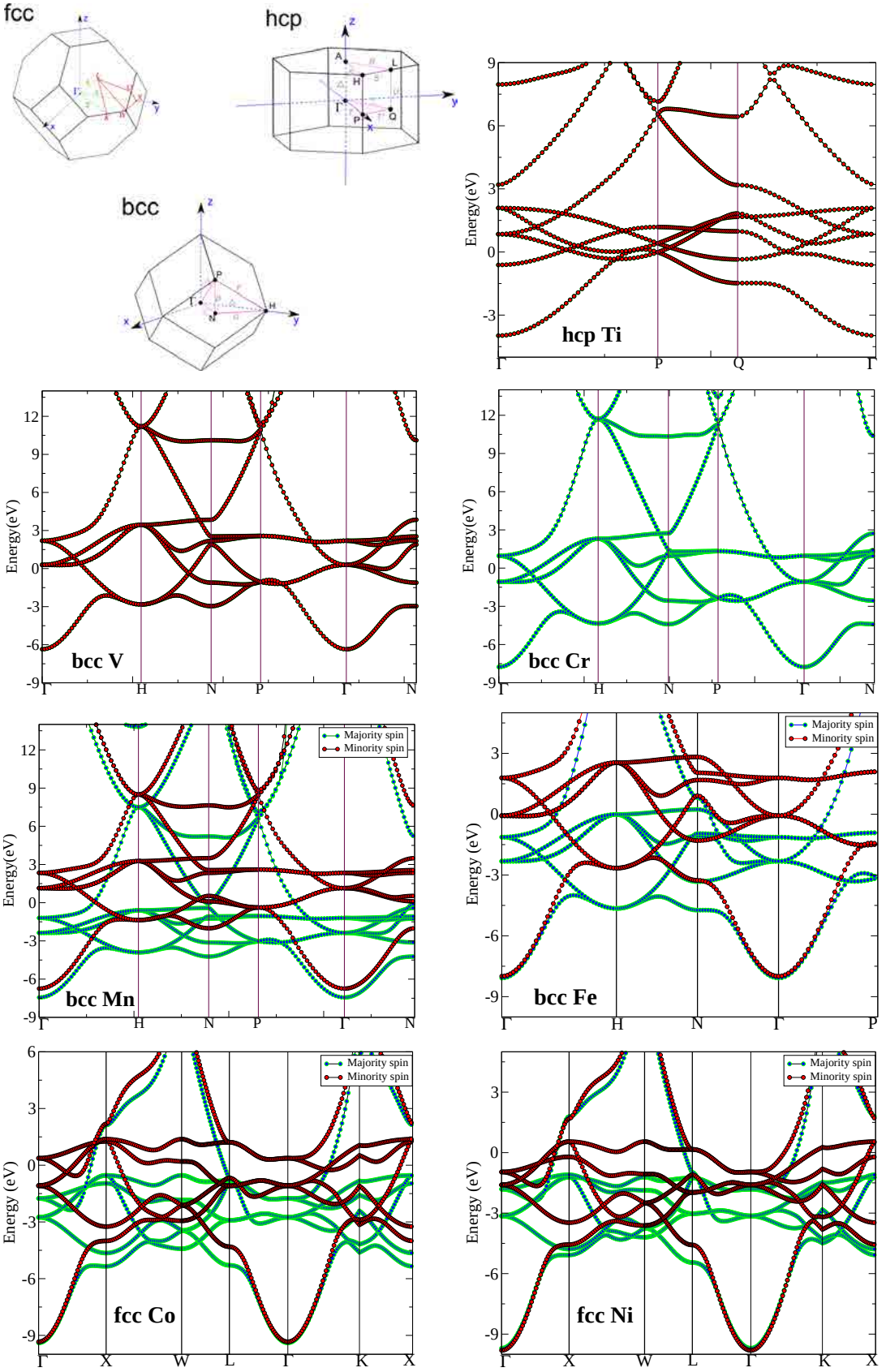

Figure 2.4: Brillouin zone for the face-centered cubic lattice (fcc), hexagonal closed-packed (hcp) and body-centered cubic lattice (bcc). Calculations of the band structures of 3d transition metals obtained using the norm-conserving pseudopotentials constructed in this thesis.

have to be used. Table 2.1 summarises all the information related to r_l. The pseudopotentials for the metal atoms also include nonlinear core corrections [101] in which the pseudocore radii (r_{core}) have been optimised for each element.

For most elements, the shape and radii of the basis sets of numerical atomic orbitals (NAOs) used with SIESTA were determined automatically by the code using an *energy shift* parameter of 50 meV. [97, 104] However, for some transition metal atoms the binding energies where slightly overestimated using these basis sets, mainly due to the confinement of the free atom. For those atoms we enlarged the radii of the basis orbitals (using smaller values of the *energy shift* parameter) until the binding energies were converged within a few tens of meV. Here, the reference calculations were those using plane-waves and projector-augmented wave potentials (PAW) as implemented in the VASP code [105, 106]. The largest radius for each element and l channel is shown in Table 2.2. Notice that the double-ζ polarized (DZP) basis of these transition metals include a p shell. In this case the radii of the p orbitals is taken equal to that of the s shell.

2.3.3 Benchmark systems: transition metals in bulk phases and graphene

In order to give some benchmarks of our calculation procedure, we present here the band structures of some transition metal atoms in bulk phases and graphene. Figure 2.4 shows the results for Ti, V, Cr, Mn, Fe, Co, Ni in body-centered cubic (bcc), hexagonal close-packed (hcp) and face-centered cubic crystals (fcc). The majority and minority spin bands are displayed in green and red curves, respectively, and E_F is set to zero. These band structures are in quite good agreement with previously published results using different methodologies and also recover, taking into account the limitations of GGA calculations, the main trends observed in photoemission experiments.

In these type of calculations, apart from **k**-sampling, basis set, smearing, mesh cutoff, etc, commented above, one of the major factors that should be considered with care is the functional utilized. In many cases a very accurate description of magnetic materials goes beyond DFT. Early calculations of elemental ferromagnets (Fe, Co, Ni) demonstrated that GGA is rather successful in the prediction of the magnetic moments when compared with Local Spin Density Approximation (LSDA). GGA calculations lead to reliable lattice constants and spin moments as we can see in Table 2.3, in which a comparison between calculations perfomed using LSDA/GGA and some experiments is also presented. We can see the very favourable comparison of our calculations using SIESTA and pseudopotentials with experiments and previous calculations using all-electron methods.

Figure 2.5 shows the band structure of graphene calculated with the pseudopotential of C presented in Table 2.1. The unit cell consists of two atoms at a distance of 1.44 Å, and a comparison between DZ (green curves) and DZP (black curves) basis set is also presented. The two curves agree quite well for states around the Fermi level and occupied states[4]. However, some deviation is observed for states higher that $\sim$7 eV above E_F which is due to the lower

[4]DZ basis set was observed to describe quite well, in comparison with the more complete basis set (DZP), many of the structural and electronic properties of systems in which carbon is the only element present (e.g. vacancies in graphene monolayers). Therefore, one of strategies used in this thesis was to perform the structural relaxations with a smaller DZ basis, while the final results for the electronic and magnetic properties were obtained using a more expensive DZP basis. This becomes instrumental to treat systems with more than $\sim$200 atoms in the supercell.

Table 2.3: Spin magnetic moments (m_{spin}) in μ_B per atom and lattice constants (a_o) in of ferromagnetic elements (Fe, Co, Ni) in the bulk phase. The experimentally determined total magnetic moment (M_{Total}) is composed of spin and orbital components. [1]Reproduced from Refs. [107–109]. [2]This thesis using pseudopotentials as described in Table 2.1.

Property	Source	Fe (bcc)	Co (fcc)	Ni (fcc)
m_{spin}	LSDA[1]	2.15	1.56	0.59
m_{spin}	GGA[1]	2.22	1.62	0.62
m_{spin}	GGA[2]	2.27	1.60	0.68
m_{spin}	Experiment[1]	2.12	1.57	0.55
M_{Total}	Experiment[1]	2.22	1.71	0.61
a_o	LDA[1]	2.73	3.41	3.47
a_o	LSDA[1]	2.76	3.47	3.47
a_o	GGA[1]	2.83	3.55	3.55
a_o	GGA[2]	2.89	3.55	3.55
a_o	Experiment[1]	2.86	3.53	3.53

variational flexibility (e.g. angular) of the DZ basis set. Some authors have also considered the inclusion of diffuse $3s$ orbitals in the valence electrons as a way to improve the electronic spectrum of graphene above 3 eV [110]. This inclusion resulted in an improvement of the description of some optical properties of graphene and carbon nanotubes as well. More details about the basis sets used in SIESTA and, in particular, about the effect of the use of diffuse orbitals in the band structure can be found in Refs. [97, 104, 110, 111].

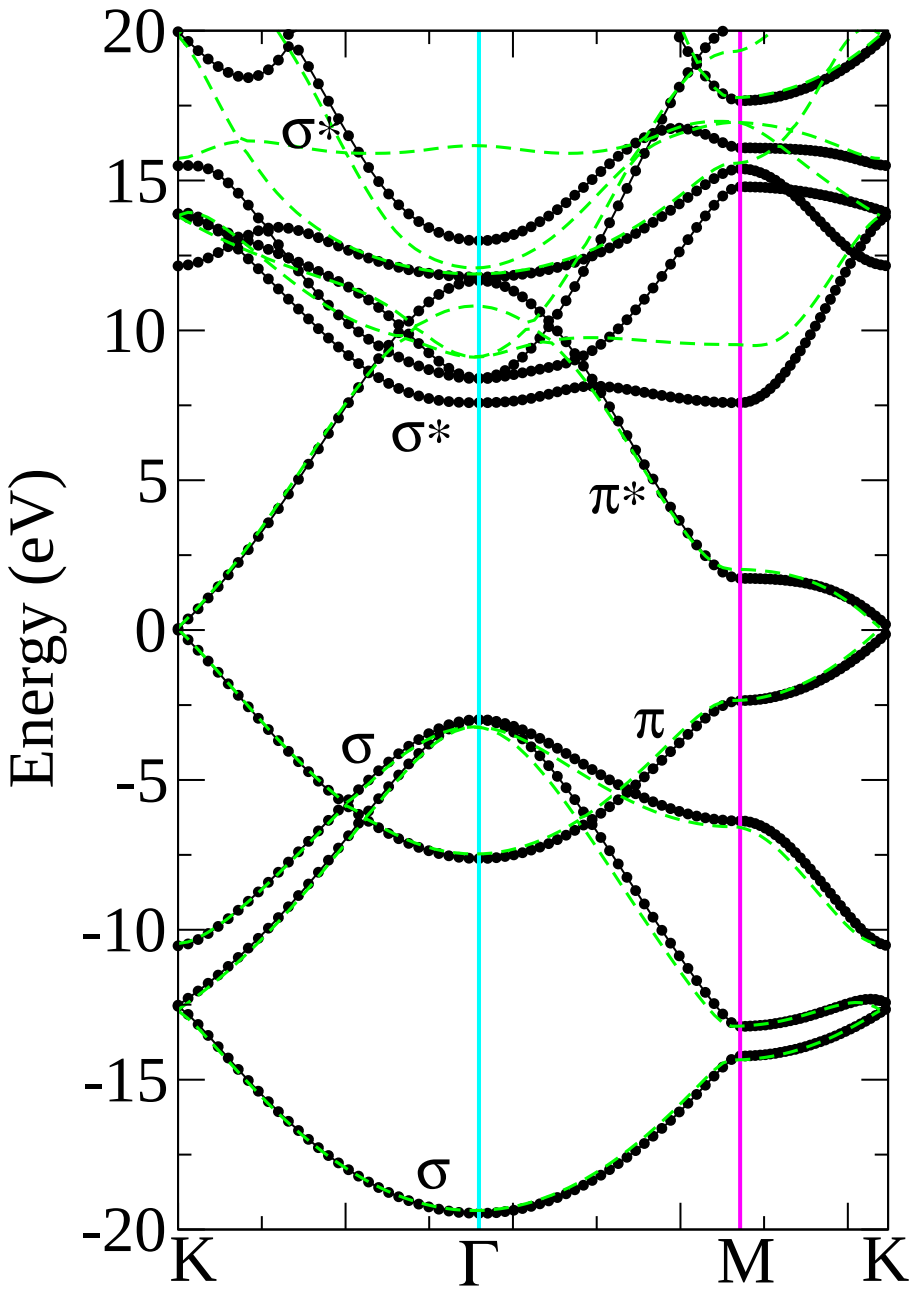

Figure 2.5: Band structure of graphene with two C atoms in the unit cell. The black and green curves show, respectively, the calculation using a DZP and DZ basis set. The Fermi energy is set to zero. Around the Fermi energy the states are classified according to the carbon orbitals that composed them: σ, σ^*, π and π^*. It is noted that bands with the σ and π character cross each other as a result of the different symmetries displayed by sp and p_z carbon states. An usual feature observed in the previous sections is the crossing of the π and π^* bands at the K point of the Brillouin zone. The bonding σ and σ^* bands are well separated in energy with a gap of about $\sim$ 12 eV at Γ.

Chapter 3

Substitutional Metallic Impurities in Graphene: Structural, Electronic and Magnetic Properties

This chapter is devoted to the study of the basic structural, electronic and magnetic properties of $3d$ metal, noble metal and Zn atoms interacting with carbon monovacancies in graphene. We pay special attention to the electronic and magnetic properties of these substitutional impurities and found that they can be fully understood using a simple model based on the hybridization between the states of the metal atom, particularly the d shell, and the defect levels associated with an unreconstructed D_{3h} carbon vacancy.

The chapter is divided as follows: we present a summary of the structure, energetics and magnetic properties of all the studied elements in Sec. 3.1. In this section we also indicate the general ideas behind our model of the metal-carbon hybridization in these systems. The electronic structure of the unreconstructed D_{3h} carbon vacancy in graphene is presented in Sec. 3.2. This is one of the key ingredients to understand the binding and electronic structure of substitutional impurities in graphene. The electronic structure of the different groups of impurities is described in Sec. 3.3. In Sec. 3.4 the Zn substitutional impurity with its Jahn-Teller distortion is described. A full section (Sec. 3.5) is devoted to describe the special role of Fe at the border between two different regimes. Finally, we close with some general conclusions.

3.1 The main properties of substitutional transition metals in graphene

We review in this section our results for the structure, binding, and spin moments of substitutional $3d$ transition metals, noble metals and Zn in graphene.

3.1.1 Geometry and structural parameters

The typical geometry of the systems studied in this chapter is presented in Fig. 3.1. The metal atom appears always displaced from the carbon layer. The height over the plane defined by its three nearest carbon neighbors is in the range 1.7-0.9 Å. These three carbon atoms are also displaced over the average position of the graphene layer by 0.3-0.5 Å. The total height (h_z)

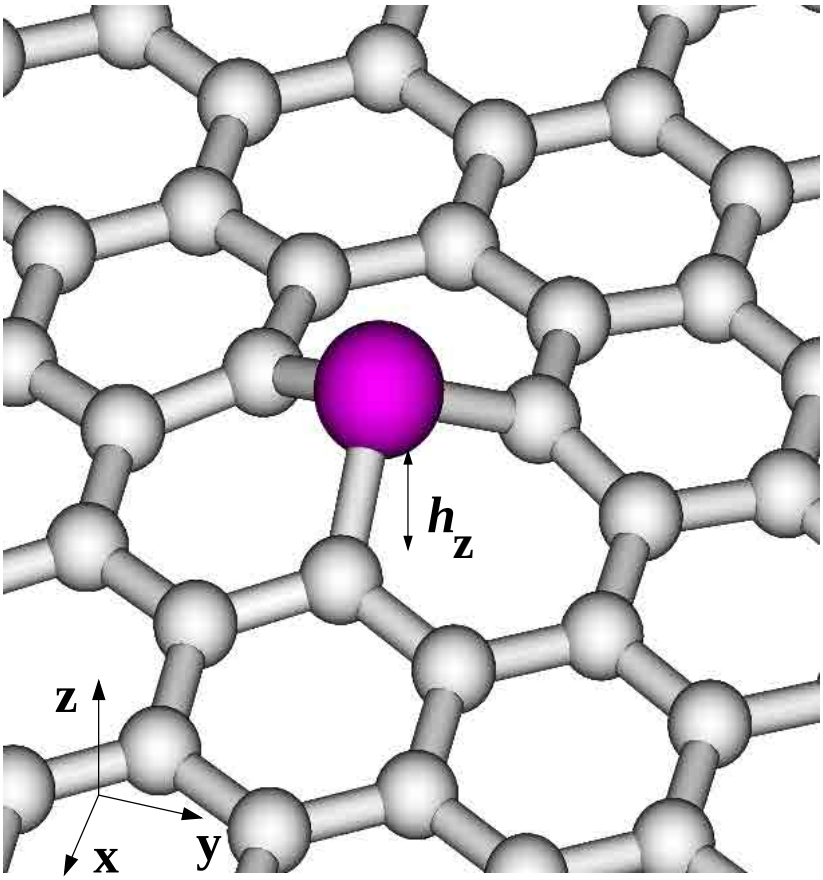

Figure 3.1: Typical geometry of transition and noble substitutional metal atoms in graphene. The metal atom moves upwards from the layer and occupies, in most cases, an almost perfectly symmetric three-fold position with C_{3v} symmetry.

of the metal atom over the graphene plane is the sum of these two contributions and ranges between 1.2-1.8 Å, as shown in panel (c) of Fig. 3.2. In most cases the metal atom occupies an almost perfect symmetric configuration with C_{3v} symmetry. Exceptions are the noble metals, that are slightly displaced from the central position, and Zn that suffers a Jahn-Teller distortion in its most stable configuration. However, we have found that it is also possible to stabilize a symmetric configuration for Zn with a binding energy only $\sim$150 meV smaller. This configuration was overlooked in a recently published study on these systems [112] and we will refer to it as $Zn_{C_{3v}}$ throughout the chapter.

Figures 3.2 presents a summary of the structural parameters of substitutional $3d$ transition metals, noble metals and Zn in graphene. Solid circles correspond to calculations using the SIESTA code with pseudopotentials and a basis set of atomic orbitals, while open squares stand for VASP calculations using plane-waves and PAW potentials. The agreement between both sets of calculations is quite remarkable. Data in these figures correspond to calculations using a 4×4 supercell of graphene. For several metals we have also performed calculations using a larger 8×8 supercell and find almost identical results. This is particularly true for the total spin moments, which are less dependent on the size of the supercell, but require a sufficiently dense k-point sampling to converge. In the following we will mainly discuss the results obtained with the smaller cell since the plots of the band structures are easier to interpret in that

case. Finally, as already mentioned, noble metals and Zn present a distorted configuration. A detailed description of the structural parameters in these cases will be given below, here we only present the averaged structural data for noble metals and those corresponding to the $Zn_{C_{3v}}$ case.

The data in Fig. 3.2 are basically consistent with those reported by Krasheninnikov *et al.* in Ref. [112]. The behavior of the metal-carbon bond length and the height (h_z) of the impurity over the layer reflects approximately the size of the metal atom. For transition metals these distances decrease as we increase the atomic number, with a small discontinuity when going from Mn to Fe. The carbon-metal bond length reaches its minimum for Fe (d_{C-Fe}=1.76 Å), keeping a very similar value for Co and Ni. For Cu and Zn the distances increase reflecting the fully occupied $3d$ shell and the large size of the $4s$ orbitals. Among the noble metals we find that, as expected, the bond length largely increases for Ag with respect to Cu, but slightly decreases when going from Ag to Au. The latter behavior can be understood from the compression of the $6s$ shell due to scalar relativistic effects.

3.1.2 Binding energies

The binding energies of the studied substitutional metal atoms in graphene can be found in panel (d) of Fig. 3.2. In general, the behavior of the binding energies can be correlated with that of the carbon-metal bond length, although the former is somewhat more complicated. Binding energies for transition metals are in the range of 8-6 eV. Ti presents the maximum binding energy, which can be easily understood since for this element all the metal-carbon bonding states (see Sec. 3.3.1) become fully occupied. One could expect a continuous decrease of the binding energy as we move away from Ti along the transition metal series and first the non-bonding $3d$, and later the metal-carbon antibonding levels become populated. However, the behavior is non-monotonic and the smaller binding energies among the $3d$ transition metals are found for Cr and Mn, while a local maximum is observed for Co. This complex behavior is related to the simultaneous energy down-shift and compression of the $3d$ shell of the metal as we increase the atomic number. This will become more transparent when discussing in detail the metal-carbon hybridization levels. In brief, the behavior of the binding energies of the substitutional $3d$ transition metal comes from two competing effects:

(*i*) as the $3d$ shell becomes occupied and moves to lower energies the hybridization with the carbon vacancy states near the Fermi energy (E_F) is reduced, which decreases the binding energy;

(*ii*) the transition from Mn to late transition metals is accompanied by a shift of the metal-carbon bond length of $\sim$0.1 Å, which increases the carbon-metal interaction and, correspondingly, the binding energy.

Binding energies for noble metals are considerably smaller than for transition metals and mirror the reverse behavior of the bond lengths: 3.69, 1.76 and 2.07 eV, respectively, for Cu, Ag and Au. The smallest binding energy ($\sim$1 eV) among the metals studied here is found for Zn, with filled s-d electronic shells.

3.1.3 Spin moments

The spin moments of substitutional transition and noble metals in graphene are shown in Fig. 3.3. Again they are in agreement with the results of Ref. [112]. However, we advance a

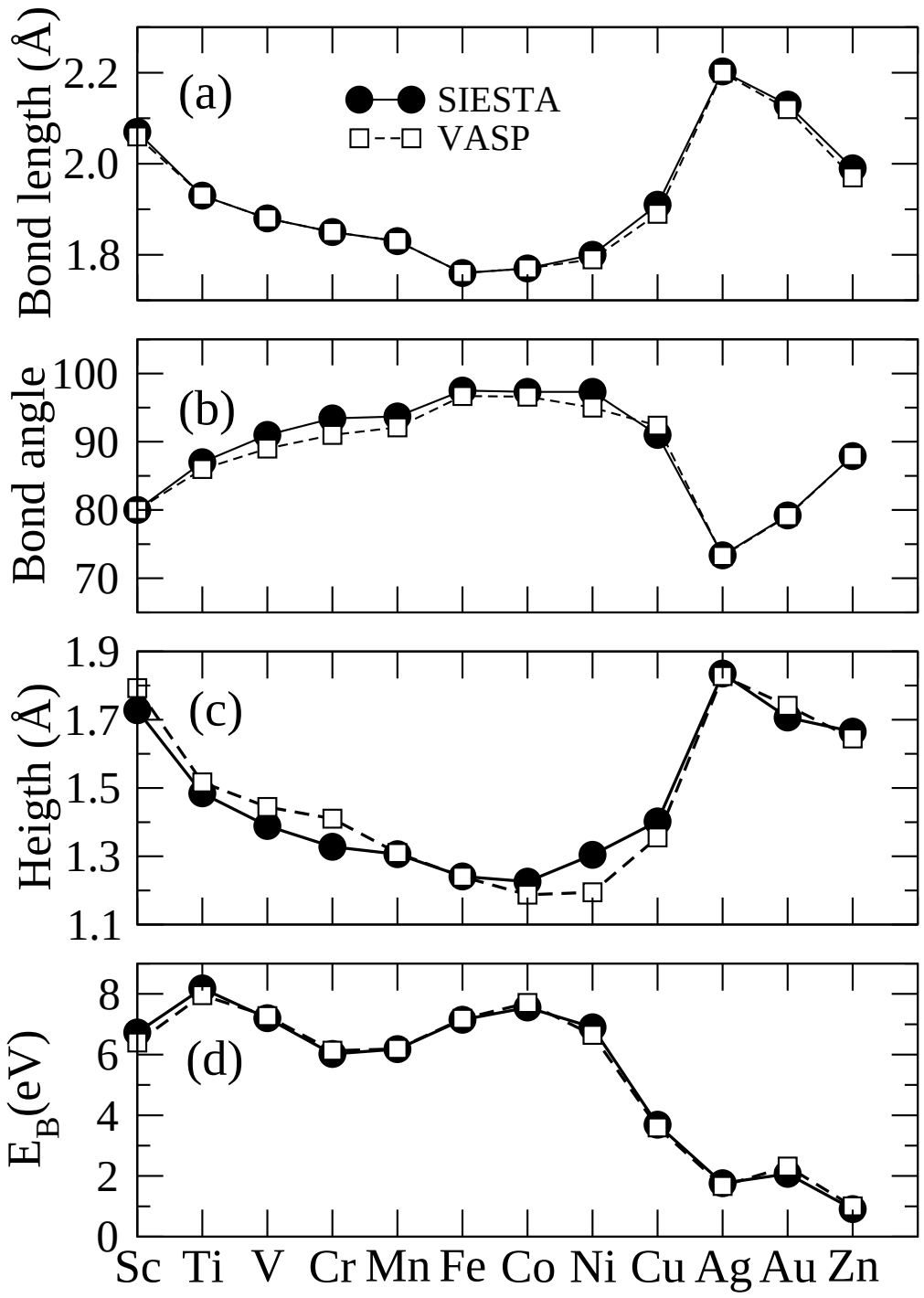

Figure 3.2: Structural parameters and binding energies of substitutional transition and noble metals in graphene. Bond lengths and angles have been averaged for the noble metals. The data presented for Zn correspond to the high-spin solution with C_{3v} symmetry, and are very close to the averaged results for the most stable distorted solution.

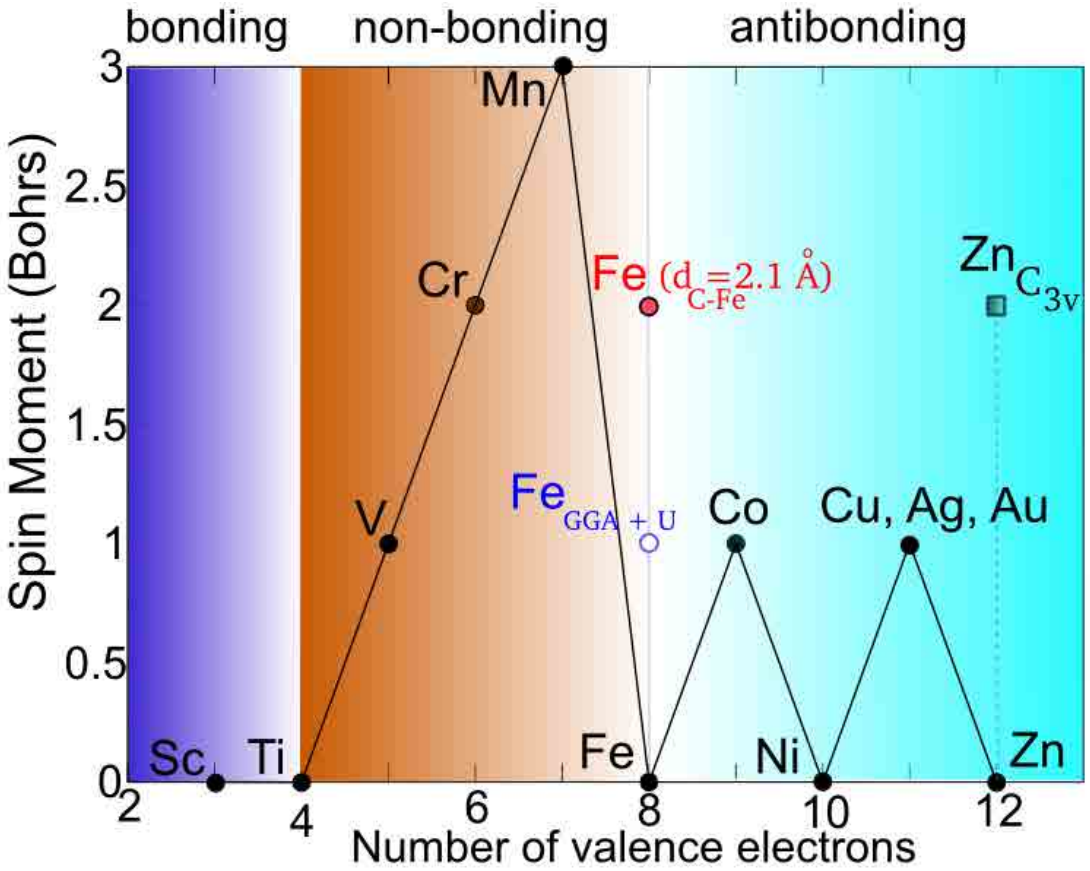

Figure 3.3: Spin moment of substitutional transition and noble metals in graphene as a function of the number of valence electrons (Slater-Pauling-type plot). Black symbols correspond to the most stable configurations using GGA. Results are almost identical using SIESTA and VASP codes. Three main regimes are found as explained in detail in the text: (*i*) filling of the metal-carbon bonding states gives rise to the non-magnetic behavior of Ti and Sc; (*ii*) non-bonding d states are filled for V, Cr and Mn giving rise to high spin moments; (*iii*) for Fe all non-bonding levels are occupied and metal-carbon antibonding states start to be filled giving rise to the observed oscillatory behavior for Co, Ni, Cu and Zn. Open and gray (red online) symbols correspond, respectively, to calculations of Fe using GGA+U and artificially increasing the height of the metal atom over the graphene layer (see the text). Symbol marked as $Zn_{C_{3v}}$ corresponds to a Zn impurity in a high-spin symmetric C_{3v} configuration.

simple model to understand the observed behavior which was not presented in that reference. One of the fundamental results of our study is a detailed model of the bonding and electronic structure of substitutional transition metals in graphene. As we will see below, the evolution of the spin moment can be completely understood using such model. In brief, we can distinguish different regimes according to the filling of electronic levels of different (bonding, non-bonding and antibonding) character:

(*i*) all the carbon-metal bonding levels are filled for Sc and Ti and, correspondingly, the spin-moment is zero;

(*ii*) non-bonding $3d$ levels become populated for V and Cr giving rise to a spin moment of, respectively, 1 and 2 μ_B with a strong localized d character;

(*iii*) for Mn one additional electron is added to the antibonding d_{z^2} level and the spin moment increases to 3 μ_B;

(*iv*) finally, for Fe and heavier atoms all the non-bonding $3d$ levels are occupied and the

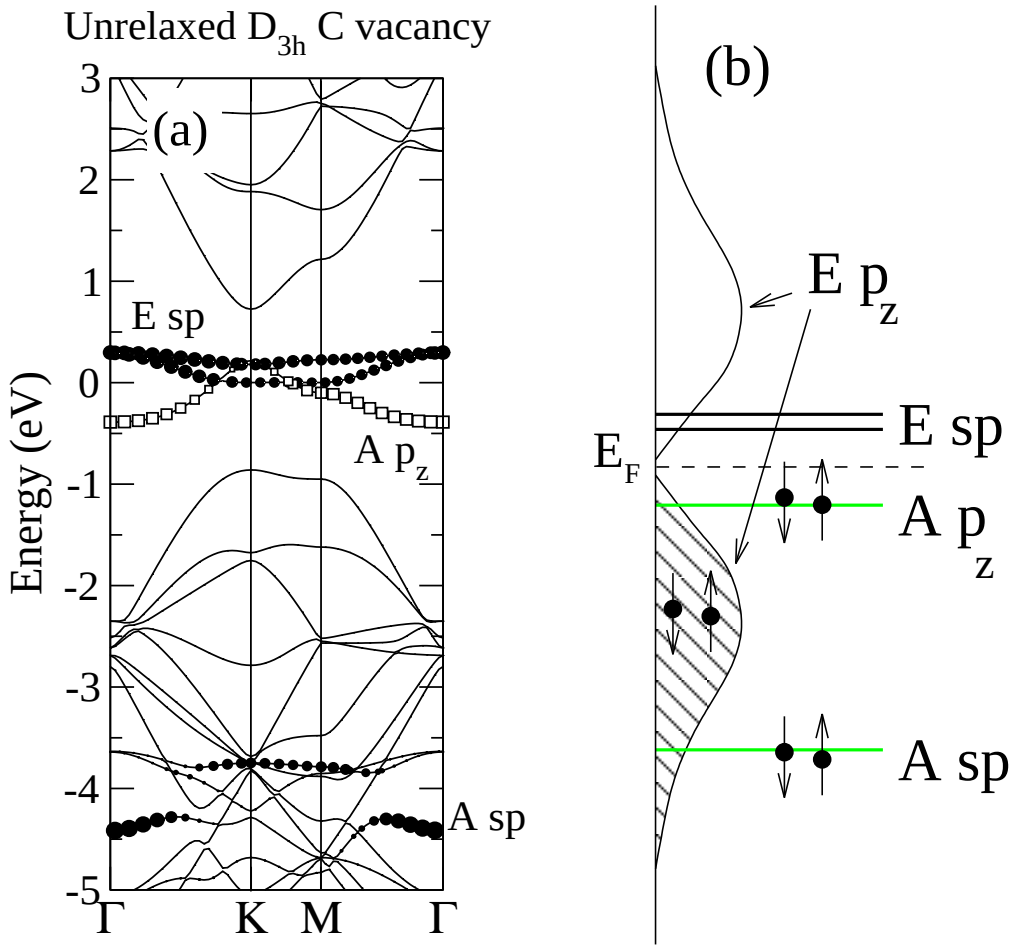

Figure 3.4: (a) Spin-compensated calculation of the band structure of an unrelaxed carbon vacancy (D_{3h} symmetry) in a 4×4 supercell of graphene. Symbols indicated those bands with larger weight on the carbon atoms around the vacancy (solid symbols for bands with sp character and open symbols for a band with p_z character). The electronic structure near E_F is dominated by a fully symmetric p_z level (A p_z) and two defect levels with E symmetry and sp character (E sp). Notice that, due to the strong hybridization with the rest of the graphene layer, it is not possible to identify well defined defect levels with E symmetry and p_z character. (b) Approximate scheme of the electronic structure of the spin-compensated D_{3h} C vacancy indicating the character and symmetry of the different levels and their occupations. Signal associated with the E p_z level extends over the whole valence and conduction band.

spin moment oscillates between 0 and 1 μ_B as the antibonding metal-carbon levels become occupied.

The sudden decrease of the spin moment from 3 μ_B for Mn to 0 μ_B for Fe is characterized by a transition from a complete spin-polarization of the non-bonding $3d$ levels to a full occupation of those bands. However, this effect depends on the ratio between the effective electron-electron interaction within the $3d$ shell and the metal-carbon interaction (see Sec. 3.5). As we will see below, if the hybridization with the neighboring atoms is artificially reduced, for example by increasing the Fe-C distance, Fe impurities develop a spin moment of 2 μ_B. Our results also show that it is also possible to switch on the spin moment of Fe by changing the effective electron-electron interaction within the $3d$ shell. This can be done using the so-called GGA+U method. For a large enough value of U (in the range 2-3 eV), Fe

impurities develop a spin moment of 1 μ_B. This will be also explained in detail in Sec. 3.5. For the time being we just point out that this behavior is unique to Fe: using similar values of U for other impurities does not modify their spin moments.

At the level of the GGA calculations Fe constitutes the border between two different characters of the spin moment associated with the substitutional metal impurities in graphene: $3d$ magnetism for V-Mn and a "defective-carbon" -like magnetism for heavier atoms. For Co, Ni, the noble metals and Zn the electronic levels close to the E_F have a stronger contribution from the carbon nearest-neighbors and resemble the levels of the isolated D_{3h} carbon vacancy. In particular, Mulliken population analysis show that the spin moment of the noble metals impurities has a dominant contribution for the three nearest carbon neighbors (see Table 3.1). For Zn two electrons occupy a two-fold degenerate level reminiscent of the E sp level of the unreconstructed carbon vacancy (see Sec. 3.2). As a consequence, the system suffers a Jahn-Teller distortion and has a zero spin moment. However, it is possible to stabilize a symmetric configuration ($Zn_{C_{3v}}$) with a moment of 2 μ_B and only slightly higher in energy.

3.2 Unreconstructed D_{3h} carbon vacancy

We have seen in the previous summary of results that, as substitutional impurities in graphene, most of the metal atoms studied here present a threefold symmetrical configuration. For this reason we have found particularly instructive to analyse their electronic structure as the result of the hybridization between the atomic levels of the metal atoms with the electronic levels associated with an unrelaxed D_{3h} symmetrical carbon vacancy.

Figure. 3.4 (a) shows the electronic structure of a spin-compensated D_{3h} carbon vacancy as calculated using 4×4 graphene supercell, while panel (b) presents a simplified scheme that highlights the defect levels associated with the vacancy and indicates their different character and symmetry. The actual D_{3h} vacancy shows a considerable spin polarization, however, here we only consider the spin-compensated case since the purpose of this calculation is to find the symmetries and approximate energy positions of the different energy levels. The defect levels of the D_{3h} vacancy can be easily classified according to their sp or p_z character and whether they transform according to A or E-type representations. Close to the E_F we can find a fully symmetric A p_z level (thus belonging to the A_2'' irreducible representation) and two degenerate (at Γ) defect levels with E symmetry and sp character (E′ representation). Approximately 4 eV below E_F we find another defect level with A sp character (A_1' representation).

It is interesting to note that it is not possible to identify any localized defect level with E p_z (E″) character. This is due to the strong coupling with the delocalized states in the graphene layer and contrasts to the case of the A p_z level. The A p_z level lies very close to E_F, where the density of states is low, and due to its A symmetry cannot appreciably couple to the delocalized p_z states of graphene in that energy range. On the contrary, the E p_z combinations present a very strong hybridization with the rest of the states of the graphene layer. Indeed, an inspection of the Projected Density of States (PDOS) (see the scheme in Fig. 3.4 (b)) reveals that the spectral weight associated with such E-symmetry linear combinations of p_z orbitals of the carbon atoms surrounding the vacancy extends over the whole valence and conduction band of graphene. It is important to take the last observation into account when developing a model of the electronic structure for the metal substitutionals in graphene. Note that we need to have the correct number of electrons from carbon available for forming localized (covalent)

bonds.

The three carbon atoms around the vacancy provide three unpaired electrons associated with the unsaturated sp lobes and three electrons coming from the p_z orbitals. As shown in Fig. 3.4 (b), two of these electrons stay in p_z states delocalized over the graphene layer while the other four electrons fill the A sp and A p_z levels localized at the vacancy.

3.3 Analysis of the electronic structure

We now turn to the problem of the electronic structure of $3d$ transition and noble metal atoms as substitutional impurities in graphene. We first present a model of the hybridization between carbon and metal levels and, subsequently, we show that this model allows to understand in detail the band structures obtained in our calculation for all the metals.

3.3.1 Sc and Ti: filling the vacancy-metal bonding levels

Figure 3.5 (a) presents a schematic representation of the hybridization of the $3d$ levels of Ti with those of an unreconstructed D_{3h} carbon vacancy. We only consider explicitly the $3d$ states of the metal atom since our calculations show that, for transition metals, the main contribution from $4s$ orbitals appears well above E_F. Due to the symmetric position of the metal atom over the vacancy the system has a C_{3v} symmetry and the electronic levels can still be classified according to the A or E irreducible representations of this point group. Of course, metal and carbon vacancy states only couple when they belong to the same irreducible representation. Thus, occupied A p_z and A sp vacancy levels can only hybridize with the $3d_{z^2}$ orbitals (A_1 representation), while all the other $3d$ metal orbitals can only couple to the unoccupied E sp vacancy levels.

With these simple rules in mind and taking into account the previous trends in the relative energy position of carbon and metal levels, that changes as we move along the transition metal series, we can propose a model of the electronic structure of substitutional transition metals in graphene as represented in Fig. 3.5 (a) and (b). Some parameters in the model can be approximated from calculations. For example, a rough estimate of the position of the $3d$ shell of the metal atom respect to the graphene E_F can be obtained from the positions of the atomic levels and the relative strengths of the different carbon-metal hoppings can be estimated from those of the corresponding overlaps. With such information it is already possible to obtain most of the features of the model in Fig. 3.5. However, some uncertainties remain, particularly concerning the relative position of levels with different symmetry. To solve these uncertainties the simplest approach is to compare with our first-principles calculations and this is what we have done here. The details of the model presented in Fig. 3.5 have been obtained from a thorough analysis of our calculated band structures. In particular, we have used the projection of the electronic states into orbitals of different symmetry as an instrumental tool to classify the levels and to obtain the rational that finally guided us to the proposed model. However, it is interesting to note that some features that derive from our way to understand the electronic structure of these defects are very robust and can actually be guessed without direct comparison with the calculated band structures. For example, the fact that for V we start to fill the non-bonding $3d$ states and, therefore, that this impurity, as well as Cr and Mn, develops a spin moment, can be argued from simple symmetry and electron-counting arguments.

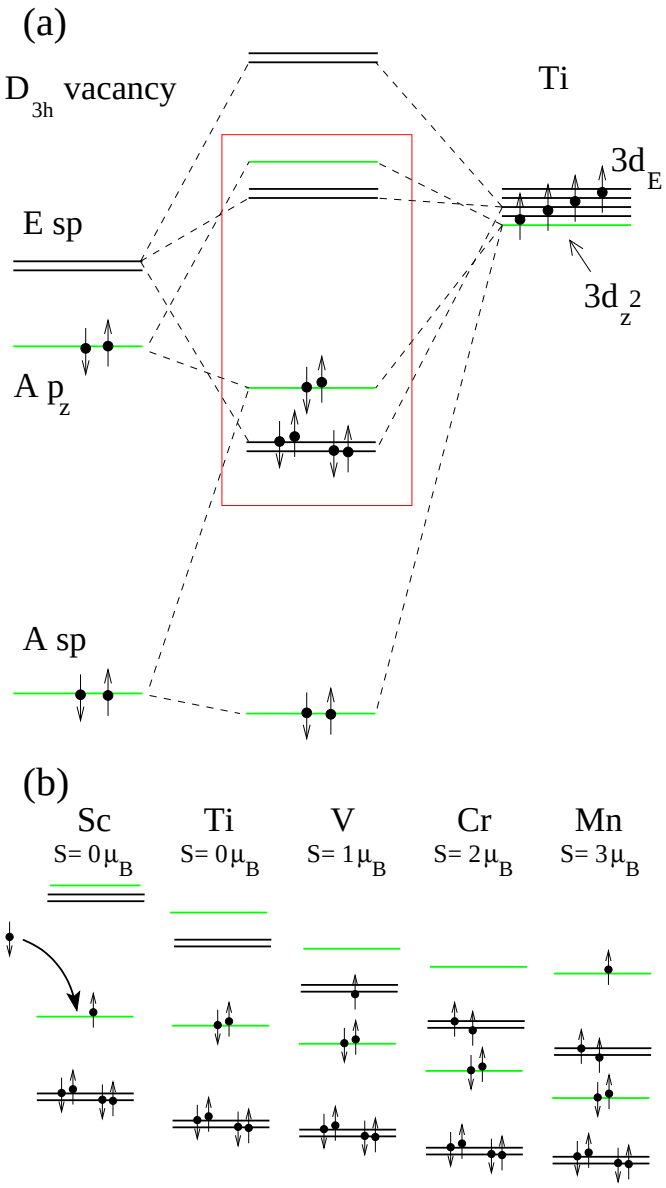

Figure 3.5: (a) Scheme of the hybridization between the 3d levels of Ti and the localized impurity levels of the D_{3h} C vacancy. Only d levels of Ti are represented since our calculations show that, at least for transition metals, the main contribution from s levels appears well above E_F. Levels with A symmetry are represented by gray (green) lines, while those with E symmetry are marked with black lines. The region close to E_F is highlighted by a (red) square. (b) Schematic representation of the evolution of the electronic structure near E_F for several substitutional transition metals in graphene. The spin moment (S) is also indicated. Substitutional Sc impurities act as electron acceptors, causing the p-doping of the graphene layer.

According to our model there are three localized defect levels with A_1 character and three twofold-degenerate levels with E character. Two of these E levels correspond to bonding-antibonding sp-d pairs, while the third one corresponds to $3d$ non-bonding states. For Sc-Mn the three A_1 levels can be pictured as a low lying bonding level with A sp-d_{z^2} character and a bonding-antibonding pair with A p_z-d_{z^2} character.

Therefore, as shown in Fig. 3.5 we have four metal-vacancy bonding levels (two A and one doubly-degenerate E levels) that can host up to eight electrons. Ti contributes with four valence electrons, and there are four electrons associated with the localized carbon-vacancy levels. Thus, for Ti the bonding states are completely occupied. Consequently, Ti presents the highest binding energy among all $3d$ transition metals and has a zero spin moment.

The situation for Sc ought to be discussed in detail. As Sc has three valence electrons, in principle we could expect an incomplete filling of the metal-vacancy bonding levels and a spin moment of $\sim$1 μ_B. However, in our model the highest bonding state (with A p_z-d_{z^2} character) appears below E_F and the Sc impurity can act as an acceptor impurity. Our calculations show that this is indeed the case. The Sc-vacancy p_z-d_{z^2} impurity level captures an electron from the extended states of the graphene layer which becomes p-doped. In total, the substitutional Sc-graphene system does not show any spin polarization.

We can now contrast the expectations from our model with actual calculations. Figure 3.6 shows the band structure of Sc (a) and Ti (b) close to the E_F. As expected, the main contribution from the $3d$ shell is found above E_F. Below E_F we find one defect band with p_z-d_{z^2} character and two bands (degenerate at Γ) with sp-d character. These bands are in close correspondence with the bonding A and E levels appearing in our model. In the case of Ti the E_F is located inside a gap of $\sim$0.5 eV that opens at K point in the Brillouin zone. This gap appears due to the relatively small 4×4 supercell used in these calculations and is reduced when larger supercells are used. Thus, the filling of the graphene extended bands is not appreciably changed by substitutional doping with Ti. For Sc the situation is different. As shown in Fig. 3.6 (a) E_F moves away from the K point, the Sc-vacancy complex captures one electron and the graphene layer becomes doped with holes.

Regarding the unoccupied bands, the $3d$ contribution for Sc above E_F appears quite broadened due to the strong hybridization with the graphene states. Indeed, the defect levels are somewhat difficult to identify and to correlate with our model. One exception is a flat band with strong d_{z^2} character appearing at $\sim$1.5 eV that, due to its symmetry, does not couple so efficiently with the host states. The case of Ti is much easier to interpret in terms of the simplified model presented in Fig. 3.5 (a). In particular, we can find two bands at $\sim$0.6 eV with strong d_{xy} and $d_{x^2-y^2}$ contribution that correspond with the non-bonding d impurity levels, and one band with d_{z^2} character at $\sim$0.8 eV corresponding with the A p_z-d_{z^2} antibonding level. Around 2.6 eV we can also find the two E sp-d antibonding defect levels, although in this case much more hybridized with the host.

3.3.2 V, Cr and Mn: 3d magnetism

As we have seen above, the metal-vacancy bonding levels are completely filled for substitutional Sc and Ti and, as a consequence, the spin moment associated with these impurities is zero. However, following our model in Figures 3.5 (a) and (b), as we move along the transition metal series the number of valence electrons increases and the non-bonding $3d$ impurity states start to become occupied. Hence, due to the strong atomic character and localization of these

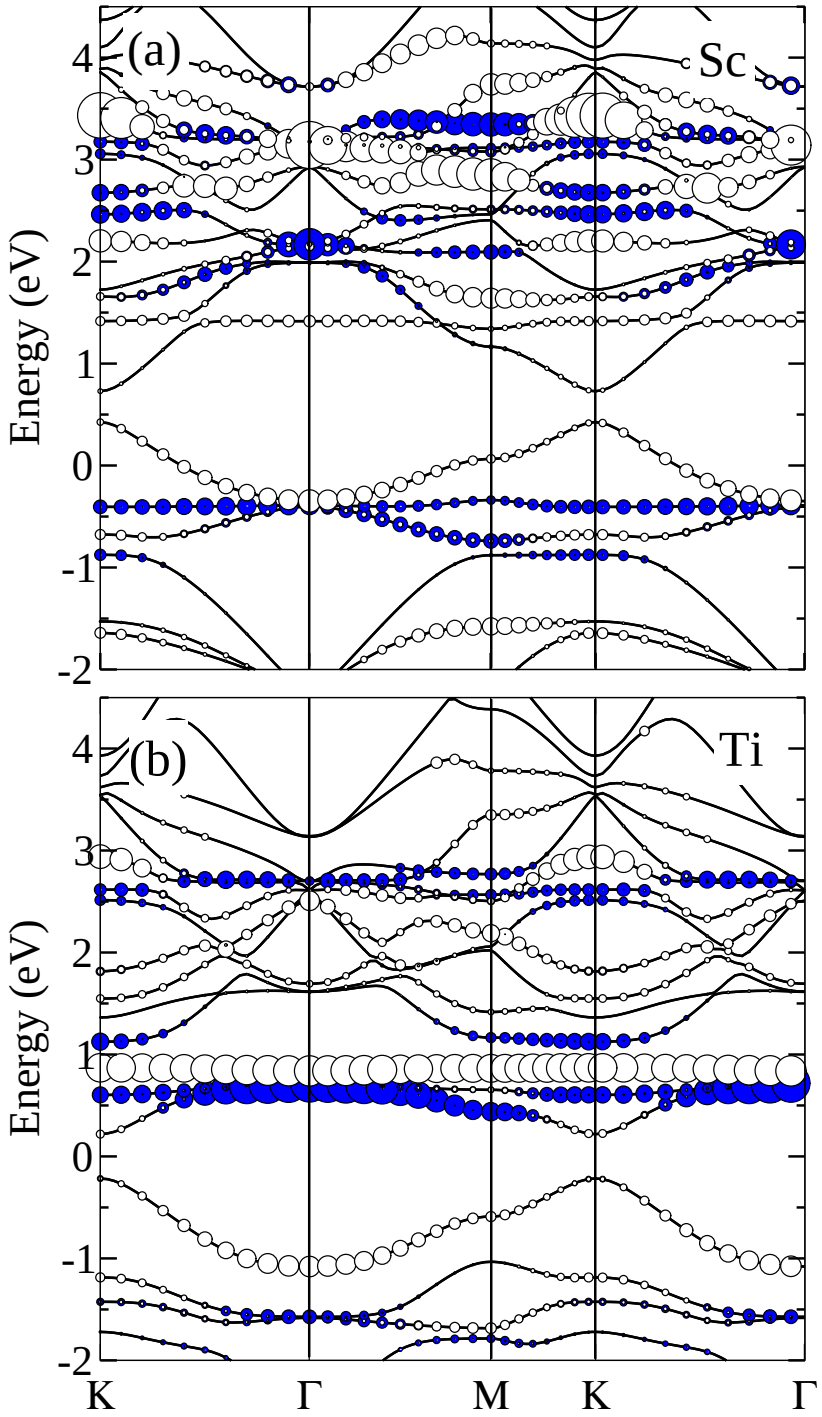

Figure 3.6: Calculated band structure of substitutional Sc (a) and Ti (b) impurities in 4×4 supercell of graphene. Open circles indicate the contribution from $3d_{z^2}$ orbitals of the metal atom and C $2p_z$ orbitals of the neighboring C atoms. Solid circles indicate contributions from the rest of the $3d$ orbitals and C $2p_x$ and $2p_y$ orbitals. Energies are referred to the Fermi energy.

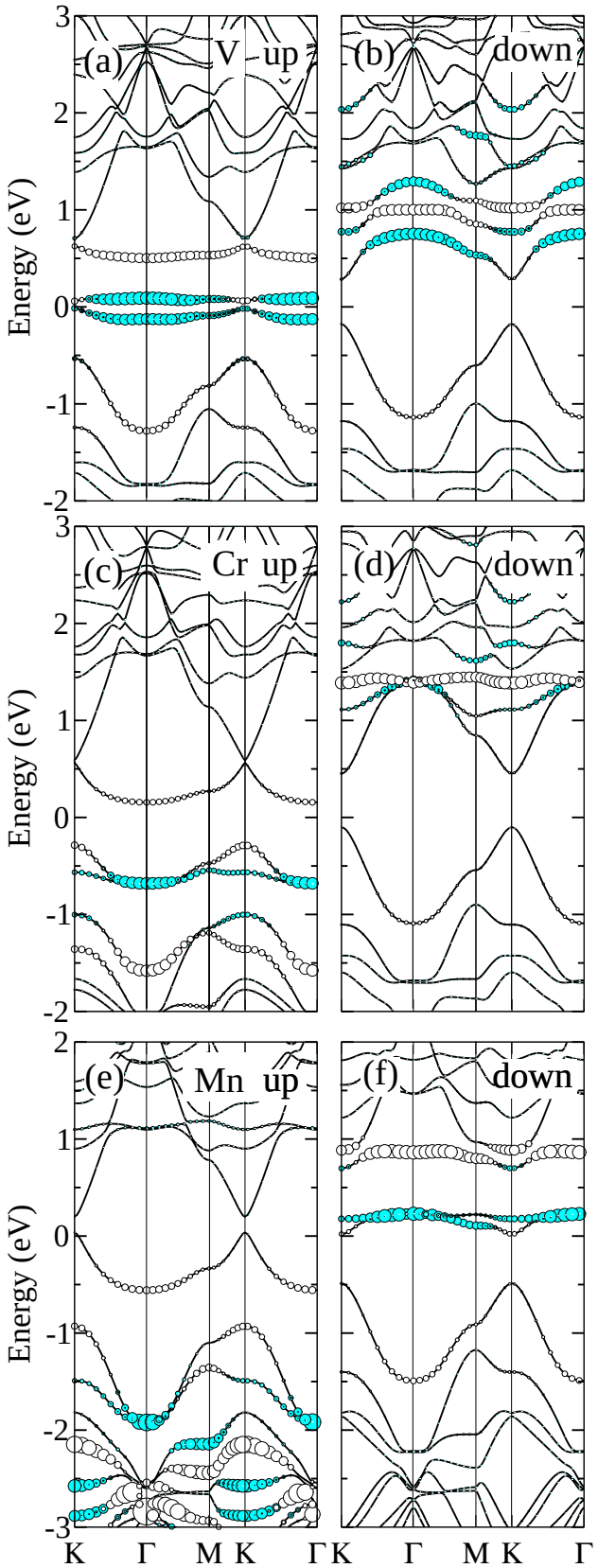

Figure 3.7: Calculated band structure of substitutional V (panels (a) and (b)), Cr ((c) and (d)) and Mn ((e) and (f)) impurities in a 4×4 supercell of graphene. Open and filled circles indicate, respectively, the contribution from $3d_{z^2}$ and the rest of the $3d$ orbitals of the metal and, therefore, also indicates levels with A and E symmetries. Energies are referred to the Fermi energy

Table 3.1: Mulliken population analysis of the spin moment in the central metal impurity (S_M) and the carbon nearest neighbors (S_C) for different substitutional impurities in graphene. S_{tot} is the total spin moment in the supercell.

	$S_M(\mu_B)$	S_C (μ_B)	S_{tot} (μ_B)
V	1.21	-0.09	1.0
Cr	2.53	-0.20	2.0
Mn	2.91	-0.10	3.0
Co	0.44	0.06	1.0
Cu	0.24	-0.03, 0.31, 0.31	1.0
Ag	0.06	-0.31, 0.54, 0.54	1.0
Au	0.16	-0.28, 0.50, 0.50	1.0
$Zn_{C_{3v}}$	0.23	0.37	2.0

states, the system develops a non-zero spin moment.

Figure 3.7 shows the calculated band structures for V, Cr and Mn impurities in a 4×4 supercell of graphene. The full calculations and the predictions of our simplified model agree remarkably, at least in the neighborhood of E_F. For V and Cr this correspondence is particularly evident: one and two electrons, respectively, occupy the degenerate non-bonding E d levels. These non-bonding levels have a dominant contribution from the $3d_{xy}$ and $3d_{x^2-y^2}$ orbitals of the metal atoms. As expected, the spin moments associated with these impurities are, respectively, 1 and 2 μ_B. The strongly localized character of these spin moments is corroborated by the Mulliken population analysis shown in Table 3.1. This analysis indicates that the spin moment is mainly localized at the metal impurity. The contribution from the neighboring carbon atoms is much smaller and has the opposite sign. The localized character of the moment is also consistent with the relatively large values of the spin splitting of the impurity bands. From Figure 3.7 we calculate a spin splitting of ∼0.9 eV for V and almost 2 eV for Cr for the E d levels at E_F. These splittings are comparable to those of d-electrons in magnetic bulks, in the order of 1 eV.

Figure 3.7 (e) and (f) show the majority and minority spin band-structures for Mn substitutionals in graphene. In addition to the non-bonding $3d$ levels, the antibonding A p_z-d_{z^2} defect level also becomes occupied and spin-polarized. This level has an important contribution from the $3d_{z^2}$ state of Mn (given by open symbols). Therefore, it is relatively localized within the Mn atom and presents a significant tendency towards spin polarization. Indeed, our calculations show that Mn substitutions in graphene give rise to a spin moment of 3 μ_B. The Mulliken decomposition for Mn in Table 3.1 confirms again the localized character of this spin moment. However, some differences respect to V and Cr are also found. In those cases, the moment associated with the metal atoms was always larger that the total moment and the only significant additional contributions came from the nearest carbon neighbors. However, for Mn the atomic moment is somewhat smaller (2.91) than the total moment (3.0). Taking into account the contribution from the nearest carbon neighbors (-0.3), a moment of ∼0.4 μ_B is assigned to carbon atoms that are further away from the defect. This indicates a slightly more delocalized character of the spin moment of Mn, since for V and Cr the "long range" contribution was smaller than 0.1 μ_B. From the band structures in Fig. 3.7 (e) and (f) we

obtain a spin splitting of ∼2.1 eV for the non-bonding d levels of the Mn impurity , similar to the case of Cr. The spin splitting for the antibonding A p_z-d_{z^2} state has a smaller value of ∼1.5 eV, indicative of its larger spatial extension.

From the simple scheme presented in Fig. 3.5 (a) we cannot completely determine the value of the spin moment of the Mn impurity. It can be 3 μ_B as found in our first principles calculations and schematically depicted in Fig. 3.5 (b). However, a magnetic moment of 1 μ_B is also a possible answer. In the latter case, the additional electron in Mn with respect to Cr could populate one of the minority-spin non-bonding d impurity levels instead of the antibonding A p_z-d_{z^2} level. In such situation, the spin moment is determined by a delicate balance between the on-site exchange energy within the $3d$ shell, and the energy cost ($\Delta\epsilon_{Ad}$) to promote one electron from the non-bonding d levels to the higher energy antibonding A p_z-d_{z^2} state. Note that the electron-electron repulsion is also reduced when the electron moves into the less localized A p_z-d_{z^2} level. An estimate of the exchange energy can be obtained from the spin splitting (Δ_S) of the defect levels nearby E_F. The relative position of the $3d$ states respect to the A p_z level of the carbon vacancy and the interaction matrix element between these levels determine $\Delta\epsilon_{Ad}$. Thus, within our GGA-DFT calculations we can expect the high spin solution to be favoured approximately when $\Delta_S > \Delta\epsilon_{Ad}$. From the band structures in Fig. 3.7 (e) and (f) we obtain $\Delta\epsilon_{Ad} \sim 1.0$ eV, which is smaller than the values of Δ_S discussed previously and, therefore, is consistent with the calculated moment of 3 μ_B for Mn. Fe impurities considered below in detail present a similar situation where two spin configurations are possible. However, in the case of Fe the low spin (spin compensated) solution is preferred at the level of DFT-GGA calculations as a result of the stronger metal-carbon hybridization.

In short, both the results of the calculations and the expectations based on our model of the metal-vacancy bonding point towards a very strong $3d$ character of the defect levels appearing nearby of E_F for V, Cr and Mn substitutional impurities in graphene. The filling of these localized levels favours high spin solutions in accordance with the first Hund's rule of atomic physics. Thus, we can picture the appearance of spin polarization for V, Cr and Mn substitutionals in graphene as "standard" d-shell magnetism.

3.3.3 Fe, Co, Ni: strong contribution from the carbon vacancy levels

As we have seen in the previous section the defect levels appearing in the neighborhood of E_F associated with the presence of V, Cr and Mn substitutional impurities in graphene have a strong $3d$ character. Consequently, these impurities exhibit large spin moments. However, when increasing the atomic number along the transition series, the atomic $3d$ levels move to lower energies and we enter a different regime: the defect states nearby E_F have a predominant contribution from the carbon atoms neighboring the metal impurity. For $3d$ late transition metals heavier than Fe, the noble metals and Zn we can establish a strong link between the electronic structure of these impurities around E_F and that of the unreconstructed D_{3h} carbon vacancy.

A detailed scheme of the hybridization of the Ni $3d$ states with those of the carbon vacancy, and the resulting electronic structure, is presented in Fig. 3.8 (a). All the bonding and non-bonding metal-vacancy states are filled in this case and the levels appearing closer to E_F have antibonding character and a strong contribution from the three carbon nearest-neighbors. Closely below E_F we find a level with A character and a strong C $2p_z$ contribution and a smaller weight in the Ni $3d_{z^2}$ state. Above E_F there are two degenerate levels with E charac-

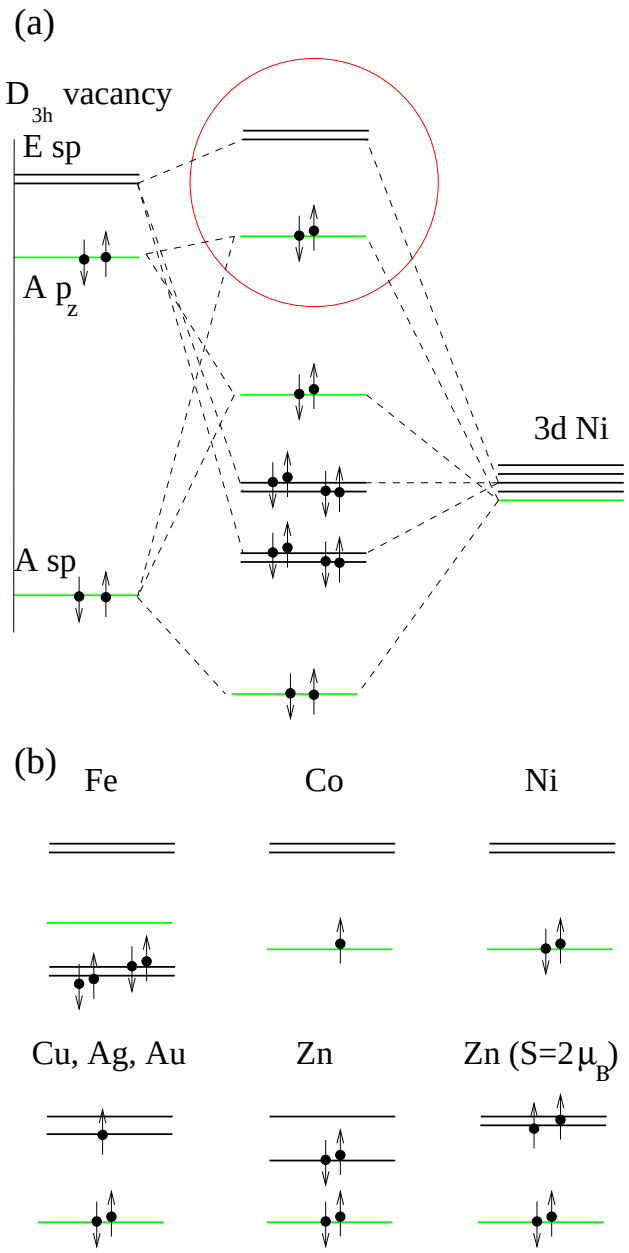

Figure 3.8: (a) Similar to Fig. 3.5 (a) for the case of Ni. The region close to the Fermi level is indicated by a (red) circle. (b) Scheme of the levels close the E_F for Fe, Co, Ni, noble metals and Zn. For Fe, in addition to the antibonding metal-vacancy levels, we have also included the non-bonding d levels that also appear quite close to E_F. The noble metals slightly break the C_{3v} symmetry. For Zn there are two solutions: a high spin solution that preserves symmetry and a distorted one with zero spin moment.

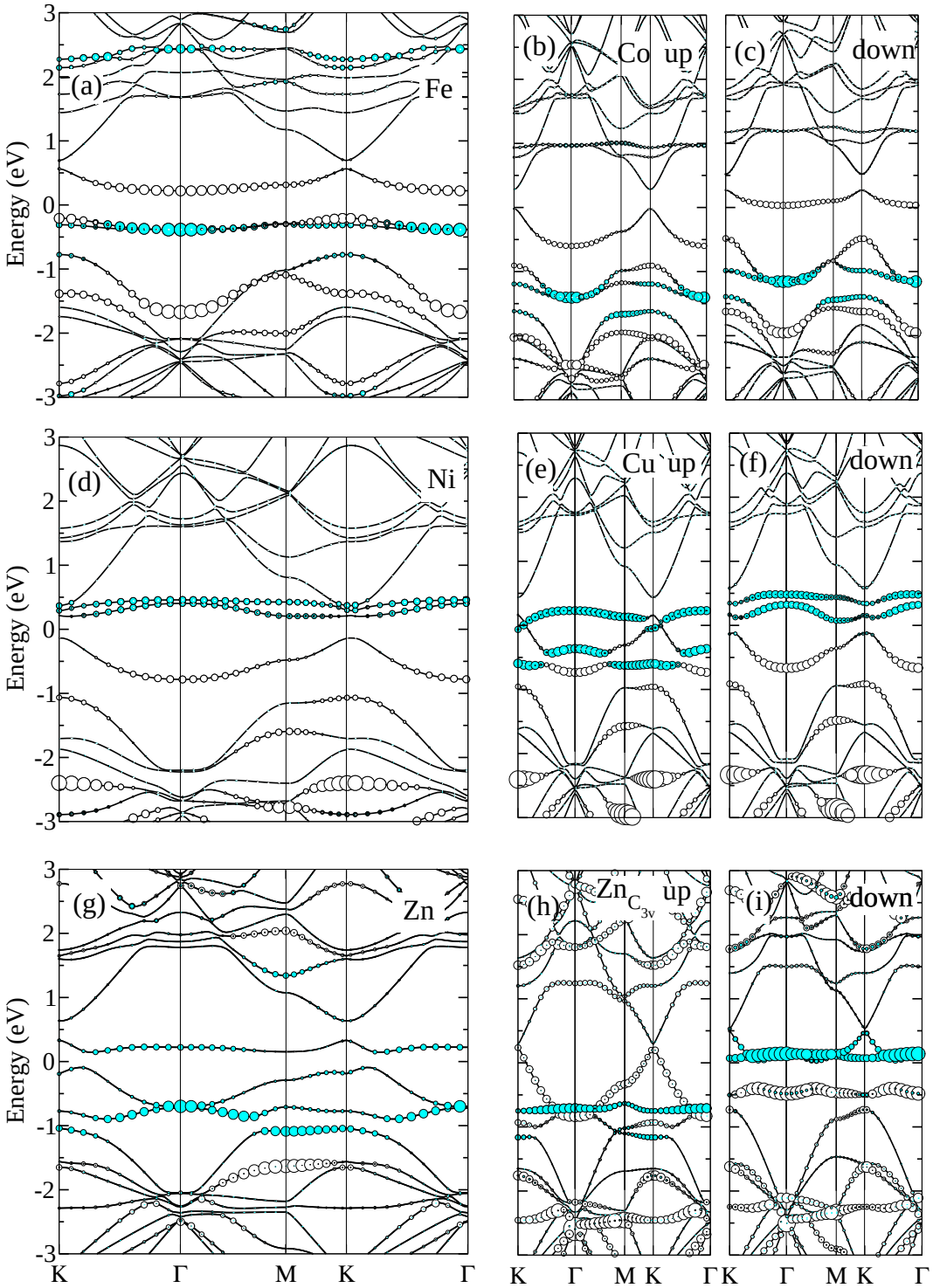

Figure 3.9: Like Fig. 3.7 for Fe (a), Co (b) and (c), Ni (d), Cu (e) and (f), Zn (g) and symmetric $Zn_{C_{3v}}$ (h) and (i) substitutional impurities in graphene.

ter mainly coming from the C $2sp$ lobes and hybridized with the Ni $3d_{xz}$ and $3d_{yz}$ orbitals. The resulting electronic structure strongly resembles that of the isolated D_{3h} (unreconstructed) carbon vacancy as can be checked by comparing the band structures in Fig. 3.4 (a) and Fig. 3.9 (d). The main difference stems from the slightly higher position of the unoccupied E levels in the case of the Ni impurity. This upward shift is due to the antibonding interaction with the d states of Ni and contributes to the stability of the C_{3v} spin-compensated solution. In the case of the D_{3h} carbon vacancy, the E C $2sp$ levels lie closer to E_F and make the system unstable against spin and structural distortions. This clear connection between the electronic structure of Ni and that of the D_{3h} vacancy was already emphasized in Ref. [113].

Thus, our GGA calculations predict Ni substitutional to be a closed shell system with zero spin moment. One could expect that a better description of the electron-electron interaction within the $3d$ shell would enhance any tendency of the system towards a magnetic instability. For this reason we have performed GGA+U calculations (using the VASP code) with values of U up to 4.5 eV. However, Ni substitutional impurities in *flat* graphene always remain non-magnetic in the calculations.

In Ref. [113] we proposed a different way to switch on the magnetism of Ni substitutionals: the possibility of spin-moments induced by curvature. The idea consists in lifting the degeneracy of the two unoccupied E sp-d levels by applying a structural distortion. If the distortion is large enough one of these levels close to E_F becomes partially populated and, due to its small band width, spin polarized. We have checked that the curvature of the carbon layer in (n,n) nanotubes with n ranging between 4 and 8 induces spin moments as large as 0.8 μ_B per Ni substitutional impurity. The spin moment in these substitutionally Ni-doped nanotubes is strongly dependent, not only on the layer curvature, but on the density and arrangement of defects in the tube. We have recently demonstrated that a similar switching of the magnetic moment can be obtained in flat Ni-doped graphene by applying adequate structural distortions, thus providing a simple way to control the spin of this system. [114]

As suggested by our scheme in Fig. 3.8 (b), we can now try to understand the electronic structure of Co and Fe impurities from that of the Ni substitutional but removing, respectively, one and two electrons. According to this image Co substitutionals should present a spin moment of 1 μ_B, while Fe substitutionals should be non-magnetic. This is indeed confirmed by our GGA calculations.

Figures 3.9 (b) and (c) show, respectively, the majority and minority spin band structures of the Co impurity. In the neighborhood of E_F we find a spin-polarized band associated with the antibonding A p_z-d_{z^2} impurity level. The spin splitting of this band is $\sim$0.5 eV. The hybridization character of this level is confirmed by the Mulliken analysis in Table. 3.1. Only a contribution of 0.44 μ_B to the total spin moment comes from the Co atom. The relatively delocalized character of the A p_z-d_{z^2} level also becomes evident. Only a moment of 0.18 μ_B comes from the three carbon nearest neighbors, while 0.38 μ_B comes from carbon atoms at larger distances. The slow distance decay of the A p_z-d_{z^2} defect level translates into quite strong and long-range magnetic interactions between moments associated with neighboring Co defects [115]. Indeed, the peculiar electronic structure of the Co impurities has important consequences for the magnetism of this system: couplings show a complex dependence with distance and direction, while the total spin-moment is determined by the number of Co substitutions in each sublattice of the graphene layer [115]. We refer the interested reader to Chapter 4 (Section 4.3.1).

Figure 3.9 (a) presents the GGA band structure for a Fe substitutional defect in a 4×4

Table 3.2: Structural parameters for substitutional noble metals in graphene.

	d_{C-M}(Å)	h_z(Å)	θ (°)
Cu	1.93, 1.90, 1.90	1.40	88.9, 88.9, 95.2
Ag	2.23, 2.19, 2.19	1.84	71.7, 71.7, 76.7
Au	2.09, 2.12, 2.12	1.71	78.0, 78.0, 81.6

supercell of graphene. Similar results are found using a larger 8×8 supercell. This band structure is again in reasonable agreement with the simple model presented in Fig. 3.8. The non-bonding d levels are completely filled and appear ∼0.4 eV below E_F in the vicinity of Γ. The A p_z-d_{z^2} level is mostly unoccupied and close to 0.2 eV above E_F near Γ. However, we can see that nearby the K point the p_z-d_{z^2} band becomes partially occupied, indicating a small charge transfer from the dispersive π bands of graphene to the defect. Mulliken analysis also reflects a small charge accumulation of ∼0.16 electrons in Fe. In spite of this small partial population, the spin compensated solution is the most stable for Fe substitutionals at the GGA level.

As already pointed out in Sec. 3.1.3, the magnetic behavior of the Fe impurity is a consequence of a delicate balance between the on-site electron-electron interaction and the metal-carbon hybridization. For this reason, we devote a whole Section below (Sec. 3.5) to explore how the band structure and spin moment of Fe substitutionals are modified when these factors are independently controlled by changing the Fe-C bond length and using the GGA+U approximation to describe the effects of the electron-electron repulsion within the d-shell.

3.3.4 Noble metals

In the previous sections we have seen that some of the traditional ferromagnets, like Fe and Ni, become non-magnetic as substitutional impurities in graphene. Also quite surprisingly, we find here that substitutional impurities of noble metals are magnetic with a spin moment of 1 μ_B. The reason for this behavior becomes clear once the electronic structure of these defects is understood.

The band structures can be found in Fig. 3.9 (e) and (f) for Cu and in Fig. 3.10 for Ag and Au. In agreement with the predictions of our simplified model in Fig 3.8, we can see that in the case of the noble-metal impurities the two-fold degenerate E sp-d antibonding levels [116] are now occupied with one electron. The system undergoes a small structural distortion that removes the degeneracy of these levels and the unpaired electron becomes spin polarized. Therefore, substitutional impurities of the noble metals in graphene exhibit a spin moment of 1 μ_B. Relativistic effects are known to be much more important for Au than for Ag and Cu. Although we have not included spin-orbit coupling in our calculations, scalar relativistic effects are taken into account in the construction of the pseudopotentials. However, the similarities between the electronic structure of all three noble metals are evident, which indicates that bonding and magnetic behavior is mainly dictated by the number of valence electrons.

Structural parameters for all noble metals impurities can be found in Table 3.2. For Cu and Ag one of the metal-carbon bond lengths is slightly larger than the other two, whereas for

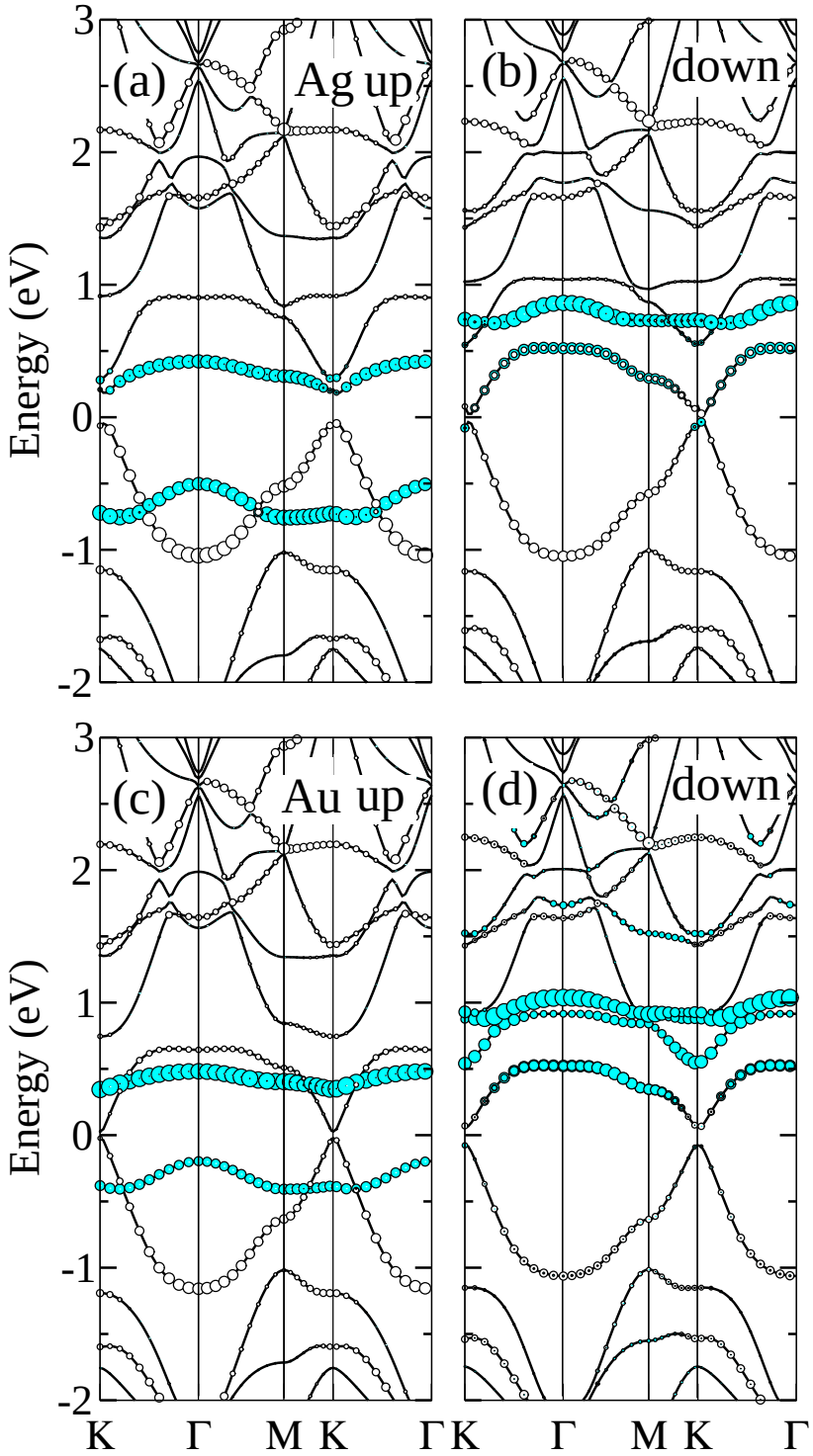

Figure 3.10: Like Fig. 3.7 for Ag and Au. The similarities with the band structure of Cu in Fig. 3.9 are evident.

Table 3.3: Structural parameters and binding energies for substitutional Zn impurities in graphene for the symmetric C_{3v} and most stable distorted configurations.

	E_B (eV)	d_{C-M} (Å)	h_z (Å)	θ (°)
$Zn_{C_{3v}}$	0.91	1.99	1.67	87.9
Zn	1.07	2.06, 1.89, 1,89	1.54	88.3 88.3 103.9

Au one is shorter than the others. However, the distortions are rather small with variations of the bond lengths smaller than 2 %. The differences introduced by the larger scalar relativistic effects of Au mainly reflect in the slightly smaller metal-carbon bond length for this metal as compared with Ag.

Table 3.1 shows the distribution of the spin moment among the metal atom and the nearest carbon neighbors. We can see that the contribution from the metal atom is almost negligible, particularly in the case of Ag. This can be expected from the lower energy position of the d shell in the case of the noble metals as compared with transition metals. Although slightly hybridized with the p shell of the metal impurity, the defect states nearby E_F in this case are mainly coming from the carbon neighbors. Still the spin moment is rather localized in the complex formed by the metal atom and its three nearest neighbors, which for Cu and Ag contributes with a moment of 0.83 μ_B, and up to 0.88 μ_B for Au. The contribution from the rest of the graphene layer is much smaller than, for example, in the case of Co. This reflects the dominant contribution from the relatively localized carbon sp lobes in the description of the defect states nearby E_F for these impurities. This analysis reinforces the link with the electronic structure of the unreconstructed D_{3h} carbon vacancy in graphene as presented in Sec. 3.3.3. In fact, we can picture the main role of late transition- and noble-metals substitutionals in graphene as to stabilize the structure of the carbon monovacancy, that otherwise will severely reconstruct, and to change its charge state.

3.4 Jahn-Teller distortion of substitutional Zn

For Zn impurities a second electron is added to the two-fold degenerate E sp-d shell. Under these circumstances two scenarios are possible: (*i*) a non-magnetic solution in which the system has undergone a Jahn-Teller-like distortion, or (*ii*) a high-spin solution that maintains the symmetric C_{3v} geometry of the defect. The relative energy of both solutions depends on the balance between the energy gain associated with the distortion and the exchange energy of the electrons. Both types of solutions are obtained in our density functional calculations for Zn substitutional impurities in graphene.

The details of the structure and the binding energies of the Zn impurity are presented in Table 3.3 as calculated with SIESTA. Very similar results are obtained for both configurations using VASP. The distorted configuration presents one larger Zn-C bond (by ∼3.5%) and two shorter bonds (∼5%) compared with the bond length (1.99 Å) of the undistorted geometry. The distorted configuration is more stable by 160 meV (120 meV using VASP). This rather small energy difference between the two configurations might point to the appearance of non-adiabatic electronic effects at room temperature.

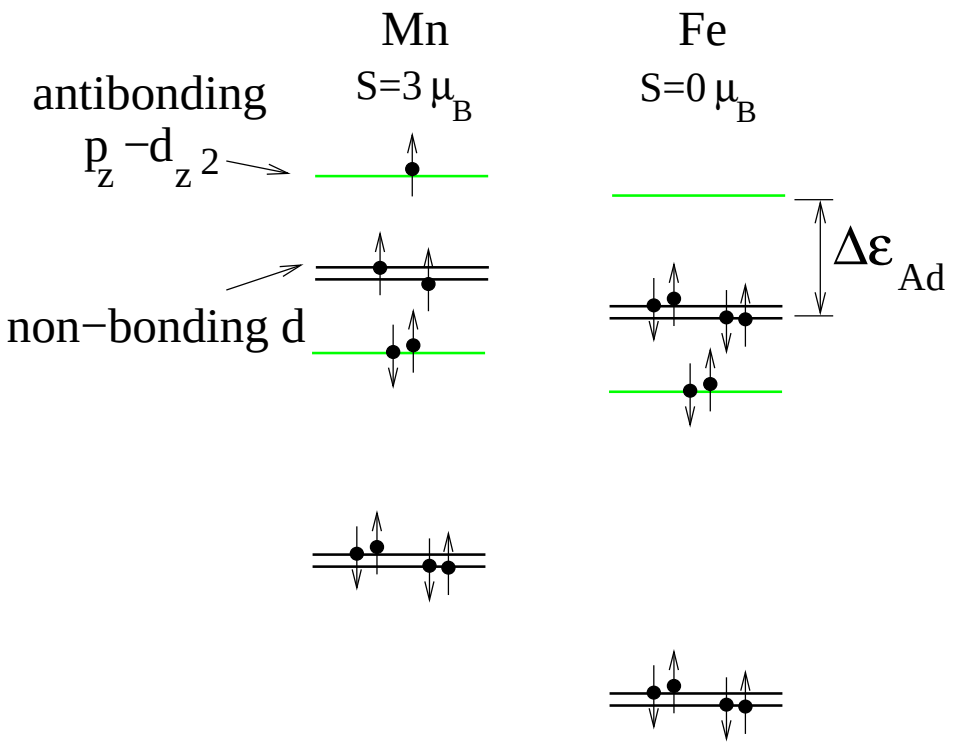

Figure 3.11: Scheme of the electronic levels near E_F for Mn and Fe substitutionals in graphene as deduced from our model of bonding and GGA calculations. $\Delta\epsilon_{Ad}$ is the energy cost to promote an electron to the antibonding A p_z-d_{z^2} hybridization level from the non-bonding $3d$ states. The magnitude of $\Delta\epsilon_{Ad}$, relative to that of the spin-splitting Δ_S of these defect levels, is crucial to determine the spin state of these impurities.

The band structure for both configurations of Zn substitutionals can be found in Fig. 3.9. Again they confirm the model presented in Fig. 3.8. The distorted Zn [Fig. 3.9 (g)] breaks the degeneracy of the E sp-d levels: one of them appears fully occupied ∼0.8 eV below E_F, while the other appears a few tenths of eV above E_F. For the C_{3v} Zn impurity both E sp-d bands are degenerate and the splitting between majority and minority levels is ∼0.71 eV. Table 3.1 shows the Mulliken population analysis of the spin moment for the C_{3v} Zn systems. As in the case of the noble metals the contribution from the three nearest carbon neighbors is the most important. However, the contribution of Zn is somewhat larger and the total spin moment is more delocalized with a contribution form the rest of the graphene layer of ∼0.66 μ_B. We should note that here we have one additional electron as compared to the noble metal systems.

3.5 Fe substitutionals: competition between intra-atomic interactions and metal-carbon hybridization

We have already pointed out that Fe substitutionals in graphene occupy a rather special place at the border between two well defined regimes (see Fig. 3.3): (*i*) the strong $3d$ character of the defect levels nearby E_F and large spin moments found for V, Cr and Mn impurities, and (*ii*)

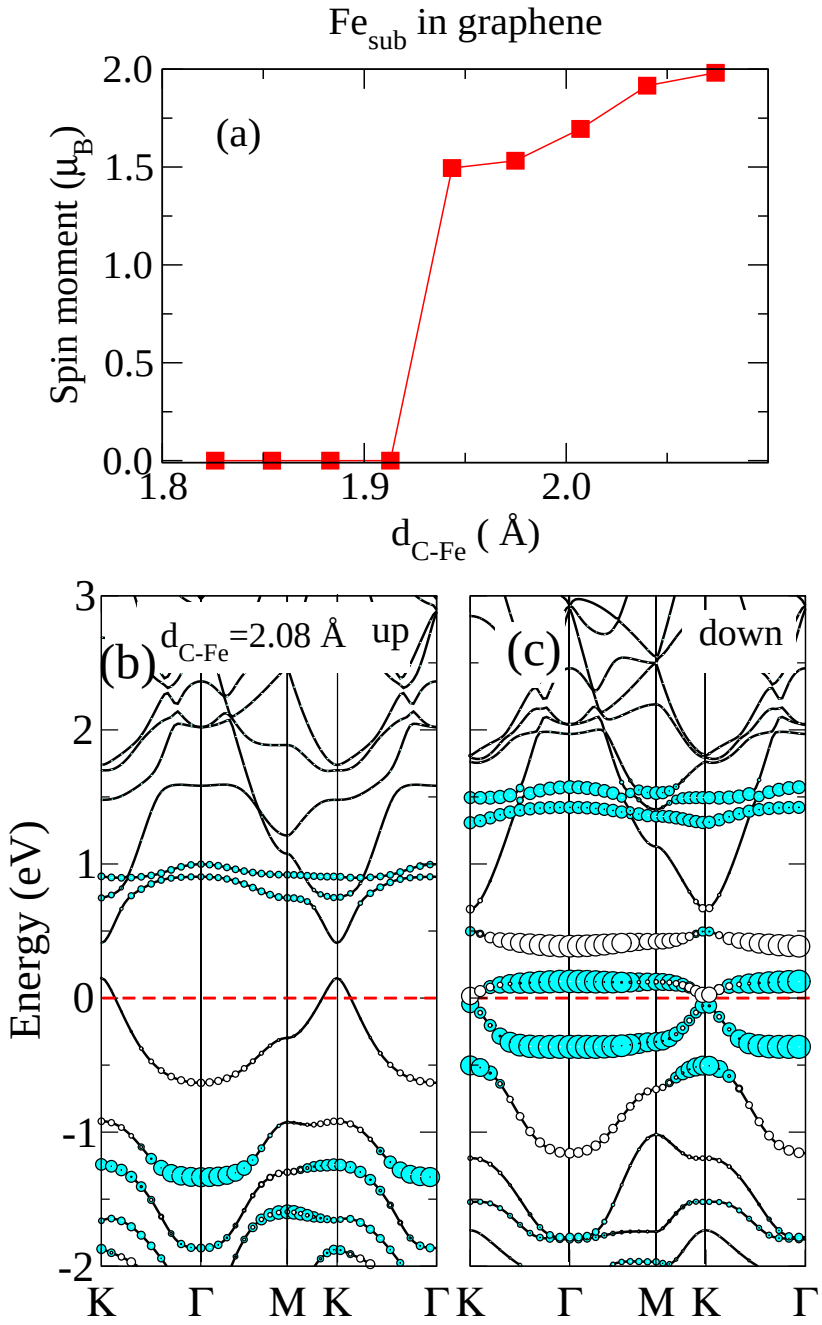

Figure 3.12: Panel (a) shows the spin moment of a substitutional Fe impurity in graphene as a function of the C-Fe bond length. Equilibrium position corresponds to d_{C-Fe}=1.78 Å. Panels (b) and (c) show the band structure for d_{C-Fe}=2.08 Å. Symbol code similar to that of Fig. 3.7. Energies referred to the Fermi level (indicated by a dashed line).

the larger carbon character of those electronic levels and the small oscillatory spin-moments of Co, Ni and the noble metals. GGA calculations [Fig. 3.9 (a)] locate Fe impurities within the second group, with all the $3d$ non-bonding levels fully occupied and non-magnetic. Thus, the spin moment drops from 3 μ_B for Mn impurities to zero for Fe, showing a quite discontinuous behavior as a function of the number of valence electrons. In analogy with the standard Slater-Pauling rule for transition metals, one could expect to find a more gradual decrease of the spin moment as the number of valence electrons is increased, i.e. Fe would have a moment of 2 μ_B. In the present section we study in detail why the non-magnetic solution is more stable for Fe.

3.5.1 Key parameters: metal-carbon hopping and intra-atomic Coulomb interactions

Figure 3.11 shows a scheme of the electronic structure of both Mn and Fe defects. Depending on how electrons are arranged among the A p_z-d_{z^2} antibonding level and the non-bonding $3d$ states, Mn can exhibit spin moments of 3 μ_B or 1 μ_B, while Fe can have a moment of 2 μ_B or can be non-magnetic. At the GGA level Mn prefers the high-spin configuration, while the low-spin one is more stable for Fe. As commented in the Section 3.3.2, the relative stability of the different spin states depends on the balance between the effects of Coulomb repulsion and exchange within the $3d$ levels and the relative energy position of the impurity levels given by $\Delta\epsilon_{Ad}$ (see Fig. 3.11). The hybridization with the neighboring C atoms is crucial in this interplay since it influences (*i*) the degree of localization of the defect levels and the screening of Coulomb interactions, which modify the spin splitting of the electronic levels Δ_S, and (*ii*) the value of $\Delta\epsilon_{Ad}$ through the effective hopping parameter between the $3d$ states and the A p_z carbon vacancy level. Next, we shall deal with both aspects for substitutional Fe in graphene.

Changing Fe-graphene hopping with distance.

By tuning the interaction with the host structure it should be possible to change the spin moment of these impurities. We can modify the hopping by artificially changing Fe-graphene distance. The results of such calculation are shown in Fig. 3.12 (a). While maintaining the three-fold symmetry of the system, we have performed a series of calculations by progressively increasing the height of the Fe atom over the graphene layer. Increasing the C-Fe bond length by $\sim$9% we observe an abrupt jump of the spin moment from zero to 1.5 μ_B. The spin moment continues to rise and saturates at a value of 2.0 μ_B for $d_{C-Fe}\sim$2.07 Å. This convincingly shows that the metal-carbon hybridization is the key parameter to explain the non-magnetic state of Fe substitutional impurity in graphene. When increasing the C-Fe distance we mainly decrease $\Delta\epsilon_{Ad}$. Thus, we reduce the energy penalty for promoting electrons from the non-bonding d to the A p_z-d_{z^2} defect levels. At the same time we also increase the atomic character of the non-bonding d states and reduce the effect of the screening due to the electrons in the graphene layer. This $\Delta\epsilon_{Ad}$ reduction promotes the electron-electron repulsion within the $3d$ states of Fe and, eventually, stabilizes the solution with 2.0 μ_B.

Figures 3.12 (b) and (c) present the band structure for the high-spin state of Fe, where the C-Fe bond length has been elongated up to 2.08 Å. We notice the differences with the spin-compensated ground state in Fig. 3.9 (a). On the one hand, one electron is promoted from the non-bonding d states to the more delocalized antibonding A p_z-d_{z^2} impurity level in

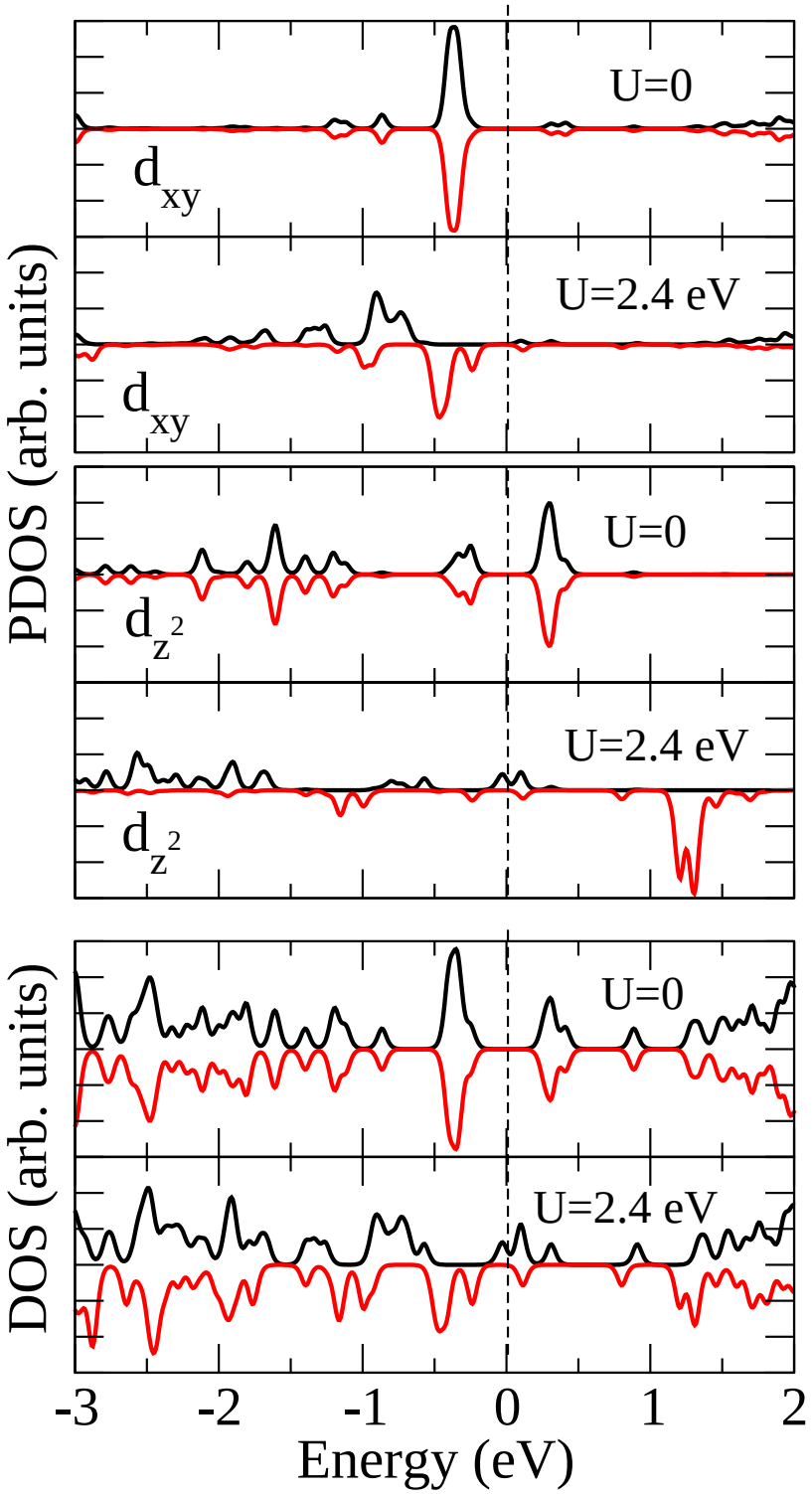

Figure 3.13: Projected density of states (PDOS) and total density of states (DOS) for a Fe substitutional impurity in graphene calculated with VASP using GGA and GGA+U with U=2.4 eV. Positive (negative) values for majority (minority) spin. When U=0 the system shows zero spin-polarization and the Fe $3d_{z^2}$ state is partially occupied. A large enough Hubbard U forces an integer population of the Fe $3d_{z^2}$ state and produces a spin moment of 1 μ_B.

order to reduce the effect of electron-electron repulsion. On the other hand, the spin moment is maximized in accordance with Hund's first rule.

Therefore, we have seen that the non-magnetic character of the Fe substitutionals in the GGA calculations is due to the larger interaction with the graphene layer, as compared for example with the Mn impurity. This is consistent with the fact that Fe, together with Co and Ni, presents the smaller carbon metal bond length among the whole series of $3d$ transition metals. Fe impurities also have one of the largest binding energies. By artificially reducing this interaction it could be possible to obtain magnetic Fe substitutional impurities in graphene.

Changing intra-atomic Coulomb interaction U.

Another route to explore would be to increase the size of intra-atomic electron-electron interactions. We have done so by using the so-called GGA+U methodology in which a Hubbard term is explicitly added to the DFT Hamiltonian and solved within the mean-field approximation. Our results indicate that with a reasonable value of U ($\sim$2 eV or larger) we obtain a magnetic solution for Fe substitutionals. However, contrary to our initial expectation this solution does not correspond to the 2 μ_B high-spin solution discussed above, but to a new solution with 1 μ_B. The key reason to understand this behavior is the partial occupation of the Fe $3d_{z^2}$ state at the level of GGA calculations. The d_{z^2} state is strongly coupled to the delocalized A p_z vacancy level appearing nearby E_F and both, this hybridization and the population of the atomic orbital, are strongly modified when the value of U is increased.

Figure 3.13 shows the results of the electronic structure of Fe impurities calculated using GGA+U with U=2.4 eV and compared with those with U=0. The two upper panels show the projected density of states (PDOS) onto the d_{xy} orbital (the projection onto the $d_{x^2-y^2}$ orbital is identical by symmetry), the two middle panels show the PDOS onto the d_{z^2} orbital of Fe and the two lower panels the total density of states. At the level of GGA, with U=0, there is a very well defined peak closely below E_F in the d_{xy} PDOS corresponding to the position of the non-bonding d states. The spectral weight coming from the d_{z^2} orbital is more spread: presents some broad structure around -1.5 eV corresponding to the bonding A p_z-d_{z^2} defect level interacting with the valence band of graphene, and a narrower peak near E_F with origin in the slightly occupied antibonding A p_z-d_{z^2} impurity state. Therefore, from the Fe $3d$ states appearing nearby E_F we can picture the d_{xy} and $d_{x^2-y^2}$ states as fully occupied and the d_{z^2} as partially occupied due to the larger interaction with the carbon neighbors.

For a sufficiently large value of U the C $2p_z$-$3d_{z^2}$ hybridization is overcome by the tendency of the electrons to have an integer population within the localized $3d$ shell. Thus, the $3d_{z^2}$ localizes one electron and, as a consequence, the system develops a 1 μ_B spin-polarization. This changes can be appreciated in Fig. 3.13. The majority-spin $3d_{z^2}$ PDOS shifts downwards, while a strong unoccupied peak appears around 1.5 eV in the $3d_{z^2}$ minority spin PDOS. Simultaneously, a more delocalized level mostly coming from the $2p_z$ orbitals of the neighboring C atoms appears half-filled at E_F. Note that other levels, such as the d_{xy}, do not suffer such strong modifications since they are already almost fully occupied with U=0. It is also interesting to note that, due to symmetry considerations, they couple with the graphene layer very differently from the d_{z^2} level.

3.5.2 Relevance for recent experiments of Fe implantation in graphite

There are recent reports on the paramagnetism of iron-implanted graphite that indicate the existence of local magnetic moments associated with the implanted Fe atoms. [117, 118] This would be in contradiction with the present GGA results if we assume that the Fe atoms are incorporated to the graphene layer as substitutionals. However, the final geometry of the implanted atoms in these experiments is not known. Furthermore, a considerable amount of defects is created during the implantation process. Although it has been argued that a large part of the damage is healed by vacancy-interstitial recombination [118], the influence of these defects, specially interstitials and big voids, on the observed magnetic response can be determinant.

Therefore, it is not fully clear if we can compare our calculations for Fe substitutional impurities in an otherwise perfect graphene layer with these experimental data. However, as we have shown in detail in this section, Fe substitutionals are very close to a transition and, depending on the details of the calculations, it is possible to obtain a magnetic ground state. In particular, Fe substitutionals develop a spin moment of 1 μ_B at the level of GGA+U calculations for reasonable values of the U parameter. This might be an indication that the non-magnetic ground state found in GGA calculations is a consequence of the limitations of the used functionals.

3.6 Conclusions

We have presented a DFT study of the structure, energetics, and electronic and magnetic properties of several metal atoms as substitutional impurities in graphene, i.e., bound to a carbon monovacancy in the layer. We have considered the cases of all $3d$ transition metals, noble metals and Zn. We have paid special attention to their electronic and magnetic properties and develop a simple model to understand the observed trends. Our model is based on the hybridization of the states of the metal atoms with those of an unreconstructed carbon vacancy. The main ingredients of the model are the assumption, after our calculations, of a three-fold symmetric bonding configuration and the approximate knowledge of the relative energy positions of the levels of the carbon monovacancy and the d shell of the metal impurity as we move along the transition series. With this model we can understand the observed the variations of the electronic structure of the defect, the size and localization of the spin moment, and the binding energy. We have identified three different regimes corresponding to filling of carbon-metal hybridization shells with different character: bonding, non-bonding and antibonding.

In more detail:

(*i*) Most substitutional metal impurities present an almost perfectly symmetric three-fold configuration with C_{3v} symmetry. Noble metals slightly depart from this perfect configuration. Only Zn presents a considerable structural distortion.

(*ii*) For Sc and Ti the metal-carbon bonding shell is completely filled. Therefore, these impurities present the highest binding energies and zero spin moments. Sc substitutionals act as p-dopants for graphene: each Sc impurity localizes one extra electron from the carbon layer.

(*iii*) The non-bonding d shell becomes partially populated for V, Cr and Mn, which develop a very localized spin-moment of 1, 2 and 3 μ_B, respectively. The binding energy decreases slightly as the d shell moves to lower energies, thus reducing its hybridization with the higher

carbon vacancy levels.

(*iv*) For Co, Ni, the noble metals and Zn, the metal-carbon levels are progressively populated. This gives rise to a oscillatory behavior of the spin moment between 0 and 1 μ_B. The spin moments are more delocalized than those found for V, Cr and Mn and present a considerable contribution from the carbon atoms around the impurity. The binding energy presents a local maximum for Co, but suddenly drops for the noble metals and has its minimum for Zn.

(*v*) The electronic structure, nearby E_F, of substitutional impurities of Co, Ni, the noble metals and Zn has a strong resemblance to that of the unreconstructed D_{3h} carbon monovacancy. We can draw an analogy between the electronic structure of these impurities and that of the unreconstructed D_{3h} carbon monovacancy with different number of electrons (charge states). The spin moment of these impurities can be fully understand exploiting this equivalence. In particular, the result that noble metals develop a spin moment of 1 μ_B emerges naturally within this picture.

(*vi*) For the Co impurity, the equivalence can be pushed a step further and we can draw an analogy with the electronic structure of a π-vacancy in a simple π-tight-binding description of graphene. This can be used to explain the peculiar behavior found for the magnetic couplings between Co substitutionals in graphene. [115]

(*vii*) Fe impurities occupy a distinct position at the border between two different regimes. Their magnetic behavior stems from the competition between the carbon-metal hybridization and the electron-electron interaction within the $3d$ shell. As a result, although Fe impurities are non-magnetic at the GGA level, GGA+U calculations with moderate values of U (above $\sim$2 eV) produce a spin-moment of 1 μ_B.

(*viii*) We have found that the unexpected result that Au substitutionals [112, 119] present a spin moment of $1\mu_B$ also holds for all noble metals, i.e., also Ag and Cu present a 1 μ_B spin moment.

(*ix*) We have found that the ground state of the Zn substitutional is non-magnetic due to a Jahn-Teller distortion. Yet, it is possible to stabilize a symmetric configuration with a spin moment of $2\mu_B$ with a very small energy penalty of $\sim$150 meV.

Substitutional impurities of metals in graphene present some interesting magnetic and electronic properties and, therefore, can provide an interesting route to add functionalities or to tune the response of devices based on graphenic materials. Furthermore, recent experiments by Rodriguez-Manzo and Banhart [83] have demonstrated the possibility to create individual vacancies at desired locations in carbon nanotubes using electron beams. This ability, in combination with the high stability of substitutional impurities, can open a route to fabricate ordered arrays of these impurities at predefined locations. Such devices would allow, among other applications, the experimental verification of the theoretical predictions of unusual magnetic interactions mediated by graphene. [84, 85, 115]

Chapter 4

Real Systems that Behave Like π-Vacancies: Co Doping and Covalent Functionalization

The peculiar electronic and magnetic properties of graphene monolayers have recently attracted much attention. New types of electronic and, particularly, spintronic devices based on graphene have been proposed [7, 12, 20, 120]. These graphene structures also drive an increasing interest to study defects, which are always expected in real-life devices. Intrinsic defects have been already widely studied [12, 33, 45, 54, 121] and extrinsic defects, like substitutional atoms studied in the previous chapter, are presently under intense research. [53, 113, 115, 122–124]

In this chapter, we extend further our study of defects in graphene. We will explore other alternatives to generate magnetism in graphene and carbon nanotubes using defects. We will also examine the mechanisms of magnetic coupling between the spin moments linked to defects, giving details of the exchange interaction and its distance decay. We also extent the analysis to organic and inorganic molecules chemisorbed on graphene and carbon nanotubes (CNTs). We show that all these calculations can be understood on the basis of a simple model presented in the Chapter 1, the so-called $\pi-$vacancy (see Section 1.6.1). This model captures the main features of the defects and the physics behind in a simple way. The present chapter is divided into four main sections: In Section 4.1 we introduce the $\pi-$vacancy model in the context of a graphene monolayer substitutionally doped with Co (Co_{sub}) atoms. We observe that there is a one-to-one correspondence between the expected behavior for single vacancies in a simple π-tight binding model of graphene and that found for the Co_{sub} defects. The electronic structure of the Co_{sub} defect at the Fermi energy (E_F) is dominated by a level with a strong contribution from the p_z orbitals of the neighboring C atoms. Moreover, each Co_{sub} defect shows a spin moment of 1.0 μ_B, partly divided between the metallic impurity and the C-neighbours. In sections 4.2 and 4.3 we focus on chemisorbed molecules on top of C in graphene and nanotubes, respectively. We demonstrate that when a single covalent C-C bond is established between an adsorbate and a carbon atom in the graphitic structure, a spin magnetic moment of 1.0 μ_B is induced in the system. This moment is largely independent of the particular adsorbate. This effect occurs for organic and inorganic molecules.

In the fourth part, Section 4.4, we consider magnetic couplings. This is an important issue because it deals with the possibility to create spin order in graphene based on defects.

We start by studying the magnetic coupling between Co_{sub} defects sited either in the opposite or same sublattice. Our calculations show the dependence of the couplings on the crystalline direction and relative position of the defects. The results derived from the Lieb's theorem for $\pi-$vacancies are used as a reference, and a RKKY-like model is used to fit the exchange energies. For the case of molecules covalently bonded to graphene and nanotubes, we have also studied the alignment of neighboring moments. We found that either in graphene or in nanotubes (metallic and semiconducting), the spin moments of the adsorbates at the same(opposite) sublattice do (do not) align ferromagnetically.

Furthermore, in the case of graphene we found that if the two molecules are located at the same sublattice (e.g. AA), the ferromagnetic (FM) configuration is more stable than the antiferromagnetic (AFM) one. In the FM case the total spin magnetization integrates to 2.00 μ_B, with a local spin population that remains nearly constant at every defect site. The exchange coupling falls off very slowly with the adsorbate position, roughly proportional to $\sim |r_{ij}|^{-(1+\epsilon)}$ with $|\epsilon| \sim 0.20$. Conversely, if the two molecules are located at the different sublattices (e.g. AB), we could not stabilize any magnetic solution, and the system converges to a spin compensated solution with no local spin moment.

In the case of metallic nanotubes, adsorbates at the same sublattice exhibit FM behaviour over non-magnetic solutions. Semiconducting tubes have almost degenerate FM and AFM spin solutions and consequently the effective exchange interaction between adsorbates is negligible. Other important result is that adsorption of molecules at different sublattices is always more stable than in the same sublattice.

In all the studied cases, the bipartite graphene lattice plays an important role in the stabilization of these solutions and the observed phenomenology is very close to that found for vacancies in a simple π-tight-binding description of graphene. The chapter ends with the conclusions in Section 5.4.

4.1 Co substitutional impurities in graphene: Realization of single π-vacancies

In Chapter 3 we studied the structural, electronic and magnetic properties of substitutional transition metals in graphene. There, we explored the main features of the doping, moment formation, and we constructed simple diagrams for understanding the bonding between the impurities and the unreconstructed D_{3h} carbon vacancy. Here, we examine in detail an analogy that can be established for Co_{sub} defects in graphene with a simple model. The Co_{sub} impurity is analogous to the toy model system presented in section 1.6.1 for the $\pi-$vacancy. We begin by looking at the spin-polarization induced by a Co_{sub} impurity as shown in Figure 4.1 (a). The spin polarization induced in the carbon atoms has a p_z-like shape and decays slowly as we move away from the impurity. The sign of the spin polarization follows the bipartite character of graphene: the polarization aligns parallel (antiparallel) to the spin moment located in the Co impurity for carbon atoms in the opposite (same) sublattice. The value of the total spin moment is 1.0 μ_B per defect. Using Mulliken population analysis, a value of 0.44 μ_B is assigned to the Co atom; 0.18 μ_B, to the three first carbon neighbors; and 0.38 μ_B, delocalized in the rest of the layer. Therefore, both Co and carbon orbitals contribute to the spin moment formation, as already seen in Section 3.3.3.

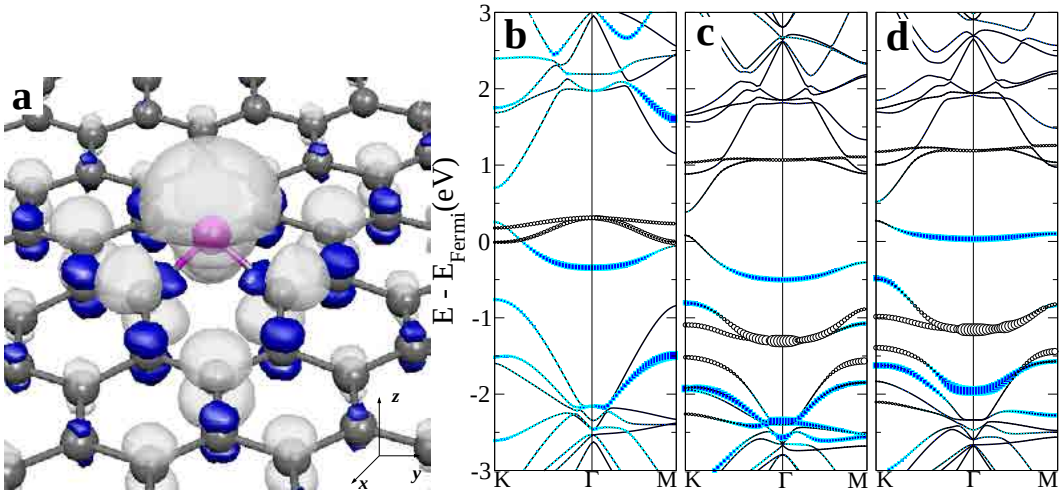

Figure 4.1: (a) Isosurface of the spin density induced by a Co_{sub} defect. Positive and negative spin densities correspond to light and dark surfaces with isovalues of ± 0.008 e^-/Bohr^3, respectively. Panel (b) presents the spin-unpolarized band structure of an unreconstructed D_{3h} carbon vacancy. Panel (c) and (d) show, respectively, the band structure of majority and minority spins for a Co_{sub} defect in a similar cell. The size of filled symbols in panel (b) indicate the contribution of the p_z orbitals of the C atoms surrounding the vacancy, whereas empty symbols correspond to the sp^2 character. In panels (c) and (d), the filled and empty circles denote the contribution of hybridised Co $3d_{z^2}$-C $2p_z$ and Co $3d$-C $2sp^2$ characters, respectively. E_F is set to zero.

To understand the origin of this spin polarization, we now analyse in detail the band structure. Figures 4.1 (c) and (d) present the results for a Co_{sub} defect in a 4×4 graphene supercell. Similar results are obtained using a 8×8 cell. For comparison, panel (b) shows the spin-compensated band structure of a single unreconstructed D_{3h} carbon vacancy (see Section 3.2). For the D_{3h} vacancy, three defect states appear in a range of ∼0.7 eV around the Fermi energy (E_F). Two states appearing at 0.3 eV above E_F have a large contribution from the sp^2 lobes of the C atoms surrounding the vacancy. Another state at 0.35 eV below E_F shows a predominant p_z contribution. This last level corresponds with the defect state at E_F for a vacancy in a simplified π-tight-binding description.

For a Co_{sub}, the defect states of the vacancy described above hybridise with the Co $3d$ states of Co. The two $2sp^2$ defect bands, now an antibonding combination of Co $3d$ and the original C $2sp^2$ vacancy levels, are pushed at higher energies, ∼1.0 eV above E_F (see Fig. 4.1 (c) and (d)). The singly occupied p_z state, now hybridised mainly with the Co $3d_{z^2}$ orbital, remains at the E_F and becomes almost fully spin-polarized. The Co_{sub} impurity becomes thus analogous to a vacancy in the π-tight binding model of graphene.

This p_z C band at the Fermi energy brings our results concerning magnetic moments into contact with Lieb's theorem, where spin polarization is an intrinsic property of the defective bipartite lattice. However Lieb's theorem is global referring to the total system magnetization and does not enter into the local description of the magnetic interaction, which is going to be described in the following sections taking into account several Co_{sub} defects in the cell.

The connection between Co substitutionals in graphene and a simple π-vacancy is not restricted to this system. Other systems do show a similar trend as well. In the next section, we see that complex adsorbates chemisorbed on graphene generate magnetism and that the spin moment due to such doping displays a π-vacancy behaviour similar to Co_{sub}. Some concepts already used here will be again invoked to explain the main features of the magnetism associ-

ated with these defects, leading to an universal magnetic behaviour in graphene independent of the particular adsorbate.

4.2 Organic adsorbates chemisorbed on graphene: Universal spin moment

Chemical functionalization of graphene will play an increasingly important role in graphene based technologies. For instance, new derivatives can be synthesised by addition of foreign radicals or molecules at the carbon surface and they could offer a way to control the electronic structure of graphene. These chemical changes are of great interest in many potential applications such as electronics. In the following, we study covalently functionalized graphene, focusing on the spin moment induced by the adsorption. We later calculate the electronic structure for long CNTs containing chemisorbed adsorbates.

4.2.1 Geometry and structural parameters

We first calculate the geometry with the different molecules chemisorbed on top of a carbon in the graphene monolayer. Figure 4.2(a) represents the C_1-X bond and its three C_2-nearest neighbors. The adsorbate X is either a C atom as in CH_3, C_2H_5, C_6H_{11}, C_6H_5, C_6H_4F, $C_6H_4NO_2$, $C_6H_4OCH_3$, toluene, $C_6H_4NH_2$, $CONH_2$, COOH, poly(methyl methacrylate) (Pmma), poly(tetrafluoroethylene) (PTFE), Adenine group ($C_5H_4N_5C_3H_3ON$), D-glucose group ($C_6H_{11}O_6$), polystyrene ($(C_8H_8)_2CH_3$), polyacetylene $(C_2H_2)_4H$) or a different atom such as H, N, O, F when considering H, NH_2, OH and F as adsorbates. All the adsorbates that form a single covalent bond with the graphene layer adsorb on top of a carbon atom (C_1). The C_1 atom displace vertically and keeps a symmetric three-fold structure. Table 4.1 gives the distance d_X, between adsorbates X(C) and the carbon C_1 as well as the atomic angles Θ_X and Θ_2, which determines the bonding geometry. The adsorption induces geometrical changes that can be explained by a slight modification of the hybridization at a local level towards a certain sp^3-like character [125]. The angles Θ_X and Θ_2 are in a range of $102.13^o - 106.76^o$ and $112.02^o - 115.70^o$, respectively. These values are half-way when compared with those in a pure sp^2-bonded layer, $\Theta_X = 90^o$ and $\Theta_2 = 120^o$, or in a pure sp^3-bonded solid, $\Theta_X = \Theta_2 = 109.5^o$. The largest sp^3-bonding character among the studied adsorbates with C-C bonds is for the Pmma and other polymers. For systems where the bond is C-X(X= H, N, O, F) only minor deviations with respect to the behaviour commented above are observed.

4.2.2 Spin polarization and electronic structure

We would like to understand the origin of the magnetic moment in the functionalized monolayer and we look at the spin polarization of some adsorbates chemisorbed on top of a carbon atom in a 8×8 graphene supercell. In Table 4.1 we summarise the main results for the all studied adsorbates. The energy gain with respect to the paramagnetic solution ($E_M = E_{PM} - E_{FM}$) gives ∼45.10 meV in average. As examples of adsorbates forming a single C-C bond with the layer, Figure 4.2(f) and 4.2(g) show the band structure for an Adenine group and

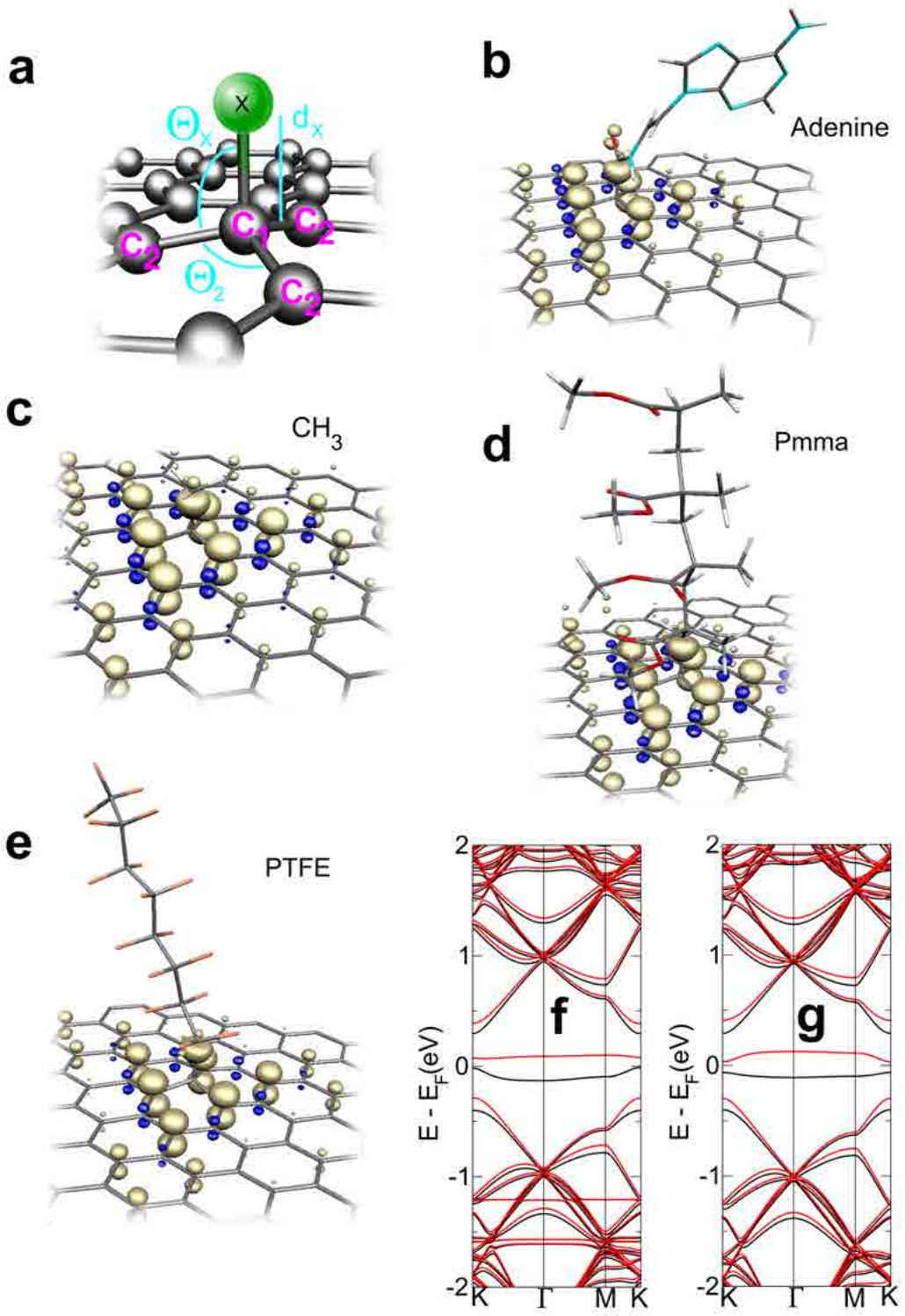

Figure 4.2: (a) The structure of C-X bond in graphene: bond length d_X between the adsorbate X and the C_1 atom and the bond angles Θ_2 and Θ_X. Panels (b)-(e) show the isosurfaces for the magnetization density induced by adenine group, CH_3, Pmma and PTFE on the carbon surface. The cutoff is at $\pm 0.0191431\ e^-/bohr^3$. Positive and negative spin densities correspond respectively to light and dark surfaces. Spin alternates on graphene atoms in different sublattices and has long decay length. Spin polarized band structures for a 8×8 graphene supercell with a (f) single adenine group and (g) a CH_3 molecule are also shown. The black (dark) and red (lighter) lines denote the majority and minority spin bands, respectively. E_F is set to zero.

Table 4.1: Results of the structural parameters (bond length d_X, atomic angles Θ_X and Θ_2) and energetic and electronic data (magnetic stabilization energy E_M, spin moment S, spin splitting δE_s) for all studied systems. The results are for 8×8 graphene supercell with a single molecule. The numbers in parentheses are using FSM method.

$X = C$	d_X(Å)	$\Theta_X(^o)$	$\Theta_2(^o)$	E_M(meV)	S(μ_B)	δE_s(eV)
CH_3	1.59	104.5	113.9	48.6	1.00	0.23
C_2H_5	1.59	105.0	114.0	48.0	1.00	0.23
C_6H_{11}	1.67	105.9	112.5	47.3	1.00	0.23
C_6H_5	1.59	105.7	112.9	46.1	1.00	0.23
C_6H_4F	1.61	106.5	112.1	45.5	1.00	0.23
$C_6H_4NO_2$	1.60	106.9	111.8	32.2	1.00	0.20
$C_6H_4OCH_3$	1.59	106.9	111.9	38.4	1.00	0.21
$C_6H_4CH_3$	1.61	106.6	112.1	46.6	1.00	0.23
$C_6H_4NH_2$	1.60	106.5	112.3	42.8	1.00	0.22
$CONH_2$	1.65	104.9	113.6	43.1	1.00	0.21
COOH	1.60	104.5	113.6	41.6	1.00	0.22
Pmma	1.67	106.7	112.0	47.1	1.00	0.23
PTFE	1.67	105.8	112.8	64.8	1.00	0.19
Adenine	1.65	104.7	113.7	42.5	1.00	0.23
D-Glucose	1.64	105.1	113.5	41.4	1.00	0.21
Polystyrene	1.60	106.8	111.9	40.0	1.00	0.21
Polyacetylene	1.58	105.0	113.5	50.1	1.00	0.24
$X = H, N, O, F$						
H	1.12	102.6	115.3	46.5	1.00	0.24
NH_2	1.52	105.2	113.3	27.7	0.89	0.20
OH	1.52	103.6	114.5	8.4	0.56	0.12
F	1.55	102.1	115.7	0.0	0.0	0.0
				(-24.1)	(1.00)	(0.16)

a CH_3 molecule, respectively. The magnetic moment comes from a very narrow defect state that is pinned at the Fermi level (E_F). This state shows a predominant p_z contribution from the nearest C_2 neighbors of the defect site, with a much smaller component from the adsorbate itself. The small dispersion of this p_z-defect band combined with its partially filled character favours the spin-uncompensated solutions. Under these conditions, the splitting energy between majority and minority spin p_z-defect bands (δE_s) gives a common value of ∼0.20 eV at the Γ point. This value is observed for all adsorbates anchored with a single C-C bond as displayed in Table 4.1. We can see in Figs. 4.2(f)-(g) that other bands also suffer a splitting due to the spin polarization induced by the defect, although it is smaller than for the p_z defect state close to E_F.

The observed spin moment is localized in graphene and, therefore, it is mainly derived from the electronic states of the carbon layer. However, the spin moment is induced by the adsorption of the studied non-magnetic molecules. These adsorbates saturate a p_z state in the layer and create a defect which is analogous to a π-vacancy. Still, according to the results in the Table 4.1, another important ingredient seems to be the polarity of the bond formed between graphene and the adsorbate. When the ionic character of the bond between graphene

and the adsorbate increases we observe a smooth transition from a magnetic to a non-magnetic system that in part reflects the partial polarization of the covalent bond between the carbon host and the adsorbate (charge transfer). In order of increasing electronegativity, the C-X(N, O, F) bonds (see Table 4.1) show an increasing polar behaviour compared to the C-C bond. Thus, H or N bonds that do not have a considerable difference in electronegativities respect to C present spin-uncompensated solutions and an electronic structure quite similar to the C-C bond; but for C-O and mainly C-F bonds, where the latter has the largest difference in electronegativity, the system suffers a drastic reduction of the spin moment or even reaches a non-magnetic ground state. Nevertheless, careful calculations using fixed spin moment method (FSM), indicated in parentheses in Table 4.1, show that the energy penalty needed to develop a spin solution is small even for our most polar bond ($E_M = -24.1$ meV for C-F).

Therefore, this indicates that the C-F bond could easily be polarized by an external perturbations (e.g. magnetic field), so that graphene covalently functionalized with F can show a strong magnetic susceptibility[1] .

To visualise the spin polarization induced by the adsorbates on the graphene lattice, we plot the magnetization density in Figure 4.2: (b) Adenine group, (c) CH_3, (d) Pmma polymer chain and (e) PTFE. It is remarkable to observe that in all the panels a molecule bound to the carbon surface is stabilising a spin pattern in the neighboring carbon atoms with a clear p_z-like shape. The sign of the spin polarization follows the bipartite character of the graphene lattice: carbon spins polarize parallel (antiparallel) respect to the C atom that binds to the surface when sitting in the opposite (same) sublattice. The total spin moment is 1.0 μ_B and a Mulliken analysis assigned to 0.34 μ_B in the three first C_2 nearest-neighbors (see Fig. 4.2(a)), -0.13 μ_B in the next nearest-neighbors, to 0.26 μ_B in the third-neighbors, and to 0.40 μ_B integrated over larger distances. The saturated carbon atom (C_1) in graphene and the carbon atom in the adsorbate that bonds to the layer, show a local spin polarization smaller than $\sim$0.10 μ_B.

We now look at Figure 4.3 which shows the calculated density of states (DOS) per spin channel for different chemisorbed adsorbates at the graphene surface. Despite of the curves have been shifted and smoothed with a Lorentzian broadening, the data over the whole energy range collapse onto a single pattern. This confirms the universality of the origin of the spin moment in covalently functionalized graphene, independently of the particular type of adsorbate. Chemisorbed H also shows the same DOS. Variations from these collapsed curves can be observed for adsorbates with different bond character from a single covalent C-C bond (not shown in Figure 4.3). These results point out the analogy between a C-H bond and a C-C bond of adsorbates, which in principle, is not an obvious behaviour.

It is interesting to note that notwithstanding the biological and chemical activity, different adsorbates present several common points that are worth mentioning in Table 4.1 and Figure 4.3: (i) All the molecules induce a spin moment of 1.0 μ_B that is fairly independent of the supercell size and is mainly localized at the graphene layer; (ii) The origin of the spin polarization corresponds to the p_z-defect state, as was explained above by analysing band structure for two of them; (iii) The δE_s varies in a small range 0.19-0.24 eV, what really points to a very similar localization of the defect states on all the studied systems.

[1] In particular for C-F bond, the FSM calculations indicate an energy cost of less than $\sim$2.0 meV to create a spin moment of 0.50 μ_B in a 8$\times$8 graphene supercell. This tiny energy value reaches the accuracy limit of the calculation which means that a spin polarized solution is equally possible even at the ground state.

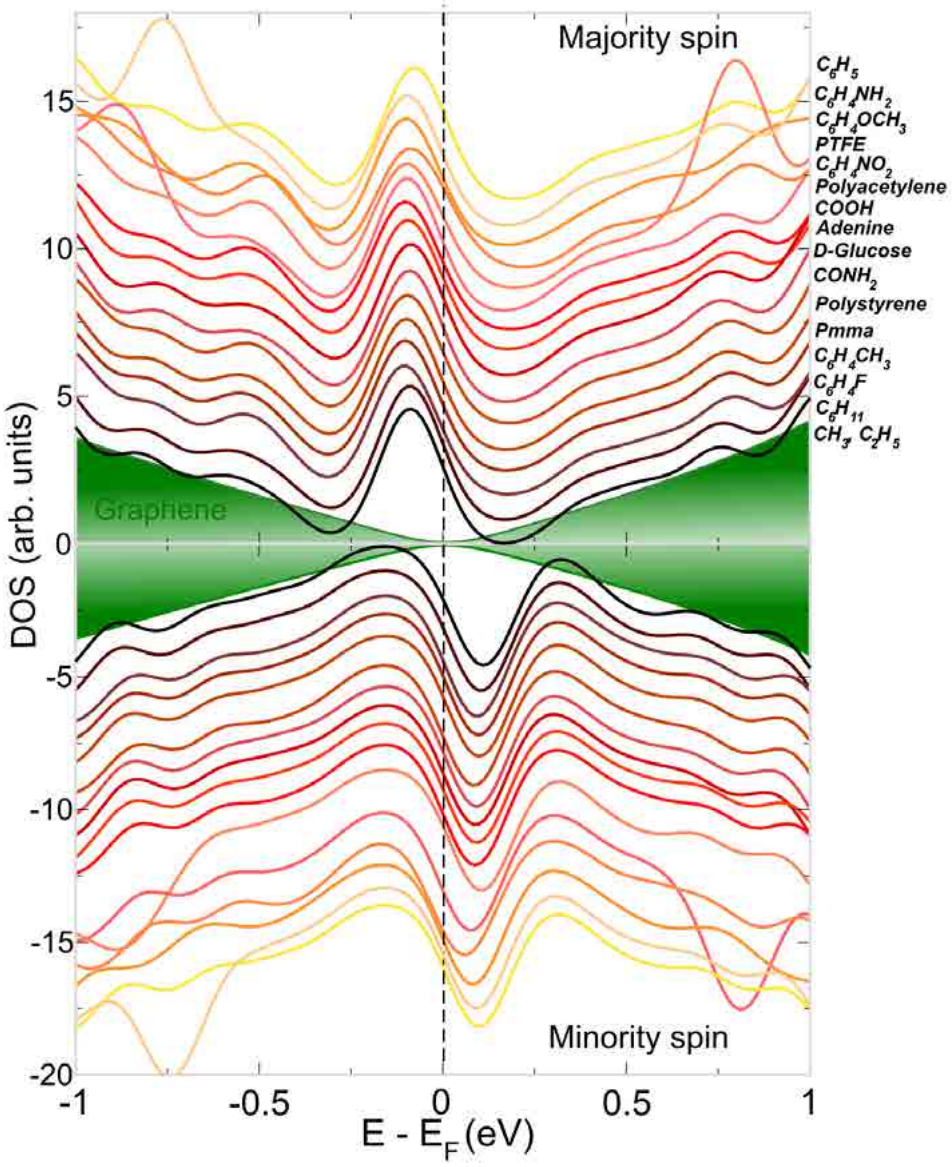

Figure 4.3: Spin polarized density of states for a graphene monolayer with a single chemisorbed molecule on top of a C atom. For clarity, the curves for different adsorbates have been vertically shifted and smoothed with a Lorentzian broadening of 0.12 eV. The Fermi energy (E_F) is marked by the dashed line and is set to zero. The shaded regions represent the density of states of a pristine graphene monolayer. These results are for a 8×8 graphene supercell.

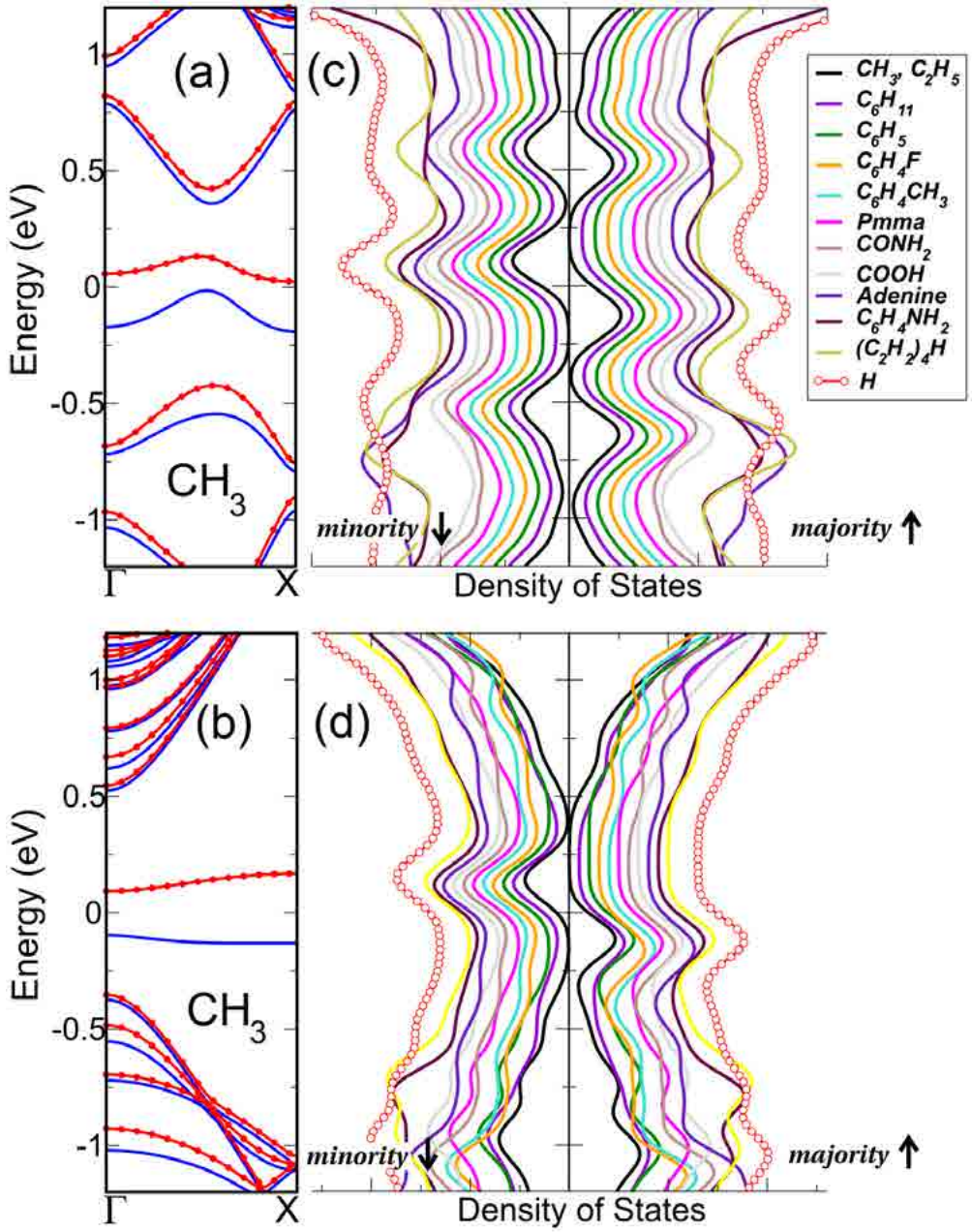

Figure 4.4: Spin polarized band structure and density of states for (a)-(b) (5,5) and (c)-(d) (10,0) SWNTs with a single adsorbate of different types chemisorbed on top of a carbon atom. In panels (a) and (c), the blue (dark) and red (bright) lines denote the majority and minority spin bands, respectively. For clarity, the curves in panel (b) and (d) have been shifted and smoothed with a lorentzian broadening of 0.12 eV. Fermi energy is marked by the dashed lines and is set to zero in all panels.

4.3 Sidewall spin functionalization in carbon nanotubes

Similar to graphene, when a single C-C covalent bond is attached to the nanotube wall, a universal spin moment of 1.0 μ_B is created. In order to understand the origin of this common spin moment, the spin polarized band structure of a CH_3 molecule chemisorbed on top of a C atom is shown in Figure 4.4 for (a) (5,5) and (b) (10,0) SWNTs. In both cases, a defect state

appears pinned at the Fermi level (E_F) with full spin polarization. This state is mainly composed by p_z orbitals of the C neighbors to the saturated site, with almost no contribution from the adsorbate. In fact, a detailed Mulliken analysis of this p_z-defect state assigns a small contribution of the spin moment to the adsorbate. This indicates that the adsorbate has a primary role in creating the bond with the nanotube, and the associated defect level, but it does not appreciably contribute to the spin moment. More complex adsorbates, notwithstanding their biological and chemical activity (e.g. alkanes, polymers, diazonium salts, aryl and alkyl radicals, nucleobases, amido and amino groups, acids), show a similar behaviour. This is observed in the density of states (DOS) per spin channel for metallic (5,5) and semiconducting (10,0) SWNTs shown in Figure 4.4(c) and 4.4(d), respectively. Several common points are worth mentioning: (i) All molecules induce a spin moment of 1.0 μ_B localized at the carbon surface; (ii) The origin of the spin polarization corresponds to the p_z-defect state as explained above for the CH_3 molecule; (iii) The DOS around E_F follows the same pattern in all cases. This match demonstrates that the spin moment induced by the covalent functionalization is independent of the particular type of adsorbate. These results also point out the complete analogy between a single C-H bond with more complex adsorbates that link to graphene through a single C-C bond. This complete similarity is far from obvious and could not be easily anticipated.

Next we study the spin polarization texture induced by the adsorbates on the carbon nanotube wall. The analysis of local magnetic moments for all the adsorbates assigns general trends to both SWNTs. The C atoms that participate directly in the bond formation, at either the molecule or the surface, show a local spin moment smaller than $\sim 0.10\mu_B$. However, the wall carbon atoms contribute with 0.40 μ_B in the three first C nearest-neighbors, -0.10 μ_B in the next nearest-neighbors, 0.20 μ_B in the third-neighbors. The adsorbate removes a p_z electron from the adsorption site, and leaves the p_z states of the nearest carbon neighbours uncoordinated. This gives rise to a defect state localized in the carbon layer, reminiscent of that of a vacancy in a π-tight-binding model of graphenic nanostructures. The carbon spins polarize parallel (antiparallel) respect to the C atom that binds to the surface when sitting in the opposite (same) sublattice. Figure 4.5 shows the magnetization density in semiconducting (10,0) and metallic (5,5) SWNTs for several molecules: (a) Pmma polymer chain [126], (b) Adenine group nucleobase [127], (c) CH_3 molecule [128] and (d) C_6H_4F salt [129]. The spin density in the metallic (5,5) (Figure 4.5(c) and 4.5(d)) is more spread over the whole surface than in the semiconducting (10,0) (Figure 4.5(a) and 4.5(b)). This indicates that the electronic character of the nanotube wall plays a role in determining the localization of the defects states and, most probably, in mediating the interaction between adsorbates. We will confirm this role in subsequent sections.

4.4 Magnetic coupling between defects in graphene

4.4.1 Co impurities in graphitic carbon

We consider next the magnetic couplings between Co_{sub} defects in a large 8×8 supercell with two Co_{sub} impurities. We calculate the energy difference between spin alignments as a function of the relative position of the defects. Figure 4.6 shows the results along with a schematic representation of our notation. Positive values indicate FM spin alignment while negative values are AFM ones. Several observations from spin couplings in Fig. 4.6 can

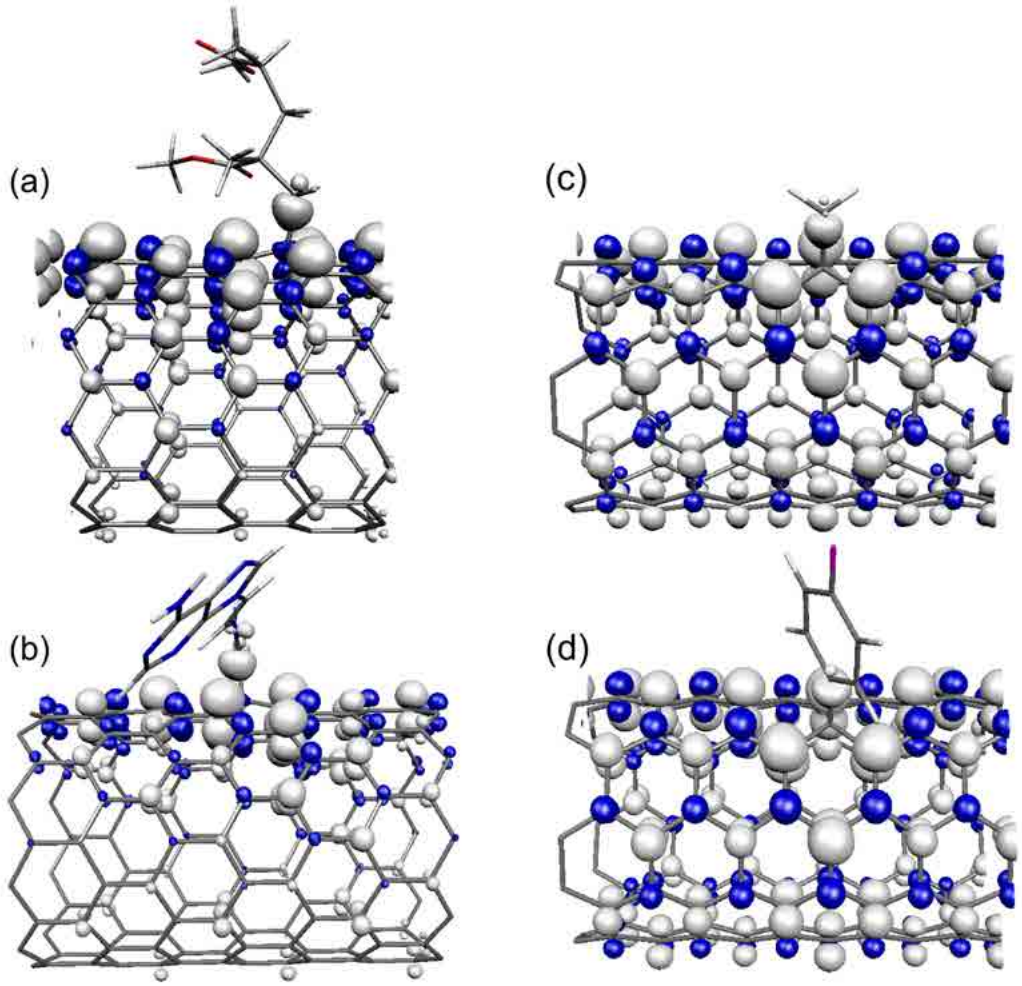

Figure 4.5: Isosurface of the magnetization density induced by some adsorbates at the SWNT surface: (a) Pmma and (b) Adenine group in a (10,0); and (c) CH_3 and (d) C_6H_4F in a (5,5). Majority and minority spin densities correspond respectively to light and dark surfaces, which alternate on the honeycomb lattice with a long decaying order in all cases. The cutoff is at $\pm 0.0133\ e^-/bohr^3$.

be made: (*i*) when the impurities are located in the same sublattice (AA systems) the FM configuration is more stable than the AFM one; (*ii*) if the Co atoms are in opposite sublattices (AB systems) it is very difficult to reach a FM solution, [2] instead the system finds either a spin-compensated (PM) or an AFM solution; (*iii*) at short distances (< 3.0 Å) the systems always converge to spin compensated solutions.

In the FM cases of Fig. 4.6, the total spin magnetization integrates to 2.00 μ_B. The spin population on every Co atom remains almost constant $\sim$0.50 μ_B and it is $\sim$0.30 μ_B for the three C-nearest neighbors. In other cases the total spin is zero. Thus, the total magnetic moment of the system follows the equation $S = |N^A_{sub} - N^B_{sub}|$, where $N^{A(B)}_{sub}$ is the number of Co_{sub} defects in the A(B) sublattices. Our total moment is consistent with Lieb's theorem for bipartite lattices [52]. This supports our analogy between the electronic structure of Co_{sub} defects and single vacancies in a simplified π-tight-binding description of graphene.

The spin magnetization density for some selected configurations is plotted in Fig. 4.7. Al-

[2] When we could stabilize a FM solution, it lies at higher energy, around 0.2 eV above the PM one.

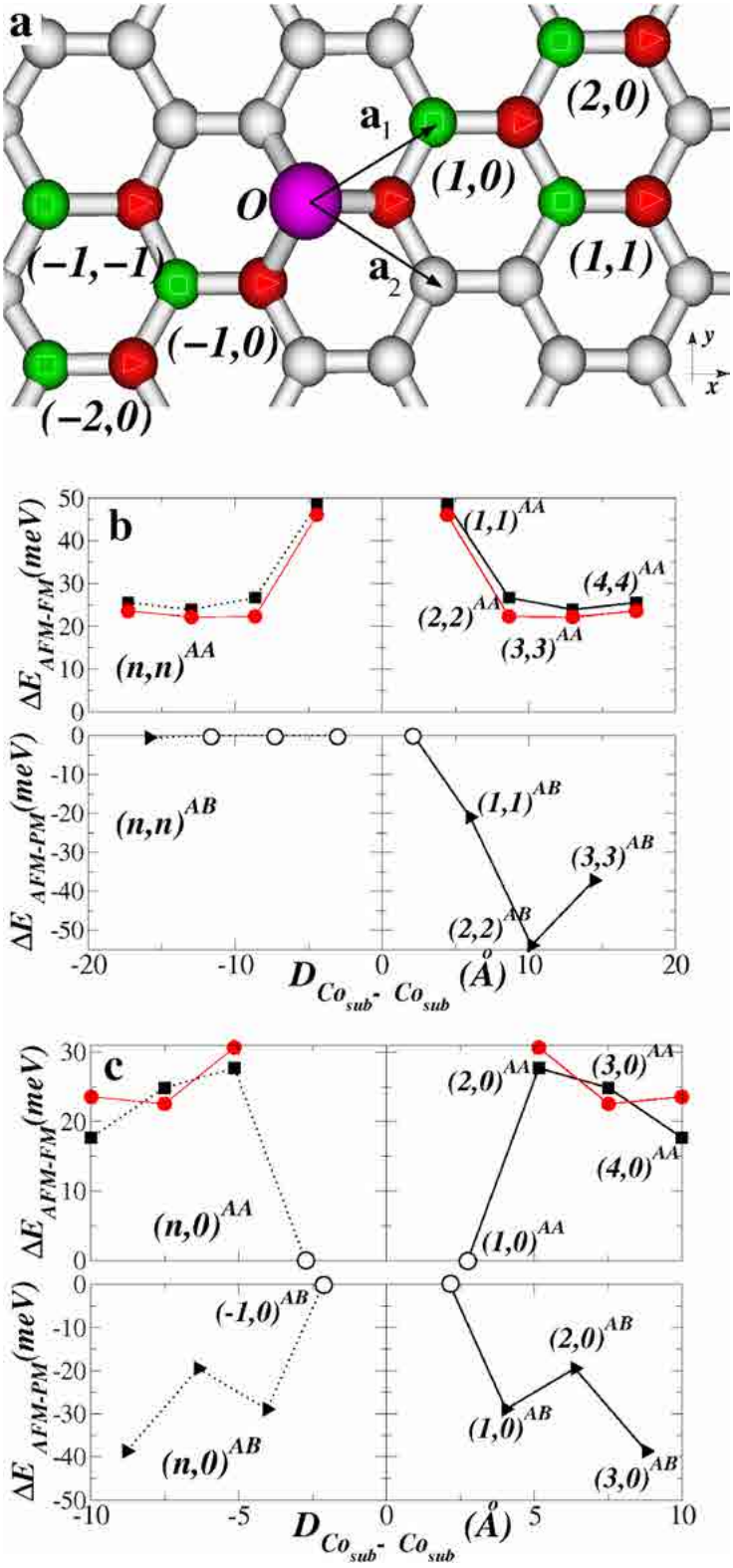

Figure 4.6: (a) Schematic representation of the geometry used to calculate the relative stability of FM, AFM and spin compensated (PM) solutions as a function of the positions of two Co_{sub} impurities. Sublattices A and B are indicated by squares and triangles, respectively. One of the impurities is fixed in a central A-type site, whereas the other is moved along the (b) (n, n) and (c) $(n, 0)$ directions. The empty circles represent spin compensated solutions and the full circles correspond to a fit with a Heisenberg model (see text). Positive values indicate FM spin alignment while negative values are AFM ones.

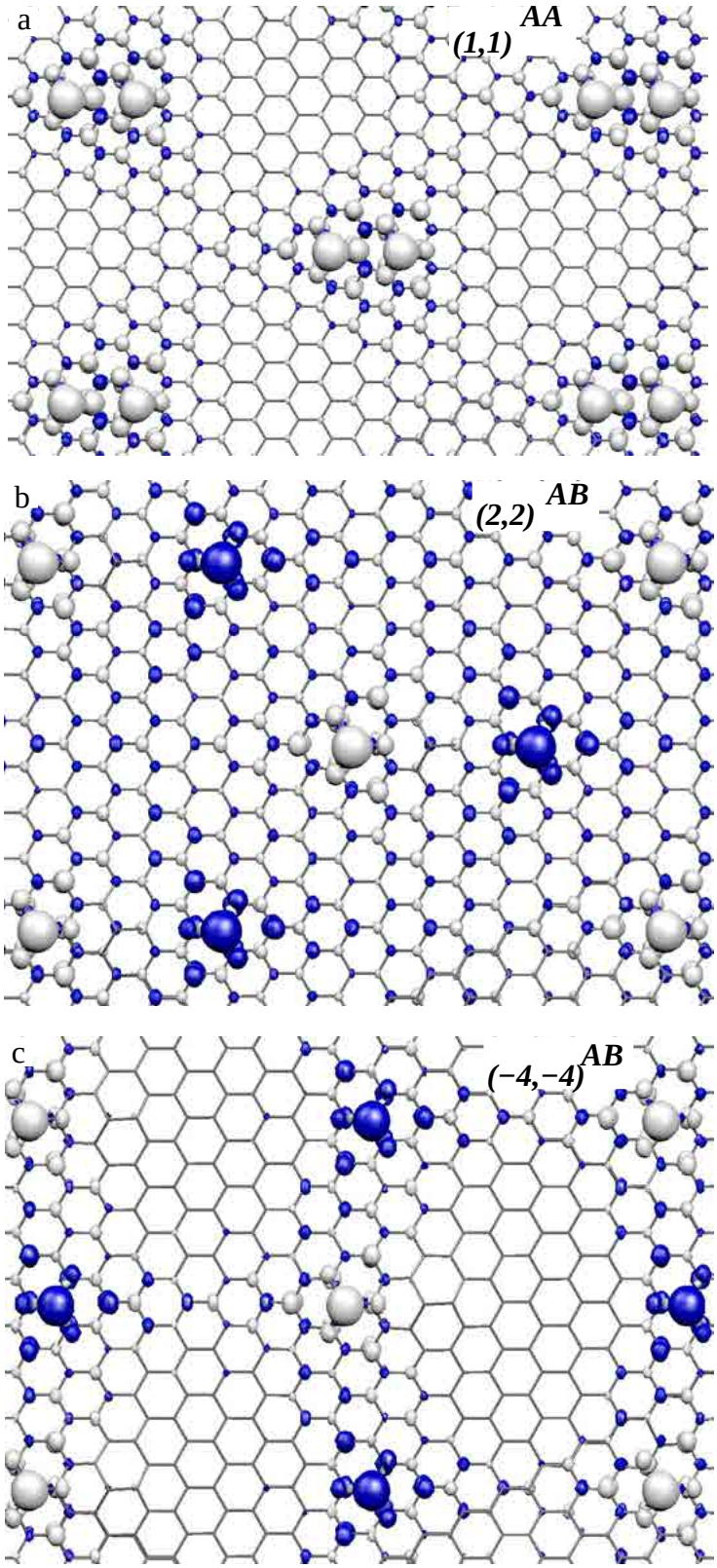

Figure 4.7: (a) Spin densities for configurations (a) $(1,1)^{AA}$, (b) $(2,2)^{AB}$ and (c) $(-4,-4)^{AB}$(see Fig. 4.6(a) for the nomenclature). Positive and negative spin densities are indicated by light (gray) and dark (blue) isosurfaces corresponding to ± 0.001 e$^-$/Bohr^3, respectively.

though the spin is fairly localized on the Co atom and the neighboring C atoms, the presence of the defect also causes a delocalized magnetization density with alternated signs in the two sublattices. The triangular pattern, that reflects the three-fold symmetry of the layer, shows different orientations for A and B substitutions. This explains the very anisotropic AB interaction along the (n, n) direction seen in Fig. 4.6 (b): the energy difference between AFM and PM solutions for $(n, n)^{AB}$ configurations strongly depends on the relative position of the impurities, showing such a directionality. Similar patterns have already been observed experimentally [47, 130–132] in point defects on graphene by STM techniques and also theoretically discussed for π-vacancies. [53,54,133] For Co_{sub} in graphene, similar STM experiments should display the topology of the spin densities given in Fig. 4.7.

We have also investigated the magnetic interactions within the framework of a classical Heisenberg model:

$$H = \sum_{i<j} J_{AA/AB}(\mathbf{r}_{ij})\mathbf{S}_i\mathbf{S}_j \tag{4.1}$$

where $\mathbf{S}_i$ is the local moment for a Co_{sub} impurity at site i. The expression for the $\mathbf{r}_{ij}$ dependence of the exchange has been taken from analytical RKKY coupling given in Ref. [134], except for the exponent of the distance decay, which is fitted to our *ab initio* results. The exchange interaction for AA systems can be fitted with a $|r_{ij}|^{-2.43}$ distance dependence (see the full circles in Fig.4.6 (b) and (c)). This distance dependence is in reasonable agreement with the $|r_{ij}|^{-3}$ behavior obtained with analytical models for substitutional defects and voids [134, 135]. In the case of AB systems a simple RKKY-like treatment fails to satisfactorily describe the interactions, at least for the relatively short distances between defects considered in our calculations.

Next, we explain the appearance of PM solutions in Fig. 4.6. The appreciable interaction between defect levels in neighboring impurities for AB systems opens a *bonding-antibonding* gap in the p_z defect band [3] and, thus, contributes to the stabilization of PM solutions. For AA systems, however, the bipartite character of the graphene lattice makes the interaction between defects much smaller. This explains why AA configurations show a local spin polarization. At very short distance between impurities, a larger defect-defect interaction opens a large gap and, in consequence, stabilises the PM configurations. It is interesting to point out that similar behaviours have been observed for vacancies in ribbons of graphene described within a π-tight-binding model (see Section 1.6.1). [54, 57, 133]

4.4.2 Chemisorbed molecules in graphene

Concerning the magnetic couplings between adsorbates at low concentrations, we use H or CH_3 as examples of chemisorbed molecules at the graphitic surface. In a 8×8 supercell, we calculate the energy difference (ΔE) between ferromagnetic (FM) and antiferromagnetic (AFM) spin alignments as a function of the distance between defects, the so-called exchange coupling. The geometries used in these calculations are shown in the insets of Figure 4.8 (a)-(b). We made several observations: *(i)* if the two molecules are located at the same sublattice

[3] For the AB systems, we find bonding-antibonding gaps in the bands ranging from 0.3 eV to 0.9 eV for $(1, 1)^{AB}$ and $(-1, -1)^{AB}$ configuration, respectively. These values are similar to the $\sim$0.5 eV spin-splitting of the Co_{sub} defect. In fact, all those AB systems with gaps larger than 0.4 eV converge to PM solutions.

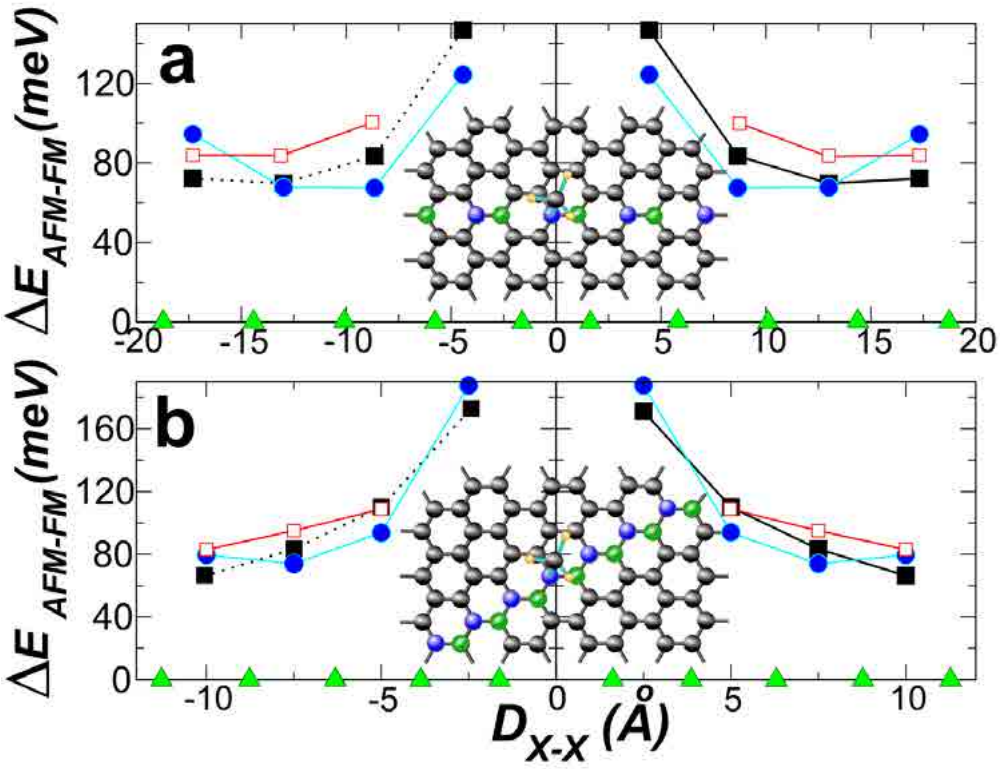

Figure 4.8: Exchange coupling as a function of the position for two adsorbates, H and CH_3, chemisorbed on top of a C atom in a 8×8 graphene supercell. One of the molecules is moved along the (**a**) armchair and (**b**) zigzag directions and the other remains at the origin. The filled and empty squares correspond, respectively, to H and CH_3 at the same sublattice (AA) and the triangles correspond to both adsorbates at different sublattices (AB). The circles correspond to the best fit to a Heisenberg model for the AA sites.

(AA), the FM configuration is most stable than the AFM one. In the FM case, the total spin magnetization integrates to 2.00 μ_B for both H and CH_3, with a local spin population that remains nearly constant at every defect site; *(ii)* if both molecules are located at different sublattices (AB), we could not stabilize any magnetic solution, and the system converge to a spin compensated solution with no local moment; *(iii)* at short distances (< 5.0 Å) the system with chemisorbed CH_3 molecules converges to FM solutions, while it was not possible to stabilize any AFM spin order.

The above magnetic behaviour for adsorbates at different sublattices can be rationalised as follows. When the molecules are located at opposite sublattice the interaction between defect levels in neighboring adsorbates is appreciable. Similar to what we have already seen for Co_{sub} impurities, and in close analogy to the behaviour observed for π-vacancies [54], this interaction opens a bonding-antibonding gap in the p_z defect bands which contributes to the stabilization of spin compensated solutions. If the gap is larger than the splitting δE_s of the majority and minority spin defect bands around E_F the system will be non-magnetic [115]. A detailed analysis of the band structure for both adsorbates fully confirms this interpretation. It is noteworth that a similar behavior was also observed for hydrogen [136] and vacancies [57]. All of them have thus an electronic structure similar to that of H in graphene, which in turn is

equivalent to the simple π-vacancy toy model.

We have also investigated the magnetic interactions within the framework of a classical Heisenberg model using Eq. (4.1), where now $\mathbf{S}_i$ is the local moment induced by H or CH_3 at the adsorption sites i. We find that the magnetic interaction between chemisorbed molecules is long range and falls off slowly with the distance. It is roughly proportional to $J_{AA}(\mathbf{r}_{ij}) \sim |r_{ij}|^{-(1+\epsilon)}$ with $|\epsilon| \sim 0.20$, as can be seen by the circles in Fig.4.8 (b) and (c). This distance decay differs from that of substitutional Co impurities [115] in graphene monolayer ($\sim |r_{ij}|^{-2.43}$) as shown above. However, it agrees with a recent theoretical study [137] where the interactions of the adatoms on graphene, using a π-tight-binding model, is an inverse function of the distance.

4.4.3 Adsorbates in nanotubes

Now we address the energy stability of the different magnetic solutions when two molecules are adsorbed in the walls of CNTs. We focus on a chemisorbed molecule at the nanotube surface by looking at H as an example. For the metallic (5,5) and semiconducting (7,0) single wall CNTs, we calculate the variation of the total energy for several spin alignments as a function of the distance between the adsorbates. The used geometry along the tubes is schematically shown in the insets of Figure 4.9(a) and 4.9(b). One H is sited at the origin; and another, in different positions along of the tube axis (see background pictures). Several observations can be first made on the stability when two adsorbates are located at the same sublattice (AA configurations). In the metallic (5,5), the FM configuration is most stable than the non-magnetic one (PAR). The energy difference between these two spin solutions along the tube axis oscillates and no AFM solution could be stabilized at all. In the semiconducting (7,0), the FM and AFM solutions are almost degenerate, with a small energy difference (exchange coupling).

If the two molecules are now located at different sublattices (AB configurations), we were not able to stabilize any magnetic solution for both nanotubes. Instead the systems is more stable without a local spin moment. This behaviour for adsorbates at opposite sublattices can be traced back to the interaction between the defect levels. While for AA configurations the interaction is negligible, for AB ones this interaction opens a bonding-antibonding gap around E_F in the p_z defect band and, thus, contributes to the stabilization of PAR solutions. If the gap is larger than the spin splitting of the majority and minority spin defect bands the system will be non-magnetic [54, 115]. In fact, our detailed analysis of the band structure fully confirmed this explanation. However, it is worth noting that AB adsorption seems to be always more stable in our calculations. This indicates that if the adsorption takes place at random sites, the magnetic solutions will only be stable for low density functionalization.

4.5 Conclusions

This chapter deals with the spin moment induced by several defects that can be understood in terms of the simple model provided by the π-vacancy. We also consider the magnetic couplings between those defects in graphenic structures. We focus on substitutional Co atoms as well as on chemisorbed molecules in graphene and carbon nanotubes. Co_{sub} defects show many similarities with the fictitious π-vacancy in graphene. The spin density generated by a Co_{sub} defect shows maxima in those C atoms that occupy the opposite sublattice to that where

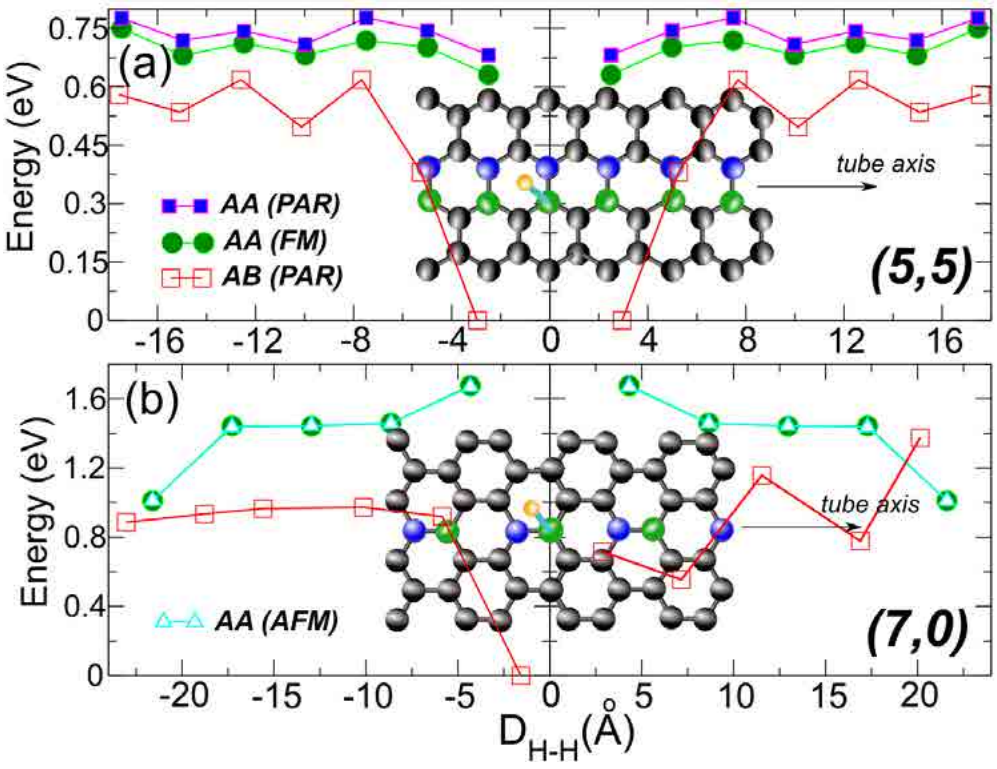

Figure 4.9: Variation of total energy with the H positions for the distinct magnetic solutions in the two graphitic sublattices (AA and AB). One of the molecules is moved along the axis of a (a) (5,5) and a (b) (7,0) SWNT; and, the other remaining at the origin (see background pictures). The empty and filled squares correspond to PAR spin solutions at AB and AA sublattices, respectively. The circles and triangles indicate the FM and AFM solutions, respectively, at the same sublattice.

Co sites, following the bipartite character of the graphene lattice. For two Co substitutionals, we distinguish between AA and AB positions. For AA cases, the induced moments align ferromagnetically and the strength of the couplings depends on the relative distance as $|r_{ij}|^{-2.43}$. The total moment follows Lieb's theorem similarly to a collection of π-vacancies. For AB cases, the band structures around Fermi energy show the opening of antibonding-bonding gaps between defect levels in neighboring defect sites, which suggests large interactions between them. The alignments of the magnetic moments are AFM or PM, a trend that is also similar to that found for π-vacancies [54, 57, 133]. To end this part we ought to remark that the origin of the spin moments and the sign of the couplings stem from the bipartite lattice of graphene.

The analysis of the magnetic properties induced by chemisorbed molecules in graphene and carbon nanotubes was conducted using many types of adsorbates: polymers, diazonium salts, aryl and alkyl radicals, nucleobases, amide and amine groups, sugar, organic acids. A spin moment of 1.00 μ_B is induced at the carbon surface always that a single C-C bond is formed between an adsorbate and the graphenic layer. This moment was observed to be independent of the supercell size, and it is stabilized by several tenths of meV respect to the non-magnetic phase. AA adsorption always leads to FM alignment. AB adsorption, however, always stabilises non-magnetic solutions. The global spin moment follows again the Lieb's theorem. Similarly to Co impurities, a RKKY-like model was used to fit the calculated

magnetic interactions. The interactions decay slowly in the bipartite lattice, being roughly proportional to the inverse of distance.

Metallic carbon nanotubes behave similarly to graphene. For molecules chemisorbed at the same sublattice (AA adsorption) we could only stabilize FM or PM configurations. The FM solutions are more stable than the PM ones. In semiconducting nanotubes, FM and AFM solutions are almost degenerate even for AA adsorption, with a small energy difference along the tube axis. For two molecules in different sublattices (AB adsorption), we could not stabilize any magnetic solution and the system is more stable without a local spin moment.

Chapter 5

Effect of Strain on the Electronic and Magnetic Properties of Defects in Carbon Nanostructures

This chapter contains a study of the structural, electronic and magnetic properties of several defects in carbon nanostructures under an external applied strain. We will address how the presence of strain can be used to modify the electronic and structural properties of vacancies and substitutional metals in carbon nanostructures, and how the interplay between magnetism and mechanical perturbations can play an important role in this class of systems. The chapter is divided as follows:

Sec. 5.1 considers monovacancies in a graphene sheet. We find that the applied strain can modify the properties of a monovacancy, so that the defect could show a very rich spin and geometric phase diagram. Stretching increases the size of the spin moment in different phases while compression reduces or even kills the magnetic signal. The transition to non-magnetic solution is linked to changes in the global structure of graphene that are associated with the formation of long range ripples. For compressions slightly greater than 3%, this rippling leads to the formation of a heavily reconstructed vacancy structure at saddle point positions that consists of two twisted hexagons and pentagons. We propose that the control of defect-induced magnetism in graphenic structures is feasible by mechanical deformations.

Sec. 5.2 shows that substitutional metallic impurities in carbon nanotubes can display a different magnetic behaviour from that observed in a flat graphene monolayer. We use Ni dopants as an example and we demonstrate that the intrinsic curvature already present in the SWCNT's can be used to switch on the magnetism of Ni substitutionals. Ni substitutionals are non-magnetic in flat graphene. A strong dependence of the spin moment on the impurity distribution, tube metallicity and diameter of the nanotube is also observed. A simple model taking account the curvature-induced anisotropy of the hopping between Ni and the first three C neighbours is presented and qualitatively explains all features observed in the ab initio calculations.

Finally, Sec. 5.3 focus on calculations on the effect of uniaxial strain applied to Ni doped graphene. We show that besides the curvature, the application of a uniaxial strain can also be used to induce and control the magnitude of spin moment in a practical way. In a short range of applied strain the spin moment changes from zero at equilibrium up to 1.9 μ_B at $\sim$7.0% strain. This strong variation can be traced back to modifications of the local structure of the

defect. These structural changes can be related to those of the unreconstructed carbon vacancy in graphene under strain which presents strong similarities with Ni substitutionals impurities.

The chapter ends with the conclusions in Sec. 5.4.

5.1 A general spin-strain phase diagram for a monovacancy in graphene

In this section we study the effect of isotropic strain on the electronic structure of vacancies in graphene. The interplay between global and local structures reflects directly in the simultaneous observation of new types of spin solutions, defect reconstruction and corrugation on the whole system. The 2D-character of graphene combined with its intrinsic rippled geometry provide the necessary framework for this new kind of effects. We focus on carbon monovacancy, and find that it shows a rich structural and spin phase diagram as a function of strain.

5.1.1 Structure versus strain

We start taking a look at Figure 5.1 which illustrates the relaxed geometry of one of our models of a free-standing defective graphene layer under a 1.2 % isotropic compression. While under tension the layer remains perfectly flat, and small compression produces the spontaneous rippling of graphene with a characteristic deformation around the vacancy. At zero strain, the monovacancy tends to undergo a Jahn-Teller–like distortion that lowers its energy by $\sim$200 meV: atoms of type 1 (see the inset of Fig. 5.1) reconstruct to form a pentagon with the neighboring atoms, while atom 2 is left with the dangling bond responsible for the spin polarization. Although we herein consider a non-planar structure under strain, our findings at low compressions are similar to results previously obtained for flat graphene [42, 121]. However, atom 2 in our rippled structure is progressively lifted from the graphene surface by as much as $\sim$1.0 Å for strains slightly below 3%, just before the occurrence of a strong vacancy reconstruction. The data of Figure 5.1B reveal a particularly striking result. In contrast to 2D vacancy, for which previous authors invariably described a 'pentagon-goggles' structure, our own calculations show that the vacancy is strongly reconstructed under rippling. For compressive strains greater than 3%, an altogether new defect structure is produced consisting of two heavily distorted hexagons and pentagons and resembling the transition states for the movement of a planar monovacancy. We shall now focus on the description of this region of transition for compression of up to 2.8%.

Figure 5.2A shows the maximum amplitude of the rippling h as a function of strain for defective graphene (shown by the solid symbols). We removed the defects from each rippled structure by adding carbon atoms to the vacancy sites and relaxing the structure. We obtained rippled pristine graphene with maximum amplitudes as shown in Figure 5.2A (open symbols). The amplitudes and the topographic patterns (insets in Figure 5.2A) show little difference between pristine or defective graphene, particularly for compressive strains greater than $\sim$1%. It seems that even for large supercells, the main determinant to observe ripples is the applied strain. However, the structural patterns that occurs in defective graphene define a preferential direction and break the up-down symmetry that exits perpendicular to the layer. This preferential direction and the symmetry breaking are explained by the presence of the

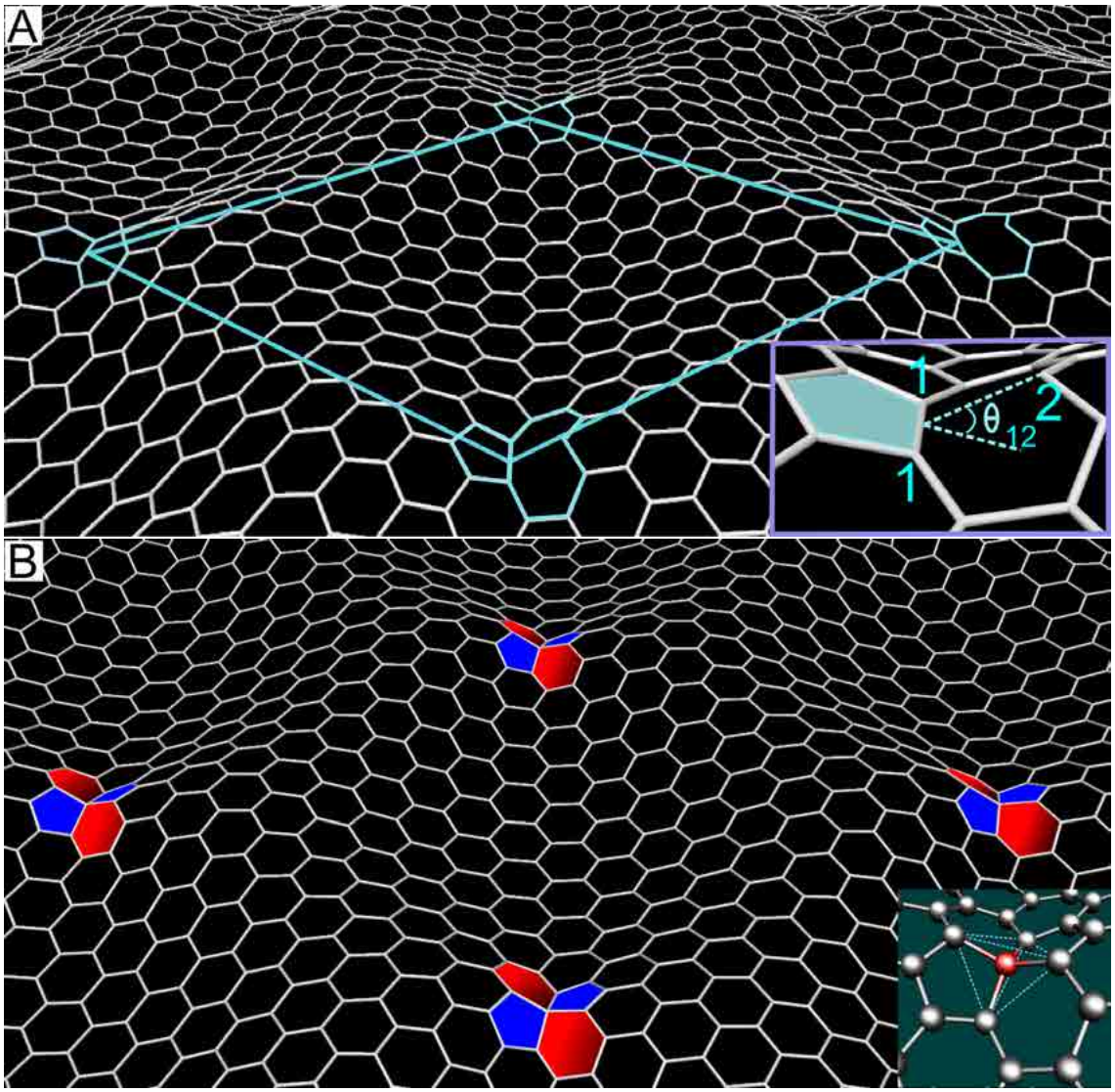

Figure 5.1: (A) Graphene with vacancies under an isotropic compression of 1.2%. As an example we use the 10×10 unit cell (highlighted). The inset shows the geometry of the vacancies and the atomic labels. The local bending at the vacancies is described by the angle θ_{12} between the pentagon and the plane defined by three C atoms around the vacancy, i.e. two equivalent atoms labeled 1 and a third atom labeled 2. Note the rippling of the graphene sheet with the vacancies at the saddle points. (B) A different vacancy structure for a higher compression slightly under 3%. It has two distorted hexagons and pentagons, while the central C atom shows a sp^3 hybridization.

reconstructed vacancies. The vacancy breaks the hexagonal symmetry of graphene with their goggles-pentagon structure and thus play a key role in determining the shape and symmetry of the global deformation patterns of graphene.

We simultaneously characterise the local curvature at the vacancies and the height of atom 2 above the local tangent-plane in terms of the bending angle θ_{12}, as defined in Figure 5.1. In Figure 5.2B, we plot the bending angle for both defective and pristine graphene. Under moderate compression (1-2%), the local bending angle for defective graphene is about three times greater than that of pristine graphene and the graphene rippling is clearly favoured by the presence of the vacancies. The dependence of θ_{12} on the size of the supercell, as shown

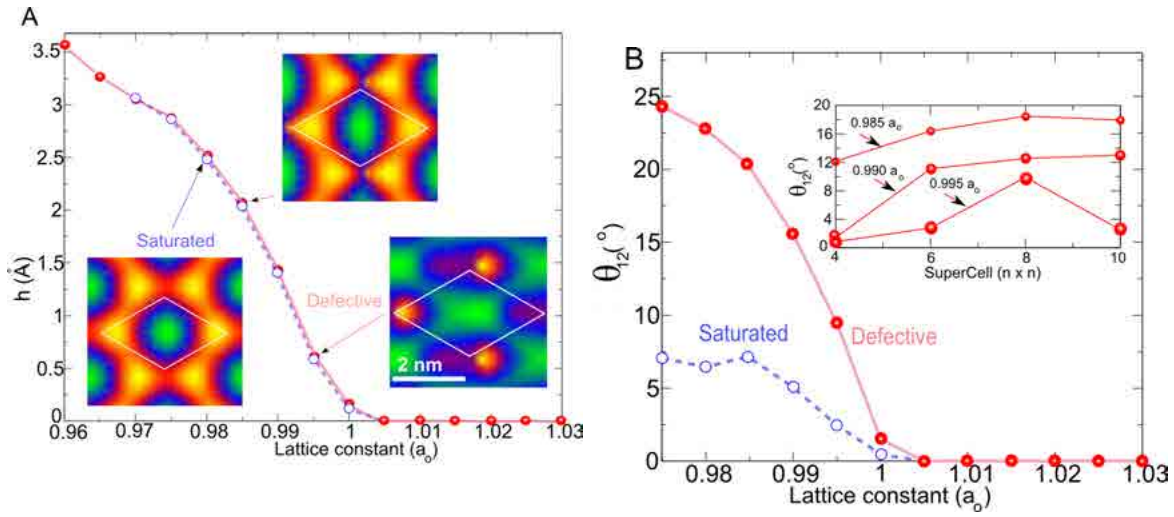

Figure 5.2: (A) Maximum amplitude h(Å) of rippling for 10×10 graphene supercells versus strain in units of the equilibrium lattice constant a_o. The filled circles denote defective graphene, while the empty circles denote the pristine layer that has been recovered by adding a carbon atom to the vacancy. The insets show the corrugation patterns: the bright/yellow (dark/green) areas indicate the higher (lower) regions. (B) Bending angle θ_{12} (see definition in Figure 5.1) as a function of strain. The inset shows the behavior of the bending angles with size of supercell for different values of strain. The local induced deformation clearly depends on the presence of vacancies and on the size of the supercell.

in the inset of Fig.5.2B, further demonstrates the coupling between the local geometry of the defect and the global deformation. For example, for a 4×4 supercell, a strain larger than 1.0% is required to obtain an increase in θ_{12} and to allow the corrugation of the layer to begin. However, for larger supercells, much smaller strains cause appreciable deformations around the vacancies.

5.1.2 Energetics

It is worth mentioning that the range of applied strain used here (a few percent) is comparable to that present in experiments in which an appreciable corrugation of graphene was reported for supported layers [138–140], chemically functionalized graphene [141] , or defective layers [142]. As a result of the imposed periodicity and the finite-sizes used in our calculations, long-wavelength deformations appear primarily to be related to the strain, i.e. vacancies do not create significant corrugation in the relaxed geometry at the equilibrium lattice constant. However, we observe that for the range of strain considered here, the system is compressed and thereby assumes a rippled configuration at an energy between two and three times lower for defective graphene than for the pristine layer. For a 10x10 supercell, the energy required to create ripples for a compression of 3% is reduced to almost half its value in the presence of vacancies, as seen in Figure 5.3A. This difference in energy is consistent with the proposed role of vacancies as a source of ripples in recent experiments [142].

5.1.3 Magnetism versus strain: several spin solutions

Earlier we commented on the fact that isotropic strain can be used to tune the vacancy structure and the curvature of the layer at the site of the defect. We now focus on the influence of these

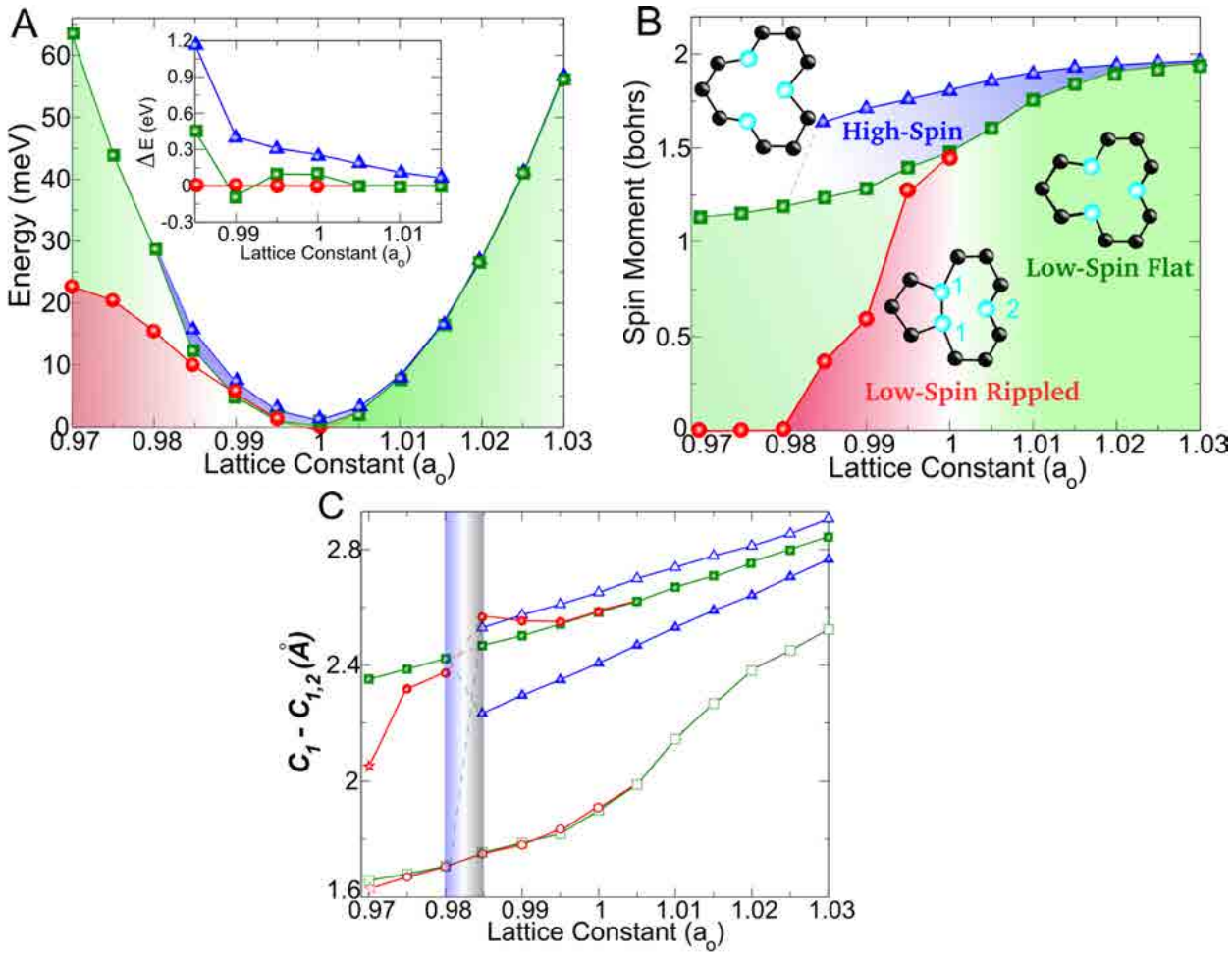

Figure 5.3: Variation in total energy per atom (A), spin moment (B), and bond length (C) versus strain for three different configurations of vacancy in the 10×10 supercell: high-spin flat (triangles), low-spin flat (squares) and low-spin rippled (circles). The inset in panel (a) details the change in total energy with respect to the low-spin solutions at about zero strain. The filled and empty symbols in panel (C) represent the 1-2 and 1-1 distances, respectively (see the inset of Figure 5.1 for atomic labels). The marks given by stars refer to the average distances as the geometry departs from the usual vacancy to the structure in Figure 5.1B. Note that the magnetism disappears at a strain of ∼2% when allowing for out-of-plane deformations.

structural changes on the magnetic and electronic properties of the vacancies. We first consider the case of zero strain, i.e. at the equilibrium lattice constant. The usual reconstruction [42, 121] is accompanied by a decrease in the 1-1 distance in Figure 5.1 and an increase in the 1-2 distances. The two dangling bonds in the type 1 atoms are thus saturated while atom 2 remains uncoordinated. It is the polarization of the corresponding dangling bond that is the main reason behind the appearance of a spin moment of $\sim 1.5\mu_B$ associated with the carbon monovacancy. However, we were able to stabilize another reconstruction characterized by a different structural distortion, in which the 1-2 distance decreases, while the 1-1 distance increases [see the local structures and distances in Fig.5.3B,C]. This structure has a larger spin moment of $\sim 1.82\mu_B$. We refer to this latter structure as the high-spin (HS) configuration, and to the former as the low-spin (LS) configuration. At zero strain the LS structure is more stable than the HS by around 250 meV.

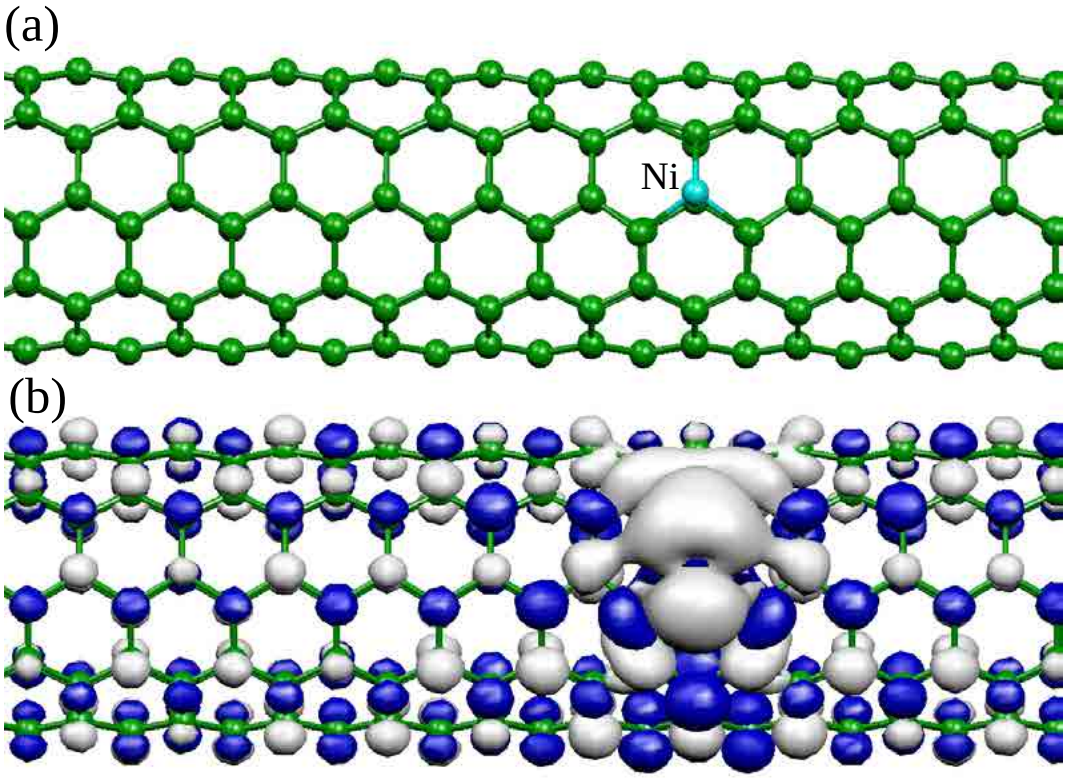

Figure 5.4: (a) Relaxed geometry of a substitutional Ni (Ni_{sub}) impurity in a (5,5) SWCNT, and (b) isosurface ($\pm$0.004 e^-/Bohr^3) of the magnetization density with light (gray) and dark (blue) surfaces corresponding, respectively, to majority and minority spin.

The behavior of these two structures as a function of strain is summarised in Figure 5.3. When applying tension to the layer, both the HS and LS structures remain flat and almost become degenerate. In both cases the spin moments show a slight increase. Conversely, when the layer is compressed, the HS structure becomes unstable. Indeed, it is only possible to stabilize the HS configuration under compression provided that the layer is constrained to remain flat. Even for flat graphene, the energy difference between the HS and LS states increases significantly with compression, and for strains greater than 1.5% the HS configuration spontaneously transforms into LS-flat (i.e. low-spin constrained to be flat). In both structures, the spin moments decrease as the layer is compressed. The change is greater for the LS-flat configuration, which varies from 1.98 μ_B for a $+3\%$ deformation to 1.15 μ_B at -3%. A more dramatic reduction in the spin moment is seen if ripples are allowed to form in the graphene layer. Figure 5.3B shows that the spin moment of the LS-rippled (i.e. low-spin free to ripple) vacancy decreases sharply when the compressions exceeds 0.5%. In fact, the ground state of the monovacancy becomes non-magnetic for compressive strains in the range of 1.5-2%.

The changes in the spin moments of vacancies may be understood by analysing their electronic structure. When carbon atom 2 is restricted to remain in the plane, the spin moment is mainly associated with the $2sp^2$ dangling bond, and the contribution from the $2p_z$ states is smaller. The strain-induced deformation of the vacancy and subsequent out-of-plane displacement of atom 2 gives rise to the hybridization between the out-of-plane $2p_z$ states and

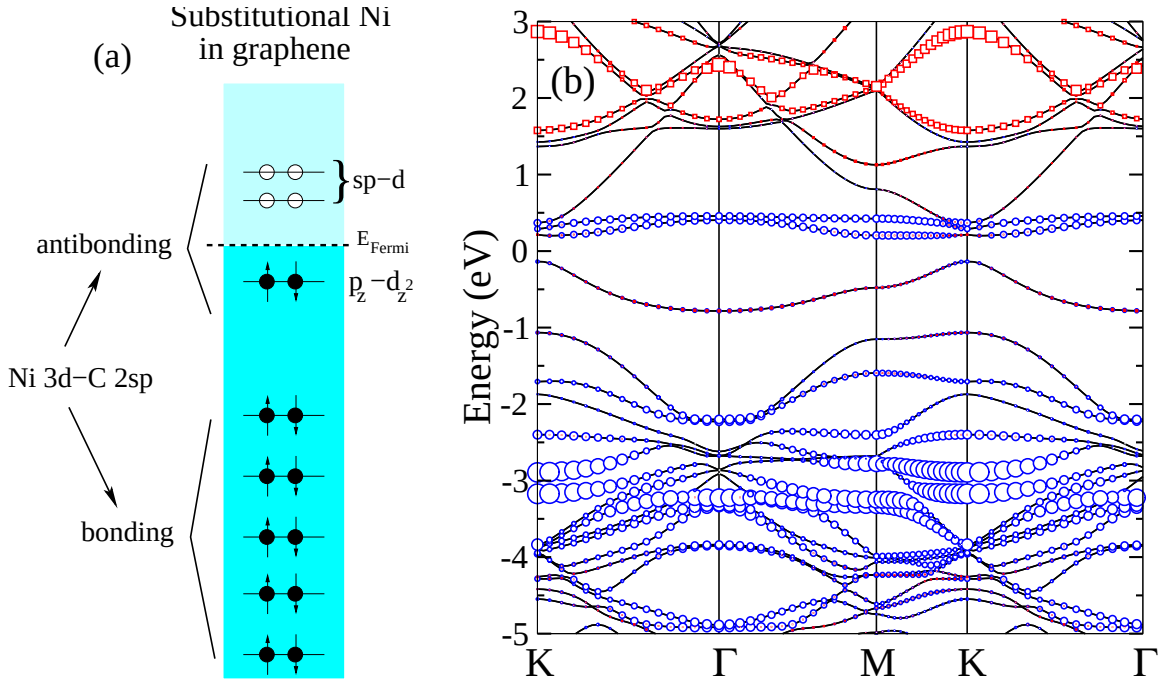

Figure 5.5: (a) Schematic representation of the electronic structure of a Ni_{sub} impurity in graphene. Panel (b) shows the calculated band structure for a Ni_{sub} impurity in a 4×4 graphene supercell. The size of the circles and squares corresponds to the amount of Ni $3d$ and $4s$ character respectively. Energies are referred to the Fermi energy.

the in-plane $2sp^2$ states. For flat graphene the spin-polarized impurity level associated with the vacancy therefore has a strong $2sp^2$ character and remains essentially decoupled from the delocalized electronic levels of graphene due to their different symmetries. For the rippled layer, these two types of electronic states are strongly hybridized. This hybridization results in the delocalization of the defect levels which eliminate the magnetism and explains why the LS-rippled configuration has a lower spin moment. In other words, the rippling is believed to transform the hybridization of the C vacancy atoms in $2sp^3$, thereby removing the cause of local magnetism, as seen at the higher compression of the case of Figure 5.1B.

Rippling of the graphene layer occurs in many cases. One such case is where graphene is deposited on substrates, in which there is a significant mismatch between lattice parameters. For example, ripples have been observed for graphene deposited on Ru(0001) [140], as well as on other metallic substrates. Strain can also be applied and controlled by placing exfoliated graphene on flexible substrates, as recently reported [143, 144]. Then, it may be possible to create defects in regions of different curvature using a focused electron beam as already demonstrated [83].

5.2 Ni doped graphene and carbon nanotubes

Similar to what we have observed with monovacancies under the application of strain, in which the total spin moment is sensitive to the presence of mechanical deformations, for substitutional defects created in graphene the magnetic properties depend on the deformations and/or induced curvature on the sheet. So far, we have studied substitutional transition metals

(TM_{sub}) only at a flat graphene surface. However, as already mentioned in Chapter 1, the first experimental evidence of TM_{sub} doped carbon nanostructures was observed in a cylindrical carbon onion [81] and latter on in single wall carbon nanotubes [63, 78, 80]. Therefore, the study of the electronic and magnetic properties of TM_{sub} in single wall carbon nanotubes is a relevant issue. Now we will examine in detail the effect of Ni_{sub} defects in armchair and zigzag SWCNTs of different diameters [1].

5.2.1 Geometry and magnetization density

As we have already seen in Chapter 3, Ni_{sub} impurities are non-magnetic in flat graphene. However, their magnetic moment can be switched on by applying curvature to the structure. To understand why, we will begin taking a look at the equilibrium structure of Ni_{sub} in the case of a (5,5) SWCNT. The Ni atom appears displaced $\sim$0.9 Å from the carbon plane. Although both outward and inward displacements can be stabilized, the outward configuration is always more stable. The calculated Ni-C distances (d_{Ni-C}) are in the range 1.77-1.85 Å in agreement with experiment [80, 81]. Armchair tubes exhibit two slightly shorter and one larger values of d_{Ni-C}, the opposite happens for $(n, 0)$ tubes, whereas for graphene we obtain a threefold symmetric structure with d_{Ni-C}=1.78 Å. Ni adsorption inhibits the reconstruction [121] of the carbon vacancy. Furthermore, we have checked that a symmetric structure is obtained even when starting from a relaxed vacancy.

Figure 5.4 (b) shows the magnetization density for a Ni_{sub} defect in a (5,5) metallic nanotube at large dilution (0.3 % Ni concentration). The total magnetic moment of this system is 0.5 μ_B. The magnetization comprises the Ni atom and its C neighbors. However, it also extents considerably along the tube, particularly in the direction perpendicular to the tube axis. This indicates the polarization of some of the delocalized electronic states in the nanotube. Indeed, as we clarify below, the magnetism in substitutionally Ni-doped SWCNTs only appears associated with the curvature and the metallicity of the host structure.

5.2.2 Electronic structure of Ni_{sub} impurities in graphene and nanotubes

Figure 5.5 (a) shows a scheme of the electronic structure of Ni_{sub} in graphene, while Fig. 5.5 (b) presents the calculated band structure using a 4×4 supercell. Very similar results were already presented in Chapter 3 for larger supercells. Here, we will use this electronic structure as a basis to understand the main modifications that appear when curvature is present in the structure around the defect. Several levels with Ni-C bonding character and a strong Ni $3d$ contribution can be found between 2 and 6 eV below the Fermi energy (E_F). This considerable band width is a signature of the strong Ni-C interaction. As a consequence of the bonding interaction the Ni $3d$ band is stabilized and can be pictured as fully occupied. Close to E_F we find three levels with Ni-C antibonding character. One of them is occupied and appears around 0.7 eV below E_F close to Γ. This level comes from a fully symmetric linear combination of the $2p_z$ orbitals (z-axis normal to the layer) of the nearest C neighbors interacting with the $3d_{z^2}$ orbital of Ni. Two levels coming from the hybridization of the in-plane sp lobes of the carbon neighbors with the Ni $3d_{xz}$ and $3d_{yz}$ orbitals appear $\sim$0.5 eV above E_F.

[1] The reason to choose Ni atoms among all other metals is that it was the first metal experimentally detected by TEM, STM and EXAFS experiments as a substitutional impurity in graphenic nanostructures.

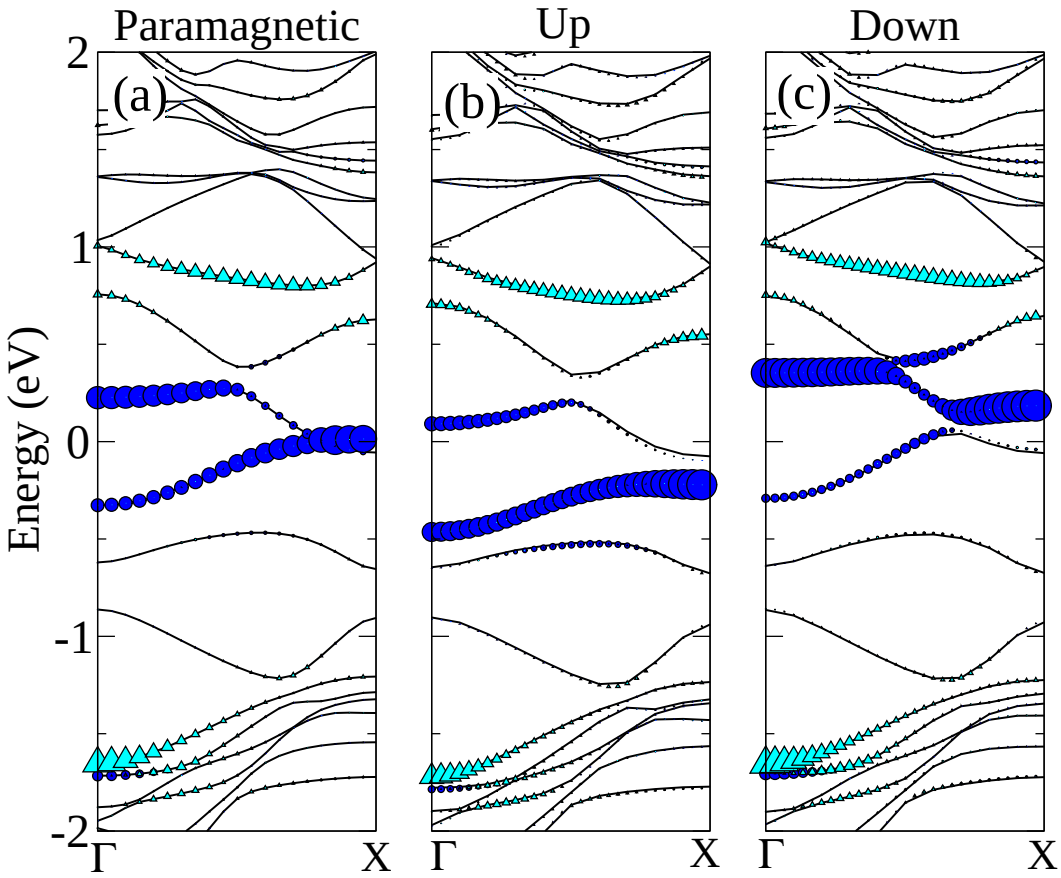

Figure 5.6: Band structure of a (5,5) nanotube containing a Ni impurity every 4 unit cells (Ni_{sub}-Ni_{sub} distance of ∼9.8 Å) for (a) a paramagnetic calculation, and for (b) majority and (c) minority spins. Circles and triangles correspond respectively to the amount of Ni $3d_{yz}$ and $3d_{xz}$ character. X-axis is parallel to the tube axis and y-axis is tangential.

The basic picture described above is still valid for the electronic structure of the Ni_{sub} impurity in SWCNTs. However, the modifications that appear due to the curvature of the carbon layer are responsible for the appearance of a magnetic moment. Figure 5.6 (a) shows the band structure of a paramagnetic calculation of a (5,5) SWCNT with a Ni_{sub} impurity every four unit cells. Here the distance between neighboring Ni_{sub} impurities is similar to that of the graphene layer in Fig. 5.5 (b), although the Ni concentration is 2.5 times lower (1.3 %). Comparing these two Figures we can appreciate the effects of curvature. The degeneracy between d_{xz} and d_{yz} states is removed (x-axis taken along the tube axis and y-axis along the tangential direction at the Ni site). The d_{yz} contribution is stabilized by several tenths of eV and a quite flat band with strong d_{yz} character is found *pinned* at E_F close to the Brillouin-zone boundary. Under these conditions the spin-compensated solution becomes unstable and a magnetic moment of 0.48 μ_B is developed. Figures 5.6 (b) and (c) show, respectively, the band structure for majority and minority spins. The exchange splitting of the d_{yz} level is ∼0.4 eV and the energy gain with respect to the paramagnetic solution is 32 meV.

In general, whenever a flat impurity with appreciable Ni $3d$ character becomes partially filled we can expect the appearance of a magnetic moment. The population of such an impurity level occurs at the expense of the simultaneous depopulation of some of the delocalized carbon

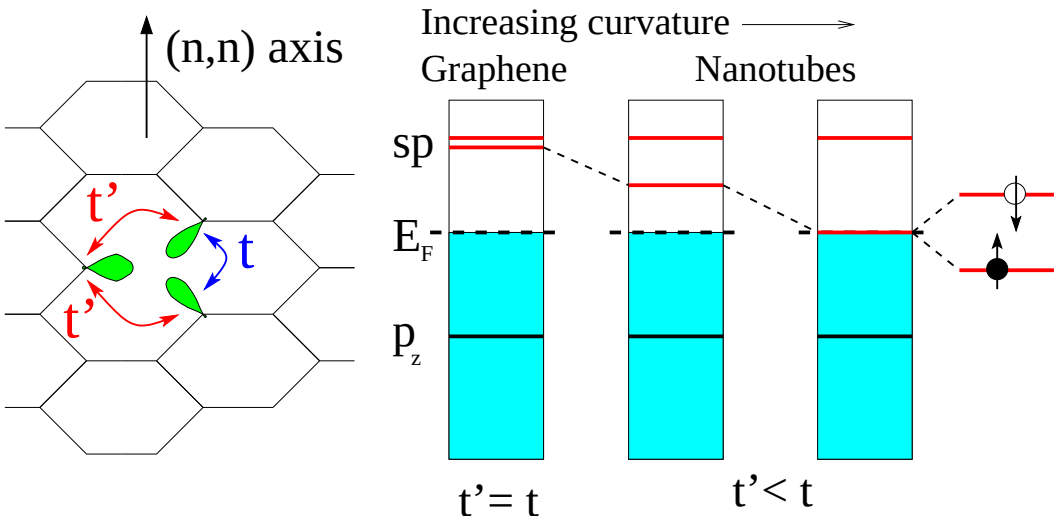

Figure 5.7: Effect of curvature (anisotropic strain) on Ni_{sub} in (n,n) tubes. The electronic structure of Ni_{sub} is similar to that of the unreconstructed carbon vacancy. One of the impurity levels with antibonding C $2sp$-Ni $3d$ character is shifted downwards and, for large enough curvatures, becomes partially populated and spin-polarized.

$2p_z$ levels of the host structure. For this reason the development of a magnetic moment is more likely for Ni_{sub} impurities in metallic structures like the armchair tubes. The crucial role of the host states also explains the delocalized character of the magnetization density depicted in Fig. 5.4 (b). However, it is important to stress that the driving force for the formation of a magnetic moment associated with the Ni_{sub} impurity in a SWCNT is the local curvature of the carbon layer that shifts the energy position of one of the impurity levels downwards until it crosses E_F. A schematic representation of this phenomenon can be found in Fig. 5.7 where we also emphasize the similarities between the levels of the Ni_{sub} defect and those of the unreconstructed carbon vacancy. At large tube diameters we must recover the limit of flat graphene with zero magnetic moment.

For semiconducting tubes the situation is somewhat different. The d_{xz} and d_{yz} derived levels will remain unoccupied unless their energies are shifted by a larger amount that pushes one of them below the top of the valence band. Therefore, if the tube has a large enough gap the magnetic moment will be zero irrespective of the tube diameter. We have explicitly checked that a zero magnetic moment is obtained for (8,0) and (10,0) semiconducting tubes for Ni concentrations ranging from 1.5% to 0.5%. The different magnetic behavior of Ni_{sub} impurities depending on the metallic and semiconducting character of the host structure provides a route to experimentally identify metallic armchair tubes.

5.2.3 Oscillations of the spin moment

Figure 5.8 displays the magnetic moment per Ni_{sub} atom for Ni-doped armchair tubes of different diameters. All of them present a magnetic moment that oscillates as a function of the tube diameter and the size of the supercell used in the calculation, i.e., the Ni_{sub}-Ni_{sub} distance. For (4,4), (5,5) and (6,6) tubes the first supercell showing a non-zero magnetic moment contains four unit cells. For (7,7) and (8,8) tubes this minimum length increases up to eight and six unit cells, respectively. The appearance of a complex oscillatory pattern as a function of the Ni_{sub}-Ni_{sub} distance is easily understood if we recall that the magnetic moment criti-

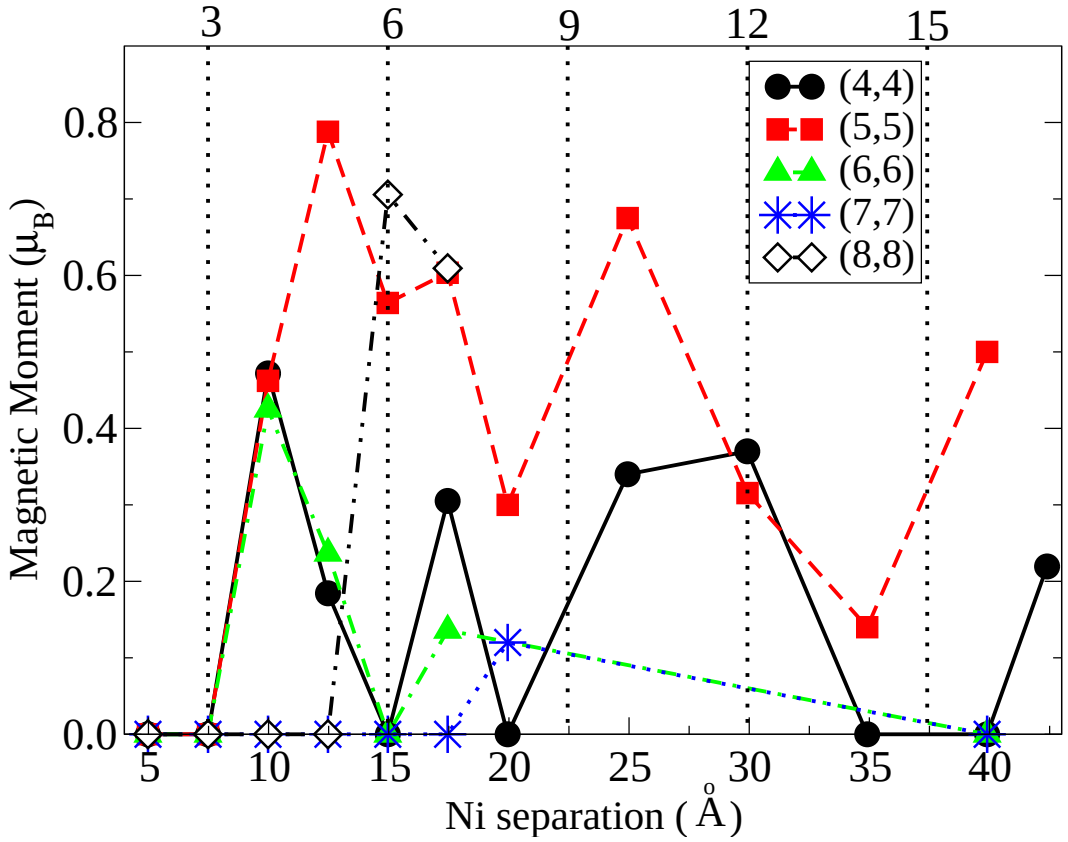

Figure 5.8: Magnetic moment per Ni impurity for different (n,n) tubes as a function of the distance between periodic images of the impurity, i.e., the length of the supercell. The vertical lines and the numbers at the top indicate the number of unit cells in a supercell of a given length.

cally depends on the energy position of a particular impurity level nearby E_F and the strong hybridization of this level with the delocalized states of the nanotube. Another consequence of this hybridization is the long range of the interaction between Ni_{sub} impurities: for example, the magnetic moment in (5,5) and (4,4) tubes still presents strong oscillations in a range of Ni_{sub}-Ni_{sub} distances between 20 and 40 Å. Unfortunately, a meaningful exploration of larger distances between impurities requires a methodology different from the *ab initio* supercell approach used here.

Finally, we have examined the magnetic coupling between Ni_{sub} impurities in the (5,5) tube. We have doubled some of the simulation cells considered above, so they contain two Ni atoms, and calculated ferromagnetic (FM) and antiferromagnetic (AFM) arrangements. Only when the two Ni_{sub} impurities shared a common C neighbour the AFM arrangement was favoured by a few meV. FM configurations were the most stable in all other cases. Although more work is necessary to accurately determine the size and distance dependence of the effective exchange interaction (probably using model calculations similar to those in Ref. [85]), our results indicate that Ni_{sub} impurities in small diameter metallic nanotubes, where they develop a magnetic moment, can exhibit relatively large FM couplings that slowly decay with distance. For example, for Ni_{sub} impurities at distances of 10 Å in a (5,5) tube we estimate a J_{eff} of $\sim$9 meV. This FM interactions can have important implications for the experimental detection of the curvature dependent magnetism of the Ni_{sub} impurities described in this work

and its influence in the observation of magnetism in carbon nanotube samples.

5.3 Uniaxial strain in Ni doped graphene

In this section we study the effect of uniaxial strain on the electronic structure of Ni_{sub} defects in graphene. We find that the magnetic moment of Ni-doped graphene can be controlled by applying a tensile strain along the zigzag and armchair direction. The spin moment of the system and its stability is greatly enhanced. At zero strain, Ni_{sub} defects are non-magnetic [113], but develop a spin moment that increases nearly linearly as a function of the uniaxial strain. The changes are more dramatic when graphene reaches a critical strain ($\sim$7.0%) around which an abrupt increase of the spin moment is observed. This magnetoelastic effect can be utilized to design a strain-tunable spin device based on defective graphene. We also propose an experimental set up based on a scanning tunneling microscopy with a magnetic tip and using a flexible substrate on top of which graphene is deposited, allowing for the direct measurement of the observed magnetic switch effect.

5.3.1 Effect of uniaxial strain on the spin moment

Figures 5.9 (a)-(b) show the spin moment of a Ni_{sub} defect as a function of applied strain along the (n, n) and $(n, 0)$ directions, respectively. The curves with filled squares show simulations using geometries from a non-spin polarized calculation with a DZ basis set. The spin moment and electronic structure are always calculated using a DZP basis. The open squares indicate systems that were calculated using the previous procedure, i.e. a DZ basis, but the geometries have been obtained from spin-polarized calculations. The triangles display calculations with DZP basis set for both geometry and spin moment. At zero strain the Ni_{sub} defect is non-magnetic as was previously analyzed in previous sections (Section 5.2). As the uniaxial tension is applied, the system starts to deform. We see that at $\sim$3.5% strain the system becomes magnetic with a magnetic moment that evolves nearly linearly with the uniaxial strain up to values of $\sim 0.30-0.40\ \mu_B$ at $\sim$6.0%. In spite of using different basis set (see caption in Figure 5.9), all calculations present a very similar behaviour. At $\sim$6.8% the spin moment increases sharply from $\sim$0.40 μ_B to $\sim$1.9 μ_B. The transition is similar for both directions, although it is somewhat more abrupt along the (n, n) direction (Figure 5.9(a)) where no intermediate steps are observed. This suggest that the local defect geometry and the defect orientation relative to the applied strain play an important role to have magnetic properties. The insets I and II in Figure 5.9(a)-(b) present the local defect geometry. When the strain is applied, the triangle formed by the three C neighboring atoms to the Ni impurity deforms. C-C distances along the strain direction increase, whereas distances along the perpendicular direction decrease in response to such elongation. The distance of the Ni atom to the first carbon neighbours also increases, but this bond lenght changes for the studied strains are less than $\sim$5.0% (average on both strain directions) in comparison with $\sim$20.0% for the C-C distances. We can conclude that there is a strong interaction between the carbon neighbours and the central Ni impurity, which is also reflected in the high stability of the defect. The formation energy for the Ni_{sub} defect was observed to be highly favourable, with 7.9 eV binding energy to the vacancy.

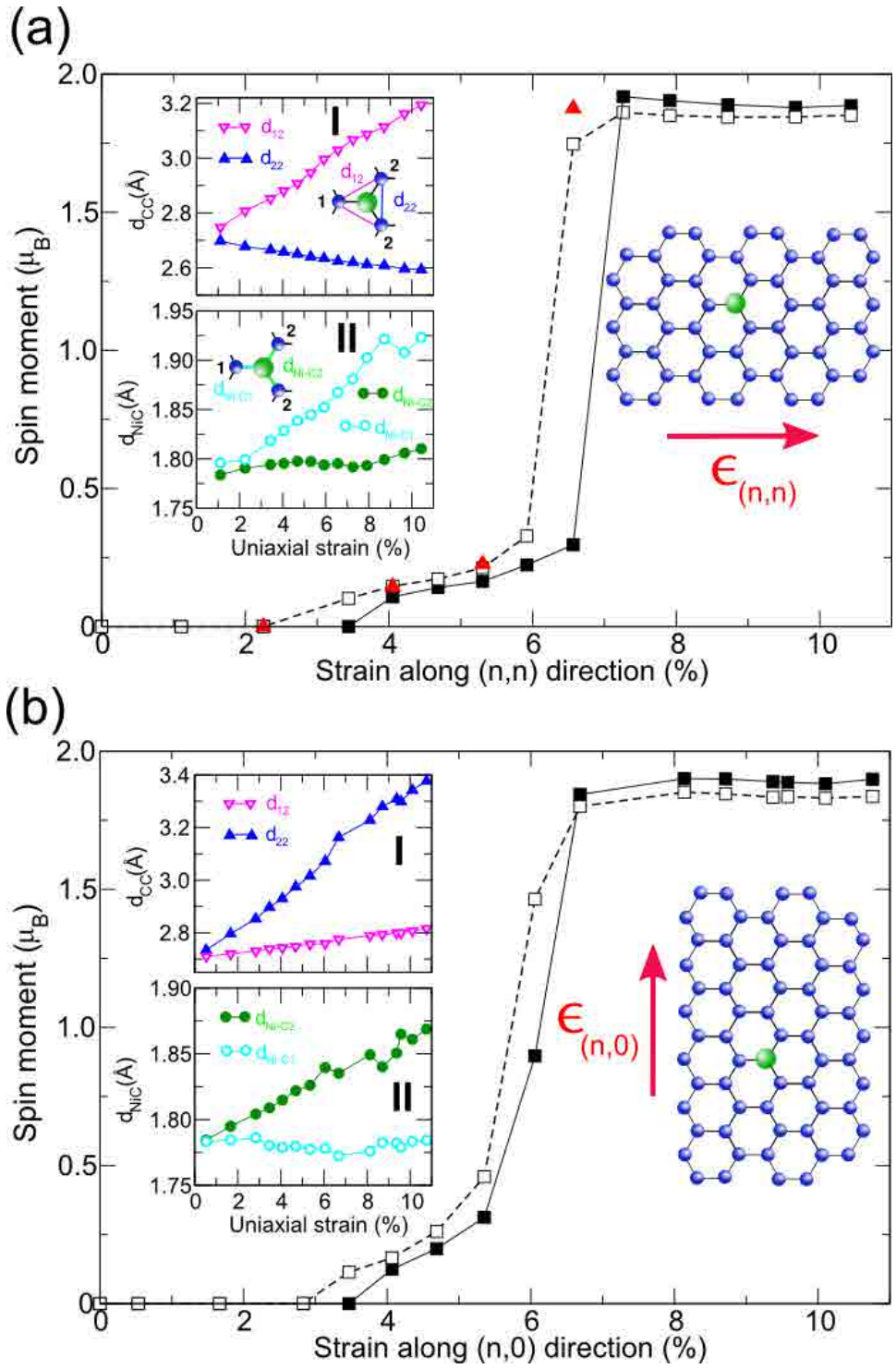

Figure 5.9: Spin moment as a function of applied strain(ϵ) along the (a) (n,n) and (b) $(n,0)$ directions with a schematic illustration of the structure at the right side. In panels (a) and (b), filled squares indicate results obtained using geometries from a non-spin polarized calculation using a DZ basis. The spin moment and electronic structure is calculated using a DZP basis using such geometry. Open squares indicate a similar calculation, but the geometries have been obtained from a spin-polarized calculation. The triangles represent full calculations (geometry and spin moment) with DZP basis set. The insets I and II in panels (a) and (b) show the results for the structural parameters (bond length between carbons C1 and C2: $d_{12,22}$; and bond lenght between Ni and C atoms: $d_{Ni-C1,Ni-C2}$) as a function of applied strain calculated with DZ basis set.

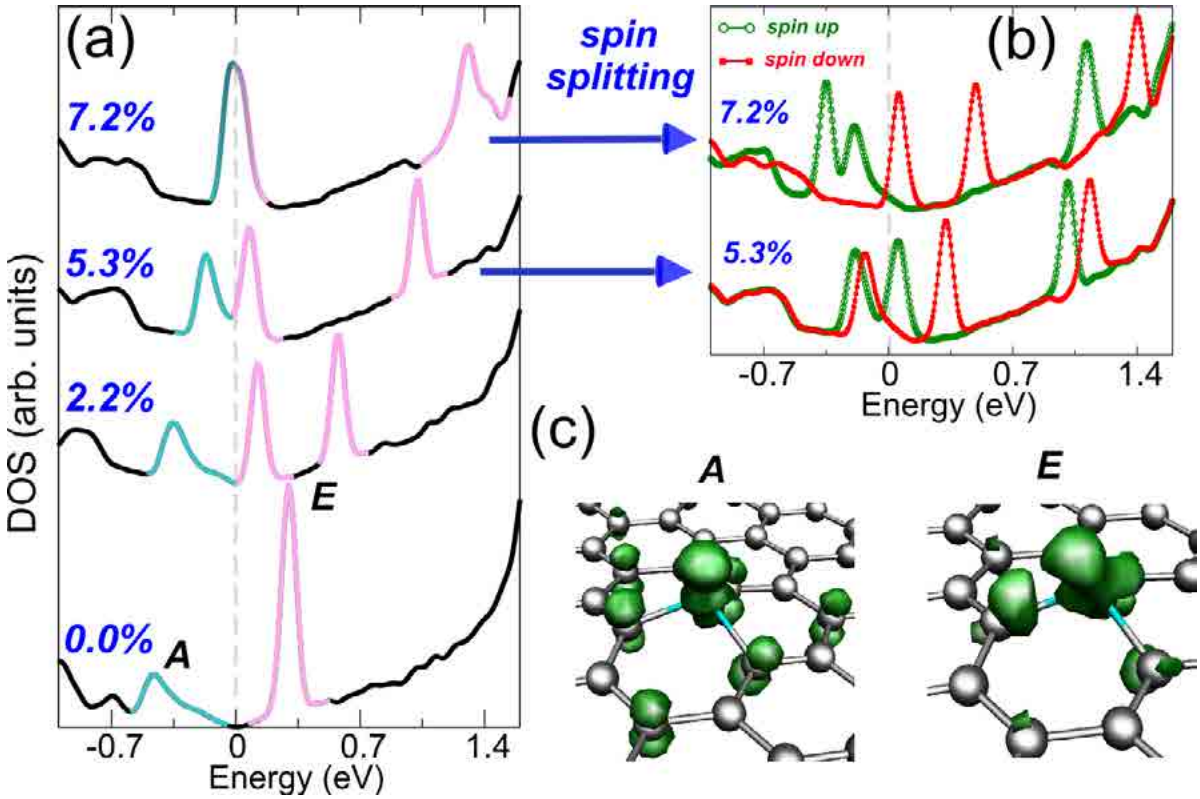

Figure 5.10: (a) Spin-unpolarized DOS of the Ni_{sub} defect under 0.0%, 2.25%, 5.30% and 7.26% strains along the (n, n) direction. Symbols A and E indicate the character and symmetries of the defect states, with large weight of Ni hybridized with C states. A corresponds to Ni $3d_{z^2}-$C $2p_z$ and E represents Ni $3d_{xz}, 3d_{yz}-$C $2sp$. (b) Spin polarized DOS showing the spin splitting observed at strains of 5.3% and 7.2%. The open squares (green curve) represents the spin up channel and filled squares (red curve) the spin down. For clarity, the curves in panels (a) and (b) have been shifted. The Fermi energy is marked by the dashed (gray) line and is set to zero. (c) Spatial representation of the A-, and lowest E-state at a strain of 5.3% with an isovalue of ± 0.002 e^-/Bohr^3.

5.3.2 Electronic structure of Ni_{sub} defects under strain

In order to understand the origin of the tunable magnetic moment in Ni_{sub} defects, the density of states (DOS) of the spin-unpolarized calculations under strains of 0.0%, 2.2%, 5.3% and 7.2% are shown in Figure 5.10(a). The strain is along the (n, n) direction although the qualitative behaviour is similar if we consider other directions. We can see several defect levels with Ni and C mixed character around the Fermi energy (E_F). We will only consider explicitly the $3d$ states of the metal atom since our calculations show that the main contribution from the $4s$ orbitals appears well above E_F (see Chapter 3 and previous section). Due to the symmetric position of the metal atom over the vacancy, the system has a C_{3v} symmetry at zero strain and the electronic levels can be classified according to A or E irreducible representations of this point group. Essentially three defect states and their evolution as a function of the applied strain determine all the observed physics.

One of them with A character is occupied and appears around $\sim$0.50 eV below E_F at zero strain. This level comes from a fully symmetric linear combination of the $2p_z$ orbitals (z-axis normal to the layer) of the nearest C neighbors interacting with the $3d_{z^2}$ orbital of Ni. The other twofold-degenerate levels with E character, coming from the hybridization of the in-

plane sp lobes of the carbon neighbors with the Ni $3d_{xz}$ and $3d_{yz}$ orbitals, appear at 0.50 eV above E_F at zero strain. As a consequence of this electronic structure, with the Ni $3d$ states far from E_F and no flat bands crossing E_F, the magnetic moment of the Ni_{sub} impurity in graphene is zero. Interestingly, these three levels appearing close to E_F in Figure 5.10(a) are reminiscent of those found for the unreconstructed carbon vacancy in graphene (see Chapter 3).

As we will see below the energy position of these three levels shifts as a function of the applied strain. When the strain is applied, the degeneracy between $3d_{xz} - 2sp$ and $3d_{yz} - 2sp$ states is removed and a gradual shift towards E_F of one of them is observed. This level becomes partially populated and the system starts to develop a magnetic moment. The Ni $3d_{z^2}$−C $2p_z$ state also change its positions approaching E_F. As a result, around a 7% strain both the $3d_{z^2} - 2p_z$ and the $3d_{xz,yz} - 2sp$ levels become fully polarized and the system developes a moment close to 2.00 μ_B. The spatial distribution of A and E states can be seen in Figure 5.10(c).

Figure 5.10(b) shows the resulting spin up and spin down DOS at 5.3% and 7.2% strain. The exchange splitting of the $3d_{xz}$ and $3d_{yz}$ levels is, respectively, ∼0.29 eV and ∼0.13 eV at 5.3% and increases with the magnitude of the tensile strain and the simultaneous increment of the spin moment. Likewise the energy gain with the respect to the non-magnetic solutions enhances from 13.9 meV at 5.3% to 184.1 meV at 7.26%. This means that a moderate variation of the applied strain on the graphene layer induces a great change of the magnetic moment and the stability of the defect-induced magnetism. An important consequence of these results is that, if the applied strain on the graphene layer can be controlled, as shown in recent experiments [143, 144], it would be possible to turn on and off the Ni-doped graphene to a magnetic state, likewise switches used in *magnetoelastic devices*, however with no applied magnetic field. It suggests a sensitive and effective way to control the magnetic properties of graphene which is interesting for its possible applications in nanoscale devices.

5.3.3 Magnetization density and an experiment proposal

Figure 5.11(a)-(b) displays the spin magnetization patterns induced by the presence of a Ni_{sub} defect under two different magnitudes of uniaxial strain applied along the (n, n) direction. The spin polarization is induced in the neighboring carbon atoms with shape and contribution depending sensitively on the strain intensity. At 5.30% the spin density is mainly localized at the Ni impurity and at the C atom that makes the bond directly oriented along the strain direction. The anti-bonding character of the E defect state that originates the magnetization is also notorious (see the node along the bond direction). The $2sp$-like shape of the spin density at this C atom should be contrasted with that at 7.26% strain, in which apart of the $2sp$-like shape, a $2p_z$ component is clearly observed. Other neighboring-carbons also contribute to the spin density, however this additional contribution has a dominate $2p_z$ character. The origin of the modification of the spin polarization patterns as a function of strain corresponds to a larger contribution of the Ni $3d_{z^2}$−C $2p_z$-defect state at E_F for a strain above ∼7%, as was explained in the previous section using the DOS.

Figure 5.12 shows the proposed experimental setup that could be used to test our predictions. This is similar to a mechanically controlled break junction setup with an elastic substrate [143, 144]. Graphene is deposited on the center of such substrate in order to obtain a uniform strain. Bending or stretching the substrate causes an expansion of the surface

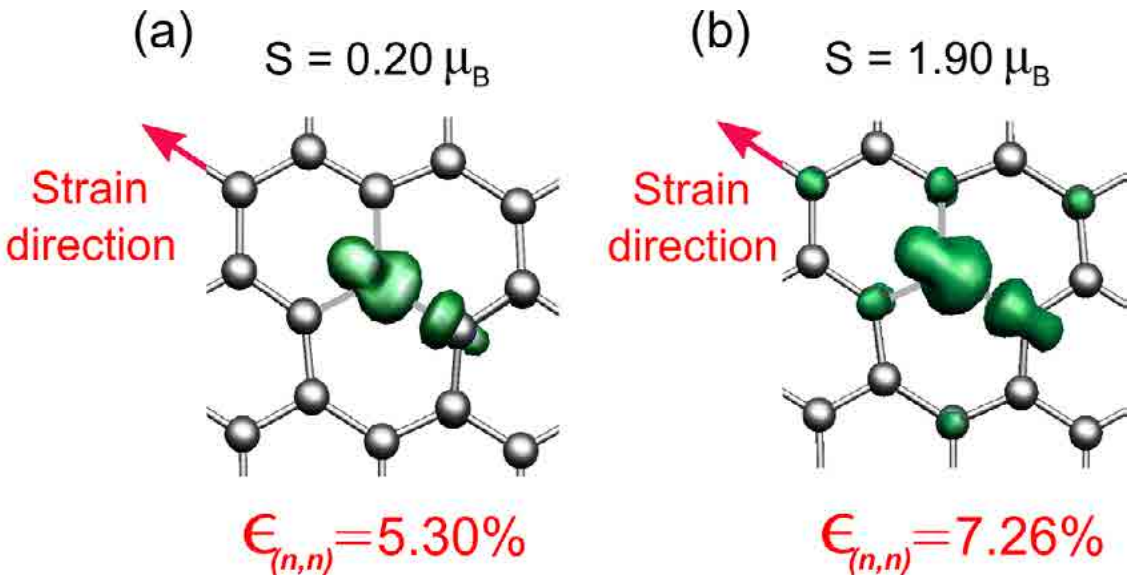

Figure 5.11: (a)-(b) Spin densities for Ni_{sub} defects at strains of 5.30% and 7.26% along the (n, n) direction. The strain direction is marked by the red arrows in both panels. The isovalue cutoff at (a) and (b) panels is ± 0.035 and ± 0.060 e^-/Bohr^3.

and the deposited graphene will follow this deformation. In principle, the modifications on the electronic structure can be detected using a scanning tunneling microscope (STM) since the defect levels that are involved are localized around the Fermi energy. If the magnetic anisotropy of the defect is high enough, at sufficiently low temperatures, a preferential orientation of the moment would be stabilized and, therefore, a STM with a spin polarized tip (Spin-STM) could allow to monitor the evolution of the magnetic properties of the Ni-doped graphene with strain. Instead, an external magnetic field may be used to align the magnetic moment of the defects and define the hard/easy axis of the system. It is noteworth that the break junction-like setup has already been successfully used [145], and the STM capabilities for the single-atom manipulation make the fabrication of the tip ending with magnetic atoms feasible.

5.4 Conclusions

In the present chapter, we have analyzed in detail the effect of different mechanical deformations (isotropic strain, curvature and uniaxial strain) on the structural and magnetic properties of two types of defects, carbon monovacancies and Ni substitutional impurities in graphenic structures. We have seen that mechanical deformations have a strong influence on the magnetic properties of these defects. In some cases, like a Ni_{sub} impurity in graphene under uniaxial strain, this can be used to turn on and off the spin moment and can be of use in future spintronic devices.

We have presented a first-principles density functional theory study of the carbon monovacancy in graphene under an applied strain. The stress was observed to play an important role in determining the electronic, geometrical and magnetic properties of this system. We have shown that the magnetic and structural properties of the carbon monovacancy exhibit a strong dependence on the local curvature of the graphene layer at the defect position. This

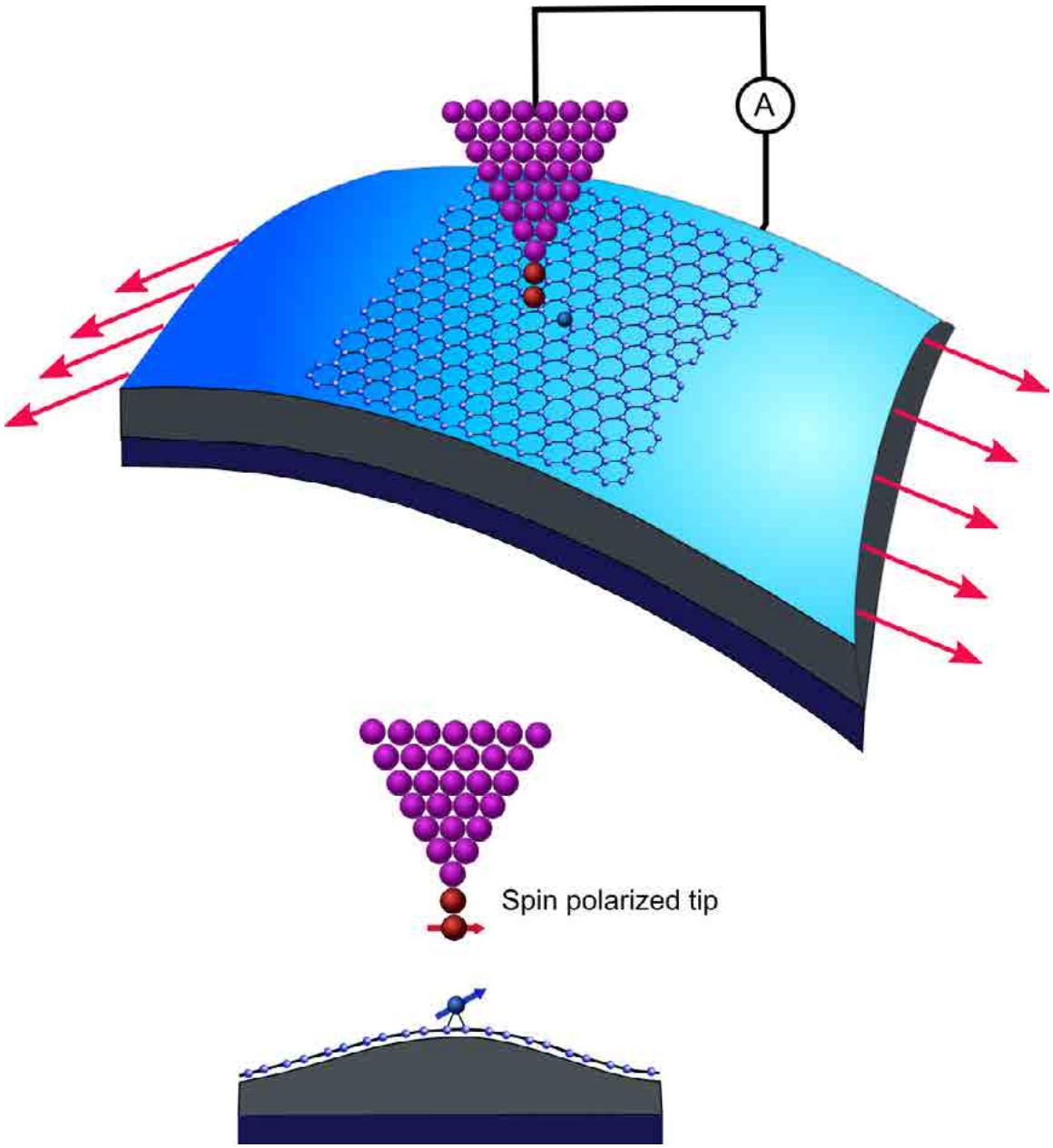

Figure 5.12: Experimental setup proposed to measure the effect of strain on the magnetic properties of Ni-doped graphene. The layer is deposited on a stretchable substrate which keeps a large lenght-to-width ratio in order to obtain a uniform tensile strain on the graphene film. A STM device is also coupled to the system and it has a spin polarized tip which is sensitive to the presence and orientation of a magnetic moment at the defect site. When the strain field is switch on, the modifications on the magnetic structure of Ni-doped graphene could be observed by means of the spin-polarized tunneling that will appear between tip and sample.

curvature, along with the global rippling pattern, can be controlled by straining the layer. With a compression of the layer up to 2% we can tune the spin moment of the vacancy between 0 and 1.5 μ_B. This range of deformations can be accessible experimentally, and are comparable to those found for a graphene layer deposited on several substrates. From a more general perspective, our results suggest that the magnetism induced in graphene by the presence of point defects can be controlled using isotropic strain and other mechanical deformation.

An important consequence of these results is that, due to the two dimensional character of graphene and thus prompt to undergo bending and other deformations, it is difficult to talk about the *intrinsic* electronic and magnetic properties of point defects like the monovacancy. To have a complete characterisation of the defect is necessary either to specify the local curvature of the layer at the defect position or to consider explicitly the stresses applied to the layer. This is in clear contrast to the case of three dimensional crystals, where elastic deformations are typically much smaller.

Regarding our study of Ni_{sub} defects in graphene and SWCNT's, the main conclusions for this study are:

(*i*) the magnetic moment of substitutionally Ni-doped graphene can be controlled by applying mechanical deformations that break the hexagonal symmetry of the layer, like curvature does. As we have already seen in Chapter 3, Ni_{sub} impurities are non-magnetic in flat graphene. However, their magnetic moment can be switched on by applying curvature to the structure. For metallic carbon nanotubes the curvature of the carbon layer around the defect can drive the transition of the Ni_{sub} impurities to a magnetic state. For semiconducting tubes, the Ni_{sub} impurities remain non-magnetic irrespective of the tube diameter. Therefore, the magnetic or non-magnetic character of Ni_{sub} impurities in metallic carbon nanostructures can be controlled by the local curvature. This surprising result can be fully understood and rationalised from the electronic structure of the Ni_{sub} defect;

(*ii*) We have analyzed in detail the origin and distribution of the magnetic moment. We found that the formation of the magnetic moment associated with Ni_{sub} impurities is accompanied by the polarization of the delocalized electronic states of carbon layer. Furthermore, the magnetic moment of Ni_{sub} also becomes a signature of the metallicity of the structure: only metallic tubes develop a moment that depends on the tube diameter and Ni concentration;

(*iii*) The magnetic moment for armchair nanotubes as a function of the concentration of Ni_{sub} impurities shows a complex oscillatory behavior, which points to very long-range interactions between Ni_{sub} defects. We have also analyzed the magnetic couplings between Ni_{sub} impurities in a (5,5) tube and found that they are predominantly ferromagnetic for the set of structures studied;

(*iv*) We found that Ni atoms have a very large affinity for carbon vacancies. Therefore, deposited Ni atoms on a graphene layer or carbon nanotube will present a strong tendency to attach to existent carbon vacancies. This opens a route to fabricate structures where the phenomenology presented in this work can be experimentally explored in a controlled way.

(*v*) The electronic and magnetic structure of the Ni_{sub} defect strongly depends on uniaxial strain. We observe that stretching the layer by a few percents along different crystalline directions is enough to turn the non-magnetic ground state of Ni atoms embedded in graphene to a magnetic state.

(*vi*) The magnetic moment increases its magnitude and energetic stability with the applied strain. At a critical strain value of 6.8%, a transition is observed in the magnitude of spin moment which is weakly dependent on the orientation of the applied strain. A detailed analysis

indicates that this strain-tunable magnetic moment is the result of changes in the position of three defect levels around Fermi energy which are antibonding combinations of the Ni $3d$ states and the $2p_z$ and $2sp$ orbitals of the neighboring C atoms.

(*vii*) The tunable magnetism observed in Ni_{sub} defects and its stability via strain control may play an interesting role in flexible spintronics devices. We also propose an experimental setup to measure this dependence based on a flexible substrate where graphene is deposited on top and a spin polarized STM device is used.

Our work predicts a complex magnetic behavior for Ni_{sub} impurities in carbon nanotubes and graphene. This investigation is highly relevant for the interpretation of experimental results since it has been proposed that appreciable amounts of metal atoms can be incorporated into the carbon network, forming this type of substitutional defects, during synthesis and are very difficult to eliminate afterwards. Furthermore, our results point to the existence of a large coupling between the magnetic and elastic response in Ni-doped carbon nanostructures. This can be of fundamental and technological interest and might be verified experimentally.

Chapter 6

Summary and outlook

Graphenic nanostructures represent an important research subject in the fields of nanoscience and nanotechnology. These materials possess extraordinary properties which are supposed to revolutionise the performance of electronic components in the next generation of electronic devices. Several applications within electronics, materials science, condensed matter physics, etc, have been predicted or are already available [146]. The study of graphene has changed in recent years from a theoretical topic to a field where experimental and theoretical advances go hand in hand. In particular, the theoretical studies shown in this thesis are either linked or directly motivated by new experiments.

This thesis focuses on the modeling electronic and magnetic properties of defects in carbon nanostructures. The SIESTA method, based on density functional theory (DFT), was used as the main tool to compute all chemical and physical properties of the studied systems. Other *ab initio* method was also used in the simulations, the VASP code, which using a different methodology based on plane waves and projector-augmented wave potentials (PAW), allows us to check the possible limitations of the pseudopotentials and localized basis set used in SIESTA. Remarkably, the agreement between both set of calculations is excellent. Other programs were also utilized to analyze and treat the huge amount of data obtained in the simulations. From simple programs in AWK, PYTHON, FORTRAN, up to sophisticated graphical packages used to create some figures displayed in this thesis.

Our results have shown in Chapter 3, how the electronic (and mainly magnetic) properties of a graphene monolayer can be modified by doping with substitutional transition metals (M_{sub}). Some results of this chapter are the following:

- We have developed a model based on the hybridization between the states of the metal atom, particularly the d shell, and the defect levels associated with an unreconstructed D_{3h} carbon vacancy. This allowed us to have a simple way to understand the trends observed for the bonding, energetics, and electronic and magnetic properties of several metal impurities in graphene.

- Using the previous model, we identified three different regimes associated with the occupation of different carbon-metal hybridized electronic levels and we use them to classify the substitutional dopants in graphene: bonding states (Sc, Ti), non-bonding states (V, Cr, Mn) and antibonding states (Fe, Co, Ni, Cu, Ag, Au, Zn).

- Consequently, Sc and Ti do not show a spin moment. On the contrary, V, Cr and Mn

display spin moments of increasing size with a strong 3d component. Co, Ni, the noble metals and Zn present an oscillatory behaviour of the spin moment between 0 and 1 μ_B. The spin moment for these later impurities has a strong contribution from the C neighbours in the layer.

- The Fe defect occupies a special position between the non-bonding and antibonding regimes. Their magnetic behavior stems from the competition between the carbon-metal hybridization and the electron-electron interaction within the $3d$ shell. Although Fe impurities are non-magnetic at the GGA level, GGA+U calculations with moderate values of U (above $\sim$2 eV) produce a spin-moment of 1 μ_B.

- Substitutional Zn atoms also display a peculiar behaviour because Jahn-Teller-like distortions end in a zero spin moment. A symmetric configuration with a spin moment of $2\mu_B$ and a very small energy penalty of $\sim$150 meV has also been identified.

Many of the interesting results shown in this chapter are still waiting for experimental verification. Some of these observations are consistent with the experimental data in the literature. For example, our energetic and structural analysis agree with recent experiments [63, 78, 80]. The analysis shown here might be important to understand the doping by transition metals in other carbon nanostructures.

In Chapter 4 we have studied the electronic structure and magnetic properties, including exchange couplings, of several defects in graphene. These can be approximately mapped onto a monovacancy in graphene calculated by a π-tight-binding model. Such systems are Co substitutional impurities (Co$_{sub}$), several adsorbates chemisorbed on graphene through a single covalent C-C bond.

The main results of this chapter can be summarised in the following:

- At either Co$_{sub}$ or $C-X$ defects, the observed magnetic behaviour follows that observed for a single π-vacancy in a simple tight-binding model of graphene. The electronic structure of both defects nearby the Fermi energy is dominated by a single level with a strong contribution from the p_z orbitals of the neighboring C atoms.

- The Co$_{sub}$ or $C-X$ isolated defects show a spin moment of 1.0 μ_B. When several defects are present, the spin moment follows closely Lieb's theorem for bipartite lattices and depends on the number of defects in each sublattice.

- The magnetic couplings are predominantly (anti)ferromagnetic for Co$_{sub}$ defects sited in the (opposite) same sublattice. However, some differences for $C-X$ defects were observed and adsorbates at different sublattices always converge to non-magnetic solutions.

- A RKKY-like model was used to fit the magnetic interactions obtained from DFT calculations for both Co$_{sub}$ and $C-X$ defects. This model pointed out that the dependence of the exchange constants on the distance between defects differ for Co atoms and adsorbed molecules. The interaction between chemisorbed molecules on top of a C atom in graphene surface is long range and falls off slowly with the distance, roughly proportional to $J_{AA}(\mathbf{r}_{ij}) \sim |r_{ij}|^{-(1+\epsilon)}$ with $|\epsilon| \sim 0.20$, where $J_{AA}(\mathbf{r}_{ij})$ are the exchange constant for defects at the same graphenic sublattice. For Co$_{sub}$ defect the magnetic

interactions decay faster and have a distance dependence given by $J_{AA}(\mathbf{r}_{ij}) \sim |r_{ij}|^{-2.43}$. This means that although the spin moment for both defects has a similar origin, the 3d component of the Co dopants and slightly more localized character modifies the interactions.

- For Co_{sub} impurities it is possible to stabilize antiferromagnetic solutions for A-B configurations. Exchange couplings for such configurations show a complex behaviour with a strong anisotropy, dependent on the relative positions of the dopants, along certain crystalline directions.

In Chapter 5 we have studied the effect of strain on the electronic and magnetic properties of substitutional Ni impurities (Ni_{sub}) and vacancies in graphenic nanostructures. One of the main results of this part is that mechanical deformations (similar to those induced by substrates when graphene is deposited on top of them or the curvature present in carbon nanotubes) can be used to control the magnetism of defects in graphene. The proposed models take into account the interplay of corrugations, defect formation and magnetism. They open new opportunities for engineering carbon material properties using strain and defects. We believe that strain will play a key role in flexible electronics, in which graphene is one of the main candidates.

In more detail, we found that:

- Biaxial strain applied to monovacancies in graphene was observed to play an important role in determining the electronic, geometrical and magnetic properties of this system. We have shown that the magnetic and structural properties of the carbon monovacancy exhibit a strong dependence on the local curvature of the graphene layer at the defect position. This local curvature is strongly coupled to the global structure rippling of the layer.

- Phase diagrams of the spin solutions and geometric configurations as a function of strain are presented for a monovacancy in graphene.

- Stretching increases the moment of different spin solutions and compression reduces or even kills the magnetic polarization. The transition to a non-magnetic solution is linked to changes in the local structure of the defect which are driven by modifications in the global structure of graphene that are associated with the formation of long range ripples. For compressions slightly greater than 3%, this rippling leads to the formation of a heavily reconstructed vacancy structure at a saddle point position consisting of two twisted hexagons and pentagons.

- For metallic carbon nanotubes the curvature of the carbon layer around the defect can drive the transition of the Ni_{sub} defect to a magnetic state (Ni_{sub} defects are non-magnetic in flat graphene). For semiconducting tubes, however, the Ni_{sub} impurities remain non-magnetic irrespective of the tube diameter.

- Therefore, the magnetic or non-magnetic character of Ni_{sub} impurities in metallic carbon nanostructures can be controlled by the local curvature. This surprising result can be fully understood and rationalised from the electronic structure of the Ni_{sub} defect.

- The different magnetic behavior of Ni_{sub} dopants depending on the metallic and semiconducting character of the host structure might provide a route to experimentally identify metallic armchair tubes.
- The magnetic moment for armchair nanotubes as a function of the concentration of Ni atoms shows a complex oscillatory behavior, which points to very long-range interactions between Ni_{sub} defects. We have analyzed the magnetic couplings between Ni impurities in a (5,5) tube and found that they are predominantly ferromagnetic for the studied structures.
- The effect of uniaxial strain on Ni_{sub} shows that the magnetic moment can be controlled by applying a tensile strain.
- At zero strain, Ni_{sub} defects are non-magnetic but develop a spin moment that increases nearly linear as a function of uniaxial strain. The changes are more dramatic when a critical strain value ($\sim$6-7%) is reached, around which an abrupt transition of the spin moment is observed.
- This magnetoelastic-like effect can be utilized to design a strain-tunable spin devices based on Ni-doped graphene.

6.1 Outlook

While the major part of this thesis has focused on the analysis of defects and their interaction with the host material, which we believe is relevant for many theoreticians and experimentalists, part of the physical results and interpretations have not been experimentally validated to date. We believe, however, that this will happen sooner rather than later due to the rapid advances in the field.

In fact, day-by-day better experimental control of precise and reproducible doping, surface and defect engineering, and growth process will enable a closer comparison between experiments and our theoretical models. The recent developments of graphene, pushed ahead by observed, expected, and hoped new physics, is the great driving force for research in this branch of carbon nanoscience. For example, in the last few months before the end of this manuscript we have found experimental evidences of one of our predictions: The direct measurement of spin signal, at room temperature, in partially hydrogenated graphene samples using a superconducting quantum interference devices (SQUID) [147]. The realization of such ferromagnetic order in purely $sp-$based materials will be of importance in many areas related to spintronics, even more if the other adsorbates, as pointed out in this thesis, present a similar behaviour.

The immediate continuation of the work presented in this thesis should include the electron and phonon transport properties under the presence of substitutional metals defects in graphene as well as in carbon nanotubes. In particular, a collaboration with Prof. Mads Brandbyge at Danish Technical University (DTU), in Lyngby, Denmark, has been stablished in order to calculate the scattering properties of such metal impurities in graphenic structures and the results will be published elsewhere [148].

Another field of research in which the interplay of strain, the presence of defects and magnetism will play a role is in spin transport. Due to the low spin-orbit coupling in C, long spin-coherence times are expected, which might be of importance for spin polarized currents generated by carbon defects or adsorbates in graphenic nanostructures. If strain could be used to polarize an electric current when it interacts with a localized spin moment in the carbon host, it would avoid using expensive ferromagnetic/antiferromagnetic leads in order to obtain polarized currents and could provide a simple way to obtain spin-transport control.

At the same time, the effect of an external gate voltage on substitutional defects would be particularly relevant. For practical purposes, the use of electric fields would be desirable as their high-frequency generation is more readily achieved than for magnetic fields. Therefore, the ability to electrically control spin dynamics in defects makes it one of the most promising platforms for solid-state spin devices based on carbon [148].

Appendix A

Publications

This is a list of publications.

12. †*Gate-Field Controlled Spin Transport in Carbon Nanotubes Substitutionally Doped with Transition Metals*
Elton J. G. Santos, A. Ayuela, D. Sánchez-Portal and Mads Brandbyge
In preparation

11. †*Photoluminiscence Emission in SWNT Covered with PMMA Polymer*
Ainara Garcia-Gallastegui, Roberto Muños, Isabel Obieta, Izaskun Bustero, Jesus M. Aizpurua, Elton J. G. Santos, D. Sánchez-Portal and A. Ayuela
Submitted

10. †*Magnetism of Covalently Functionalized Carbon Nanotubes*
Elton J. G. Santos, D. Sánchez-Portal and A. Ayuela
Appl. Phys. Lett. ***2011****, 99, pp.062503-062506*
Also selected to *Virtual Journal of Nanoscale Science and Technology* **24***, Issue 8 (2011)*

9. †*Universal Spin Moment in Covalently Functionalized Graphene*
Elton J. G. Santos, A. Ayuela and D. Sánchez-Portal
Submitted

8. †*Strain-Tunable Spin Moment in Ni-Doped Graphene Monolayer*
Elton J. G. Santos, A. Ayuela and D. Sánchez-Portal
Submitted

7. †*Spin-Strain Phase Diagram of Defective Graphene*
Elton J. G. Santos, S. Riikonen, D. Sánchez-Portal and A. Ayuela
arXiv:1012.3304v1

6. †*Magnetism of Substitutional Co Impurities in Graphene: Realization of a Single π Vacancies*
Elton J. G. Santos, D. Sánchez-Portal and A. Ayuela
Phys. Rev. B **2010**, *81*, pp.125433-125439.

†Publication related to the thesis.

Also selected to *Virtual Journal of Nanoscale Science and Technology* **21***, Issue 15 (2010)*

5. †*First-Principles Study of Substitutional Metal Impurities in Graphene: Structural, Electronic and Magnetic Properties*
Elton J. G. Santos, A. Ayuela and D. Sánchez-Portal
New Journal of Physics **2010**, *12*, pp. 053012-053044.

4. *DFT based screening of novel alkali-transition metal borohydrides - a computational materials design summer school project*
J.S. Hummelshoj,..., Elton J. G. Santos, et al.
Journal of Chemical Physics **2009**, *131*, pp. 014101-014110.
This paper also made the **journal cover**

3. †*Switching on Magnetism in Ni-doped Graphene: Density Functional Calculations*
Elton J. G. Santos, A. Ayuela, S. B. Fagan, A.G. Souza Filho, J. Mendes Filho, D. L. Azevedo and D. Sánchez-Portal
Phys. Rev. B **2008**, *78*, pp. 195420-195425.
Also selected to *Virtual Journal of Nanoscale Science and Technology* **18***, Issue 22 (2008)*

2. *Ab nitio Study of 2,3,7,8-Tetrachlorinated Dibenzo-p-Dioxin Adsorption on Single Wall Carbon Nanotubes*
S. B. Fagan, Elton J. G. Santos, J. Mendes Filho, A. G. Souza Filho and A. Fazzio
Chem. Phys. Lett. **2007**, *437*, pp. 79-82.

1. *Raman Spectra in Vanadate Nanotubes Revisited*
A. G. Souza Filho, O. P. Ferreira, O. L. Alves, Elton J. G. Santos and J. Mendes Filho
NanoLetters **2004**, *4*, pp. 2099-2104.

Appendix B

Conference and Workshop Contributions

39. *Magnetism of Graphene with Defects: Vacancies, Substitutional Metals and Covalent Functionalization*. Workshop on Graphene, Donostia-San Sebastian, Spain. August 29th - September 2nd 2011.
Poster section

38. *Magnetism in Graphene Induced by Defects*. Workshop on Graphene, Donostia-San Sebastian, Spain. August 29th - September 2nd 2011.
Oral section by Elton J. G. Santos

37. *Magnetism of Graphene with Defects: Vacancies, Substitutional Metals and Covalent Functionalization.* PCAM Summer School 2011: Electronic and Optical Properties of Nanoscale Materials. Donostia-San Sebastian, Spain. July 4th - 7th 2011.
Poster section

36. *Spin-Strain Phase Diagram of Defective Graphene*. PCAM Summer School 2011: Electronic and Optical Properties of Nanoscale Materials, Donostia-San Sebastian, Spain. July 4th - 7th 2011.
Oral section presented by Elton J. G. Santos

35. *Magnetism in Graphene Induced by Defects*. The 29th International Brand Ritchie Workshop (BRW2011) on Particle Penetration Phenomena and Excitations of Solids, Matsue, Shimane, Japan. May 12nd - 15th 2011.
Oral section presented by A. Ayuela (**Invited talk**)

34. *Magnetism of Covalently Functionalized Graphene*. Graphene 2011, Bilbao, Spain. April 11st - 14th 2011.
Oral section presented by D. Sánchez-Portal

33. *Magnetism of Graphene with Defects: Vacancies, Substitutional Metals and Covalent Functionalization*. Graphene 2011, Bilbao, Spain. April 11st - 14th 2011.
Poster section

32. *Magnetism of Covalently Functionalized Graphene*. 3S'11: Symposium on Surface Science 2011, Baqueira Beret, Lleida, Spain. March 6th - 12nd 2011.
Oral section presented by D. Sánchez-Portal

31. *Spin-Strain Phase Diagram of Defective Graphene*. 5th International Meeting on Molecular Electronics - ElecMol 10, Grenoble, France. December 6th - 10th 2010.
Specially selected for Oral section, presentation by Elton J. G. Santos

30. *Spin-Strain Phase Diagram of Defective Graphene*. Passion for knowledge: The Workshops, San Sebastian, Spain. September 27th - October 1st 2010.
Poster section

29. *Graphene Interacting with Transition Metals: Tuning the Electronic and Magnetic Properties of Graphene*. Passion for knowledge: The Workshops, San Sebastian, Spain. September 27th - October 1st 2010.
Oral section presented by D. Sánchez-Portal (**Invited talk**)

28. *Substitutional Atoms in Graphene: Vacancy States Versus Metal Bonding*. Graphene Week 2010, College Park, Maryland, USA. April 19th - 23rd 2010.
Poster section

27. *Electronic Structure of Graphene Interacting with Transition Metals: Substitutional Defects and Graphene/Ru(0001)*. CIC nanoGUNE Consolider, San Sebastian, Spain. March 29th 2010.
Seminar presented by D. Sánchez-Portal

26. *Electronic Properties of Substitutional Transition Metals in Graphenic Carbon: Magnetism, Trends and Surprises*. NordForsk Spintronics Workshop, Copenhagen - Lyngby, Denmark. October 29-30th 2009.
Oral section presented by Elton J. G. Santos (**Invited talk**)

25. *Electronic Properties of Substitutional Transition Metals in Graphenic Carbon: Magnetism, Trends and Surprises*. Graphene Mini-Workshop 2009, Copenhagen - Lyngby, Denmark. October 23rd 2009.
Oral section presented by Elton J. G. Santos (**Invited talk**)

24. *On the Magnetism of Substitutional Transition-Metal Impurities in Graphenic Nanostructures*. TNT09 - Trends in Nanotechnology, Barcelona, Spain. September 7th - 11st 2009.
Poster section

23. *Magnetism of Substitutional Co Impurities in Graphene: Realization of a Single π-Vacancy*. Nanotec09 - 11th International Conference on Nanotechnology in Carbon and Related Materials, Brussels, Belgium. August 26th-29th, 2009.
Poster section

22. *Magnetism of Graphene and Carbon Nanotubes Substitutionally Doped with Catalitic Metals*. NanoteC09 - 11th International Conference on Nanotechnology in Carbon and Related Materials, Brussels, Belgium. August 26th-29th, 2009.
Oral section presented by Elton J. G. Santos

21. *Magnetism of Substitutional Co Impurities in Graphene: Realization of Single Vacancies*. NT09: Tenth International Conference on the Science and Application of Nanotubes, Beijing, China. June 21st-26th, 2009.
Poster section

20. *Substitutional Metal Atoms in Graphene: Vacancy States Versus Metal Bonding*. CCTN09: Fifth International Symposium on Computational Challenges and Tools for Nanotubes, Beijing, China. June 20th, 2009.
Oral section presented by A. Ayuela (**Invited talk**)

19. *Magnetism of Graphene and Carbon Nanotubes Substitutionally Doped with Ni*. First inanoGune Workshop, CIC - NanoGune, San Sebastian. Spain, May 25th - 26th 2009.
Poster section

18. *Magnetism of Graphene and Carbon Nanotubes Substitutionally Doped with Ni*. DNC09 - Computational Studies of Defects in Nanoscale Carbon Materials, CECAM-HQ-EPFL, Lausanne, Switzerland. May 11st - 13rd 2009.
Poster section

17. *Magnetism of Substitutional Transition-Metal Impurities in Graphenic Nanostructures*. DNC09 - Computational Studies of Defects in Nanoscale Carbon Materials, CECAM-HQ-EPFL, Lausanne, Switzerland. May 11st - 13rd, 2009.
Oral section presented by D. Sánchez-Portal (**Invited talk**)

16. *On the Magnetism of Substitutional Transition-Metal Impurities in Graphenic Nanostructures*. 14th International Workshop on Computational Physics and Materials Science: Total Energy and Force Methods, Trieste, Italy. January 8th - 11st 2009.
Poster section

15. *On the Magnetism of Substitutional Transition-Metal Impurities in Graphenic Nanostructures*. TKK - Laboratory of Physics, Helsinki University of Technology, Helsinki, Finland. November 27th 2008.
Seminar presented by D. Sánchez-Portal

14. *On the Magnetism of Substitutional Transition-Metal Impurities in Graphenic Nanostructures*. NanoSWEC - Nano South-West European Conference, Bordeaux, France. November 3rd - 5th 2008.
Oral section presented by D. Sánchez-Portal (**Invited talk**)

13. *Magnetism of Graphene Substitutionally Doped with Transition Metals*. Symposium in honour of Professor Agustin Del Moral, San Sebastian, Spain. September 22th 2008.
Oral section presented by D. Sánchez-Portal (**Invited talk**)

12. *Complex Magnetic Behaviour of Substitutional Ni Dopands in Graphenic Systems*. ISSPIC 2008 - International Symposium on Small Particles and Inorganic Clusters, Valladolid, Spain. September 15th - 19th 2008.
Poster section

11. *Complex Magnetic Behaviour of Substitutional Ni Dopands in Carbon Nanotubes and Graphene*. International CAMd 2008 Summer School, Copenhagen, Denmark. August 18th - 30th 2008.
    Poster section

10. *Complex Magnetic Behaviour of Substitutional Transition Metal Dopands in Graphenic Systems*. NT08 - Ninth International Conference no the Science and Application of Nanotubes 2008, Le Corum, Montpellier, France. June 29th - July 4th 2008.
    Oral section presented by A. Ayuela (**Invited talk**)

9. *Complex Magnetic Behaviour of Substitutional Ni Dopands in Carbon Nanotubes and Graphene*. NT08 - Ninth International Conference no the Science and Application of Nanotubes 2008, Le Corum, Montpellier, France. June 29th - July 4th 2008.
    Poster section

8. *Carbon Nanostructures: Optical Properties from TDFT Studies and Complex Magnetic Behaviour of Substitutional Transition Metals Impurities*. Nanospain 2008, Braga, Portugal. April 14th - 18th 2008.
    Oral section presented by D. Sánchez-Portal (**Invited talk**)

7. *Complex Magnetic Behaviour of Substitutional Ni Dopants in Graphitic Carbon*. Symposium on Surface Science 2008, St. Christoph am Arlberg, Austria. March 2nd - 8th 2008.
    Oral section presented by D. Sánchez-Portal (**Invited talk**)

6. *Ab initio Study of Substitutionally Ni-Doped Single-Wall Carbon Nanotubes: Structural, Electronic and Magnetic Properties*. 1st Towards Reality in Nanoscale Materials, Levi, Lapland - Finland. December 10th - 12nd 2007.
    Poster section

5. *Ab initio Study of Substitutionally Ni-Doped Single-Wall Carbon Nanotubes: Structural, Electronic and Magnetic Properties*. Workshop Nanomateriales, San Sebastian, Spain. November 8th, 2007.
    Oral section presented by Elton J. G. Santos

4. *Ab initio Study of Substitutionally Ni-Doped Single-Wall Carbon Nanotubes: Structural, Electronic and Magnetic Properties*. GDR-I Nano-I Annual Meeting on Science and applications of Nanotubes, Autrans - France. October 15th - 19th, 2007.
    Oral section presented by Elton J. G. Santos

3. *Magnetic Effect in Ni-Doped Single Wall Carbon Nanotubes*. Trends in Nanotechnology 2007 - TNT07, San Sebastian, Spain. September 3rd - 7th 2007.
    Poster section

2. *Ni-Doped Single-Wall Carbon Nanotubes: Structural and Electronic Properties*. 8th International Conference on the Science and Application of Nanotubes-*NanoTube07*, Ouro Preto, Minas Gerais, Brazil. June 24th - 29th 2007.
    Poster section

1. *Ni-Doped Single-Wall Carbon Nanotubes: Structural and Electronic Properties*. 4th Nanoquanta Young Researchers' Meeting 2007, Donostia, Spain. May 15th - 18th 2007. Oral section presented by Elton J. G. Santos

Bibliography

[1] P. Pasanen, "Graphene: Prospects for Future Electronics," *http://research.nokia.com/publication/11540*.

[2] M. S. Dresselhaus and H. Dai, "Carbon Nanotubes: Continued Innovations and Challenges," *MRS Bulletin*, vol. 29.

[3] R. P. Feynman, "There's Plenty of Room at the Bottom," *Journal of Microelectromechanical Systems*, vol. 1, no. 1, pp. 60–66, 1992.

[4] G. E. Moore, "Progress in digital integrated electronics," *Tech. Dig. IEDM*, vol. 21, pp. 11–13, 1975.

[5] S. E. Thompson and S. Parthasarathy, "The future of Si microelectronics," *Materials Today*, vol. 9, no. 6, pp. 20–25, June 2006.

[6] ITRS, *International Technology Roadmap for Semiconductors*. www.itrs.netreports.html, 2010.

[7] K. S. Novoselov, A. K. Geim, S. V. Morozov, D. Jiang, Y. Zhang, S. V. Dubonos, I. V. Grigorieva, and A. A. Firsov, "Electric Field Effect in Atomically Thin Carbon Films," *Science*, vol. 306, no. 5696, pp. 666–669, October 2004.

[8] A. K. Geim and K. S. Novoselov, "The raise of graphene," *Nature Materials*, vol. 6, no. 3, pp. 183–191, 2007.

[9] P. R. Wallace, "The Band Theory of Graphite," *Phys. Rev.*, vol. 71, no. 9, pp. 622–634, May 1947.

[10] A. Chuvilin, U. Kaiser, E. Bichoutskaia, N. A. Besley, and A. N. Khlobystov, "Direct transformation of graphene to fullerene," *Nature Chemistry*, vol. 2, pp. 450–453, 2010.

[11] G. Otero, G. Biddau, C. Sanchez-Sanchez, R. Caillard, M. F. Lopez, C. Rogero, F. J. Palomares, N. Cabello, M. A. Basanta, J. Ortega, J. Mendez, A. M. Echavarren, R. Perez, B. Gomez-Lor, and J. A. Martin-Gago, "Fullerenes from aromatic precursors by surface-catalysed cyclodehydrogenation," *Nature*, vol. 454, pp. 865–868, 2008.

[12] A. H. Castro Neto, F. Guinea, N. M. R. Peres, K. S. Novoselov, and A. K. Geim, "The electronic properties of graphene," *Rev. Mod. Phys.*, vol. 81, no. 1, pp. 109–162, 2009.

[13] R. Saito, G. Dresselhaus, and M. S. Dresselhaus, *Physical Properties of Carbon Nanotubes*. Imperial College Press, 1999.

[14] H. W. Lee and D. S. Novikov, "Supersymmetry in carbon nanotubes in a transverse magnetic field," *Phys. Rev. B*, vol. 68, pp. 155 402–155 413, 2003.

[15] J. W. Mintmire and C. T. White, "Electronic and structural properties of carbon nanotubes," *Carbon*, vol. 33, no. 7, pp. 893–902, 1995.

[16] X. Blase, L. X. Benedict, E. L. Shirley, and S. G. Louie, "Hybridization effects and metallicity in small radius carbon nanotubes," *Phys. Rev. Lett.*, vol. 72, no. 12, pp. 1878–1881, 1994.

[17] M. Ouyang, J. L. Huang, C. L. Cheung, and C. M. Lieber, "Energy gaps in "metallic" single-walled carbon nanotubes," *Science*, vol. 292, no. 5517, pp. 702–705, 2001.

[18] G. E. Begtrup, W. Gannett, J. C. Meyer, T. D. Yuzvinsky, E. Ertekin, J. C. Grossman, and A. Zettl, "Facets of nanotube synthesis: High-resolution transmission electron microscopy study and density functional theory calculations," *Phys. Rev. B*, vol. 79, no. 20, pp. 205 409–205 415, 2009.

[19] H. Dai, "Carbon nanotubes: opportunities and challenges," *Surface Science*, vol. 500, pp. 218–241, 2002.

[20] K. S. Novoselov, D. Jiang, T. Booth, V. V. Khotkevich, S. M. Morozov, and A. K. Geim, "Two Dimensional Atomic Crystals," *PNAS*, vol. 102, no. 30, pp. 10 451–10 453, July 2005.

[21] R. E. Peierls, "Quelques proprietes typiques des corpses solides," *Ann. I. H. Poincare*, vol. 5, pp. 177–222, 1935.

[22] L. D. Landau, "Zur Theorie der phasenumwandlungen II," *Phys. Z. Sowjetunion*, vol. 11, pp. 26–35, 1937.

[23] N. D. Mermin, "Crystalline order in two dimensions," *Phys. Rev.*, vol. 176, pp. 250–254, 1968.

[24] N. D. Mermin and H. Wagner, "Absence of Ferromagnetism or Antiferromagnetism in One- or Two-Dimensional Isotropic Heisenberg Models," *Phys. Rev. Lett.*, vol. 17, pp. 1133–1136, 1966.

[25] J. A. Venables, G. D. T. Spiller, and M. Hanbucken, "Nucleation and growth of thin films," *Rep. Prog. Phys.*, vol. 47, pp. 399–459, 1984.

[26] J. C. Meyer, A. Geim, M. Katsnelson, K. Novoselov, T. Booth, and R. S., "The structure of suspended graphene sheets," *Nature*, vol. 446, pp. 60–63, 2007.

[27] M. Ishigami, J. H. Chen, W. G. Cullen, M. S. Fuhrer, and E. D. Williams, "The structure of suspended graphene sheets," *NanoLetters*, vol. 7, pp. 1643–1648, 2007.

[28] E. Stolyarova, K. T. Rim, S. Ryu, J. Maultzsch, L. E. Kim, P.and Brus, T. F. Heinz, M. S. Hybertsen, and G. W. Flynn, "High-resolution scanning tunneling microscopy imaging of mesoscopic graphene sheets on an insulating surface," *Proceedings of the National Academy of Sciences*.

[29] W. Bao, F. Miao, Z. Chen, H. Zhang, W. Jang, C. Dames, and C. N. a. Lau, "Controlled ripple texturing of suspended graphene and ultrathin graphite membranes," *Nature Nanotechnology*, vol. 4, no. 9, pp. 562–566, 2009.

[30] P. Le Doussal and L. Radzihovsky, "Self-consistent theory of polymerized membranes," *Phys. Rev. Lett.*, vol. 69, no. 8, pp. 1209–1212, 1992.

[31] J. C. Meyer, A. K. Geim, M. I. Katsnelson, K. S. Novoselov, D. Obergfell, S. Roth, C. Girit, and A. Zettl, "On the roughness of single- and bi-layer graphene membranes," *Solid State Communications*, vol. 143, no. 1, pp. 101–109, 2007.

[32] O. Kahn, *Molecular Magnetism*. Wiley-VCH, 1993.

[33] T. Makarova and F. Palacio, *Carbon Based Magnetism*. Elsevier, 2006.

[34] L. E. Hueso, J. M. Pruneda, V. Ferrari, G. Burnell, J. P. Valdes-Herrera, B. D. Simons, P. B. Littlewood, E. Artacho, A. Fert, and N. D. Mathur, "Transformation of spin information into large electrical signals using carbon nanotubes," *Nature*, vol. 445, no. 7126, pp. 410–413, 2007.

[35] B. Trauzettel, D. V. Bulaev, D. Loss, and G. Burkard, "Spin qubits in graphene quantum dots," *Nature Physics*, vol. 3, no. 3, pp. 192–196, 2007.

[36] N. Tombros, C. Jozsa, M. Popinciuc, H. T. Jonkman, and B. J. van Wees, "Electronic spin transport and spin precession in single graphene layers at room temperature," *Nature*, vol. 448, no. 7153, pp. 571–574, 2007.

[37] O. V. Yazyev, "Hyperfine Interactions in Graphene and Related Carbon Nanostructures," *Nano Letters*, vol. 8, no. 4, pp. 1011–1015, 2008.

[38] P. Esquinazi, D. Spemann, R. Höhne, A. Setzer, K.-H. Han, and T. Butz, "Induced Magnetic Ordering by Proton Irradiation in Graphite," *Phys. Rev. Lett.*, vol. 91, no. 22, p. 227201, 2003.

[39] H. Ohldag, T. Tyliszczak, R. Höhne, D. Spemann, P. Esquinazi, M. Ungureanu, and T. Butz, "π-Electron Ferromagnetism in Metal-Free Carbon Probed by Soft X-Ray Dichroism," *Phys. Rev. Lett.*, vol. 98, no. 18, pp. 187 204–187 208, 2007.

[40] A. V. Krasheninnikov and F. Banhart, "Engineering of nanostructured carbon materials with electron or ion beams," *Nature Materials*, vol. 6, no. 10, pp. 723–733, 2007.

[41] F. Banhart, "Irradiation effects in carbon nanostructures," *Reports on Progress in Physics*, vol. 62, no. 8, pp. 1181–1221, 1999.

[42] C. P. Ewels, R. H. Telling, A. A. El-Barbary, M. I. Heggie, and P. R. Briddon, "Metastable Frenkel Pair Defect in Graphite: Source of Wigner Energy?" *Phys. Rev. Lett.*, vol. 91, no. 2, p. 025505, 2003.

[43] R. H. Telling, C. P. Ewels, A. A. El-Barbary, and M. I. Heggie, "Wigner defects bridge the graphite gap," *Nature Materials*, vol. 2, no. 5, pp. 333–337, 2003.

[44] A. J. Stone and D. J. Walles, "Theoretical studies of icosahedral C60 and some related species," *Chemical Physics Letters*, vol. 128, no. 5-6, pp. 501–503, 1986.

[45] P. O. Lehtinen, A. S. Foster, A. Ayuela, A. Krasheninnikov, K. Nordlund, and R. M. Nieminen, "Magnetic Properties and Diffusion of Adatoms on a Graphene Sheet," *Phys. Rev. Lett.*, vol. 91, no. 1, pp. 017 202–017 206, 2003.

[46] P. O. Lehtinen, A. S. Foster, Y. Ma, A. V. Krasheninnikov, and R. M. Nieminen, "Irradiation-Induced Magnetism in Graphite: A Density Functional Study," *Phys. Rev. Lett.*, vol. 93, no. 18, pp. 187 202–187 206, 2004.

[47] K. F. Kelly and N. J. Halas, "Determination of α and β site defects on graphite using C60-adsorbed STM tips," *Surface Science*, vol. 416, no. 1-2, pp. L1085–L1089, 1998.

[48] D. M. Edwards and M. I. Katsnelson, "High-temperature ferromagnetism of sp electrons in narrow impurity bands: application to CaB_6," *Journal of Physics: Condensed Matter*, vol. 18, no. 31, pp. 7209–7225, 2006.

[49] J. Hubbard, "Electron Correlations in Narrow Energy Bands," *Proc. Roy. Soc. A*, vol. 276, no. 1365, pp. 238–257, 1963.

[50] J. Fernández-Rossier and J. J. Palacios, "Magnetism in Graphene Nanoislands," *Phys. Rev. Lett.*, vol. 99, no. 17, pp. 177 204–177 208, 2007.

[51] H. Feldner, Z. Y. Meng, A. Honecker, D. Cabra, S. Wessel, and F. F. Assaad, "Magnetism of finite graphene samples: Mean-field theory compared with exact diagonalization and quantum Monte Carlo simulations," *Phys. Rev. B*, vol. 81, no. 11, pp. 115 416–115 421, 2010.

[52] E. H. Lieb, "Two theorems on the Hubbard model," *Phys. Rev. Lett.*, vol. 62, no. 10, pp. 1201–1204, 1989.

[53] V. M. Pereira, J. M. B. Lopes Santos, and A. H. Castro Neto, "Modeling disorder in graphene," *Phys. Rev. B*, vol. 77, no. 11, pp. 115 109–115 126, 2008.

[54] J. J. Palacios, J. Fernandez-Rossier, and L. Brey, "Vacancy-induced magnetism in graphene and graphene ribbons," *Phys. Rev. B*, vol. 77, no. 19, pp. 195 428–195 442, 2008.

[55] H. Kumazaki and D. S. Hirashima, "Tight-binding study of nonmagnetic-defect-induced magnetism in graphene," *Low Temperature Physics*, vol. 34, no. 10, pp. 805–811, 2008.

[56] E. V. Castro, N. M. R. Peres, T. Stauber, and N. A. P. Silva, "Low-Density Ferromagnetism in Biased Bilayer Graphene," *Phys. Rev. Lett.*, vol. 100, no. 18, pp. 186 803–186 907, 2008.

[57] H. Kumazaki and D. S. Hirashima, "Nonmagnetic-Defect-Induced Magnetism in Graphene," *Journal Phys. Soc. Jpn*, vol. 76, no. 06, pp. 064 713–064 718, 2007.

[58] O. V. Yazyev and L. H. Helm, "Defect-induced magnetism in graphene," *Phys. Rev. B*, vol. 75, no. 12, pp. 125 408–125 413, 2007.

[59] J. C. Meyer, C. Kisielowski, R. Erni, M. D. Rossell, M. F. Crommie, and A. Zettl, "Direct Imaging of Lattice Atoms and Topological Defects in Graphene Membranes," *Nano Letters*, vol. 8, no. 11, pp. 3582–3586, 2008.

[60] A. A. El-Barbary, R. H. Telling, C. P. Ewels, M. I. Heggie, and P. R. Briddon, "Structure and energetics of the vacancy in graphite," *Phys. Rev. B*, vol. 68, no. 14, p. 144107, 2003.

[61] A. Hashimoto, K. Suenaga, A. Gloter, K. Urita, and S. Iijima, "Direct evidence for atomic defects in graphene layers," *Nature*, vol. 430, no. 7002, pp. 870–873, 2004.

[62] M. H. Gass, U. Bangert, A. Bleloch, P. Wang, R. R. Nair, and A. K. Geim, "Free-standing graphene at atomic resolution," *Nat. Nano.*, vol. 3, no. 11, pp. 676–681, 2008.

[63] J. A. Rodriguez-Manzo, O. Cretu, and F. Banhart, "Trapping of Metal Atoms in Vacancies of Carbon Nanotubes and Graphene," *ACS Nano*, vol. 4, no. 6, pp. 3422–3428, 2010.

[64] O. V. Yazyev and M. I. Katsnelson, "Magnetic Correlations at Graphene Edges: Basis for Novel Spintronics Devices," *Phys. Rev. Lett.*, vol. 100, no. 4, p. 047209, 2008.

[65] J. Zhou, Q. Wang, Q. Sun, X. S. Chen, Y. Kawazoe, and P. Jena, "Ferromagnetism in Semihydrogenated Graphene Sheet," *Nano Letters*, vol. 9, no. 11, pp. 3867–3870, 2009.

[66] J. O. Sofo, A. S. Chaudhari, and G. D. Barber, "Graphane: A two-dimensional hydrocarbon," *Phys. Rev. B*, vol. 75, no. 15, pp. 153 401–153 405, 2007.

[67] A. Bostwick, t. Ohta, J. L. McChesney, K. V. Emtsev, F. Speck, T. Seyller, K. Horn, S. D. Kevan, and E. Rotenberg, "The interaction of quasi-particles in graphene with chemical dopants," *New Journal of Physics*, vol. 12, no. 12, pp. 125 014–125 029, 2010.

[68] Y. Zheng and T. Ando, "Hall conductivity of a two-dimensional graphite system," *Phys. Rev. B*, vol. 65, no. 24, pp. 245 420–245 431, 2002.

[69] C. Bena and S. A. Kivelson, "Quasiparticle scattering and local density of states in graphite," *Phys. Rev. B*, vol. 72, no. 12, pp. 125 432–125 437, 2005.

[70] N. M. R. Peres, A. H. Castro Neto, and F. Guinea, "Conductance quantization in mesoscopic graphene," *Physical Review B*, vol. 73, no. 19, pp. 195 411–195 419, 2006.

[71] N. M. R. Peres, F. Guinea, and A. H. Castro Neto, "Electronic properties of disordered two-dimensional carbon," *Phys. Rev. B*, vol. 73, no. 12, pp. 125 411–125 434, 2006.

[72] J. Kong, N. R. Franklin, C. Zhou, M. G. Chapline, S. Peng, K. Cho, and H. Dai, "Nanotube Molecular Wires as Chemical Sensors," *Science*, vol. 287, no. 5453, pp. 622–625, 2000.

[73] W. Kim, A. Javey, O. Vermesh, Q. Wang, Y. Li, and H. Dai, "Hysteresis Caused by Water Molecules in Carbon Nanotube Field-Effect Transistors," *Nano Letters*, vol. 3, no. 2, pp. 193–198, 2003.

[74] D. C. Elias, R. R. Nair, T. M. G. Mohiuddin, S. V. Morozov, P. Blake, M. P. Halsall, A. C. Ferrari, D. W. Boukhvalov, M. I. Katsnelson, A. K. Geim, and K. S. Novoselov, "Control of Graphene's Properties by Reversible Hydrogenation: Evidence for Graphane," *Science*, vol. 323, no. 5914, pp. 610–613, 2009.

[75] S. Lebègue, M. Klintenberg, O. Eriksson, and M. I. Katsnelson, "Accurate electronic band gap of pure and functionalized graphane from GW calculations," *Phys. Rev. B*, vol. 79, no. 24, pp. 245 117–245 123, 2009.

[76] F. Schedin, A. K. Geim, S. V. Morozov, D. Jiang, E. H. Hill, P. Blake, and K. S. Novoselov, "Detection of Individual Gas Molecules Absorbed on Graphene," *Nature Materials*, vol. 6, no. 01, p. 652, 2007.

[77] P. G. Collins, K. Bradley, M. Ishigami, and A. Zettl, "Extreme Oxygen Sensitivity of Electronic Properties of Carbon Nanotubes," *Science*, vol. 287, no. 5459, pp. 1801–1804, 2000.

[78] Y. Gan, L. Sun, and F. Banhart, "One- and Two-Dimensional Diffusion of Metal Atoms in Graphene," *Small*, vol. 4, no. 5, pp. 587–591, 2008.

[79] S. Heinze, J. Tersoff, R. Martel, V. Derycke, J. Appenzeller, and P. Avouris, "Carbon Nanotubes as Schottky Barrier Transistors," *Phys. Rev. Lett.*, vol. 89, no. 10, pp. 106 801–106 805, 2002.

[80] M. Ushiro, K. Uno, T. Fujikawa, Y. Sato, K. Tohji, F. Watari, W. J. Chun, Y. Koike, and K. Asakura, "X-ray absorption fine structure (XAFS) analyses of Ni species trapped in graphene sheet of carbon nanofibers," *Phys. Rev. B*, vol. 73, no. 14, pp. 144 103–144 114, 2006.

[81] F. Banhart, J. C. Charlier, and P. M. Ajayan, "Dynamic Behavior of Nickel Atoms in Graphitic Networks," *Phys. Rev. Lett.*, vol. 84, no. 4, pp. 686–689, 2000.

[82] M. S. Dresselhaus, G. Dresselhaus, and P. Avouris, *Carbon Nanotubes: Synthesis, Structure, Properties, and Applications*. Springer Verlag, 2001.

[83] J. A. Rodriguez-Manzo and F. Banhart, "Creation of Individual Vacancies in Carbon Nanotubes by Using an Electron Beam of 1 Å Diameter," *Nano Letters*, vol. 9, pp. 2285–2289, 2009.

[84] L. Brey, H. A. Fertig, and S. Das Sarma, "Diluted Graphene Antiferromagnet," *Phys. Rev. Lett.*, vol. 99, no. 11, pp. 116 802–116 806, 2007.

[85] D. F. Kirwan, C. G. Rocha, A. T. Costa, and M. S. Ferreira, "Sudden decay of indirect exchange coupling between magnetic atoms on carbon nanotubes," *Phys. Rev. B*, vol. 77, no. 8, pp. 085 432–085 438, 2008.

[86] N. Ashcroft and N. Mermin, *Solid State Physics*. Saunders College, 1976.

[87] W. Kohn, "Nobel Lecture: Electronic structure of matter—wave functions and density functionals," *Rev. Mod. Phys.*, vol. 71, no. 5, pp. 1253–1266, 1999.

[88] P. Hohenberg and W. Kohn, "Inhomogeneous Electron Gas," *Phys. Rev.*, vol. 136, no. 3B, pp. B864–B871, 1964.

[89] R. M. Martin, *Electronic Structure: Basic Theory and Practical Methods*. Cambridge University Press, Cambridge, UK, 2004.

[90] W. Kohn and L. J. Sham, "Self-Consistent Equations Including Exchange and Correlation Effects," *Phys. Rev.*, vol. 140, no. 4A, pp. A1133–A1138, 1965.

[91] S. Lundqvist and N. H. March, *Theory of the Inhomogeneous Electron Gas*. Springer, 1983.

[92] J. P. Perdew, K. Burke, and M. Ernzerhof, "Generalized Gradient Approximation Made Simple," *Phys. Rev. Lett.*, vol. 77, no. 18, pp. 3865–3868, 1996.

[93] J. P. Perdew, R. G. Parr, M. Levy, and J. L. Balduz, "Density-Functional Theory for Fractional Particle Number: Derivative Discontinuities of the Energy," *Phys. Rev. Lett.*, vol. 49, no. 23, pp. 1691–1694, 1982.

[94] O. Gunnarsson and K. Schönhammer, "Density-Functional Treatment of an Exactly Solvable Semiconductor Model," *Phys. Rev. Lett.*, vol. 56, no. 18, pp. 1968–1971, 1986.

[95] R. W. Godby, M. Schlüter, and L. J. Sham, "Accurate Exchange-Correlation Potential for Silicon and Its Discontinuity on Addition of an Electron," *Phys. Rev. Lett.*, vol. 56, no. 22, pp. 2415–2418, 1986.

[96] M. Gruning, A. Marini, and A. Rubio, "Density functionals from many-body perturbation theory: The band gap for semiconductors and insulators," *The Journal of Chemical Physics*, vol. 124, no. 15, pp. 154 108–154 117, 2006.

[97] J. M. Soler, E. Artacho, J. D. Gale, A. García, J. Junquera, P. Ordejón, and D. Sánchez-Portal, "The SIESTA method for ab initio order-N materials simulation," *Jour. of Phys.: Condensed Matter*, vol. 14, pp. 2745–2779, 2002.

[98] W. A. Harrison, *Electronic Structure and the Properties of Solids*. Dover edition, 1989.

[99] M. C. Payne, M. P. Teter, D. C. Allan, T. A. Arias, and J. D. Joannopoulos, "Iterative minimization techniques for ab initio total-energy calculations: molecular dynamics and conjugate gradients," *Rev. Mod. Phys.*, vol. 64, no. 4, pp. 1045–1097, 1992.

[100] N. Troullier and J. L. Martins, "Efficient pseudopotentials for plane-wave calculations," *Phys. Rev. B*, vol. 43, no. 3, pp. 1993–2006, Jan 1991.

[101] S. G. Louie, S. Froyen, and M. L. Cohen, "Nonlinear ionic pseudopotentials in spin-density-functional calculations," *Phys. Rev. B*, vol. 26, no. 4, pp. 1738–1742, 1982.

[102] G. Kresse and Furthmüller, "Efficiency of ab-initio total energy calculations for metals and semiconductors using a plane-wave basis set," *Comput. Mat. Sci.*, vol. 6.

[103] H. J. Monkhorst and J. D. Pack, "Special points for Brillouin-zone integrations," *Phys. Rev. B*, vol. 13, no. 12, pp. 5188–5192, Jun 1976.

[104] J. Junquera, O. Paz, D. Sánchez-Portal, and E. Artacho, "Numerical atomic orbitals for linear-scaling calculations," *Phys. Rev. B*, vol. 64, no. 23, p. 235111, Nov 2001.

[105] G. Kresse and J. Hafner, "Ab initio molecular dynamics for liquid metals," *Phys. Rev. B*, vol. 47, no. 1, pp. 558–561, Jan 1993.

[106] G. Kresse and J. Furthmüller, "Efficient iterative schemes for ab initio total-energy calculations using a plane-wave basis set," *Phys. Rev. B*, vol. 54, no. 16, pp. 11 169–11 186, Oct 1996.

[107] M. Asato, A. Settels, T. Hoshino, T. Asada, S. Blügel, R. Zeller, and P. H. Dederichs, "Full-potential KKR calculations for metals and semiconductors," *Phys. Rev. B*, vol. 60, no. 8, pp. 5202–5210, 1999.

[108] S. Shallcross, A. E. Kissavos, V. Meded, and A. V. Ruban, "An ab initio effective Hamiltonian for magnetism including longitudinal spin fluctuations," *Phys. Rev. B*, vol. 72, no. 10, p. 104437, 2005.

[109] M. Battocletti, H. Ebert, and H. Akai, "Influence of gradient corrections to the local-density-approximation on the calculation of hyperfine fields in ferromagnetic Fe, Co, and Ni," *Phys. Rev. B*, vol. 53, no. 15, pp. 9776–9783, 1996.

[110] M. Machón, S. Reich, C. Thomsen, D. Sánchez-Portal, and P. Ordejón, "Ab initio calculations of the optical properties of 4-Å-diameter single-walled nanotubes," *Phys. Rev. B*, vol. 66, no. 15, p. 155410, 2002.

[111] S. García-Gil, A. García, N. Lorente, and P. Ordejón, "Optimal strictly localized basis sets for noble metal surfaces," *Phys. Rev. B*, vol. 79, no. 7, p. 075441, 2009.

[112] A. V. Krasheninnikov, P. O. Lehtinen, A. S. Foster, P. Pyykkö, and R. M. Nieminen, "Embedding Transition-Metal Atoms in Graphene: Structure, Bonding, and Magnetism," *Phys. Rev. Lett.*, vol. 102, no. 12, pp. 126 807–126 811, 2009.

[113] E. J. G. Santos, A. Ayuela, S. B. Fagan, J. Mendes Filho, D. L. Azevedo, A. G. Souza Filho, and D. Sánchez-Portal, "Switching on magnetism in Ni-doped graphene: Density functional calculations," *Phys. Rev. B*, vol. 78, pp. 195 420–195 425, 2008.

[114] E. J. G. Santos, A. Ayuela, and D. Sánchez-Portal, "Magnetism of Covalently Functionalized Carbon Nanotubes," *Appl. Phys. Lett.*, vol. 99, no. 6, pp. 062 503–062 506, 2011.

[115] E. J. G. Santos, D. Sánchez-Portal, and A. Ayuela, "Magnetism of substitutional Co impurities in graphene: Realization of single π vacancies," *Phys. Rev. B*, vol. 81, no. 12, pp. 125 433–125 439, 2010.

[116] For simplicity and consistency we use throughout this chapter the same nomenclature to label the different defect levels. However, it should be understood that for the noble metals and Zn the so-called antibonding A p_z-d_{z^2} level presents a sizeable contribution from the metal s orbital, while the degenerate E sp-d levels have non-negligible contributions from the p orbitals of the metal. .

[117] R. Sielemann, Y. Kobayashi, Y. Yoshida, H. P. Gunnlaugsson, and G. Weyer, "Magnetism at Single Isolated Iron Atoms Implanted in Graphite," *Phys. Rev. Lett.*, vol. 101, no. 13, pp. 137 206–137 208, 2008.

[118] J. Barzola-Quiquia, R. Höhne, M. Rothermel, A. Setzer, P. Esquinazi, and V. Heera, "A comparison of the magnetic properties of proton- and iron-implanted graphite," *Eur. Phys. Jour. B*, vol. 61, no. 2, pp. 127–130, 2008.

[119] S. Malola, H. Häkkinen, and P. Koskinen, "Gold in graphene: In-plane adsorption and diffusion," *Appl. Phys. Lett.*, vol. 94, no. 4, pp. 043 106–043 110, 2009.

[120] A. K. Geim and A. H. MacDonald, "Graphene: Exploring Carbon Flatland," *Phys. Today*, vol. 60, no. 8, pp. 35–41, January 2007.

[121] H. Amara, S. Latil, V. Meunier, P. Lambin, and J.-C. Charlier, "Scanning tunneling microscopy fingerprints of point defects in graphene: A theoretical prediction," *Phys. Rev. B*, vol. 76, no. 11, pp. 115 423–115 433, 2007.

[122] N. M. R. Peres, F. D. Klironomos, S. W. Tsai, J. R. Santos, J. M. B. Lopes dos Santos, and A. H. Castro Neto, "Electron waves in chemically substituted graphene," *Europhysics Letters*, vol. 80, no. 6, pp. 67 007–67 013, 2007.

[123] T. O. Wehling, A. V. Balatsky, M. I. Katsnelson, A. I. Lichtenstein, K. Scharnberg, and R. Wiesendanger, "Local electronic signatures of impurity states in graphene," *Phys. Rev. B*, vol. 75, no. 12, pp. 125 425–125 430, 2007.

[124] E. J. G. Santos, A. Ayuela, and D. Sanchez-Portal, "First-principles study of substitutional metal impurities in graphene: structural, electronic and magnetic properties," *New Journal of Physics*, vol. 12, no. 5, pp. 053 012–053 044, 2010.

[125] T. O. Wehling, M. I. Katsnelson, and A. I. Lichtenstein, "Impurities on graphene: Midgap states and migration barriers," *Phys. Rev. B*, vol. 80, no. 8, pp. 085 428–085 435, 2009.

[126] R. Haggenmueller, H. H. Gommans, A. G. Rinzler, and J. E. Fischer, "Aligned single-wall carbon nanotubes in composites by melt processing methods," *Chem. Phys. Lett.*, vol. 330.

[127] P. Singh, J. Kumar, F. Toma, J. Raya, M. Prato, B. Fabre, S. Verma, and A. Bianco, "Synthesis and characterization of nucleobase-carbon nanotube hybrids," *J. Am. Chem. Soc.*, vol. 131, no. 37, pp. 13 555–13 562, 2009.

[128] R. K. Saini, I. W. Chiang, H. Peng, R. E. Smalley, W. E. Billups, R. H. Hauge, and J. L. Margrave, "Covalent sidewall functionalization of single wall carbon nanotubes," *J. Am. Chem. Soc.*, vol. 125, no. 12, pp. 3617–3621, 2003.

[129] J. L. Bahr, J. Yang, D. V. Kosynkin, M. J. Bronikowski, R. E. Smalley, and J. M. Tour, "Functionalization of Carbon Nanotubes by Electrochemical Reduction of Aryl Diazonium Salts:âĂL'A Bucky Paper Electrode," *J. Am. Chem. Soc.*, vol. 123, no. 27, pp. 6536–6542, 2001.

[130] H. A. Mizes and J. S. Foster, "Long-Range Electronic Perturbations Caused by Defects Using Scanning Tunneling Microscopy," *Science*, vol. 244, no. 4904, pp. 559–562, 1989.

[131] G. M. Rutter, J. N. Crain, N. P. Guisinger, T. Li, P. N. First, and J. A. Stroscio, "Scattering and Interference in Epitaxial Graphene," *Science*, vol. 317, no. 5835, pp. 219–222, 2007.

[132] P. Ruffieux, O. Gröning, P. Schwaller, L. Schlapbach, and P. Gröning, "Hydrogen Atoms Cause Long-Range Electronic Effects on Graphite," *Phys. Rev. Lett.*, vol. 84, no. 21, pp. 4910–4913, 2000.

[133] O. V. Yazyev, "Magnetism in Disordered Graphene and Irradiated Graphite," *Phys. Rev. Lett.*, vol. 101, no. 3, p. 037203, 2008.

[134] S. Saremi, "RKKY in half-filled bipartite lattices: Graphene as an example," *Phys. Rev. B*, vol. 76, no. 18, p. 184430, 2007.

[135] M. A. H. Vozmediano, M. P. López-Sancho, T. Stauber, and F. Guinea, "Local defects and ferromagnetism in graphene layers," *Phys. Rev. B*, vol. 72, no. 15, p. 155121, 2005.

[136] D. W. Boukhvalov, M. I. Katsnelson, and A. I. Lichtenstein, "Hydrogen on graphene: Electronic structure, total energy, structural distortions and magnetism from first-principles calculations," *Phys. Rev. B*, vol. 77, no. 3, pp. 035 427–035 434, 2008.

[137] A. V. Shytov, D. A. Abanin, and L. S. Levitov, "Long-Range Interaction between Adatoms in Graphene," *Phys. Rev. Lett.*, vol. 103, no. 1, p. 016806, 2009.

[138] J. Rohrl, M. Hundhausen, K. V. Emtsev, T. Seyller, R. Graupner, and L. Ley, "Raman spectra of epitaxial graphene on SiC(0001)," *Applied Physics Letters*, vol. 92, no. 20, pp. 201 918–201 921, 2008.

[139] G. M. Rutter, N. P. Guisinger, J. N. Crain, E. A. A. Jarvis, M. D. Stiles, T. Li, P. N. First, and J. A. Stroscio, "Imaging the interface of epitaxial graphene with silicon carbide via scanning tunneling microscopy," *Phys. Rev. B*, vol. 76, no. 23, pp. 235 416–235 422, 2007.

[140] A. L. Vázquez de Parga, F. Calleja, B. Borca, M. C. G. Passeggi, J. J. Hinarejos, F. Guinea, and R. Miranda, "Periodically Rippled Graphene: Growth and Spatially Resolved Electronic Structure," *Phys. Rev. Lett.*, vol. 100, no. 5, pp. 056 807–056 811, 2008.

[141] H. C. Schniepp, K. N. Kudin, J. L. Li, R. K. PrudâĂŹhomme, R. Car, D. A. Saville, and I. A. Aksay, "Bending Properties of Single Functionalized Graphene Sheets Probed by Atomic Force Microscopy," *ACS Nano*, vol. 2, no. 12, pp. 2577–2584, 2008.

[142] U. Bangert, M. H. Gass, A. L. Bleloch, R. R. Nair, and A. K. Geim, "Manifestation of ripples in free-standing graphene in lattice images obtained in an aberration-corrected scanning transmission electron microscope," *physica status solidi (a)*, vol. 206, no. 6, pp. 1117–1122, 2009.

[143] T. M. G. Mohiuddin, A. Lombardo, R. R. Nair, A. Bonetti, G. Savini, R. Jalil, N. Bonini, D. M. Basko, C. Galiotis, N. Marzari, K. S. Novoselov, A. K. Geim, and A. C. Ferrari, "Uniaxial strain in graphene by Raman spectroscopy: G peak splitting, Grüneisen parameters, and sample orientation," *Phys. Rev. B*, vol. 79, no. 20, pp. 205 433–205 441, 2009.

[144] K. S. Kim, Y. Zhao, H. Jang, S. Y. Lee, J. M. Kim, K. S. Kim, J. H. Ahn, P. Kim, J. Y. Choi, and B. H. Hong, "Large-scale pattern growth of graphene films for stretchable transparent electrodes," *Nature*, vol. 457, no. 7230, pp. 706–710, 2009.

[145] B. Standley, W. Bao, H. Zhang, J. Bruck, C. N. Lau, and M. Bockrath, "Graphene-Based Atomic-Scale Switches," *Nano Letters*, vol. 8, no. 10, pp. 3345–3349, 2008.

[146] A. K. Geim, "Graphene: Status and Prospects," *Science*, vol. 324, pp. 1530–1534, 2009.

[147] L. Xie, X. Wang, J. Lu, Z. Ni, M. Luo, Z.and Mao, R. Wang, W. Y., H. Huang, D. Qi, R. Liu, T. Yu, Z. Shen, T. Wu, H. Peng, B. Ozyilmaz, K. Loh, A. T. S. Wee, Ariando, and W. Chen, "Room temperature ferromagnetism in partially hydrogenated epitaxial graphene," *App. Phys. Lett.*, vol. 98, no. 19, pp. 193 113–193 116, 2011.

[148] E. J. G. Santos, A. Ayuela, D. Sánchez-Portal, and M. Brandbyge, "Gate-Field Controlled Spin Transport in Graphitic Carbon," *Submitted*.

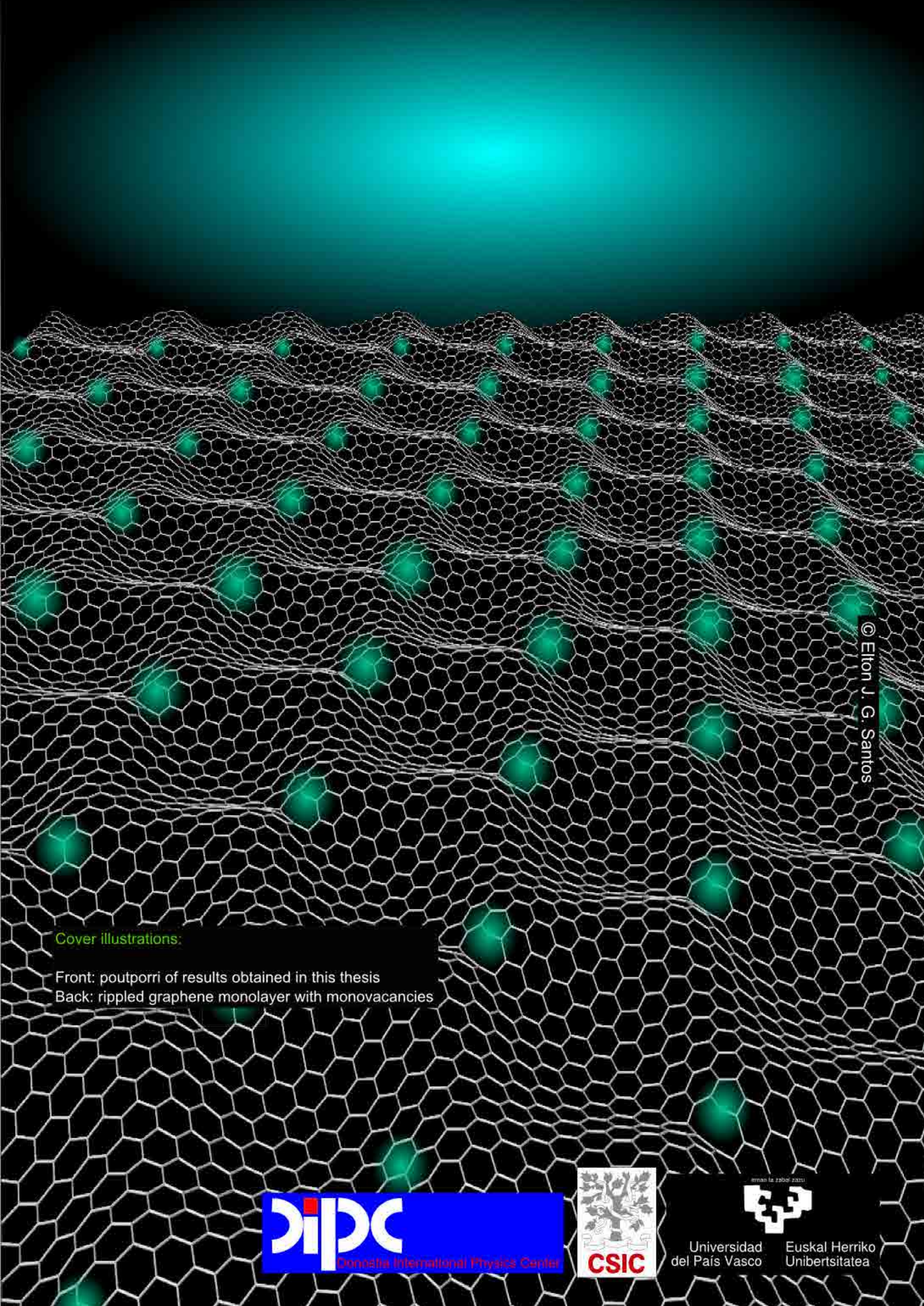

Cover illustrations:

Front: poutporri of results obtained in this thesis
Back: rippled graphene monolayer with monovacancies

DIPC
Donostia International Physics Center

CSIC

Universidad del País Vasco

Euskal Herriko Unibertsitatea